NANYANG TECHNOLOGICAL UNIVERSITY
SINGAPORE

Reinforcement Mechanism of Rockbolt System for Underground Excavation

NIE WEN

SCHOOL OF CIVIL AND ENVIRONMENTAL ENGINEERING

2019

Reinforcement Mechanism of Rockbolt System for Underground Excavation

NIE WEN

School of Civil and Environmental Engineering

A thesis submitted to the Nanyang Technological University
in partial fulfilment of the requirements for the degree of
Doctor of Philosophy

Statement of Originality

I hereby certify that the work embodied in this thesis is the result of original research, is free of plagiarised materials, and has not been submitted for a higher degree to any other University or Institution.

19/Jan/2019
Date


NIE Wen

Supervisor Declaration Statement

I have reviewed the content and presentation style of this thesis and declare it is free of plagiarism and of sufficient grammatical clarity to be examined. To the best of my knowledge, the research and writing are those of the candidate except as acknowledged in the Author Attribution Statement. I confirm that the investigations were conducted in accord with the ethics policies and integrity standards of Nanyang Technological University and that the research data are presented honestly and without prejudice.

19 Jan 2019
Date


Zhao Zhiye

Authorship Attribution Statement

This thesis contains material from 2 papers published in the following peer-reviewed journals where I was the first author.

Chapter 3 is published as Nie, W., Zhao, Z.Y., Guo, W., Shang, J., Wu, C. Bond-slip modeling of a CMC bolt element using 2D-DDA method. Tunnelling and Underground Space Technology, 2019, 85: 340-353. DOI: https://doi.org/10.1016/j.tust.2018.12.025

The contributions of the co-authors are as followings:

- A/Prof Zhao provided guidance in the numerical models.
- I initiated the project direction and wrote the drafts of the manuscript.
- Dr Guo assisted in the data analyzing and edited the manuscript drafts.
- Dr Shang and Dr Wu suggested the data analyzing methods.

Chapter 5 is published as Nie, W., Zhao, Z.Y., Ma, S.Q., and Guo W. Efforts of joints on the reinforced rock units of fully-grouted rockbolts. Tunnelling and Underground Space Technology, 2018, 71, 15-26. DOI: https://doi.org/10.1016/j.tust.2017.07.005

The contributions of the co-authors are as followings:

- A/Prof Zhao provided guidance in the numerical models and edited the manuscript drafts.
- I initiated the project direction and wrote the drafts of the manuscript.

- Dr Ma assisted in the data analyzing.
- Dr Guo assisted in the data analyzing and revised the manuscript.

Chapter 7 is published as Nie, W., Zhao, Z.Y., Goh A.T.C., Song, M.K., Guo W., and Zhu X. Performance based support design for horseshoe-shaped rock caverns using 2D numerical analysis. Engineering Geology, 2018, 245, 266-279. DOI: https://doi.org/10.1016/j.enggeo.2018.09.007.

The contributions of the co-authors are as followings:

- A/Prof Zhao provided the initial project direction and edited the manuscript drafts.
- I performed all the numerical simulation and collected the data.
- I conducted data evaluation together with Dr Zhu and Dr Guo.
- I wrote the drafts of the manuscript. The manuscript was revised by Dr Guo.
- A/Prof Goh and Dr Song suggested the data analyzing methods.

19 / Jan / 2019
Date

NIE Wen

ACKNOWLEDGEMENT

I would like to express the sincerest gratitude to my supervisor, Professor Zhao Zhiye, for his never-ending inspiration, patience and guidance. His endlessly support and invaluable suggestions came handy throughout the last three years. I have greatly benefited from his wealth of knowledge and insight. I could not ask for a better supervisor.

I also would like to thank Prof Goh Anthony, Prof Chu Jian, Prof Zhou Yingxin, Dr Lee Hong Song, Dr Song Myungkyu, Dr Ma Shuqi, Dr Shang Junlong and Dr Zhang Wengang for their technical supports and their sharing research experiences. I would like to give my appreciation to my colleagues and friends including Dr Ning Youjun, Dr Chen Huimei, Dr Wu Shifan, Ms Liu Qian, Mr Xiao Fei, Mr Yokota Yasuhiro, Dr He Lei and Dr Sun Jianping for their encouragement and friendship.

And finally, I wish to give my appreciation to my husband, colleague and best friend, Dr Guo Wei, for his technical sharing, unbiased understanding and endless support. I want to thank my little boy, Mr. Guo Youjia, for his lovely encouragement. His smiles are the therapy for me in troubles and the energy to keep me going. I also could not have done this work without the support and love from my mother Ms. Wang Lianyun, my farther Mr. Nie Peixun and my parents-in-law. I could not thank them enough.

TABLE OF CONTENTS

SUMMARY

A rockbolt is a reinforcing element installed untensioned or tensioned into the ground to restrict the deformation of the surrounding rock mass in rock engineering. The rockbolt is usually a solid bar or tube element which is installed within the boreholes drilled into the rock. To improve the rockbolt design in complex rock conditions, it is necessary to have a good understanding of the reinforcement mechanism of the rockbolts. In this thesis, the reinforcement mechanism of a rockbolt system under excavation conditions is studied using the two-dimensional discontinuous deformation analysis (2D-DDA) method and other numerical tools.

The load transfer capacity of a rockbolt element is controlled by the components of bonds at the rock and rockbolt, such as the rock mass, the mortar and the profile configuration of the rockbolt. 2D-DDA method is used to investigate the pullout performance of a continuously mechanically coupled (CMC) rockbolt element. The flat joint contact model is introduced into the 2D-DDA code to simulate the force versus displacement behaviour of an artificial joint. Parametric studies show that the confining pressure plays an important role in the bond-slip modeling. The obtained key parameters of the trilinear bond-slip model can be used to simulate the bond behaviour between the rockbolt and rock under similar conditions.

A rockbolt model is developed and integrated into the 2D-DDA code based on the load transfer theory. Three mechanical behaviours are considered in the model, i.e., the bond, the axial tension and the shear at joint. The proposed rockbolt model could be used to simulate four major failure modes of rockbolt, such as the de-bonding along the interface, tensile failure, faceplate failure and shear failure. The numerical results show that the numerical models have reasonable agreements with the experiments results. The parameter studies show that the load transfer and load capacity should be reconsidered when the ground conditions are changed.

The rock/rockbolt interactions are examined by simulating the pullout test in rock mass with systematic joint sets. The effects of the rock properties, joint orientations, rockbolt lengths and in-plane spacing are studied. The reinforcement rock unit (RRU) induced by single rockbolt is normally in a cone shape and restrained by the orientation of the discontinuities. The RRU induced by grouped rockbolts is heavily influenced by the joint orientations and the rockbolt spacing. Further applications of the RRUs on the estimation of the artificial pressure arch in the roof are illustrated.

The rockbolt to stabilize roof wedges in underground opening is studied using the joint relaxation method to consider the rock wedge in deformable rock conditions. Parametric studies are carried out to investigate the key parameters that influence the effects of rockbolts when they are used to stabilize the rock wedge. The results show that 2D-DDA could be used to find the critical horizontal pressure to sustain the rock wedges. A cross section in storage gallery in Jurong Rock Caverns (JRC), Singapore, is conducted to show the application of the 2D-DDA models for rockbolt design to support roof wedges. The stress versus vertical displacement curves showed clearly the effect of rockbolt on sustaining the movement of rock wedge. The way to create characteristic diagram could be used by the site engineers to evaluate the rockbolting design to sustain the possible roof wedges.

A support design method for horseshoe-shaped rock caverns is proposed with considerations of the progressive damage of the rock mass using the 2D finite element method (FEM) and the artificial neural network (ANN). The performances of the rock cavern during excavation are investigated based on the convergence-confinement method (CCM). The ANN models are built using the numerical results to find the complex relationships among the rock mass condition, the sequential excavation parameters and the cavern performances. An evaluation chart is proposed by integrating the ANN models into the EXCEL software. The proposed evaluation chart provides an effective method to evaluate the support safety, the functions of the patterned rockbolt and the optimization of subdivisions of the excavation cross section. More advanced function is still required to present the relationship between the parameters of sequential excavation method (SEM) and the cavern performance.

LIST OF PUBLICATIONS

1. **Nie, W.**, Zhao, Z.Y., Guo, W., Shang, J. and Wu, C.Z. Bond-slip modeling of a CMC rockbolt element using 2D-DDA method. Tunnelling and Underground Space Technology, 2019, 85: 340-353.

2. **Nie, W.**, Zhao, Z.Y., Ma, S.Q. and Guo, W. Efforts of joints on the reinforced rock units of fully-grouted rockbolts. Tunnelling and Underground Space Technology, 2018, 71: 15-26.

3. **Nie, W.**, Zhao, Z.Y., Goh, A.T.C., Song, M.K., Guo, W. and Zhu, X. Performance based support design for horseshoe-shaped rock caverns using 2D numerical analysis. Engineering Geology, 2018, 245: 266-279

4. Ma, S.Q., Zhao, Z.Y., **Nie, W.*** and Zhu, X. An analytical model for fully grouted rockbolts with consideration of the pre- and post-yielding behaviour. Rock Mechanics and Rock Engineering, 2017, 50(11): 3019-3028

5. **Nie, W.**, Zhao, Z.Y. and Ma, S.Q. Numerical evaluation of rockbolt reinforcement unit in jointed rock mass by DDA method. In Reşat Ulusay, Ömer Aydan, Hasan Gerçek, Ali Mehmet Hindistan and Ergün Tuncay(Eds), Rock Mechanics and Rock Engineering: From the past to the future, July 2016, Taylor & Francis Group, pp. 487-492. (Conference paper)

LIST OF FIGURES

LIST OF TABLES

LIST OF SYMBOLS

Symbols		Description
r_b	:	Radius of a rockbolt
D_b	:	Diameter of a rockbolt
A_b	:	Cross-section area of rockbolt
D_H	:	Diameter of borehole
E_b	:	Elastic modulus of a rockbolt
L_b	:	Length of a rockbolt
l_e	:	Assumed hinge length
l_0	:	Embedded length of a rockbolt
s_b	:	In-plane spacing of pattern rockbolts
F_s	:	Unit bond force
τ	:	Bond stress
δ	:	Slip displacement at bond
τ_{max}	:	Maximum bond strength at the rock and rockbolt interface
τ_{res}	:	Residual bond strength at the rock and rockbolt interface
k	:	Bond stiffness of a bond-slip model
K_s	:	Shear stiffness of a rockbolt element
σ_y	:	Yield strength of a rockbolt element
ε_{ext}	:	Extreme plastic strain of a rockbolt element
E_G	:	Elastic modulus of mortar
E_r	:	Elastic modulus of rock

φ	:	Friction angle of a joint
c	:	Cohesion of a joint
σ_t	:	Tensile strength of a joint
ρ	:	Density of a block
γ	:	Unit weight of a block
v	:	Poisson's ratio of a block
k_n	:	Normal stiffness of joint/contact
k_s	:	Shear stiffness of joint/contact
R_n	:	Normal contact force at a joint
R_s	:	Shear contact force at a joint
g_1	:	Pre-set maximum time increment in 2D-DDA calculation
g_2	:	Maximum allowed displacement ratio in 2D-DDA calculation
B	:	Cavern span
D_p	:	Damage depth of excavation damaged zone (EDZ)
s_f	:	Safety factor
p_i	:	Support pressure
u_i	:	Displacement at the excavation surface
p_{cr}	:	Critical horizontal confining pressure

CHAPTER 1. INTRODUCTION

1.1 Background

Underground space has been increasingly exploited in recent years. The potential for instability in the rock mass surrounding the underground excavation is a threat to the lives and safety of construction workers. To mitigate safety hazards, it is necessary to understand the causes of instability and design supports to eliminate or minimise the risks (Hoek et al., 2000).

The support is the procedures and materials used to improve the stability and maintain the load-carrying capability of rock mass surrounding the underground excavation (Brandy and Brown, 2006). Based on the application of reactive forces to the surrounding rock mass, the supports could be divided into support and reinforcement (Windsor and Thompson, 1993). Support (i.e., timber, shotcrete, steel frame, etc.) will apply reactive forces to the excavation surface. Reinforcement is targeting to improve the overall rock mass properties. Rockbolting is one of the important techniques to provide reinforcement in the rock mass.

The rockbolt has been the primary reinforcement structure in underground tunnelling and mining for quite a long period. It is usually simple to apply and can be modified to reinforce the rock mass during excavation. To mobilize the reinforcement efforts and improve the design of the rockbolt, it is necessary to have a good understanding of its reinforcement mechanism. However, the reinforcement mechanism of rockbolt system has not been fully understood as the rockbolt system design remains an art rather than a science since most designs are based on historical experiences (Hoek et al., 2000). To ensure the stability of underground excavations, the rockbolt system is usually overdesigned, leading to extra time and cost.

The load transfer capacity between rockbolt and rock is one of the most important factors controlling the reinforcement efforts of the rockbolt. When the rock moves towards the excavation surface, the rockbolt elongates. Tension is created in the rockbolt and transferred to the rock as bond stress, thus helps the rock to support itself by increasing confinement (Bobet and Einstein, 2011). To increase the efficiency of the load transfer capacity, many types of rockbolt elements have been developed. The bond-slip models are introduced to describe the relationship between the bond stress and the slip at the rock and rockbolt interface for different types of rockbolt elements (Benmokrane et al., 1995; Moosavi et al., 2005; Ren et al., 2010; BlancoMartín et al., 2011; Deb and Das, 2011; Ma et al., 2013; Ma et al., 2014; Zhandarov and Mäder, 2016). However, there is a lack of studies on the application of the bond-slip models to assess the reinforcement mechanism of the rockbolt.

The reinforcement mechanism of rockbolt is complex in field due to the existing of joints, faults and other discontinuities in rock mass. Three theories have been proposed in recent years to study the reinforcement mechanism of rockbolt in complex ground conditions (Lang and Bischoff, 1982; Hoek et al, 2000; Brandy and Brown, 2006). For massive rock blocks, the limited rock block stability analysis is used to analyse the stability of the rock wedges. For stratified rock mass, the rockbolts are designed to transfer the weight from weak strata to the strong strata. In jointed rock mass, the loose zone could be stabilized by the systematic rockbolts in the formation of artificial arch. Numerical studies have been carried out to simulate the interaction between rockbolt and rock mass (Sari and Pasmehmetoglu, 2004; Bobet and Einstein, 2011; Deb and Das, 2014; Ma et al., 2016; Nie et al., 2014a; Feng et al., 2018). Among these studies, the discontinuous element method becomes a primary choice when dealing with the study of reinforcement mechanism of rockbolt as it can simulate the the mechanical behaviour of an assembled rock blocks. Discontinuous Deformation Analysis (DDA), introduced by Shi in 1980s (Shi, 1988), is one of the discontinuum methods which could conduct the numerical simulation on rock engineering problems, such as the ground reaction after excavation. However, the rockbolt models have not been developed in the original 2D-DDA program, which makes it hard to be applied in support design for underground excavation projects.

Although the mentioned researches have made some achievements in the understanding of the reinforcement mechanism of rockbolt, there are still some limitations to assess

the interactions between rockbolt and rock mass. Attempts are made in this thesis to investigate the reinforcement mechanism and the design principles of the rockbolt.

1.2 Key objectives

The thesis aims to investigate the reinforcement mechanism of the rockbolt and improve its design efficiency for underground excavation. To achieve the objectives, the study has focus on the following items:

(1) To study the bonding behavior of the rockbolt element by considering the rockbolt rib configurations;
(2) To develop a rockbolt model in 2D-DDA based on the load transfer mechanism;
(3) To investigate the reinforced rock units of the rockbolt and rockbolt system in jointed rock mass;
(4) To construct numerical models to evaluate the stability of rockbolt reinforce rock wedge in the roof of underground opening, and
(5) To propose the rockbolt design method for horse-shoe shaped rock caverns based on the cavern performance.

1.3 Outline of thesis

This thesis investigates the reinforcement mechanism of the rockbolt for underground excavation using 2D-DDA method. It is divided into eight chapters.

In Chapter 2, literature reviews are conducted to understand the rockbolt theory and the load transfer mechanism of the rockbolt. In addition, the basic 2D-DDA method is introduced.

In Chapter 3, numerical simulations are carried out to study the load transfer between rock and rockbolt element. The influences of the rib profiles on the bond stress versus slip displacement curves are investigated, followed by the discussion of the trilinear bond model along the rock and rockbolt interface.

In Chapter 4, the rockbolt model in 2D-DDA method is improved by integrating the non-linear axial behaviour, the shear behaviour at joint and the bond behaviour at the rock and rockbolt interface. The models are verified by experimental results.

In Chapter 5, the pullout tests are simulated using the developed rockbolt model to investigate the reinforced rock unit of rockbolt in jointed rock mass. Meanwhile, the interactions between rock and rockbolt are evaluated based on the reinforce rock unit of single rockbolt and grouped rockbolts.

In Chapter 6, numerical simulations are carried out using 2D-DDA to investigate the stability of rockbolt reinforced rock wedge in the roof. The effects of the spacing and the installation angle of rockbolt on the reinforcement efforts are presented with consideration of the changes of stress state in the surrounding rock blocks.

In Chapter 7, a rockbolt design method is proposed using artificial neural network models which are built based on the numerical evaluations of ground reaction curves.

In Chapter 8, conclusions are drawn based on the current studies. Future studies on the support design/management for underground excavation are presented.

CHAPTER 2.
LITERATURE REVIEW

The research works on the rockbolt reinforcement mechanism are reviewed to understand the rockbolt behaviour and the interaction between rockbolt and rock mass. After a brief introduction of rockbolt reinforcement system, the load transfer in rock/rockbolt is explained. The reinforcement effects are then discussed with aids of ground-support diagrams using Convergence-Confinement method (CCM). The Two-dimensional Discontinuous Deformation Analysis (2D-DDA) is introduced for further development purpose.

2.1 Rockbolt

The rockbolt is a reinforcing element, normally made of solid or tube formed steel and installed un-tensioned or tensioned into the rock mass (Stillborg, 1986). The installation of rockbolts in rock mass is to reinforce and improve the inherent strength of the rock mass, so that the rock mass becomes self-supported. In general, when the rock moves towards the excavation surface, the rockbolt elongates. Tension is created in the rockbolt and transferred to the surrounding rock mass as compression, thus helps the rock to support itself by increasing confinement (Bobet and Einstein, 2011). With rockbolts, local reinforcement is used to secure and prevent detachments of individual blocks. General or systematic reinforcement is required to control the deformation occurring in the entire tunnels. Since the rockbolt is usually simple to apply and can be modified during construction, it becomes a key component in technologies used for designing tunnels, such as New Austrian Tunneling Method (NATM).

2.1.1. Types of rockbolts

Many types of devices have been developed to be used as reinforcement elements. In general, these devices are solid bars or tube elements and installed within boreholes

drilled into the rock. Based on the source of reaction forces, the rockbolt could be classified as three categories (Windsor and Thompson, 1993).

(1) Continuously Mechanically Coupled (CMC) element has continuously load transfer through the length. The source of reaction forces relies on the securing agent (such as grout or resin) which fills the annulus between the element and the borehole wall. Figure 2-1(a) presents an example of the cross-section of a fully grouted rebar.

(2) Continuously Frictionally Coupled (CFC) element also has continuously load transfer through the length. However, as the element is in contact with rock directly, the source of reaction forces relies on the friction between the element and the borehole, as well as the radial pressure set up. Figure 2-1(b) presents an example of the cross-section of a split set.

(3) Discretely Mechanically or Frictionally Coupled (DMFC) element provides either mechanical or frictional reaction forces over a short interval of its total element length. The interval is known as anchorage length which provides either mechanical or frictional load transfer over this relatively short interval. This anchorage must be sufficiently strong to sustain the full material strength of the reinforcing element. Figure 2-1(c) presents an example of the cross-section of the D-bolt (Li, 2010).

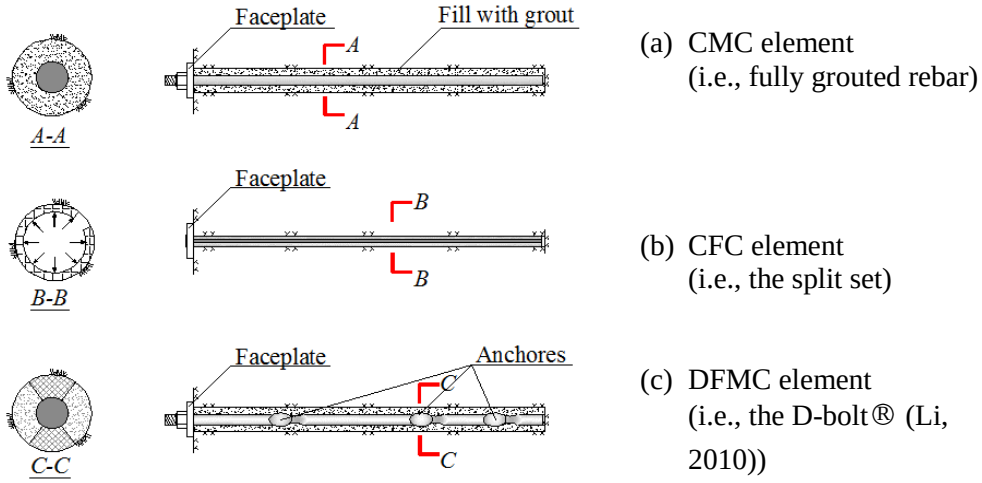

Figure 2-1 Illustration of three types of the rockbolt elements (modified after Windsor and Thompson, 1993)

Some examples of the reinforcement devices with consideration of their advantages and disadvantages are summarized in Table 2-1.

Table 2-1 Features of the reinforcement (Nie et al., 2014a)

Types	DMFC	CMC	CFC
Examples	Expansion shell or slot and wedge Mechanical anchors The D-bolt®	Fully grouted/resin rebar Fully grouted/resin threaded bar Fully grouted/resin cable bolt	Split set/tube Expanded tube (Swellex®, Omega®, etc.)
Load transfer	Two ends of the rockbolt are mechanically anchored in borehole. Once the fracture opens, the bolt shank between two ends is tensioned according with the anchoring capacity of two anchoring points.	Cement or resin is used as grouting agents to integrate bolt with the rock via ribs on the bolt surface. The load transfer through the bond between the element and the rock cause tension in the bolt. The bearing capacity is provided primarily by the shear resistance at the interface.	The frictional resistance to sliding is generated by a radial force against the borehole wall over the length of the bolt. Mechanical interlock between the bolt and the rock then prevents the bolt from sliding.
Preferred Rock type	Moderately hard to hard rock	All rock conditions	All rock conditions
Advantages	Provide immediate support action after installation; Serve as permanent reinforcement by post-grouting; High bolt loads can be achieved; A versatile system for rock reinforcement in hard rock conditions.	The most commonly used rockbolt; Predominantly used in temporary support systems Provide high bolt loads in various rock conditions; Provide immediate support if a “fast-setting” resin is used for bottom anchoring of the bar.	Rapid and simple installation; Provide immediate support action after installation; Can be used in a variety of ground conditions.
Disadvantages	Difficult to install reliably; Must be monitored and checked for proper tensioning; Lose bearing capacity as a result of blast vibrations; Not recommended for very hard rock.	Difficult to check the resin cartridges/cement; Relatively expensive; Use of standard cement in the grout requires several days curing before the bolt can take load; Affected by corrosion.	Relatively expensive; Corrosion protection required if used in long term installations; Borehole diameter is crucial in the prevention of failure.
Notes	The void between the bolt and the borehole need to be post grouted.		The bolt needs to be protected against corrosion.

Another classification of rockbolt based on the view of loading and deformation performance is also widely used in design which classifies the rockbolts as stiff, ductile and energy-absorbing rockbolt (Li et al., 2014). A stiff rockbolt has high load-carrying capacity, but a small amount of displacement prior to failure, such as the fully encapsulated rebar bolts. A ductile rockbolt can tolerate a large deformation, but relatively low load-carrying capacity, such as the split set. An energy-absorbing rockbolt can carry the load equal or close to the strength of the bolt material and deform largely, so that it can absorb a large amount of energy prior to failure, for example, the D-bolt (Li, 2010) and the CRLD bolts (He et al., 2014).

The rockbolt can also be classified based on the types of grout and the auxiliary fittings it used. Grouting materials are broadly classified as two materials, i.e., cementations and resinous materials (Windsor and Thompson, 1993). Cement grout is suited to the longer reinforcing elements due to its availability, ease of mixing and placement. Some additives can be added to aid the placement and improve the quality of cement grout and the set time. Resinous material is generally confined to the shorter elements due to the higher costs of the resin materials and placement difficulties in longer holes. Auxiliary fittings are either attached to the reinforcing element at the rock mass boundary (external fittings) or used to modify the internal response of continuously coupled devices (internal fittings) (Bawden, 2011). External fittings can provide varying degrees of surface restraint to the rock mass surface. Internal fittings are used predominantly with continuous mechanically coupled devices and comprise intermittent anchors and decoupling sleeves. The combination auxiliary fittings modify the load transfer mechanism between the rock and the reinforcing element.

2.1.2. Load transfer in rockbolt

The load transfer concept is fundamental to understand the reinforcement mechanisms of different rockbolt elements. This concept is composed of three basic mechanisms (Windsor and Thompson, 1993),

(1) Rock movement with requires load transfer from the unstable rock to the reinforcing element;
(2) Transfer load via the reinforcing element from the unstable surface region to a stable interior region, and
(3) Transfer the load of reinforcing element to the stable rock mass.

The load transfer capacity of the rockbolt is controlled by the components of bonds at the rock and rockbolt, such as the surrounding rock mass, the mortar, the profile configuration and the boundary conditions of the rockbolt. For different kinds of rockbolt element, the bonding behaviours are different. The bonding behaviour of the CMC element relies on a securing agent that fills the annulus between the element and the borehole wall. The dominant reinforcement is mainly created as a result of friction or mechanical interlocking between steel and grout (Zhandarov and Mäder, 2004; Moosavi et al., 2005; Singer, 1990). The bonding of the CFC element depends on the friction between the element and the rock. The DMFC element provides either mechanical or frictional interlocking bonding.

Take the CMC element as an example, Figure 2-2 shows the anchorage models in a view of cross-section of the element. In the field, two interfaces are the major concerns of rockbolt failure. One interface is between rockbolt and grout, whilst the other is between grout and rock mass. In laboratory test, PVC tubes or steel tubes may be used to confine the rockbolt (Gurung, 2001; Hyett et al., 1995; Kaiser et al., 1992). In such boundary condition, the major concern is the interface between rockbolt and grout.

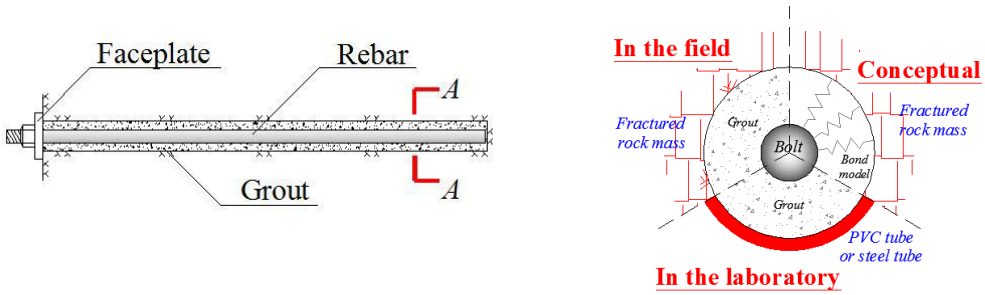

(a) Example of CMC element (b) Model of section *A-A*

Figure 2-2 Sketch of the cross-section of a CMC rockbolt element

The fully grouted rockbolt is the CMC rockbolt element. Experimental results show the bond of fully grouted rockbolt is created mainly because of the mechanical interlocking between steel and grout (Moosavi et al., 2005; Singer, 1990; He et al., 2015; Feng et al., 2018). This implies that the bond strength depends on the mechanical properties of both the rock and the mortar, the geometry of interlock devices (such as the profile of a rockbolt rib), the boundary conditions, and so on. Some parametric studies have been conducted as summarized in Table 2-2.

Table 2-2 Parameters to control the bond strength of fully grouted rockbolt/cables

Influenced mediums	Parameters	Relationship vs. Bond strength	References
Rock	Stiffness	Increase with the stiffness ratio or rock to grout	(Yazici and Kaiser, 1992; Salcher and Bertuzzi, 2018)
Mortar	Strength	Increase with the shear strength of the grouting material logarithmically	(Kılıc et al., 2003; Kılıc et al., 2002; Moosavi et al., 2005; Yazici and Kaiser, 1992; Zhu et al., 2015)
	Water cement ratio	(1) Optimum *w:c* ratio = 0.34~0.4, but groutibility (pumpability) decreases at *w:c* ratio = 0.34 (2) Higher bond strengths are results of lower *w:c* ratio grout	(Hyett et al., 1995; Kılıc et al., 2002)
	Curing time	Increases rapidly in first 7 days, but increases slowly after	(Kılıc et al., 2002)
	Stiffness	Increase with the Young's modulus	(Kılıc et al., 2002)
Geometry of interlock devices	Diameter of borehole	Inversely proportional	(Ghadimi et al., 2014; Yazici and Kaiser, 1992) (Aziz et al., 2005)
	Shape	A conical lugged bolt has larger bond strength than a ribbed bar	(Kılıc et al., 2003)
	Rib spacing	The optimum spacing width for particular type of bolt is 37.5 mm	(Aziz et al., 2008; Cao et al., 2013; Ghadimi et al., 2014)
	Rib face angle	Inversely proportional	(Cao et al., 2013; Kılıc et al., 2003)
	Rib height to length ratio	Inversely proportional	(Cao et al., 2013)
Boundary conditions	Pressure at interface	Increase with the presure, especially for confining pressure below 10 MPa	(Blanco Martín et al., 2013; Hyett et al., 1992; Kaiser et al., 1992; Yazici and Kaiser, 1992)
	Installation processes	The field results showed more variability.	(Singer, 1990)

Considering the features of the interactions among rockbolt, grout and rock mass, a bond model is developed to illustrate the load transfer in conceptual view. In the following, the bond-slip model of a CMC element is introduced to discuss the load transfer in the fully grouted rockbolt. Yazici and Kaiser (1992) have defined the bond stress as the

shear resistance along contact surface. Analytical studies and laboratory tests have been widely used to study the bond strength. Farmer (1975) has proposed a fundamental bond model which is widely used now. As shown in Figure 2-3, a diametrical unit of the CMC element between x and $x+dx$ is studied. The force equilibrium along the horizontal direction gives (Farmer, 1975),

$$\pi r_b^2 d\sigma_x = -2\pi r_b \tau_x dx \tag{2.1}$$

or: $$\frac{d\sigma_x}{dx} = -\frac{2}{r_b}\tau_x \tag{2.2}$$

where: σ_x – axial stress of rockbolt;

r_b – radius of rockbolt;

τ_x – shear stress at the rockbolt/resin interface.

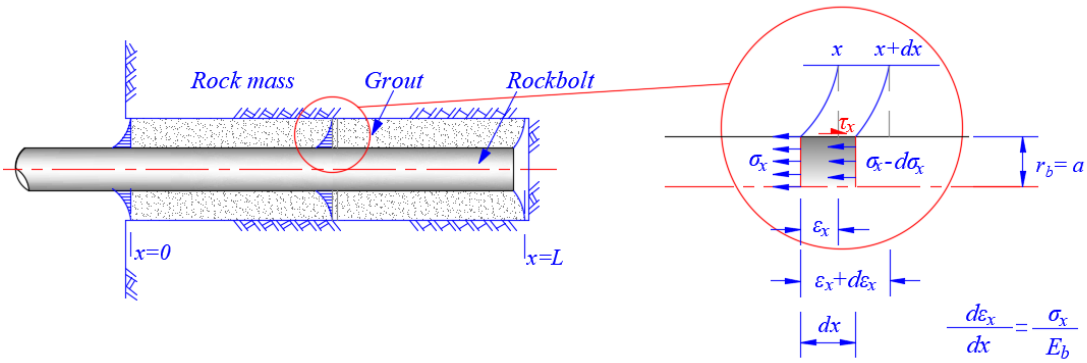

Figure 2-3 Diametrical slice of a grouted rockbolt (after Farmer, 1975)

Assuming the element is elastic, the axial stress is given as,

$$\sigma_x = -E_b \frac{d\varepsilon_x}{dx} \tag{2.3}$$

where: ε_x – axial strain of rockbolt;

E_b – elastic modulus of rockbolt.

Combining Eqs (2.2) and (2.3), gives,

$$\frac{d^2\varepsilon_x}{dx^2} = \frac{2}{r_b}\frac{\tau_x}{E_b} \tag{2.4}$$

The bond stress τ_x could be assumed as:

$$\tau_x = k\varepsilon_x \tag{2.5}$$

for $R - r_b \le r_b$: $$k = \frac{G_g}{R - r_b} \tag{2.5a}$$

for $R - r_b > r_b$: $$k = \frac{G_g}{r_b \ln R/r_b} \tag{2.5b}$$

where: k – bond stiffness which is assumed to be proportional to the shear modulus of grouting material, unit in Pa/m;

G_g – rigidity modulus of grout;

R – borehole radius.

Submitting Eq.(2.5) to Eq.(2.4) gives,

$$\frac{d^2\varepsilon_x}{dx^2} - \alpha^2\varepsilon_x = 0 \tag{2.6}$$

for $R - r_b \le r_b$ $$\alpha^2 = \frac{2G_g}{E_b r_b (R - r_b)} \tag{2.6a}$$

for $R - r_b > r_b$ $$\alpha^2 = \frac{2G_g}{E_b r_b^2} \ln \frac{R}{r_b} \tag{2.6b}$$

Integration of Eq.(2.6) gives,

$$\varepsilon_x = A\exp\alpha x + B\exp\alpha x \tag{2.7}$$

where: A and B are the integration constants.

An important assumption in Farmer's model is that the bond stress is proportional to the relative bond slip. Li and Stillborg (1999) have enhanced this model and added progressive decoupling in it if the slip displacement is too large. By adopting the above bond model, the axial load and bond stress distribution along the rockbolt are shown in Figure 2-4.

The pullout tests on short encapsulated bolts are suggested to derive the bond-slip model. Some experiments to test the bond behaviour at reinforced bar and concrete are also reviewed to verify the model as shown in Figure 2-5 (Ko et al., 2014; Lee et al., 2016; Mertoğlu et al., 2016; Mousavi et al., 2017). According to the experimental results, a trilinear bond-slip model is proposed and widely used in recent year (Benmokrane et al.,

1995; Moosavi et al., 2005; Ren et al., 2010; Blanco Martín et al., 2011; Deb and Das, 2011; Ma et al., 2013; Ma et al., 2014; Zhandarov and Mäder, 2016).

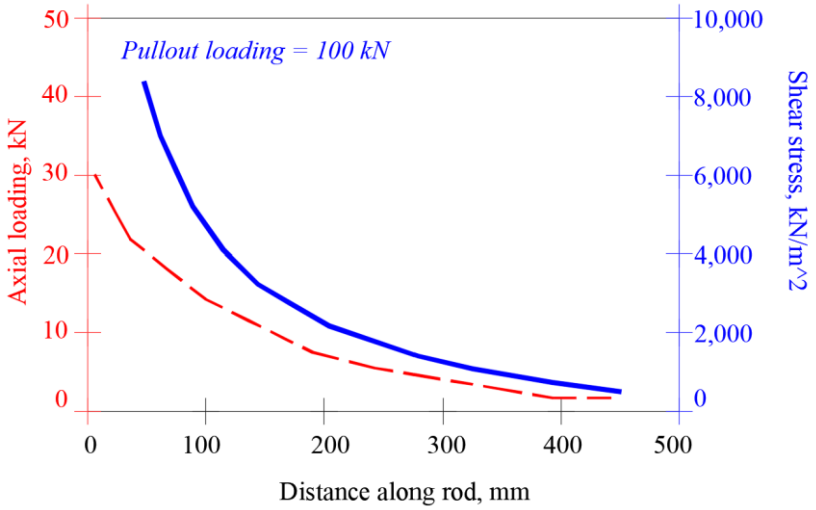

(a) Farmer's model (1975)

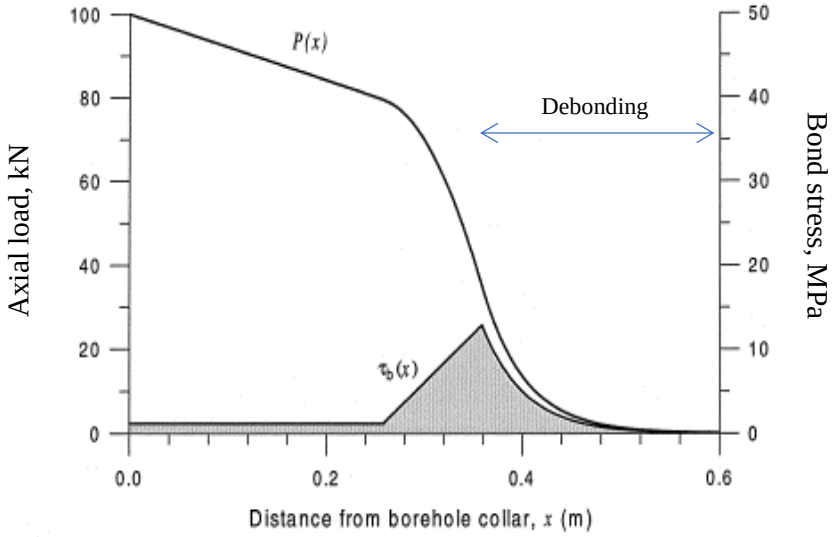

(b) Li and Stillborg's model (1999)

Figure 2-4 Axial load and bond stress distributions along the rockbolt based on illustrated bond models

Figure 2-6(a) shows a sketch of the trilinear bond-slip model. Totally three stages can be found from the plot. The first stage is a linear ascending line before the bond stress reaches the peak bond strength τ_{max}. The slope is defined as k_1. A descending bond strength with slip distance is following. The slope k_2 is a negative value which describes the decoupling process at the rock/grout interface. The third stage begins when the bond

stress reaches the residual bond strength τ_{res} and the slip distance reaches δ_2. This model can be extended to define the load transfer for other rockbolt elements, such as CFC and DFMC elements (Li and Stillborg, 1999). For example, the bond of CFC element may follow the model as shown in Figure 2-6(b). The DFMC element will have a combination of CFC and CMC elements.

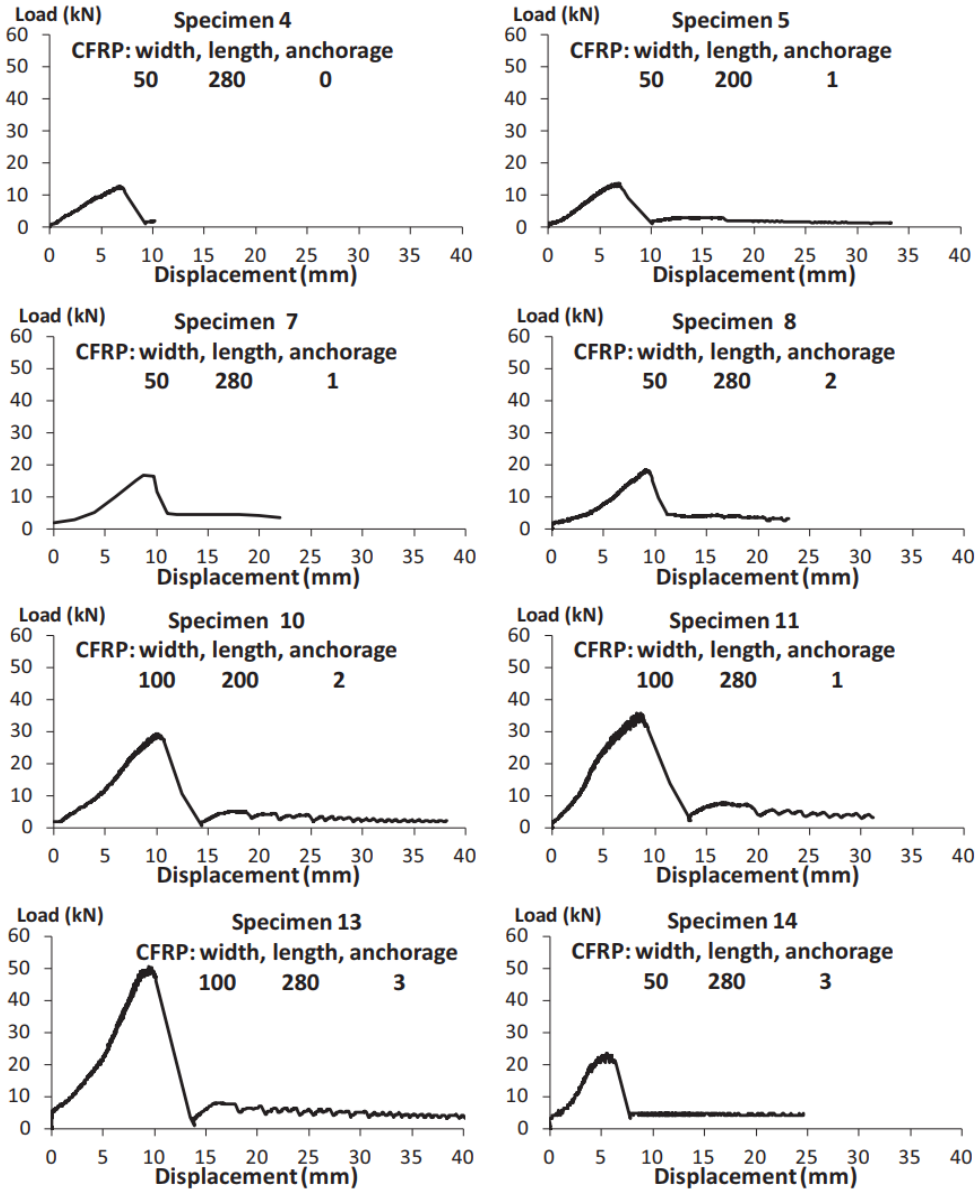

Figure 2-5 Examples of the bond load versus slip displacement relationships (after Mertoğlu et al., 2016)

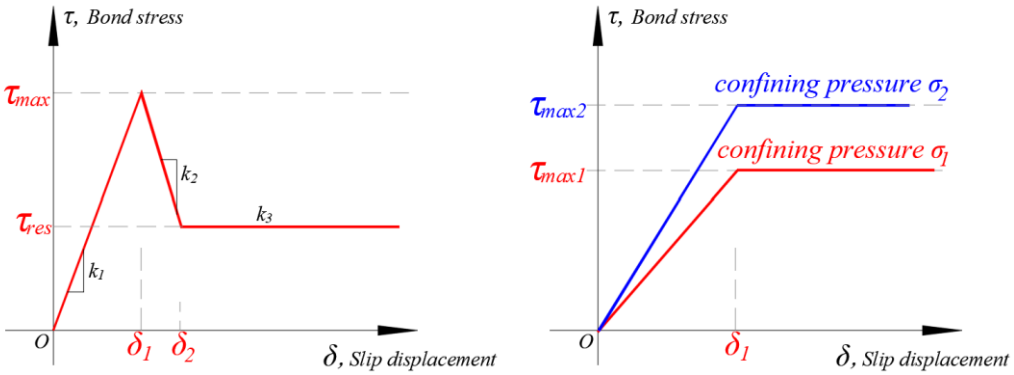

(a) Mechanical bond model (b) Frictional bond model

Figure 2-6 Illustration of the bond slip model

The mechanical behaviour of rockbolt elements subjecting to shear is important as the shear force may reduce the load carrying capacity of the rockbolt. Analytical models are developed to describe the mechanical behaviour of CMC element subjected to shear loadings. The resultant force along the bolt can be divided into a parallel component force N_0 and a normal component force Q_0. Based on the beam theory (as shown in Figure 2-7), the yield and failure shear force on rockbolt is given as (Li et al., 2015; Pellet and Egger, 1996):

Yield shear force: $$Q_{0e} = \frac{1}{2}\sqrt{p_u D_b \left(\frac{\pi D_b^2 \sigma_{el}}{4} - N_{oe}\right)} \tag{2.8a}$$

Failure shear force: $$Q_{0f} = \frac{\pi D_b^2}{8}\sigma_{ec}\sqrt{1-16\left(\frac{N_{0f}}{\pi D_b^2 \sigma_{ec}}\right)^2} \tag{2.8b}$$

where: p_u – yielding pressure of the grout;

D_b – rockbolt diameter;

σ_{el} – yield stress of the bolt material;

σ_{ec} – failure stress of the rockbolt material;

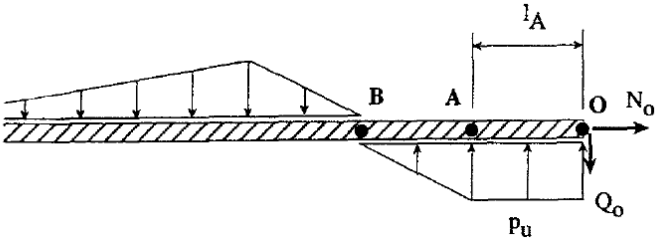

Figure 2-7 Sketch of the mechanical system at joint (Pellet and Egger, 1996)

The reaction force to the rock is (Pellet and Egger, 1996):

$$p_u = f_r \sigma_c D_b \tag{2.9}$$

where: f_r – load factor ($f_r > 1$);

σ_c – Strength of the host material (such as grout or rock).

2.1.3. *Load carrying capacity of a rockbolt*

(1) Pullout test

The pullout test results are the most used method to evaluate the load-carrying capacity of a rockbolt. Typical experimental results of the load-deformation curves of various types of rockbolt are shown in Figure 2-8. According to the model developed by Farmer (1975), if tension occurs on rod, it will be transferred to the grout, causing differential rod extension and grout shear along the length of rockbolt. The stress distribution along the rockbolt has been evaluated by experiments (Li and Stillborg, 1999; Li et al., 2014). Some typical models are shown in Figure 2-9.

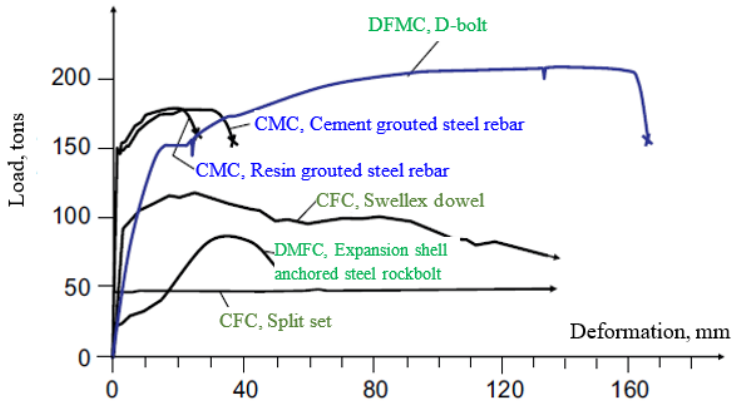

Figure 2-8 Load-deformation results by Stillborg (after Li, 2010)

It is also necessary to appreciate the fact that any pull-out test results are depends on the ground conditions. Researches have proposed analytical solutions of the model for bolts subjected to the joint opening (Deb and Das, 2011; Deb et al., 2018; Li and Stillborg, 1999; Liu et al., 2017). As shown in Figure 2-10, decoupling of the bolt interface during a joint opening is activated firstly at the joint and then propagates along the interface with an increase in the opening displacement. It also indicated when the opening displacement of the joint is small, both the bond stress and the axial stress decrease

exponentially with increasing distance from the joint. When the opening is large enough, decoupling will be activated at the bolt interface, while the bond and axial stresses will be changed their distribution as shown in Figure 2-10(b).

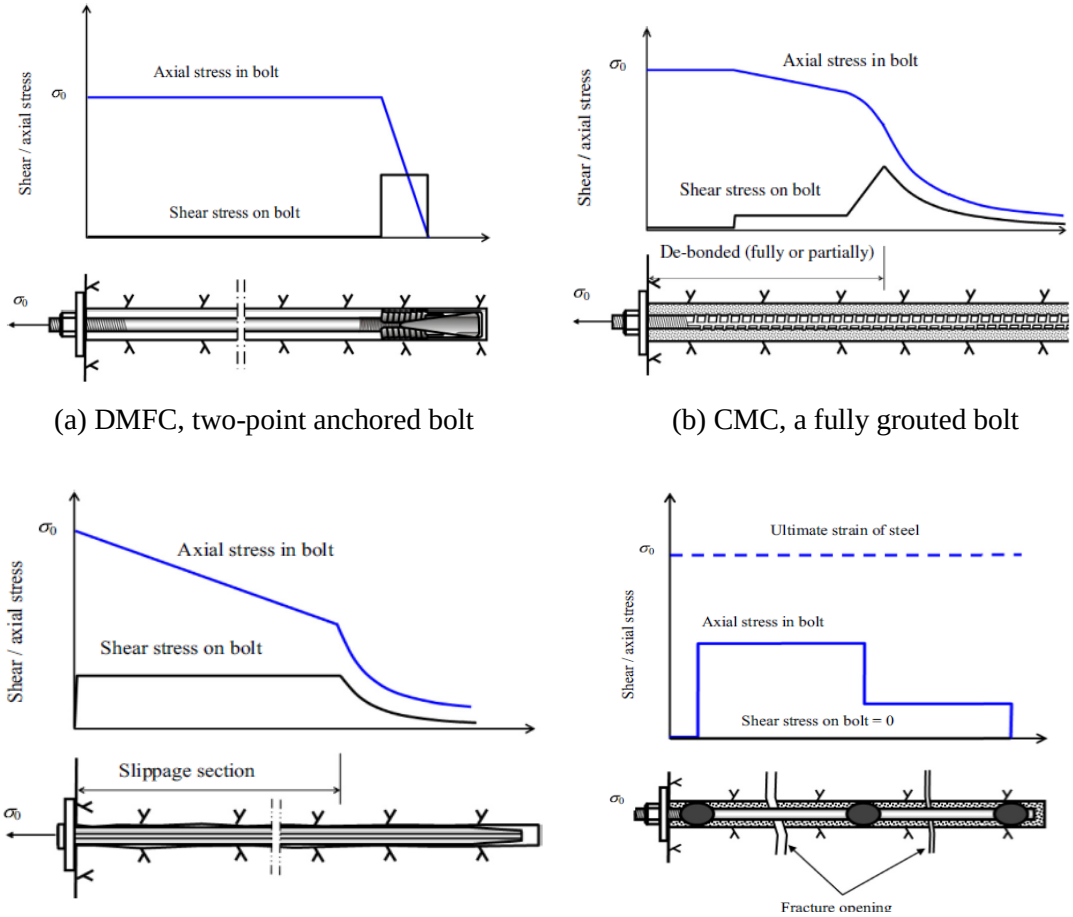

(a) DMFC, two-point anchored bolt (b) CMC, a fully grouted bolt

(c) CFC, frictional bolt (d) DMFC, multi-point anchored

Figure 2-9 Sketches of the stress/strain distributions along rockbolts when subjected to pullout loads (Li et al., 2014)

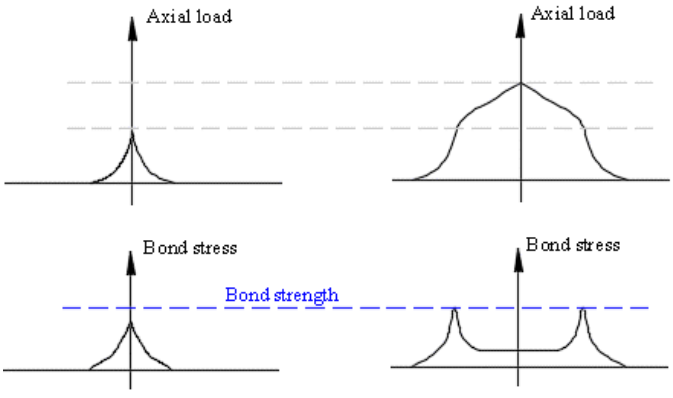

(a) Small joint opening (b) Large joint opening

Figure 2-10 Stresses along the rockbolt at joint opening (Li and Stillborg, 1999)

(2) Shear tests

The load-carrying features of the rockbolt under shear test is also examined using the load-displacement curves (see Figure 2-11). The incline angle of the rockbolt with respected to the shear face is one of the most important factors. Comparisons of shear load and shear displacement relationship with different bolt orientations are shown in Figure 2-12. When the angle between the bolt and the joint surface is less than 40°, the failure of the rockbolt is in tension. If the angle is larger than 40°, the failure is in combined tension and shear. As the angle approaches 90°, the rockbolt shows a shear type of failure. The strain/force along rockbolt induced by shearing is illustrated in Figure 2-13. The shear bearing capacity influence by cyclic shear loading is also examined by Wu et al. (2018). Forbes et al. (2017) have proposed a new technique to examine the strain along the rockbolt under shearing test. Demonstrated tests are showing the progressively failure at the joint places (see Figure 2-14).

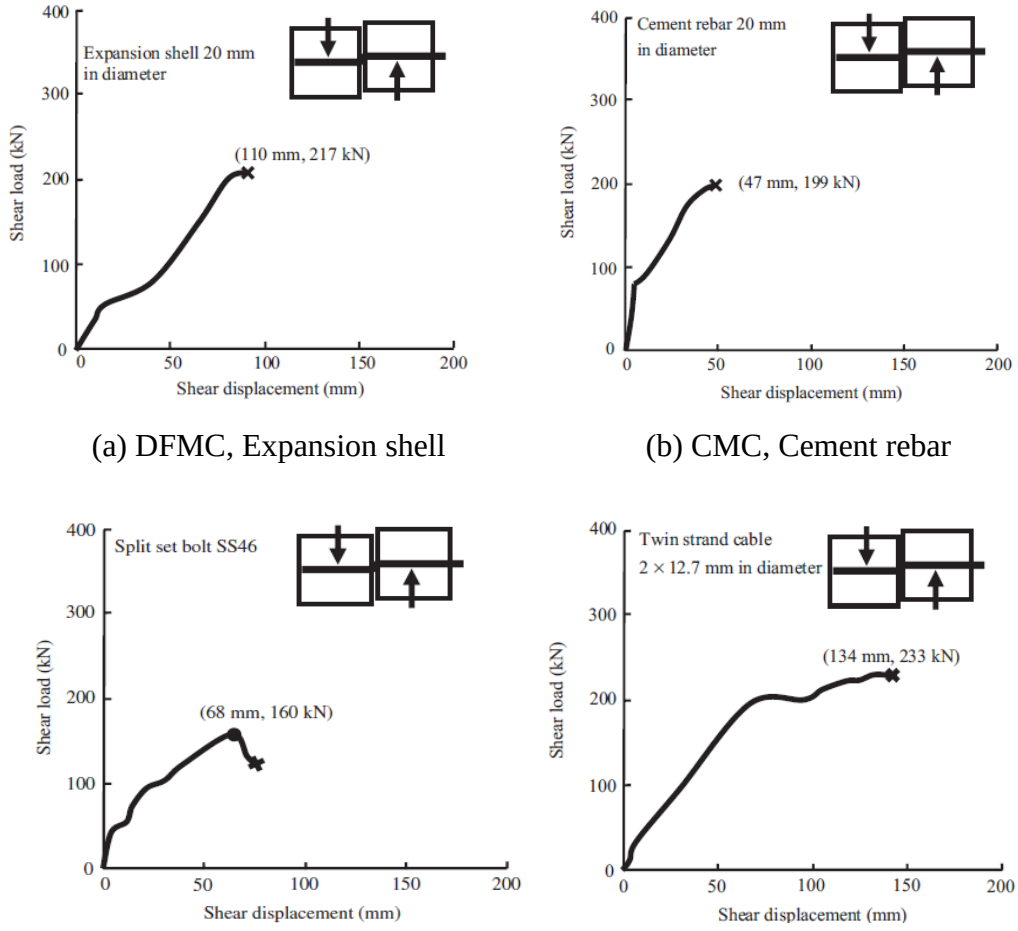

(a) DFMC, Expansion shell

(b) CMC, Cement rebar

(c) CFC, Expansion shell

d) DFMC, Twin strand cable

Figure 2-11 Shear load versus displacement of various rockbolts (Li et al., 2014)

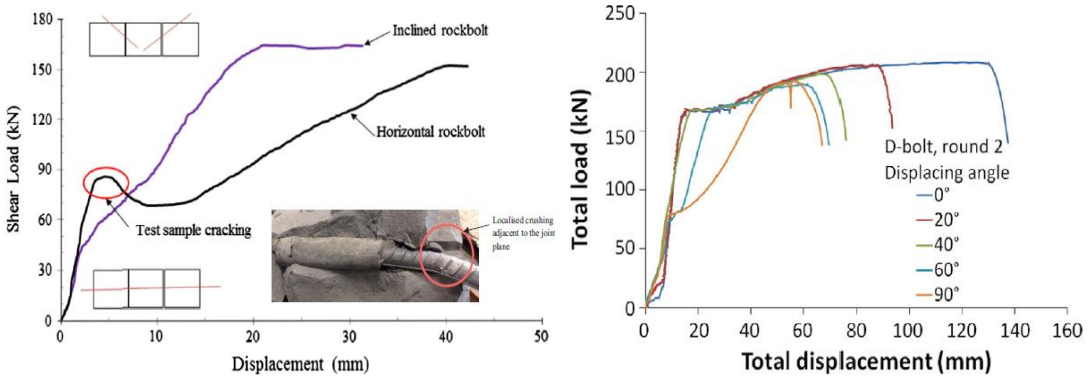

(a) CMC, fully grouted rebar (Li et al., 2016) (b) DMFC, D-bolt (Chen and Li, 2015)

Figure 2-12 Comparison of shear load and shear displacement relationship with different bolt orientations

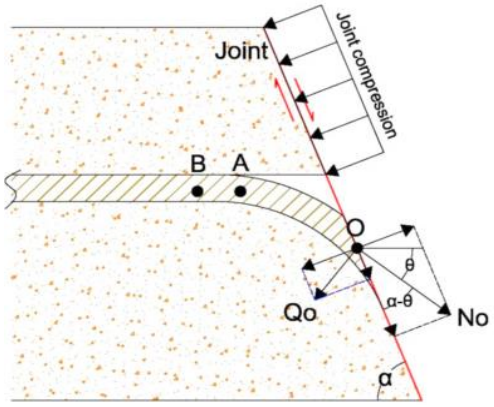

Figure 2-13 Forces on the rockbolt at the shearing joint (Pellet and Egger, 1996)

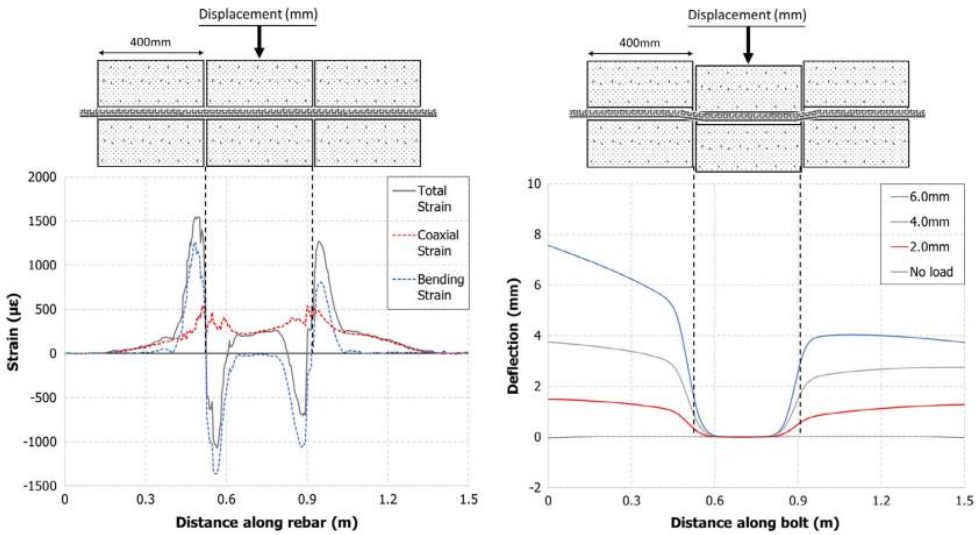

Figure 2-14 Strain distributions along the rebars under double shear tests (Forbes et al., 2017)

2.2 Rockbolt design principles

The rockbolt system is designed to minimize the movement induced by the dead weight of loosened rock, as well as those induced by stress redistribution in the rock surrounding an excavation. In principle, the rockbolt must be strong enough to support the deadweight of the loosened rocks. Thus, the strength of the rockbolt is the most important parameters in the design. Analytical, empirical and observational methods have been proposed to design the rockbolts for underground excavations (Choquet and Hadjigeorgiou, 1993). Hoek et al. (2000) have summarized the applications of rockbolts in underground excavations as shown in Table 2-3. The stability of a shallow underground excavation under low stress environment depends on the structural conditions. However, at a great depth, the relationship between the stress of rock mass and the strength of rock determines the stability of the excavation. For deep level rock excavation, where rock stresses locally exceed the inherent strength of the rock, design methods for rockbolting are more complex.

Table 2-3 Applications of rockbolt (modified after Hoek et al., 2000)

		Geological strength of rock mass		
		Massive rock	Blocky rock	Heavily jointed rock
Stress levels (= in-situ stress/UCS)	Low	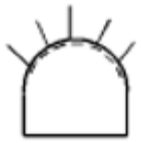		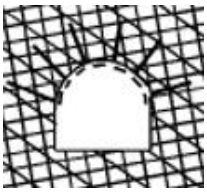
		No support or 'safety bolts' or dowels and mesh	'Pre-tensioned' rockbolts to prevent failure of individual blocks and wedges.	Light pattern rockbolts with mesh and/or shotcrete will control raveling of near surface rock pieces
	High	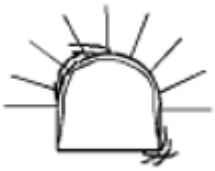	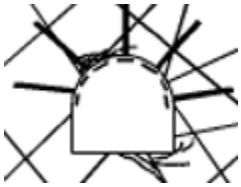	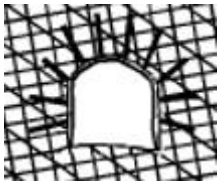
		Pattern rockbolts or dowels with mesh or shotcrete to inhibit fracturing and to keep broken rock in place	Heavy rockbolts or dowels, inclined to cross rock structure, with mesh or steel fiber reinforced shotcrete	Heavy rockbolt or dowel pattern with steel fiber reinforced shotcrete. In extreme cases, steel sets with sliding joints may be required.

2.2.1. Analytical methods

There are three theories used for the design of the rockbolt system in underground excavations.

(1) Limited stability analysis of rock block

The sketches to illustrate the method of using the rockbolt to reinforce rock wedge in an underground excavation driven by gravity is shown in Figure 2-15. The gravity of the rock wedge is denoted as *W*, while the shear friction between the boundary of rock wedge and surrounding rock is *R*. For the rock wedge formed in the roof, the friction is not considered. By introducing the safety factors, the number of rockbolt to reinforce the rock wedges is designed based on the limited stability analysis as follows (Lang and Bischoff, 1982).

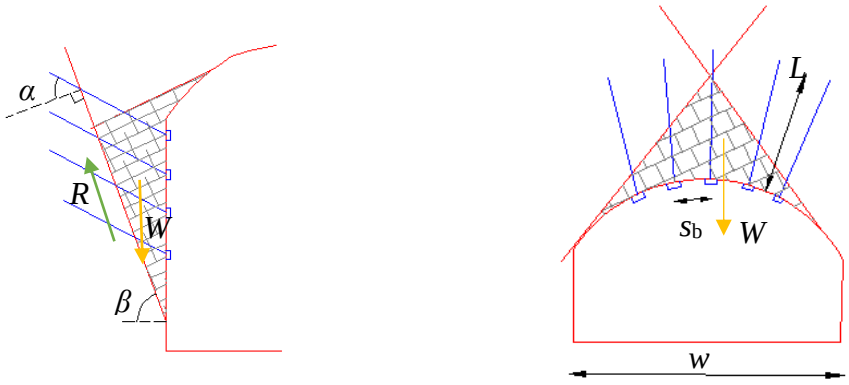

(a) Reinforcement of a wedge free to slide on the sidewall

(b) Reinforcement of a wedge free to fall on the roof

Figure 2-15 Sketches to illustrate the limited stability analysis (after Lang and Bischoff, 1982)

The number of rockbolt to reinforce the rock wedge in side wall (see Figure 2-15(a)) is calculated as:

$$n = \frac{W\left(f\sin\beta - \cos\beta\tan\varphi\right) - cA}{B\left(\cos\alpha\tan\varphi + f\sin\alpha\right)} \tag{2.10}$$

where: *R* is the shear friction between the boundary of rock wedge and is calculated as $R = cA + W\cos\beta\tan\varphi$. (2.10a)

The number of rockbolt to reinforce the rock wedge in roof (see Figure 2-15(b)) is calculated as:

$$n = \frac{Wf}{B} \tag{2.11a}$$

and:

$$s_b \le 3e,\ w \ge L_b + 1.0 \tag{2.11b}$$

where: f – Safety factor, in Figure 2-15(a), f = 1.5 for grouted bolts, f = 2.0 for nongrouted bolts; in Figure 2-15(b), $2 \le f \le 5$;

n – Number of rockbolts;

W – Weight of wedge;

B – Bolt load carrying capacity;

β – Dip of the sliding surface;

c – cohesive strength of the sliding surface;

A – Base area of sliding surface;

R – Resistance to sliding;

α – Angle between the plunge of the bolt and the normal to the sliding surface;

w – Width of excavation;

s_b – Bolt spacing;

e – Joint spacing;

L_b – Bolt length;

φ – Joint surface angle of friction.

It should be noted that the Eqs (2.10) and (2.11) cannot consider the effects of the in-situ stresses. Generally, the higher horizontal stress may increase the stability of rock wedge in roof, but its effectiveness is reduced by loosening (Crawford and Bray, 1983).

(2) The beam or slab concept for bedded rock

Assuming the stratified rock mass behaves like slabs or beams, the design is applicable to the cases where reinforcement is by suspension and the bolt transfers the weight from weak strata to the strong strata. The rockbolt must be long enough to get through the potentially unstable zone. As shown in Figure 2-16, the minimum rockbolt tension to ensure stability is calculated as (Stillborg, 1986):

$$T = f \times s_b \times s_b' \times h \times \rho \times g \tag{2.12}$$

where: f – Safety factor, recommended $1.5 \le f \le 3$;

s_b' – Bolt spacing along the axis of excavation;

h – Thickness of unstable layer of rock;

H – Thickness to reach stable rock layer;

ρ – Rock density.

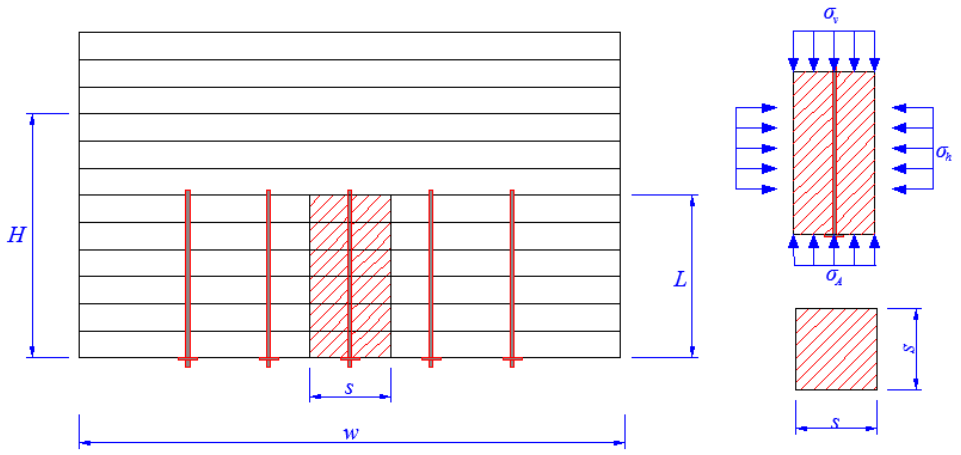

Figure 2-16 Illustration of the reinforced rock unit (after Lang and Bischoff, 1983)

Lang and Bischoff (1983) extended this analysis by incorporating the shear strength developed by the rock on the vertical boundaries of the reinforced rock unit. The axial tensiton load in rockbolt, T, should be calculated :

$$\frac{T}{AR_s} = \frac{\alpha}{\mu k}\left(1 - \frac{c}{\gamma R_s}\right)\left[\frac{1-\exp\left(-\mu k H / R_s\right)}{1-\exp\left(-\mu k L / R_s\right)}\right] \tag{2.13}$$

where: A – area of roof carrying one bolt, $A = s^2$;

R_s – shear radius of the reinforced rock unit, $R_s = A/P$;

P – shear perimeter, $P = 4s$;

α – a factor depending on the time of installation of the rockbolt, $\alpha = 0.5$ for active support; $\alpha = 1.0$ for passive reinforcement;

T – axial tension load in rockbolt;

μ – coefficient of internal friction of rock;

γ – unit weight of rock;

c – apparent cohesion of rock mass;

k – ratio of existing horizontal stress to vertical stress;

H – total length of rock zone participating in the formation of reinforced rock unit and the rockbolt length (L).

(3) The rock arch concept

A natural arch may be formed at some depth into the jointed rock mass. Illustrating experiments conducted by Hoek (2007) have presented there is a zone of compression might be induced in the reinforced area, resulting in effective reinforcement as shown in Figure 2-17. As shown in Figure 2-18, the loose zone is stabilized by systematic rockbolts. Formulas are developed to estimate the distribution of the rockbolt as:

The length: $$L_b = 1.40 + 0.184w \quad (2.14a)$$

The spacing: $$s_b \le 3e \quad (2.14b)$$

The tension force: $$0.5B < T < 0.8B \quad (2.14c)$$

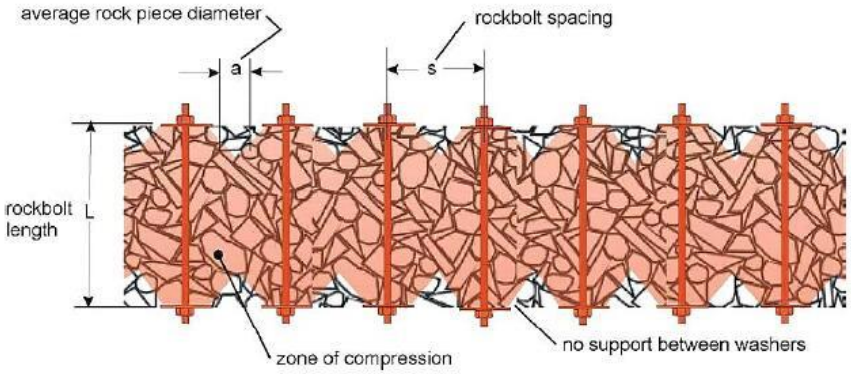

Figure 2-17 Tom Lang's explanation of the systematic rockbolts (Hoek, 2007)

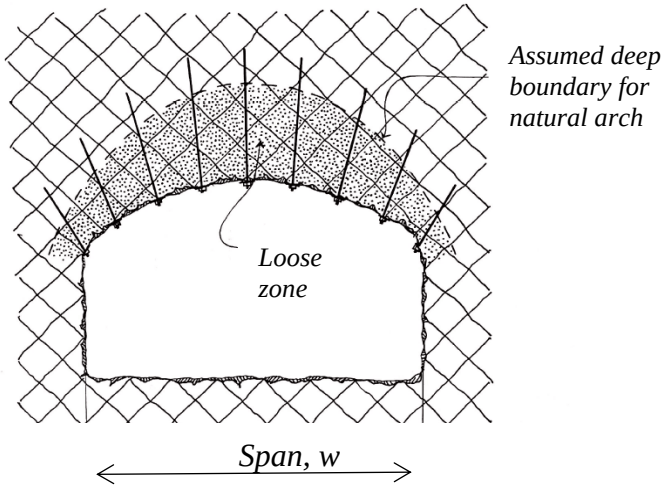

Figure 2-18 Conceptual natural arch in underground excavation (Hoek, 2007)

2.2.2. Empirical methods

Empirical design proposes spot bolting or sparsely spaced pattern bolting in jointed rock mass which may be good enough to stabilize the loosen wedges. The design parameters are mainly bolt length, diameter, spacing, pattern of rockbolt, *etc.*. The empirical design recommendations proposed by Stillborg (1986) and Li (2017b) are listed in Table 2-4.

Table 2-4 Empirical design recommendations (after Stillborg (1986) and Li (2017b))

Parameters	Description	Recommendations and suggestions
Rockbolt length, L_b	For operation	$L_b \leq 0.5h$ (Roof); $L_b \leq 0.5w$ (Wall)
	For small depth failure zone	$L_b \geq d_f + l_0$ (m)
	For moderate depth failure zone	$L_b = 1.40 + 0.184\,B$
	For highly fracture zone	$L_b = 2 \sim 3$ (m)
Spacing*, s_b	In general case	$s_b = 1.0 \sim 2.5$ (m)
	For slightly jointed rock mass (e = 0.3 ~ 1m)	$s_b = (3\sim4)e$
	For moderated jointed zone (e < 0.3)	$s_b \leq 3e$
	For highly fracture zone	$s_b \leq L_b/2$
Patterns	For gravitational rock falls	Spot bolting
	For less deformable rock	Systematic bolting
	For squeezing rock	Yield support system
Other bolt parameters	Diameters:	16 ~ 20 (mm)
	Bond stiffness	Mechanical / Frictional / others
	Ultimate strength	e.g., 339 kN for Dydidag®; 500 kN for Flexirope®; 110 kN for Split set®.
	Creep properties	e.g., Ultimate axial strain, Strain hardening index, *etc.*
Note:	h – tunnel height; w – tunnel width; d_f – the depth of the failure zone; l_0 – Embedded length, empirically = 1.2 m; e – mean joint spacing. *In practice, the spacing of a systematic bolting design includes the in-row spacing and the spacing between rows. Here, both spacings are assumed equal.	

Empirical assessment of rock reinforcement based on RMR is widely adopted in mining development. Table 2-5 shows an example of 10 m span rock tunnel using RMR methods. The proposed method is more suitable for rockbolt design when the field vertical stress is less than 25 MPa.

Table 2-5 Examples of 10 m span rock tunnels in accordance with the RMR system (Hoek, 2007)

Ground mass class	Excavation	Support design	
		Rockbolts	Others
Very good RMR:81-100	Full face: 3 m advance	Generally no support required except for occasional spot bolting	
Good RMR:61-80	Full face:1.0-1.5 m advance; complete support 20 m from face	Locally bolts in crown, 3 m long, spaced 2.5 m with occasional wire mesh	Shotcrete: 50 mm in crown where required
Fair RMR: 41-60	Top heading and bench: 1.5-3 m advance in top heading; commence support after each blast; commence support 10 m from face	Systematic bolts 4 m long, spaced 1.5-2 m in crown and walls with wire mesh in crown	Shotcrete: 50-100 mm in crown and 30 mm in sides
Poor RMR: 21-40	Top heading and bench: 1.0-1.5 m advance in top heading; install support concurrently with excavation- 10 m from face	Systematic bolts 4-5 m long, spaced 1-1.5 m in crown and walls with wire mesh	Shotcrete: 100-150 mm in crown and 100 mm in sides Steel sets: Light ribs spaced 1.5 m where required
Very poor RMR < 21	Multiple drifts: 0.5-1.5 m advance in top heading; install support concurrently with excavation; shotcrete as soon as possible	Systematic bolts 5-6 m long, spaced 1-1.5 m in crown and walls with wire mesh. Bolt invert	Shotcrete: 150-200 mm in crown, 150 mm in sides, and 50 mm on face Steel sets: Medium to heavy ribs spaced 0.75 m with steel lagging and forepoling; close invert

Empirical assessment of rock reinforcement based on the *Q*-system are more commonly used in the tunnel design. The *Q*-system developed by NGI is a classification system for rock masses. It provides the support and reinforcement designs according to historical

cases (Barton and Choubey, 1978). Using *Q*-values, the rock mass conditions, the cavern geometry and the support classes are linked. As shown in Figure 2-19, the *Q*-values are plotted along the horizontal axis, whilst the support classes are divided into 9 categories, such as:

① Unsupported or spot bolting;
② SB, Spot bolting
③ B+Sfr, Systematic bolting, fibre reinforced sprayed concrete, 5 – 6 cm
④ Sfr(E500)+B, Fibre reinforced sprayed concrete and bolting, 6 – 9 cm
⑤ Sfr(E700)+B, Fibre reinforced sprayed concrete and bolting, 9 – 12 cm
⑥ Sfr(E700)+RRS I+B, Fibre reinforced sprayed concrete and bolting, 12-15 cm + reinforced ribs of sprayed concrete and bolting
⑦ Sfr(E1000)+RRS II+B, Fibre reinforced sprayed concrete > 15 cm + reinforced ribs of sprayed concrete and bolting
⑧ CCA or Sfr(E1000)+RRS III+B, Cast concrete lining
⑨ Special evaluation

Recommended bolt spacing is an expression of quantity of bolts necessary. The position and direction of bolt should be based on an evaluation of the joint geometry. The length of the bolts depends on the span or wall height of the underground opening and to some degree on the rock mass quality. In unfavorable joint geometry, longer bolts are necessary. Illustrations of using *Q-Chart* to define the support categories are shown in Table 2-6.

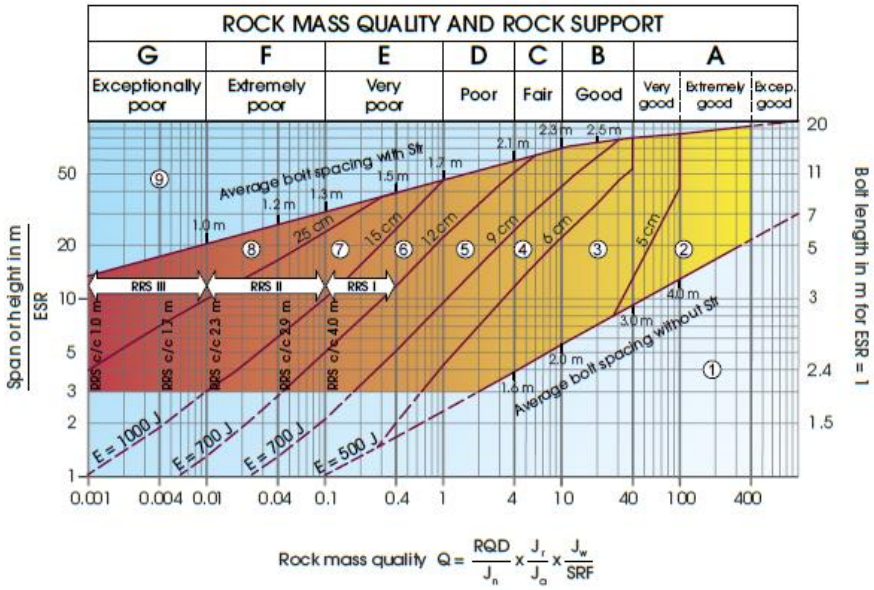

Figure 2-19 The *Q*-chart (NGI, 2015)

Table 2-6 Support category illustrated based on *Q*-chart

Classification		Cavern span	[m]	8~11	11~14	14~18	18~23	23~27	27~32
Fair - Good (Q = 4 ~ 40)	Crown	Crown Rock Bolt Length	[m]	3.4	4.0	4.7	5.6	6.4	7.3
		Crown Rock Bolt Spacing	[m]	2	2.3	2.3	2.6	2.8	3
	Side	Side Wall Rock Bolt Length	[m]	3.4	4.0	4.7	5.6	6.4	7.3
		Side Wall Rock Bolt Spacing	[m]	2.6	3.7	3.7	4.0	4.4	4.7
		Longitudinal Bolt Spacing Above/Below crown limit	[m]	2/2.6	2.3/3.7	2.3/3.7	2.6/4	2.8/4.4	3/4.7
Poor (Q = 1 ~ 4)	Crown	Crown Rock Bolt Length	[m]	3.4	4.0	4.7	5.6	6.4	7.3
		Crown Rock Bolt Spacing	[m]	1.7	1.8	1.9	2	2	2.1
	Side	Side Wall Rock Bolt Length	[m]	3.4	4	4.7	5.6	6.4	7.3
		Side Wall Rock Bolt Spacing	[m]	1.9	2	2.1	2.2	2.3	2.3
		Longitudinal Bolt Spacing Above/Below crown limit	[m]	1.7/1.9	1.8/2	1.9/2.1	2/2.2	2/2.3	2.1/2.3
Very poor (Q = 0.1 ~ 1.0)	Crown	Crown Rock Bolt Length	[m]	3.4	4	4.7	5.6	6.4	7.3
		Crown Rock Bolt Spacing	[m]	1.3	1.3	1.4	1.5	1.5	1.6
	Side	Side Wall Rock Bolt Length	[m]	3.4	4	4.7	5.6	6.4	7.3
		Side Wall Rock Bolt Spacing	[m]	1.3	1.5	1.6	1.7	1.7	1.7
		Longitudinal Bolt Spacing Above/Below crown limit	[m]	1.3/1.3	1.3/1.5	1.4/1.6	1.5/1.7	1.5/1.7	1.6/1.7
Extremely poor (Q = 0.01 ~ 0.10)	Crown	Crown Rock Bolt Length	[m]	3.4	4	4.7	5.6	6.4	7.3
		Crown Rock Bolt Spacing	[m]	1	1	1.1	1.2	1.3	1.3
	Side	Side Wall Rock Bolt Length	[m]	3.4	4	4.7	5.6	6.4	7.3
		Side Wall Rock Bolt Spacing	[m]	1	1	1.1	1.2	1.3	1.5
		Longitudinal Bolt Spacing Above/Below crown limit	[m]	1/1	1/1	1.1/1.1	1.2/1.2	1.3/1.3	1.3/1.5

2.2.3. Numerical methods

Different numerical methods are developed to assist the support design for underground structures. As the rockbolt is a popular structure to provide reinforcement for underground structure, special elements are included in most of the numerical methods to simulate the rockbolt, such as *RS*^{2}, *FLAC*, *UDEC*, *etc.*.

(1) Bolt model in *RS*^{2}

RS^2 is a 2D finite element program and offers a wide range of support modeling options (Rocscience Inc., 2011). The fully grouted rockbolt model is developed based on the studies of Farmer (1975) and Hyett et al. (1995). It is based on a bar element and only considers the axial behaviour.

The equilibrium along the axial direction of rockbolt unit gives,

$$A_b E_b \frac{d^2 u_x}{dx^2} + F_s = 0 \tag{2.15}$$

where: F_s – the shear force per unit length;
A – the cross-section area of the bolt;
E_b – the modulus of elasticity of the bolt.

The shear force per unit length could be calculated as:

$$F_s = k(u_r - u_x) \tag{2.16}$$

where: u_r – rock movement;
u_x – rockbolt element movement;
k – the shear stiffness of the bolt-grout interface.

Substitute Eq.(2.16) to Eq.(2.15) gives the weak form associated with the total potential energy which is shown as:

$$\begin{aligned}\delta \prod &= \int \left(AE_b \frac{d^2 u_x}{dx^2} - ku_x + ku_r \right) \delta u dx \\ &= \int \left\{ AE_b \left[\frac{d}{dx}\left(\frac{du_x}{dx}\delta u \right) - \frac{du_x}{dx}\frac{d\delta u}{dx} \right] - \left(ku_x - ku_r \right)\delta u \right\} dx \\ &= AE_b \delta u \frac{du_x}{dx}\bigg|_0^L - \int \left(AE_b \frac{du_x}{dx}\frac{d\delta u}{dx} + ku_x \delta u \right) dx + \int \left(ku_r \delta u \right) dx\end{aligned} \tag{2.17}$$

Eq. (2.17) can be re-written as:

$$-\int\left(AE_b\frac{du_x}{dx}\frac{d\delta u}{dx}+ku_x\delta u\right)dx+\int\left(ku_r\delta u\right)dx$$

$$=-\begin{bmatrix}u_{x1} & u_{x2} & u_{r1} & u_{r2}\end{bmatrix}\begin{bmatrix}K_b & 0\\ 0 & -K_r\end{bmatrix}\delta\begin{Bmatrix}u_{x1}\\ u_{x2}\\ u_{r1}\\ u_{r2}\end{Bmatrix} \tag{2.18a}$$

where $[K_b]$ and $[K_r]$ are calculated as:

$$\left[K_b\right]=\frac{AE_b}{L}\begin{bmatrix}1 & -1\\ -1 & 1\end{bmatrix}+\frac{kL}{3}\begin{bmatrix}1 & 0.5\\ 0.5 & 1\end{bmatrix}$$

and (2.18b)

$$\left[K_r\right]=k\begin{bmatrix}N_1N_1 & N_1N_2\\ N_2N_1 & N_2N_2\end{bmatrix}=\frac{kL}{3}\begin{bmatrix}1 & 0.5\\ 0.5 & 1\end{bmatrix}$$

The rockbolt element are not necessarily connected to the element vertices in *RS*^{2} program. Thus, a mapping procedure is carried out to transfer the effect to the element vertices. This procedure is done for each bolt segment by mapping the stiffness and the shape functions depending on the intersected side of the elements.

(2) Cable element in FLAC

Cable element is developed in Fast Lagrangian Analysis of Continua (FLAC) when the bending effects of rockbolt elements are not necessary to be considered in the simulation (Itasca Consulting Group, Inc. 2012). The cable is divided into many segments with nodal points at the segment ends. It allows the modeling of bonding resistance along the length.

The reinforcing element is treated as bar element with capacity to sustain uniaxial tension. The increment of the axial force is calculated as:

$$\Delta F^t=-\frac{E_bA_b}{L}\Delta u^t \tag{2.19}$$

where: $\Delta u^t=\Delta u_i t_i=\left(u_x^i-u_x^{i+1}\right)t_1+\left(v_y^i-v_y^{i+1}\right)t_2$

u_x^i, v_y^i – the movement of node *i*;

t_1, t_2 – the tangential (axial) direction of the cable.

In the software, a tensile yield-force limit and a compressive yield-force limit are assigned to the cable as shown in Figure 2-20. In computing the axial force, displacements are computed at nodal points along the axis of the reinforcement.

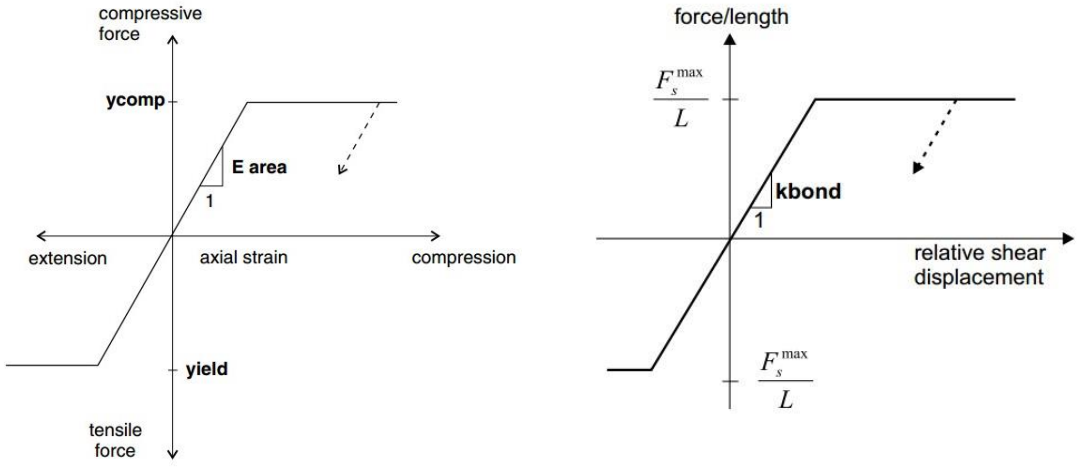

(a) Axial behaviour (b) Bond-slip model

Figure 2-20 Material models of cable element adopted in FLAC (Itasca Consulting Group, 2012)

The bond behaviour of the grout annulus is represented as a spring-slider system located the nodal points as shown in Figure 2-21. The bond force per length is calculated as:

$$\frac{F_s}{L} = k\left(u_c - u_m\right) \tag{2.20}$$

where k – the grout shear stiffness;

u_c – the axial displacement of the cable;

u_m – the axial displacement of the medium (soil or rock), and

L – the element length.

The bond stiffness k is calculated by Yazici and Kaiser (1992) and shown as:

$$k = \frac{2\pi G}{10\ln\left(1+2t/D_b\right)} \tag{2.21}$$

where: G – the shear modulus of grout;

t – the annulus thickness.

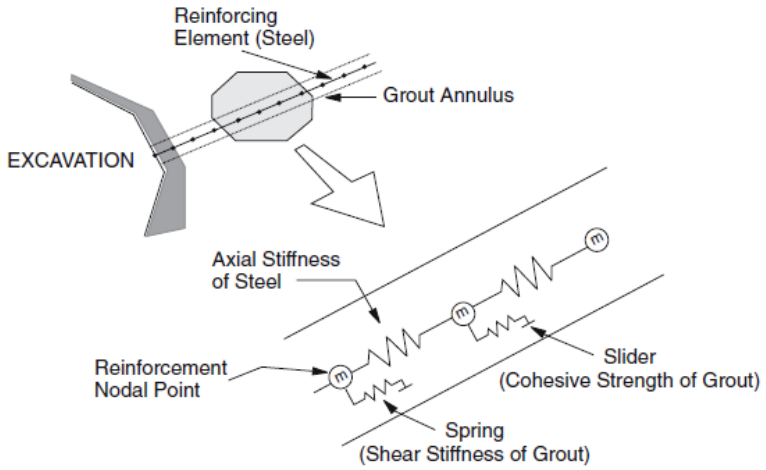

Figure 2-21 A spring-slider system to represent the bond behaviour of the grout annulus (Itasca Consulting Group, 2012)

The maximum bond force per unit length is a function of the cohesive strength of the grout and the stress-dependent frictional resistance of the grout which can be calculated as:

$$\frac{F_{s,\max}}{L} = C + \overline{\sigma_c} \times \tan\varphi \times D_b \tag{2.22}$$

where: C – intrinsic shear strength or cohesion;

σ_{zz}– out-of-plane stress;

φ – friction angle;

D_b – perimeter of the cable element.

$\overline{\sigma_c}$ – the mean effective confining stress normal to the element, which can be calculated as:

$$\overline{\sigma_c} = -\left(\frac{\sigma_{nn} + \sigma_{zz}}{2} + p\right)$$

where: $\sigma_{nn} = \sigma_{xx} n_1^2 + \sigma_{yy} n_2^2 + 2\tau_{xy} n_1 n_2$

n_i – the unit vectors;

The advantage of the shear model is that it can consider the confining pressures applying normally to the cable element. In evaluating the relative displacement at the grout/medium interface, an interpolation scheme is used to calculate the displacement of the medium in the cable axial direction at the cable node.

(3) Rockbolt element in FLAC

Rockbolt is simulated using pile element featured in 2D element with 3 degrees of freedom (two displacements and one rotation) at each end node (Itasca Consulting Group, Inc. 2012). The rockbolt interacts with the FLAC grid via shear and normal coupling springs. They are nonlinear connectors that transfer forces and motion between the elements and the grid at the pile element nodes. The formulation is similar to that for cable elements. Rockbolt breakage is based on a user-defined tensile failure strain limit. The total plastic tensile strain is calculated by:

$$\varepsilon_{pl} = \sum \varepsilon_{pl}^{ex} + \sum \frac{D_b}{2} \frac{\theta_{pl}}{L} \tag{2.23}$$

where: D_b – rockbolt diameter;

ε_{pl} – total plastic tensile strain;

ε_{pl}^{ax} – axial plastic strain;

L – bolt segment length, and

θ_{pl} – average angular rotation over the rockbolt.

A user-defined table can be adopted to give a correction factor for the effective confining stress, in case of non-isotropic stress, as a function of deviatoric stress ratio. Softening of the bonding at the rock and rockbolt interface could also considered in the software.

(4) Local reinforcement in UDEC

The cable elements and rockbolt element which are introduced in FLAC are also adopted in The Universal Distinct Element Code (UDEC) in the deformable blocks. Besides, local reinforcement can be applied to both rigid and deformable blocks (Itasca Consulting Group, Inc. 2011).

The local reinforcement formulations consider only the local effect of reinforcement installed through existing discontinuities. Large displacements are accommodated by considering the simple geometric changes that develop locally in the reinforcement near a discontinuity. During shear displacement along a discontinuity, the reinforcement model deforms as shown in Figure 2-22(a). The short length of reinforcement, which spans the discontinuity and changes orientation during shear displacement, is referred to the active length L and determined by:

$$\exp(-\beta L) = \rho_{\max} \tag{2.24}$$

where $\beta = \left[\frac{K}{4E_b I}\right]^{\frac{1}{4}}$ in which $K = 2E_g / (d_2/d_1 - 1)$

E_g – Young's modulus of the grout;

I – second moment of area of the reinforcement element;

d_2, d_1 – diameter of borehole and reinforcement element respectively, and

$\rho_{\max}$ – the proportion of maximum deflection in the reinforcement.

The model consists of two springs located at the discontinuity interface and oriented parallel and perpendicular to the reinforcement axis (see Figure 2-22(b)). Following shear displacement, the axial spring is oriented parallel to the active length, while the shear spring remains perpendicular to the original orientation. The force-displacement relation that describes the axial response is given by:

$$\Delta F_a = k_a \left|\Delta u_a\right| f\left(F_a\right) \tag{2.25}$$

where: ΔF_a – incremental changes in axial force;

Δu_a – incremental change in axial displacement;

k_a – the axial stiffness, and

$f(F_a)$ – a function describing the axial loading path.

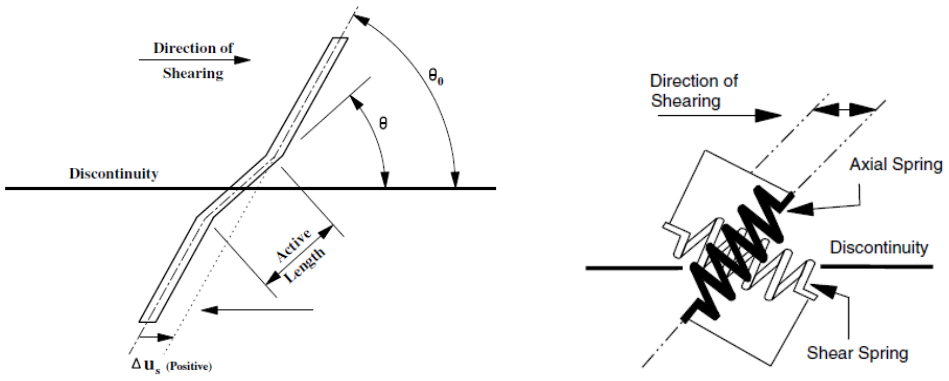

(a) (b)

Figure 2-22 Springs representing the assumed reinforcement due to shear movement (Itasca Consulting Group, Inc. 2011)

A reduction factor r_f is applied to incremental axial displacements arising from changes in orientation of the active length to account for the crushing. Note that no reduction (r_f

= 1.0) is applied for cases in which there is no change in orientation of the active length. The reduction factor in the UDEC program is calculated as:

$$r_f = \left|u_{axial}\right| \left(u_s^2 + u_n^2\right)^{-\frac{1}{2}} \tag{2.26}$$

where: u_{axial} – Summation of axial displacement increments;

u_s – Total discontinuity shear displacement;

u_a – Total discontinuity normal displacement.

The shear force-displacement relation is described in incremental form and shown as:

$$\Delta F_s = k_s \left|\Delta u_s\right| f\left(F_s\right) \tag{2.27}$$

where ΔF_s – incremental changes in shear force;

Δu_s – incremental change in shear displacement;

k_s – the shear stiffness, and

$f(F_s)$ – a function describing the shear loading path;

The axial and shear behaviour of this local reinforcement model is shown in Figure 2-23. Although the local reinforcement model can be used with either rigid blocks or deformable blocks, the representation is most applicable to cases in which deformation of individual rock blocks may be neglected in comparison with deformation of the reinforcing system.

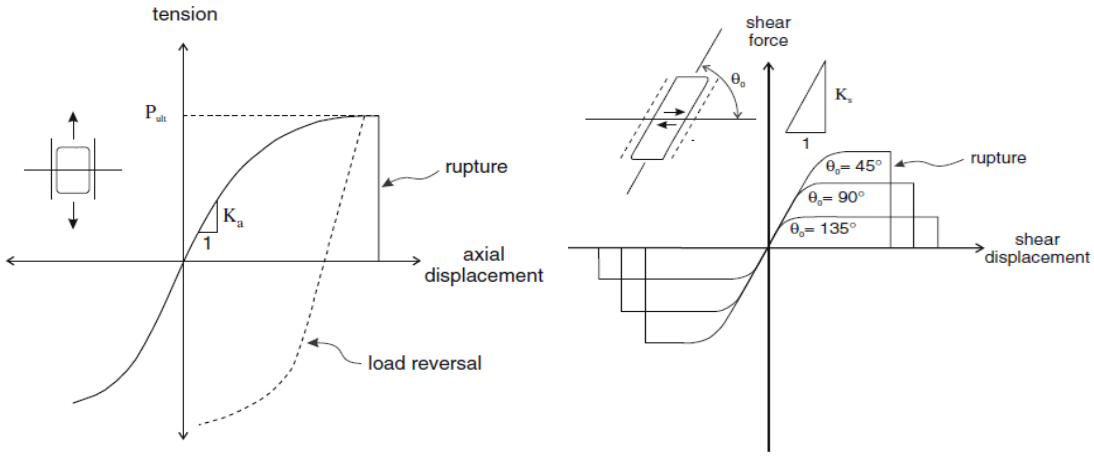

(a) Axial behaviour (b) Shear behaviour

Figure 2-23 Constitutive model of the local reinforced systems (Itasca Consulting Group, Inc. 2011)

The features of the three reinforcement elements are summarized in Table 2-7. It shows the current models have their advantages and disadvantages. Thus, a more comprehensive numerical model of the reinforcement element could consider axial, bond and shear behaviour.

Table 2-7 Examples of the numerical models of a rockbolt

	In FEM	In FDM	In DEM (UDEC)
Illustration	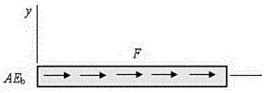 (Rocscience Inc., 2011)	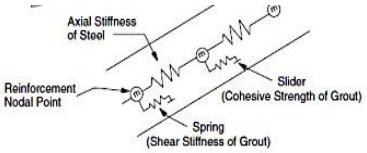 (Itasca Consulting Group, 2012)	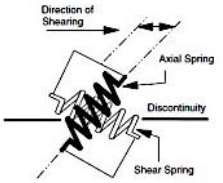 (Itasca Consulting Group, 2011)
Axial	$AE_b \frac{d^2u_x}{dx^2} + F_s = 0$	$\Delta F^t = -\frac{E_b A_b}{L} \Delta u^t$	$\Delta F_a = k_a \lvert \Delta u_a \rvert f\left(F_a\right)$
Bond	$F_s = k\left(u_r - u_x\right)$	$\frac{F_s}{L} = k\left(u_c - u_m\right)$	–
Shear	–	–	$\Delta T_s = k_s \lvert \Delta u_s \rvert f\left(T_s\right)$

2.3 Rock-rockbolt interaction in underground excavation

A full 3D mechanical analysis of the rockbolt interaction problem is practically difficult for reinforcement design in tunneling due to time constraints. The rockbolt reinforcement design often use 2D models to analyze rockbolt and rock interaction problems. Several numerical methods have been developed to calculate 3D problems using 2D models as summarized in Table 2-8. Among these methods, the convergence-confinement method (CCM) is commonly adopted to solve the 3D rock-support interaction problems associated with the installation of support near a tunnel face in underground excavations. As shown in Figure 2-24, the CCM consists of three basic components in the form of graphs: the longitudinal deformation profile (LDP), which relates tunnel deformation to distance to the tunnel face; the support characteristic curve (SCC), which represents the stress–strain relationship in the support system; and the ground reaction or response curve (GRC).

Table 2-8 Useful methods to represent 3D problems using 2D models (modified after Karakus, 2007)

Methods	Illustration	Briefing
Convergence-confinement method	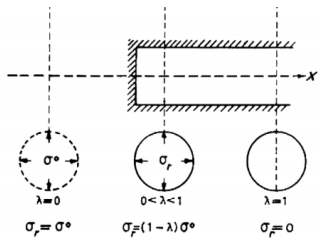	The radial stress, on the tunnel periphery simulates this face effect and is given by $\sigma_r = (1-\lambda)\sigma^0$. 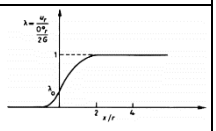 An internal pressure, initially equal to the in-situ stress is applied on the inside of the excavation boundary. The pressure is incrementally relaxed until the excavation boundary condition is that of zero normal stress.
Stiffness reduction method (material softening	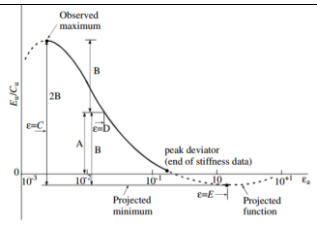	The stiffness reduction method uses a support core with a reduced modulus of elasticity. The excavation area in the tunnel face is introduced with a modified elasticity modulus. Modification of the original modulus of elasticity, E, to the modulus of support core, E_s, is given by: $E_s = \alpha E$.
Disk calculation method	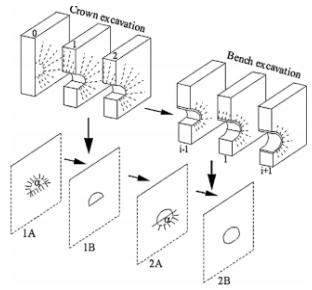 Fig. 2. Disk calculation model (reproduced from Schikora and Osterme-ier, 1988).	Tunnel excavation is divided into disks by sections perpendicular to the tunnel axis. Disk 0 is assigned as ahead of the face, disk 1 represents the excavation of the tunnel while disk 2 represents the shotcrete application. Disk 1 is weakened by the excavation of crown due to deformations partly reduced by shear stresses affecting the intersection planes to the more rigid near disks 0 and 2. At disk 1, excavation is represented by removing the soil weight at the crown and reducing the crown rigidity by the value of α.
Hypothetical modulus of elasticity soft lining method	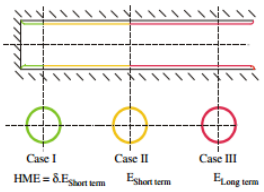	In Case I, parameter δ stands for the reduction of the short-term elasticity modulus of the lining. In Case-II, the HME value of the lining takes its short-term value that varies from 3 to 7 GPa. In Case III, the lining is fully strengthened with its long-term elasticity modulus.
The gap method	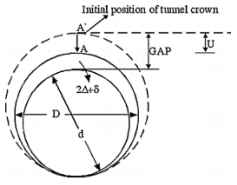 Fig. 4. Definition of Gap paran	A measure of the volume of material that has been excavated in excess of the theoretical volume within outer diameter of the tunnel lining. Gap parameters are applied to calculate the associated volume losses due to the tunnelling process. However, determination of the gap parameter is very sensitive for types of soil.
Volume loss control method	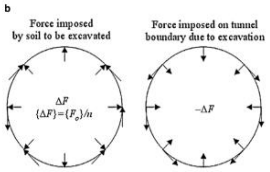 ation of solid elements (after Potts and Zdravković, 2001).	Equivalent nodal forces ΔF on the tunnel boundary, which represents the pressure exerted by soil to be excavated, are calculated and these forces divided by the number of increments, which simulates excavation stage. Equal but opposite forces ΔF are then applied to the tunnel boundary over each n increments for the excavation stage. After lining construction, ΔF is still applied to the tunnel boundary for the remainder of the n increments.

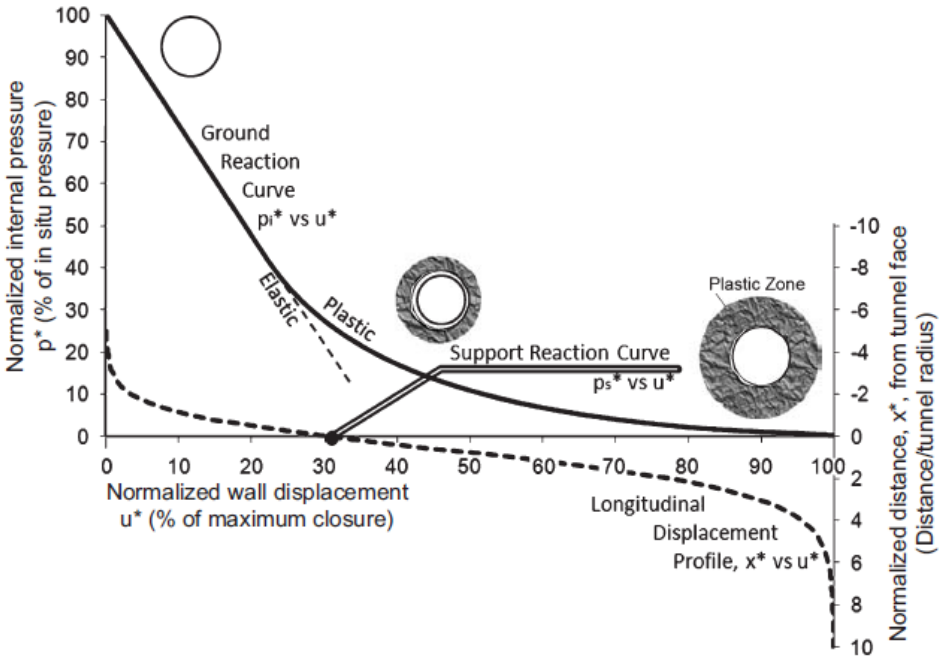

Figure 2-24 Ground reaction curve (Vlachopoulos and Diederichs, 2009)

2.3.1. GRC

As the solid line shown in Figure 2-24, the GRC is a plot of the nomralized percentage of raidal support proeesure, p^*, required at a point to limit the normalized radial boundary dispalcement u^*. Analytical solutions have been illustrated by solving a simple axisymmetric problem (Brown et al., 1983; Wu et al., 2018). It is a circular tunnel driven in a homogeneous, isotropic, initially elastic rock mass subjected to a hydrostatic stress field, σ_0. The support system is assumed to provide a uniform radial support pressure, p_s. It may happen that the stresses induced in the rock following excavation will exceed the yield strength of the rock mass and that a plastic zone of radius r_e will develop around the tunnel. The rock outside the boundary defined by r_e is assumed to remain elastic. There are other assumptions to derive the solutions as following:

(1) Plane strain conditions;

(2) The ground is homogeneous and isotropic, and remains elastic until reaching failure, which may be brittle and follows the coulomb failure envelop in which post-peak dilatancy occurs at a constant rate with major principal strain. and

(3) The bolt load is assumed as a uniformly distributed pressure.

Using the β-method to consider the 3D effects, the internal pressure at the excavation boundary is incrementally relaxed until it is zero (Bobet and Einstein, 2011). The result is continuous representation of the deformation-internal pressure relationship for a tunnel. The solution is presented in Table 2-9.

Bobet and Einstein (2011) also derives the analytical soltuions of GRCs for circular tunnel without reinforcement, circular tunnels with DMFC and CMC/CFC reinforcement using β-method to consider the 3D effects. The solutions are shown in Table 2-10, 2-11 and 2-12 respectively.

Table 2-9 Analytical solutions of typical axisymmetric circular tunnel problem (modified after Brady and Brown, 2006; Carranza-Torres and Fairhurst, 2000)

Tunnel model	Region A (Plastic)	*E-P* Boundary	Region B (Elastic)
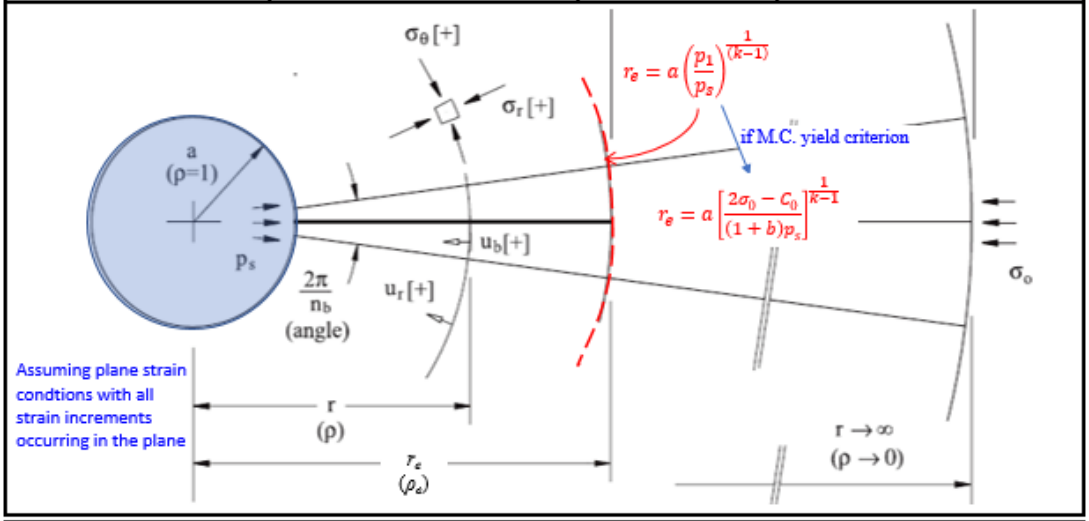			
Tangential stresses, $\sigma_{\theta\theta}$	$p_s\left(\frac{r}{a}\right)^{(k-1)}$	p_1	$\sigma_0\left(1-\frac{r_e^2}{r^2}\right)+p_1\frac{r_e^2}{r^2}$
Radial stresses, σ_{rr}	$kp_s\left(\frac{r}{a}\right)^{(k-1)}$	$2\sigma_0 - p_1$	$\sigma_0\left(1+\frac{r_e^2}{r^2}\right)-p_1\frac{r_e^2}{r^2}$
Radial dispalcement, u_r	$r\frac{\sigma_0 - p_i}{G(1+f)}\left[\frac{f-1}{2}+\left(\frac{r_e}{r}\right)^{(1+f)}\right]$	$\frac{(\sigma_0 - p_1)r_e}{2G}$	$\frac{(\sigma_0 - p_1)r_e^2}{2Gr}$
Note: The limiting states of stress in the fractured rock are given by: $\sigma_1 = b\sigma_3 + C_0$ and $\sigma_1 = k\sigma_3$ where $b = \frac{1+\sin\varphi^f}{1-\sin\varphi^f}$ According to boundary condition, the stress at E-P boundary is: $p_1 = \frac{2p - C_0}{1+b}$ and $r_e = a\left[\frac{2\sigma_0 - C_0}{(1+b)p_s}\right]^{\frac{1}{k-1}}$			

Table 2-10 Analytical solution for the circular tunnel excavation without rock reinforcement (after Bobet and Einstein, 2011)

	$a \le r \le r_e$	$r_e \le r \le \rho$	$r \ge \rho$
Radial stress, σ_r	$\sigma_r = \left(p_s + \frac{N_c}{N_\phi - 1} \right) \left(\frac{r}{a} \right)^{N_\phi - 1} \frac{N_c}{N_\phi - 1}$	$\sigma_r = \sigma_0 - \frac{\left(N_\phi^P - 1 \right) \sigma_0 + N_c^P}{N_\phi^P + 1} \left(\frac{r_e}{r} \right)^2$	
Tangential stress, σ_θ	$\sigma_\theta = N_\phi \left(p_s + \frac{N_c}{N_\phi - 1} \right) \left(\frac{r}{a} \right)^{N_\phi - 1} \frac{N_c}{N_\phi - 1}$	$\sigma_\theta = \sigma_0 + \frac{\left(N_\phi^P - 1 \right) \sigma_0 + N_c^P}{N_\phi^P + 1} \left(\frac{r_e}{r} \right)^2$	
Radial disp., U_r	$U_r = -A^i r^{-\alpha} - B^i r^{N_\phi} - C^i r$	$U_r = -\frac{1+\upsilon}{E} \frac{\left(N_\phi^P - 1 \right) \sigma_0 + N_c^P}{N_\phi^P + 1} \frac{\left(r_e \right)^2}{r}$	
Note	$A^i = -\frac{1+\nu}{E} \left[p_s + \frac{N_c}{N_\phi - 1} \right] \frac{1 + N_\psi N_\phi - \upsilon \left(1 + N_\psi \right) \left(1 + N_\phi \right)}{N_\psi + N_\phi} \left(\frac{r_e}{a} \right)^{N_\phi} a \left(r_e \right)^{N\psi}$ $+ \frac{1+\nu}{E} \left[\left(1 - 2\upsilon \right) \left(\sigma_0 + \frac{N_c}{N_\phi - 1} \right) + \frac{\left(N_\phi^P - 1 \right) \sigma_0 + N_c^P}{N_\phi^P + 1} \right] \left(r_e \right)^{N\psi + 1}$ $B^i = \frac{1+\upsilon}{E} \left(p_s + \frac{N_c}{N_\phi - 1} \right) \frac{1 + N_\psi N_\phi - \upsilon \left(1 + N_\psi \right) \left(1 + N_\phi \right)}{N_\psi + N_\phi} \left(\frac{1}{a} \right)^{N_\phi - 1}$ $C^i = -\frac{\left(1 + \upsilon \right) \left(1 - 2\upsilon \right)}{E} \left(\sigma_0 + \frac{N_c}{N_\phi - 1} \right)$ $\left(\frac{r_e}{a} \right)^{N_\phi - 1} = \frac{\left(N_\phi - 1 \right)}{\left(N_\phi - 1 \right) p_s + N_c} \left[\frac{2\sigma_0 - N_c^P}{N_\phi^P + 1} + \frac{N_c}{N_\phi - 1} \right]$		

Table 2-11 Analytical solution for the circular tunnel excavation with DMFC element reinforcement (after Bobet and Einstein, 2011)

	$a \le r \le r_e$	$r_e \le r \le \rho$	$r \ge \rho$
Radial stress, σ_r	$\sigma_r = \left(\sigma_i + p_0 + \frac{N_c}{N_\phi - 1}\right)\left(\frac{r}{a}\right)^{N_\phi - 1} - \frac{N_c}{N_\phi - 1}$	$\sigma_r = C_1 - \frac{C_2}{r^2}$	$\sigma_r = \sigma_0 - \left(\sigma_0 + \frac{p_0 r_0}{\rho} - C_1 + \frac{C_2}{r^2}\right)\frac{\rho^2}{r^2}$
Tangential stress, σ_θ	$\sigma_\theta = N_\phi\left(\sigma_i + p_0 + \frac{N_c}{N_\phi - 1}\right)\left(\frac{r}{a}\right)^{N_\phi - 1} - \frac{N_c}{N_\phi - 1}$	$\sigma_\theta = C_1 + \frac{C_2}{r^2}$	$\sigma_r = \sigma_0 + \left(\sigma_0 + \frac{p_0 r_0}{\rho} - C_1 + \frac{C_2}{r^2}\right)\frac{\rho^2}{r^2}$
Radial disp., U_r	$U_r = -Ar^{-\alpha} - Br^{N_\phi} - Cr$	$U_r = -\frac{1+\upsilon}{E}\left[(1-2\upsilon)C_1 r + \frac{C_2}{r} - (1-2\upsilon)\sigma_0 r\right]$	$U_r = -\frac{1+\upsilon}{E}\left(\sigma_0 + \frac{p_0 r_0}{\rho} - C_1 + \frac{C_2}{r^2}\right)\frac{\rho^2}{r^2}$
Note	$A = \frac{1+\nu}{E}\left[(1-2\upsilon)C_1 r_e + \frac{C_2}{r_e} - (1-2\upsilon)\sigma_0 r_e\right] r_e^{N_\psi} - B r_e^{N_\psi + N_\phi} - C r_e^{N_\psi + 1}$ $B = \frac{1+\upsilon}{E}\left(\sigma_i + p_0 + \frac{N_c}{N_\phi - 1}\right)\frac{1 + N_\psi N_\phi - \upsilon(1+N_\psi)(1+N_\phi)}{N_\psi + N_\phi}\left(\frac{1}{a}\right)^{N_\phi - 1}$ $C = -\frac{(1+\upsilon)(1-2\upsilon)}{E}\left(\sigma_0 + \frac{N_c}{N_\phi - 1}\right)$ $C_1 = \sigma_0 + \frac{p_0 r_0}{2(1-\upsilon)\rho}$ $\quad$ $C_2 = \left\{\frac{N_c^p}{N_\phi^p + 1} + \frac{N_c^p - 1}{N_\phi^p + 1}\left[\sigma_0 + \frac{p_0 r_0}{2(1-\upsilon)\rho}\right]\right\} r_e^2$ $\left(\frac{r_e}{a}\right)^{N_\phi - 1} = \frac{(N_\phi - 1)}{\left[(N_\phi - 1)(\sigma_i + p_0) + N_c\right]}\frac{1}{(N_\phi^p + 1)} \times \left[2\sigma_0 + \frac{p_0 r_0}{2(1-\nu)\rho} - N_c^p + \frac{N_\phi^p - 1}{N_\phi - 1} N_c\right]$		

Table 2-12 Analytical solution for the circular tunnel excavation with CMC/CFC element reinforcement (after Bobet and Einstein, 2011)

	$a \le r \le r_e$	$r_e \le r \le \rho$	$r \ge \rho$
Radial stress, σ_r	$\sigma_r = C_1 r^{r_1} + C_2 r^{r_2} + C_3 r^{N_\phi - 1} + C_4$	$\sigma_r = C_5 r^{r_1} + C_6 r^{r_2} + C_7 r^{N_\phi - 1} + C_4$	$\sigma_r = \sigma_0 - \left(\sigma_0 + \frac{p_0 r_0}{\rho} - C_1 + \frac{C_2}{r^2} \right) \frac{\rho^2}{r^2}$
Tangential stress, σ_θ	$\sigma_\theta = N_\phi \sigma_r + N_c$	$\sigma_\theta = N_\phi \sigma_r + N_c$	$\sigma_r = \sigma_0 + \left(\sigma_0 + \frac{p_0 r_0}{\rho} - C_1 + \frac{C_2}{r^2} \right) \frac{\rho^2}{r^2}$
Radial disp., U_r	$U_r = -A^i r^{-N\psi} - B^i r^{-N\phi} - C^i r + \frac{r_1 + 1 - N_\phi}{(r_1 + 1) r_1 \kappa} C_1 r^{r_1 + 1} + \frac{r_2 + 1 - N_\phi}{(r_2 + 1) r_2 \kappa} C_2 r^{r_2 + 1}$	$U_r = -Dr^{-1} + \frac{r_1 + 1 - N_\phi}{(r_1 + 1) r_1 \kappa} C_5 r^{r_1 + 1} + \frac{r_2 + 1 - N_\phi}{(r_2 + 1) r_2 \kappa} C_6 r^{r_2 + 1} - \frac{1 + N_\phi}{2\kappa} C_7 r^{-1} - C^i r$	$U_r = -\frac{1 + \upsilon}{E} \left(\sigma_0 + \frac{p_0 r_0}{\rho} - C_1 + \frac{C_2}{r^2} \right) \frac{\rho^2}{r^2}$
Bolt force, T	$T = -A_b E_b \left(\frac{r_1 + 1 - N_\phi}{r_1 \kappa} C_5 r^{r_1} + \frac{r_2 + 1 - N_\phi}{r_2 \kappa} C_2 r^{r_2} \right)$	$T = -A_b E_b \left(\frac{r_1 + 1 - N_\phi}{r_1 \kappa} C_5 r^{r_1} + \frac{r_2 + 1 - N_\phi}{r_2 \kappa} C_2 r^{r_2} + \frac{1 + N_\phi}{2\kappa} C_7 r^{-2} - C^i \right)$	
Note	$\kappa = A_b E_b / \left(S_z \bar{S}_\theta \right)$ $C_1 = C_5 - \frac{(r_1 + 1) r_1 \kappa}{(r_2 - r_1)(r_1 + 1 - N_\phi)} \left[\frac{1 + N_\phi}{2\kappa} (r_2 + 2) C_7 r_e^{-2} + C^i r_2 \right]$ $C_2 = C_6 - \frac{(r_2 + 1) r_1 \kappa}{(r_1 - r_2)(r_2 + 1 - N_\phi)} \left[\frac{1 + N_\phi}{2\kappa} (r_1 + 2) C_7 r_e^{-2} + C^i r_1 \right]$ $C_3 = \frac{E}{1 + \upsilon} \frac{N_\phi + N_\psi}{1 + N_\phi N_\psi - \nu (1 + N_\phi)(1 + N_\psi)} B^i \qquad C_4 = -N_c / (N_\phi - 1)$		

2.3.2. SCC

Stresses and displacement in rock tunnels depend on the rock mass properties and the in-situ stress (Alejano et al., 2009). However, the type and stiffness of the support and the timing of its installation influence the stress/displacement field significantly (Brown et al., 1983). The interdependence of these factors can be presented in a ground-support interaction diagram, such as the examples shown in Figure 2-25. Four support catogeries are discussed in this diagram. Support ① is installed at time *t1* and reaches equilibrium at point *B*. This support is too stiff to sustain the rock mass deformation. Instead, it is easy to fail due to the excessive loading on the support elements. Suport ② has a lower stiffness and it is installed at a later time *t2* and reaching equilibrium at *C*. This support provides a good time and stiffness to carry the load. Support ③ is installed at the same time *t2*, but has the lowest stiffness among the four catogeries. It reaches equilibrium at *D* where rock mass has initiated falling. This dangeous situation indicates that this support is too flexible to sustain extra loading. Support ④ which has the same stiffness with support ②, is installed at time *t3*. In this case, excessive convergence of the excavation may occur. It means the support elements are installed too late and may not reach the balance.

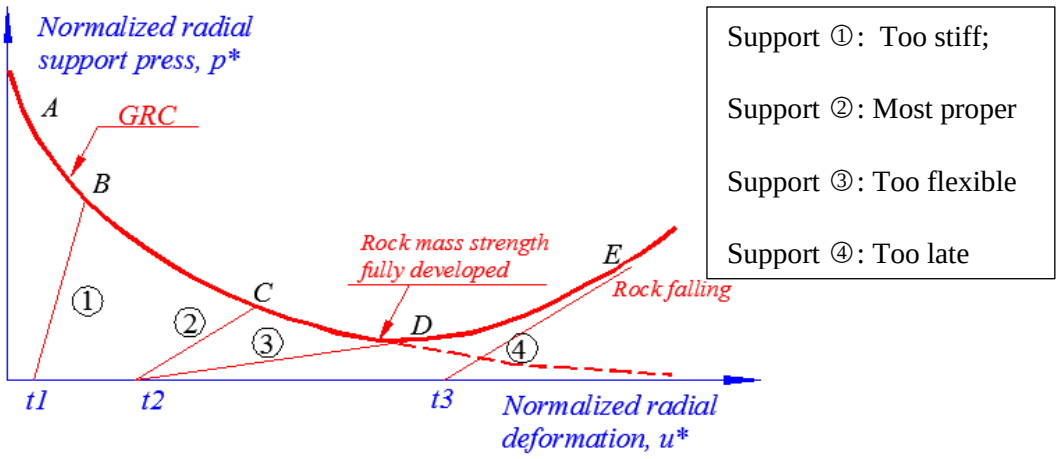

Figure 2-25 Illustration of the influence of support stiffness and timing of installation on support performance (modified after Brady and Brown, 2006)

2.3.3. LDP

LDP is developed to work with GRC to determine the appropriate timing for the installation of support or to optimize the installation of support with specific displacement capacity. In the LDP, the longitudinal profile of closure or displacement versus distance from the tunnel face are presented. As shown in Figure 2-26, a portion of the maximum radial displacements at the tunnel boundary will take place before the face advances past a specific point. The tunnel boundary will continue to displace inwards as the tunnel advances further beyond the point in question.

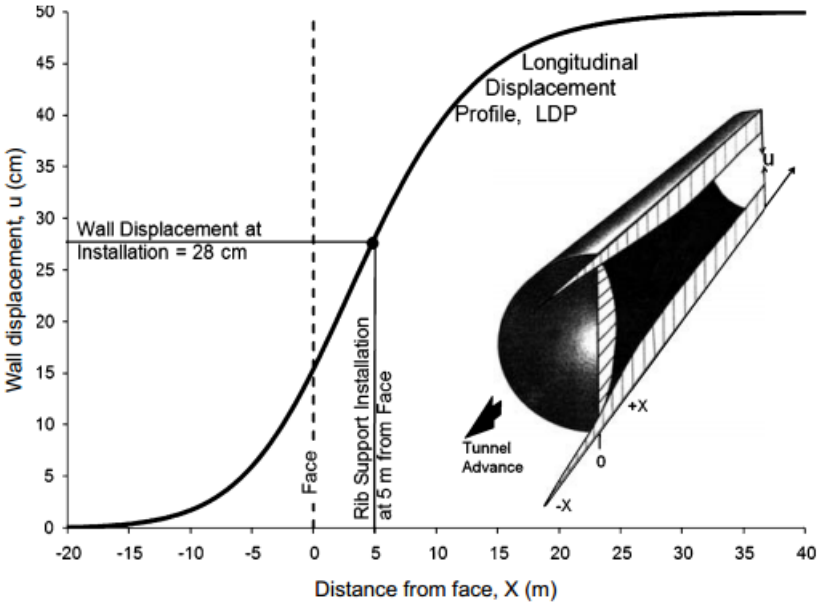

Figure 2-26 Illustration of longitudinal displacement profile (LDP) (Vlachopoulos and Diederichs, 2009)

To determine the relationship for the LDP, several researchers have suggested alternative expressions. Vlachopoulos and Diederichs (2009) improved the expressions and get the best fit relationship of the normalized closure u^* as:

For $x < 0$, in the rock mass: $$u^* = \frac{u}{u_{max}} = u_0^* \times e^x$$

For $x = 0$, at face: $$u_0^* = \frac{u_0}{u_{max}} = \frac{1}{3} e^{-0.15R^*} \quad (2.28)$$

For $x > 0$, in the tunnel: $$u^* = 1 - (1 - u_0^*) \times e^{-\frac{3x}{2R^*}}$$

where: R^* – the normalized plastic radius, $R^* = R_P / R_T$;

R_T – tunnel radius;

R_P – radius of plastic zone;

u_{max} – maximum radial displacement

u_0 – radial displacement at the face location

Graphical LDP templates are also developed by Vlachopoulos and Diederichs (2009) to provide an alternative way to determine the displacement. It should be noted that, when adopt this method, u_{mas} and R_P need to be determined prior to the sequenced analysis (Alejano et al., 2010; Vlachopoulos and Diederichs, 2014).

2.3.4. Application of rock-rockbolt interaction diagram

The application of rock-rockbolt interaction diagram is evaluated by researchers (Alejano et al., 2010; Carranza-Torres and Fairhurst, 2000; Dias, 2011; Lü et al., 2012). The typical approach to use the diagram is summarized as follows.

(1) Calculate the GRC for a tunnel without reinforcement. The relationship between the pressure applied on the tunnel face and maximum extrusion is calculated.

(2) Simulate the LDP using full 3D analysis (if possible). For 2D analysis, the methods introduced in Table 2-8 could be adopted to simulate the LDP. The results could be converted to location along the tunnel using Eq. (2.28).

(3) Plotting GRC and LDP in the same diagram, the intersection point allows defining the working point of the soil/bolts system. Figure 2-27 illustrates a typical application process.

However, the application of CCM in engineering practice has some limitations. Some of them are common in the rock mechanics field, such as the stringent assumptions to derive equations, the variability of rock mass, complexity of rock structure, etc. The limitations and caveats when applying the CCM in engineering practice are summarized in Table 2-13.

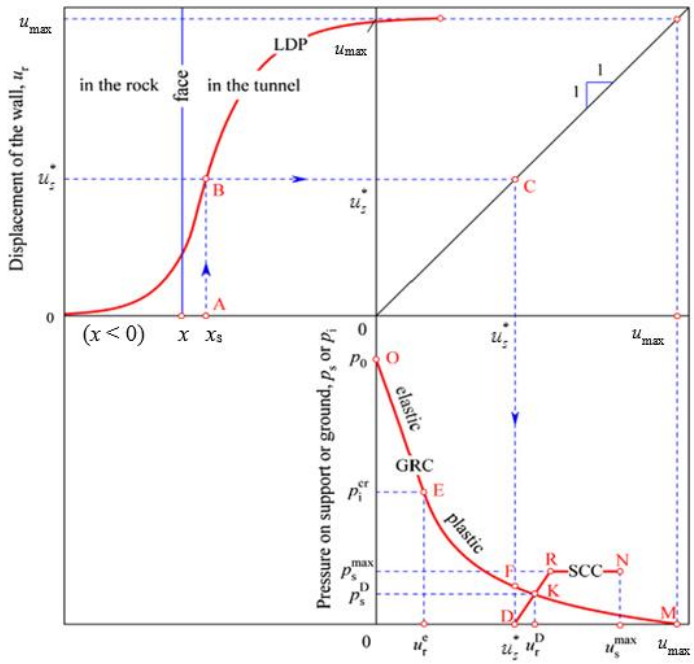

Figure 2-27 Schematic representation of LDP, GRC and SCC (Lü et al., 2012)

Table 2-13 Limitations and caveats when applying CCM in engineering

Limitations (Alejano et al., 2010)	Caveats (Vlachopoulos and Diederichs, 2014)
Difficulties in defining GRC	The core replacement method is less sensitive to element type (more deviation between roof, floor, wall) in the circular case, and both are subject to deviations caused by non-ideal geometry (in the case of the horseshoe).
Difficulties in defining LDP	• Non-isotropic stresses render the standard LDP approach inaccurate. For moderate values of stress ratio, k_0, some assumptions and adjustments can be made to make the approach practically viable. • Sequenced excavation such as top heading and bench excavation poses a problem for the LDP approach unless the second excavation stage is distant from the first.
Complex construction behaviour	• For simple tunnel geometries, the 2D LDP and GRC are not sensitive to the choice of face replacement or pressure reduction technique but are sensitive to the step size (face too soft or pressure increment too great). • Tunnel shape is an important factor for the application of 2D staged modelling although results can be practically acceptable provided the aspect ratio of tunnel geometry is not extreme
Complex boundary condition in engineering	Fixed boundaries should be a minimum of 12 radii from the tunnel or at least 3 plastic radii away from the plastic zone.
Availability of numerical models to analyze the problem	It is critical to correctly locate the installation step within a staged 2D modelling sequence to prevent overloading or excess deformation

2.4 Basic discontinuous deformation analysis (DDA) theory

The discontinuous deformation analysis (DDA) method is developed and programmed by Shi (1988) to perform a complete deformation analysis of a block system. As a numerical method with a discrete modelling feature, DDA has been widely used in rock mechanics and rock engineering problems, such as underground structure failures and reinforcement (Zhao et al., 2007; Kim et al., 1999; Tsesarsky and Hatzor 2006), and slope-stability analysis (Wu and Chen 2011; Sun et al. 2011). The DDA computes the static and dynamic behaviours of discrete blocky systems based on block kinematics. It uses six block deformations as the basic variables in the first-order approximations. In each time step, an individual block has constant stresses and strains. The displacements of any point (x, y) inside a block are represented as:

$$\begin{pmatrix} u \\ v \end{pmatrix} = \begin{pmatrix} 1 & 0 & -(y-y_0) & (x-x_0) & 0 & (y-y_0)/2 \\ 0 & 1 & (x-x_0) & 0 & (y-y_0) & (x-x_0)/2 \end{pmatrix} \begin{pmatrix} u_0 \\ v_0 \\ r_0 \\ \varepsilon_x \\ \varepsilon_y \\ \gamma_{xy} \end{pmatrix} \tag{2.29}$$

where (u_0, v_0) − the rigid body translation at a specific point (x_0, y_0) within the block;

r_0 − the rotation angle of the block with respect to (x_0, y_0);

ε_x and ε_y − the normal strains in the x and y directions, respectively, and

γ_{xy} − the shear strain.

Rewriting Eq.(2.29) into a generalized form gives:

$$\begin{Bmatrix} u_i \\ v_i \end{Bmatrix} = \begin{bmatrix} t_{11} & t_{12} & t_{13} & t_{14} & t_{15} & t_{16} \\ t_{21} & t_{22} & t_{23} & t_{24} & t_{25} & t_{26} \end{bmatrix} \begin{Bmatrix} d_{1i} \\ d_{2i} \\ d_{3i} \\ d_{4i} \\ d_{5i} \\ d_{6i} \end{Bmatrix} \tag{2.29a}$$

or

$$[u_i] = [T_i]\{D_i\} \tag{2.29b}$$

For a system with n blocks, the simultaneous equilibrium equations have the following form:

$$\begin{bmatrix} K_{11} & K_{12} & \cdots & K_{1n} \\ K_{21} & K_{22} & \cdots & K_{2n} \\ \vdots & \vdots & \ddots & \vdots \\ K_{n1} & K_{n2} & \cdots & K_{nn} \end{bmatrix} \begin{bmatrix} D_1 \\ D_2 \\ \vdots \\ D_n \end{bmatrix} = \begin{bmatrix} F_1 \\ F_2 \\ \vdots \\ F_n \end{bmatrix} \tag{2.30}$$

or $$\left[K_{ij}\right]\left\{D_i\right\} = \left[F_i\right] \tag{2.30)a}$$

where K_{ij} ($i \neq j$) is a 6×6 sub-matrix to represent the contacts between blocks i and j, K_{ij} ($i = j$) is the local stiffness matrix, D_i and F_i are 6×1 sub-matrices, and D_i represents the deformation variables (u_0, v_0, r_0, ε_x, ε_y, γ_{xy}) and F_i represents the loading on block i distributed to the six deformation variables. Figure 2-28 illustrates the structure of the global stiffness matrix of a 3-block system.

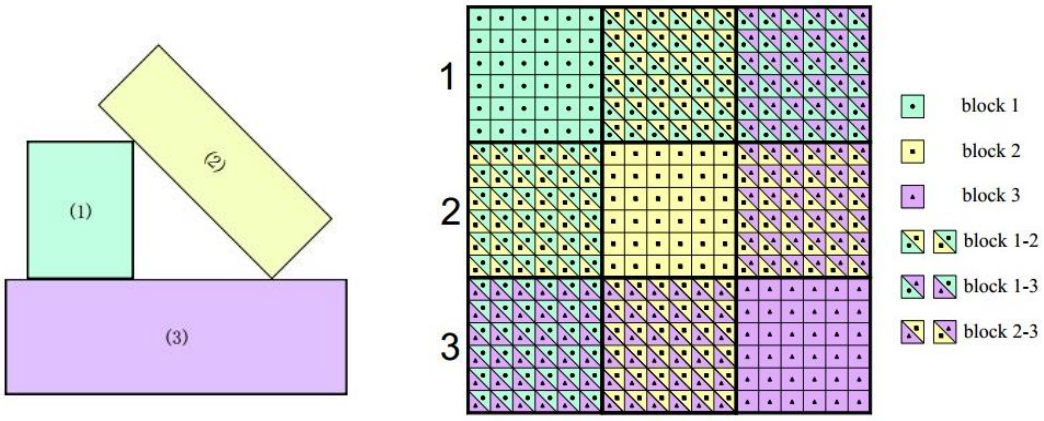

Figure 2-28 Schematic illustration of global stiffness matrix for a 3-block DDA model (Bao, 2010)

These equilibrium equations are derived by minimizing the total potential energy (Π) of the block system. The i^{th} row of Eq.(2.30) consists of 6 linear equations:

$$\frac{\partial \Pi_i}{\partial d_{ri}} = 0, r = 1, 2, ..., 6 \tag{2.31}$$

where Π_i is the potential energy of block i.

Considering the components of d_{ri}, the above equation the equilibrium of all the loads and contact forces acting on block i along the x and y axes respectively, gives:

$$\frac{\partial \Pi_i}{\partial u_0} = 0, \frac{\partial \Pi_i}{\partial v_0} = 0$$

The moment equilibrium of all the loads and contact forces on block *i.* gvies:

$$\frac{\partial \Pi_i}{\partial r_0} = 0$$

The equilibrium of the external forces and stress of block *i*, gives

$$\frac{\partial \Pi_i}{\partial \varepsilon_x} = 0, \frac{\partial \Pi_i}{\partial \varepsilon_y} = 0, \frac{\partial \Pi_i}{\partial \gamma_{xy}} = 0$$

2.4.1. Submatrices of elastic strains

In the original DDA method, the block is deforming under Hooke's law. The stress and strain relationship can be expressed as:

$$\begin{Bmatrix} \sigma_x \\ \sigma_y \\ \tau_{xy} \end{Bmatrix} = \frac{E}{1-\nu^2} \begin{bmatrix} 1 & \nu & 0 \\ \nu & 1 & 0 \\ 0 & 0 & \frac{1-\nu}{2} \end{bmatrix} \begin{Bmatrix} \varepsilon_x \\ \varepsilon_y \\ \gamma_{xy} \end{Bmatrix} \tag{2.32}$$

where E is the elastic modulus of block, ν is the Poisson's ratio. For the plane strain problem, using E' and ν' to instead the E and ν reprehensively. They are calculated as:

$$E' = \frac{E}{1-\nu^2}, \nu' = \frac{\nu}{1-\nu} \tag{2.32a}$$

Substituting $[d_{ri}]$ to replace $[\varepsilon_i]$, the potential strain energy Π_e as:

$$\begin{aligned} \Pi_e &= \iint \frac{1}{2} \{\varepsilon_i\}^T \{\sigma_i\} \, dxdy \\ &= \frac{1}{2} \iint \{d_{ri}\}^T [E_i] \{d_{ri}\} \, dxdy \\ &= \frac{S_i}{2} \{d_{ri}\}^T [E_i] \{d_{ri}\} \end{aligned} \tag{2.33}$$

where S_i is the area of the i^{th} block.

For block *i*, the matrix $[E_i]$ is given as:

$$[E_i] = \frac{E}{(1-\nu^2)} \begin{bmatrix} 0 & 0 & 0 & 0 & 0 & 0 \\ 0 & 0 & 0 & 0 & 0 & 0 \\ 0 & 0 & 0 & 0 & 0 & 0 \\ 0 & 0 & 0 & 1 & \nu & 0 \\ 0 & 0 & 0 & \nu & 1 & 0 \\ 0 & 0 & 0 & 0 & 0 & \frac{1-\nu}{2} \end{bmatrix} \tag{2.34}$$

By taking the derivatives to minimize the strain energy, the contribution of elastic strain to the stiffness matrix $[K_{ij}]$ can be calculated as:

$$\frac{\partial^2 \Pi_e}{\partial d_i \partial d_i} = S_i \left[E_i\right] \rightarrow \left[K_{ii}\right] \tag{2.35}$$

2.4.2. Submatrices of point loading

The potential energy Π_p of a point load acting at point (x,y) of block i is derived as:

$$\Pi_p = -\begin{pmatrix} u & v \end{pmatrix} \begin{pmatrix} F_x \\ F_y \end{pmatrix} = -\left[D_i\right]\left[T_i(x,y)\right]^T \begin{pmatrix} F_x \\ F_y \end{pmatrix} \tag{2.36}$$

To minimize Π_p, the derivatives are computed and formed a 6×1 sub-matrix $[F_i]$ which is calculated as:

$$\begin{bmatrix} t_{11} & t_{21} \\ t_{12} & t_{22} \\ t_{13} & t_{23} \\ t_{14} & t_{24} \\ t_{15} & t_{25} \\ t_{16} & t_{26} \end{bmatrix} \begin{bmatrix} F_x \\ F_y \end{bmatrix} \rightarrow \left[F_i\right] \tag{2.37}$$

2.4.3. Submatrices of inertia forces

The time dependent displacements of a point (x_i, y_i) of block i are denoted as $u(t)$ and $v(t)$ respectively. The mass per unit area is m. The force of inertia per unit area is given as:

$$\begin{pmatrix} f_x \\ f_y \end{pmatrix} = -m \begin{pmatrix} \dfrac{\partial^2 u(t)}{\partial t^2} \\ \dfrac{\partial^2 v(t)}{\partial t^2} \end{pmatrix} \tag{2.38}$$

The potential energy Π_m is derived as:

$$\begin{aligned} \Pi_m &= -\iint \begin{pmatrix} u & v \end{pmatrix} \begin{pmatrix} f_x \\ f_y \end{pmatrix} dxdy \\ &= \iint m\left[D_i\right]^T \left[T_i\right]^T \left[T_i\right] \frac{\partial^2 \left[D(t)\right]}{\partial t^2} dxdy \end{aligned} \tag{2.39}$$

where: $$\frac{\partial^2[D(t)]}{\partial t^2}=\left(\frac{\partial^2 u_0(t)}{\partial t^2}\quad\frac{\partial^2 v_0(t)}{\partial t^2}\quad\frac{\partial^2 r_0(t)}{\partial t^2}\quad\frac{\partial^2 \varepsilon_x(t)}{\partial t^2}\quad\frac{\partial^2 \varepsilon_y(t)}{\partial t^2}\quad\frac{\partial^2 \gamma_{xy}(t)}{\partial t^2}\right)^T$$

Using time integration, assume $[D_i(t)]$ as the initial block displacement, Δ as the time interval of this step, we get:

Initial velocity: $$[V_0]=\frac{\partial[D(t)]}{\partial t} \tag{2.40a}$$

Velocity: $$[V_i]=\Delta\frac{\partial[D^2(t)]}{\partial t^2}+[V_0]=\frac{2}{\Delta}[D_i]-[V_0] \tag{2.40b}$$

Acceleration: $$\frac{\partial^2[D(t)]}{\partial t^2}=\frac{2}{\Delta^2}[D_i]-\frac{2}{\Delta}\frac{\partial[D(t)]}{\partial t}=\frac{2}{\Delta^2}[D_i]-\frac{2}{\Delta}[V_0] \tag{2.40c}$$

Displacement: $$[D_i]=\frac{\Delta^2}{2}\frac{\partial^2[D(t)]}{\partial t^2}+\Delta\frac{\partial[D(t)]}{\partial t} \tag{2.40d}$$

By taking the derivatives to minimize the potential energy Π_m, the submatrices of inertia forces are calculated as:

$$\frac{\partial^2\Pi_m}{\partial d_i\partial d_i}=\frac{2m}{\Delta^2}\iint[T_i]^T[T_i]dxdy\rightarrow[K_{ii}] \tag{2.41}$$

$$-\frac{\partial\Pi_m}{\partial d_i}=\frac{m}{\Delta^2}\left(\iint[T_i]^T[T_i]dxdy\right)[V_0]\rightarrow[F_i] \tag{2.42}$$

2.4.4. Submatrices of bolting connection

The DDA code considers bolting connection between two points. As shown in Figure 2-29, a bolt is connecting point (x_i, y_i) of block i and point (x_j, y_j) of block j. The displacement of the end point is given as:

$$\begin{aligned} dx_i &= u_i = u(x_i, y_i)\\ dy_i &= v_i = v(x_i, y_i)\\ dx_j &= u_j = u(x_j, y_j)\\ dy_j &= v_j = v(x_j, y_j) \end{aligned} \tag{2.43}$$

The increment of bolt length is given as:

$$\mathrm{d}l=\left[\begin{pmatrix}u_i & v_i\end{pmatrix}\begin{pmatrix}l_x\\ l_y\end{pmatrix}-\begin{pmatrix}u_j & v_j\end{pmatrix}\begin{pmatrix}l_x\\ l_y\end{pmatrix}\right]=\left\{[D_i]^T[T_i]^T\begin{pmatrix}l_x\\ l_y\end{pmatrix}-[D_j]^T[T_j]^T\begin{pmatrix}l_x\\ l_y\end{pmatrix}\right\} \tag{2.44}$$

The force of bolt due to elongation is given as:

$$f = -E_b \frac{dl}{l} \tag{2.45}$$

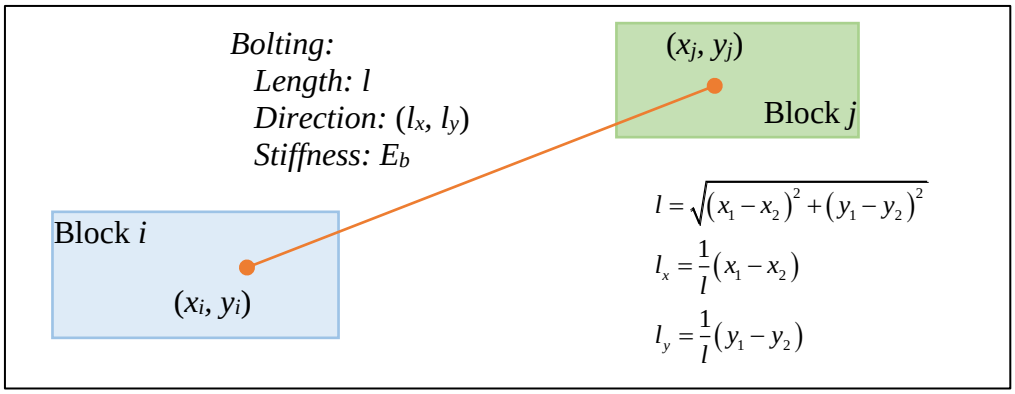

Figure 2-29 Bolting connection in original DDA by Shi (1998)

The strain energy of the bolt is calculated as:

$$\begin{aligned}\Pi_b &= -\frac{1}{2} fdl = \frac{E_b}{2l}(dl)^2 \\ &= \frac{E_b}{2l}\left([D_i]^T [E_i]^T [E_i][D_i] + [D_j]^T [E_j]^T [E_j][D_j]\right) \\ &\quad - \frac{E_b}{l}[D_i]^T [E_i]^T [E_j][D_j]\end{aligned} \tag{2.46}$$

where:

$$[E_i] = [T_i]^T \begin{pmatrix} l_x \\ l_y \end{pmatrix} \tag{2.46a}$$

$$[E_j] = [T_j]^T \begin{pmatrix} l_x \\ l_y \end{pmatrix} \tag{2.46b}$$

By taking the derivatives to minimize the strain energy Π_b, the submatrices of bolting connection can be calculated as:

$$\frac{\partial^2 \Pi_b}{\partial d_i \partial d_i} = \frac{E_b}{l}[E_i][E_i]^T \rightarrow [K_{ii}] \tag{2.47}$$

$$\frac{\partial^2 \Pi_b}{\partial d_i \partial d_j} = \frac{E_b}{l}[E_i][E_j]^T \rightarrow [K_{ij}] \tag{2.48}$$

Since the introduction of DDA method in 1980s, rockbolt elements have been developed. For example, Moosavi and Grayeli (2006) implemented the fully grouted cable element into the DDA according to the load transfer mechanism. Nie et al. (2014a, b) have

extended the model to simulate different kinds of rockbolt, such as the fully grouted rockbolt and the D-bolt. He et al. (2018) also have introduced the Euler-Bernoulli beam elements to simulate the rockbolt element. The results have shown that 2D-DDA could provide an effective framework to simulate the load transfer between rockbolt and rock mass.

2.4.5. Submatrices of contacts

In general, there are three kinds of contacts between blocks in DDA: angle to angle, angle to edge and edge to edge. All the contacts transformed into point-line crossing inequalities in the calculation. By assuming a point P_1 (x_1, y_1) in block i which has displacement increment as (u_1, v_1), the point has potential to pass an inter-penetration line P_2P_3 constituted by points (x_2, y_2) and (x_3, y_3) in block j. The displacement increments for the points in the inter-penetration line are assumed as (u_2, v_2) and (u_3, v_3) respectively.

(1) Normal contact

If P_1 passes through P_2P_3, the artificial interpenetration distance d_n should be negative and calculated as:

$$d_n = \frac{\Delta}{l} \tag{2.49}$$

where: Δ is the area of triangle $P_1P_2P_3$ and $\Delta = \begin{vmatrix} 1 & x_1+u_1 & y_1+v_1 \\ 1 & x_2+u_2 & y_2+v_2 \\ 1 & x_3+u_3 & y_3+v_3 \end{vmatrix}$,

l is the length of edge P_2P_3 and $l = \sqrt{\left(x_2+u_2-x_3-u_3\right)^2+\left(y_2+v_2-y_3-v_3\right)^2}$.

Neglect the second order infinitesimal terms, Eq. (2.49) could be revised as:

$$d_n = \frac{1}{l}\begin{pmatrix} S_0+\begin{pmatrix} y_2-y_3 & x_3-x_2 \end{pmatrix}\begin{Bmatrix} u_1 \\ v_1 \end{Bmatrix} \\ +\begin{pmatrix} y_3-y_1 & x_1-x_3 \end{pmatrix}\begin{Bmatrix} u_2 \\ v_2 \end{Bmatrix}+\begin{pmatrix} y_1-y_2 & x_2-x_1 \end{pmatrix}\begin{Bmatrix} u_3 \\ v_3 \end{Bmatrix} \end{pmatrix} \tag{2.50}$$

where: $S_0 = \begin{vmatrix} 1 & x_1 & y_1 \\ 1 & x_2 & y_2 \\ 1 & x_3 & y_3 \end{vmatrix}$.

By introducing Eq. (2.19b), Eq. (2.50) could be revised as:

$$d_n = \frac{S_0}{l} + \begin{pmatrix} e_1 & \cdots & e_6 \end{pmatrix} \begin{pmatrix} d_{1i} \\ \vdots \\ d_{6i} \end{pmatrix} + \begin{pmatrix} g_1 & \cdots & g_6 \end{pmatrix} \begin{pmatrix} d_{1j} \\ \vdots \\ d_{6j} \end{pmatrix} \tag{2.51}$$

where: $e_r = \frac{1}{l}\left[(y_2 - y_3) t_{1r}(x_1, y_1) + (x_3 - x_2) t_{2r}(x_1, y_1) \right]$ and

$$g_r = \frac{1}{l}\begin{bmatrix} (y_3 - y_1) t_{1r}(x_2, y_2) + (x_1 - x_3) t_{2r}(x_2, y_2) \\ + (y_1 - y_2) t_{1r}(x_3, y_3) + (x_2 - x_1) t_{2r}(x_3, y_3) \end{bmatrix}.$$

The strain energy of the normal contact spring forces is:

$$\Pi_{nc} = \frac{k_n}{2} d_n^2 = \frac{k_n}{2}\left(\sum_{r=1}^{6} e_r d_{ri} + \sum_{r=1}^{6} g_r d_{rj} + \frac{S_0}{l} \right)^2 \tag{2.52}$$

By taking the derivatives to minimize the strain energy Π_{nc}, the submatrices of contacts are calculated as:

$$\frac{\partial^2 (\Pi_{nc})}{\partial d_{ri} \partial d_{si}} = \frac{k_n}{2} \frac{\partial^2}{\partial d_{ri} \partial d_{si}} \left(\sum_{r=1}^{6} e_r d_{ri} \right)^2 \longrightarrow [K_{ii}] \tag{2.53a}$$

$$\frac{\partial^2 (\Pi_{nc})}{\partial d_{ri} \partial d_{sj}} = \frac{k_n}{2} \frac{\partial^2}{\partial d_{ri} \partial d_{sj}} \left(\sum_{r=1}^{6} e_r d_{ri} \right)\left(\sum_{r=1}^{6} g_r d_{rj} \right) \longrightarrow [K_{ij}] \tag{2.53b}$$

$$\frac{\partial^2 (\Pi_{nc})}{\partial d_{rj} \partial d_{si}} = \frac{k_n}{2} \frac{\partial^2}{\partial d_{rj} \partial d_{si}} \left(\sum_{r=1}^{6} e_r d_{ri} \right)\left(\sum_{r=1}^{6} g_r d_{rj} \right) \longrightarrow [K_{ji}] \tag{2.53c}$$

$$\frac{\partial^2 (\Pi_{nc})}{\partial d_{rj} \partial d_{sj}} = \frac{k_n}{2} \frac{\partial^2}{\partial d_{rj} \partial d_{sj}} \left(\sum_{r=1}^{6} g_r d_{rj} \right)^2 \longrightarrow [K_{jj}] \tag{2.53d}$$

$$-\frac{\partial \Pi_{nc}(0)}{\partial d_{ri}} = -\frac{k_n S_0}{l} \frac{\partial}{\partial d_{ri}} \left(\sum_{r=1}^{6} e_r d_{ri} \right)^2 \longrightarrow [F_i] \tag{2.53e}$$

$$-\frac{\partial \Pi_{nc}(0)}{\partial d_{rj}} = -\frac{k_n S_0}{l} \frac{\partial}{\partial d_{rj}} \left(\sum_{r=1}^{6} e_r d_{rj} \right)^2 \longrightarrow [F_j] \tag{2.53f}$$

(2) Shear contact

Assume P_0 with coordinates (x_0, y_0) is the projection of point P_1 on the inter-penetration line P_2P_3, the shear displacement is d_s is:

$$d_s = \frac{1}{l}\begin{pmatrix} x_1+u_1-x_0-u_0 & y_1+v_1-y_0-v_0 \end{pmatrix}\begin{pmatrix} x_3+u_3-x_2-u_2 \\ y_3+v_3-y_2-v_2 \end{pmatrix} \tag{2.54}$$

Ignoring the 2nd order infinitesimal small terms and introducing Eq. (2.19b), Eq. (2.54) was rearranged as:

$$d_s = \frac{S_0'}{l} + \begin{pmatrix} e_1' & \cdots & e_6' \end{pmatrix}\begin{pmatrix} d_{1i} \\ \vdots \\ d_{6i} \end{pmatrix} + \begin{pmatrix} g_1' & \cdots & g_6' \end{pmatrix}\begin{pmatrix} d_{1j} \\ \vdots \\ d_{6j} \end{pmatrix} \tag{2.55}$$

where, $S_0' = \begin{pmatrix} x_3-x_2 & y_3-y_2 \end{pmatrix}\begin{pmatrix} x_1-x_0 \\ y_1-y_0 \end{pmatrix}$,

$$e_r' = \frac{1}{l}\left[(y_3-y_2)t_{1r}(x_1,y_1) + (x_3-x_2)t_{2r}(x_1,y_1)\right] \text{ and}$$

$$g_r' = \frac{1}{l}\begin{bmatrix} (2x_0-x_1-x_3)t_{1r}(x_2,y_2) + (2y_0-y_1-y_3)t_{2r}(x_2,y_2) \\ +(x_1+x_2-2x_0)t_{1r}(x_3,y_3) + (y_1+y_2-2y_0)t_{2r}(x_3,y_3) \end{bmatrix}.$$

The strain energy of the shear contact spring forces is:

$$\Pi_{sc} = \frac{k_s}{2}d_s^2 = \frac{k_s}{2}\left(\sum_{r=1}^{6} e_r' d_{ri} + \sum_{r=1}^{6} g_r' d_{rj} + \frac{S_0'}{l}\right)^2 \tag{2.56}$$

By taking the derivatives to minimize the strain energy Π_{sc}, the submatrices of contacts are calculated as:

$$\frac{\partial^2(\Pi_{sc})}{\partial d_{ri}\partial d_{si}} = \frac{k_s}{2}\frac{\partial^2}{\partial d_{ri}\partial d_{si}}\left(\sum_{r=1}^{6} e_r' d_{ri}\right)^2 \longrightarrow [K_{ii}] \tag{2.57a}$$

$$\frac{\partial^2(\Pi_{sc})}{\partial d_{ri}\partial d_{sj}} = \frac{k_s}{2}\frac{\partial^2}{\partial d_{ri}\partial d_{sj}}\left(\sum_{r=1}^{6} e_r' d_{ri}\right)\left(\sum_{r=1}^{6} g_r' d_{rj}\right) \longrightarrow [K_{ij}] \tag{2.57b}$$

$$\frac{\partial^2(\Pi_{sc})}{\partial d_{rj}\partial d_{si}} = \frac{k_s}{2}\frac{\partial^2}{\partial d_{rj}\partial d_{si}}\left(\sum_{r=1}^{6} e_r' d_{ri}\right)\left(\sum_{r=1}^{6} g_r' d_{rj}\right) \longrightarrow [K_{ji}] \tag{2.57c}$$

$$\frac{\partial^2(\Pi_{sc})}{\partial d_{rj}\partial d_{sj}} = \frac{k_s}{2}\frac{\partial^2}{\partial d_{rj}\partial d_{sj}}\left(\sum_{r=1}^{6} g_r' d_{rj}\right)^2 \longrightarrow \left[K_{jj}\right] \tag{2.57d}$$

$$-\frac{\partial \Pi_{nc}(0)}{\partial d_{ri}} = -\frac{k_n S_0'}{l}\frac{\partial}{\partial d_{ri}}\left(\sum_{r=1}^{6} e_r' d_{ri}\right)^2 \longrightarrow \left[F_i\right] \tag{2.57e}$$

$$-\frac{\partial \Pi_{sc}(0)}{\partial d_{rj}} = -\frac{k_n S_0'}{l}\frac{\partial}{\partial d_{rj}}\left(\sum_{r=1}^{6} e_r' d_{rj}\right)^2 \longrightarrow \left[F_j\right] \tag{2.57f}$$

(3) Criterion to determine the contact status

Two types of iterative solver, namely directly equation solver and the Successive Over-Relaxation (SOR) solver are used, depending the block number in the model. After solving the equilibrium equations, the block displacement variables, the artificial interpenetration distance and the contact forces among the blocks could be solved. The possible contact status is shown in Table 2-14. The simultaneous equations Eq. (2.30) are changed in accordance with the spring selection. The procedure of solving equations and selecting springs are repeated until no penetration and tension constraints are satisfied, which is also called “open-close (O-C) iteration”. Hatzor et al. (2018) has mensioned that the numerical damping is essential for DDA analysis as it allows the oscillations caused by contact forces. The numerical damping is also proportional to the time step size. The high stiffness evoked by the penalty parameter means that the time step size must be reduced. An allowable soft contact spring is particularly advantageous in dynamic solutions.

Table 2-14 Contact status in DDA

Contact states	Contact forces	Lock/Spring applied	Illustration
Open	$R_n = -k_n d_n \le \sigma_t$	No springs and forces applied.	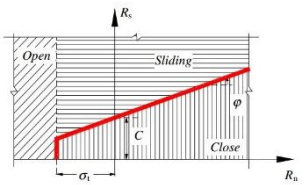
Close	$R_s < R_n \tan\varphi + c, R_n > \sigma_t$	Lock with normal and shear springs.	
Sliding	$R_s \ge R_n \tan\varphi + c, R_n > \sigma_t$	Lock with normal spring and a pair of friction forces.	

2.4.6. DDA coding framework

DDA is a displacement method where the unknowns in the equilibrium equations are displacements as shown in Eq. (2.30). Using an incremental solution procedure, the block movements are solved at each time step. The framework of the DDA calculation is illustrated in Figure 2-30.

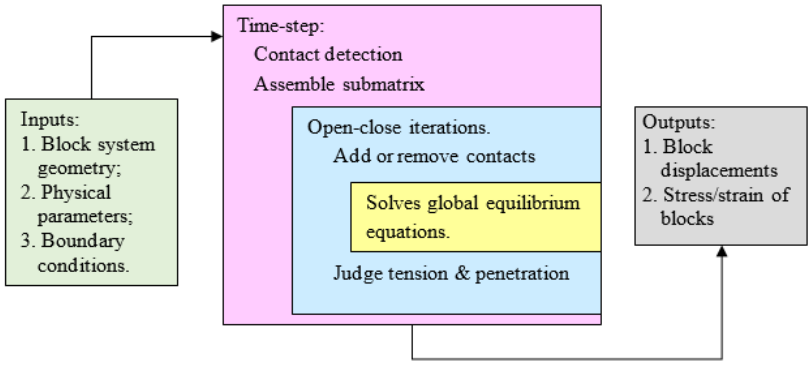

Figure 2-30 Framework of the multi-time step calculation adopted in DDA

2.5 Summaries and conclusions

The rockbolt load transfer mechanism, the rockbolt design principles and the rockbolt field application are reviewed in this chapter. Although significant progresses have been made in analytical, experimental, and numerical studies, the rockbolt design in underground excavations is still "in the state of art" (Hoek, 2007). The problem in applying these results is that the properties of the rock mass, particularly a jointed rock mass, are not fully understood which has been recognized and are common in rock mechanics. Practically, numerical modelling of specific geometrical and rock properties can gain insights into the reinforcement mechanism of rockbolt system. This is especially important for rockbolt design in underground construction. The following conclusions can be drawn.

(1) Varies types of rockbolts have been developed to restrain the rock movements in tunnels. However, the reinforcement of different rockbolts are results from their load transfer capacities to the rock mass which have not been fully studied. Further researches are required to develop a more general bond-slip model to present the load transfer mechanism of different rockbolt elements.

(2) One of the challenges in underground construction is the large displacement at the excavation surface. Numerical models using FEM may not get the ground reaction curve due to its convergence problems. DEM has advantages in simulating the large displacement of rock system, however, the rockbolt elements are not comprehensive enough. A more general rockbolt model should be developed to present various kinds of rockbolt with consideration of their featured reinforcing behaviours.

(3) The design of rockbolt system in underground construction is complex. The analytical methods, empirical methods and numerical methods are working together to propose a reasonable design. Among these methods, numerical methods have advantages in modelling the ground reactions. More simulations should be carried out in the future to support and analyze the empirical methods.

(4) The characteristic curves generated using Convergence-Confinement Method (CCM) are useful expressions to justify the reinforcement going to be adopted during underground constructions. However, the application is limited by the complex rock conditions in site. The characteristic curves can be further studied and the reinforcement mechanism of rockbolt system in underground excavation will be examined based on the rock/rockbolt interactions.

CHAPTER 3.
DETERMINATION OF THE LOAD TRANSFER OF A ROCKBOLT ELEMENT

The load transfer of a rockbolt element is studied using 2D-DDA. The load transfer mechanism is represented by the bond behaviour of a rockbolt element under shearing in constant normal loading conditions. The bond stress versus slip displacement curves of different rockbolt elements are simulated and observed. The effects of the rib profile configurations and the confining pressure are presented.

3.1 Introduction

As discussed in Chapter 2, the load transfer concept is fundamental in understanding reinforcement mechanism of rockbolt. Many experimental works have been carried out to study the load transfer in the fully grouted rebars. However, few researches have discussed the progressively de-bonding and the relationship between the bond-slip model of the rockbolt element and its profile configuration.

A typical rib profile configuration of a rock element is shown in Figure 3-1. The profile can be defined by a section along rockbolt axis, i.e., rib height H, rib width w, rib face angle α and rib spacing s. Due to the variations of the configuration of lab tests, three potential failure modes in mortar have been detected, such as the parallel shear slip, the dilational slip, and the wedge slip as shown in Figure 3-1 (Hyett et al., 1992; Yeih et al., 1997; Ito et al., 2001; Cao et al., 2014).

Several analytical solutions have been presented to judge the different failure modes of the typical rockbolt profiles (Cao e al., 2014; Ghadimi et al., 2014). These failure modes are examined and further discussed by numerical analyses. The numerical

models can consider multiple parameters or/and avoid variability caused by sampling in physical tests.

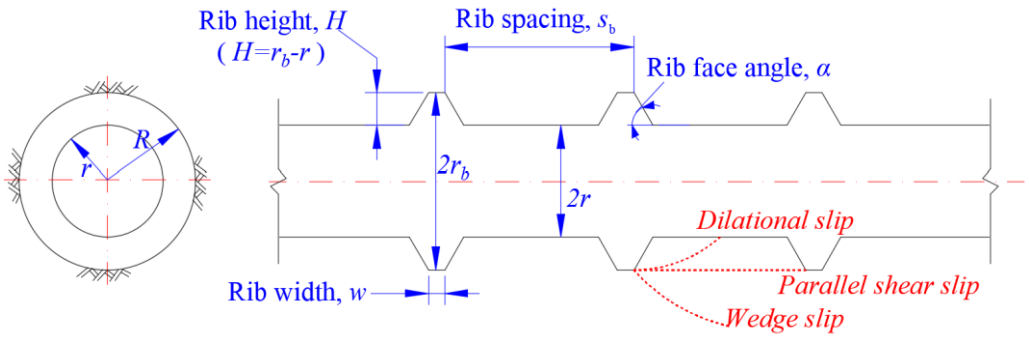

Figure 3-1 Sketch of the rib profile of a CMC rockbolt element

In this chapter, the two-dimensional Discontinuous Deformation Analysis (2D-DDA) method is used to investigate the pullout performance of the CMC rockbolt element. The CMC rockbolt element is modeled as three components, i.e. the rock, the rockbolt and the mortar. The crack propagations at the rockbolt elements with particular rib profile configurations are simulated using the sub-block approach (Lin et al., 1996; Jiao et al., 2012). The material properties of mortar blocks are calibrated against the experiment results presented by Yokota et al. (2018). Parameter studies are carried out to investigate the effects of the rib profile configurations and the confining pressures on the bond stress versus slip displacement curves.

3.2 Trilinear bond-slip model

The sketch of a section of the CMC rockbolt element with length of Δl is shown in Figure 3-2(a). The rockbolt has a diameter of D_b and a radius of r_b. The axisymmetric section can be simplified as shown in Figure 3-2(b). The slip displacement of the rockbolt element is denoted as $\Delta\delta$. The bond stress at the bolt-rock interface is written as τ. The unit shear force F_s with unit of force per meter acting on the bolt-rock interface for an element can be calculated as,

$$F_s = 2\pi r_b \tau \tag{3.1}$$

where: r_b is the radius of rockbolt;

τ is the bond stress at the bolt-rock interface.

The axial stress $\Delta\sigma_b$ on the cross-section of the rockbolt element is given as,

$$\Delta\sigma_b = \frac{F_s\left(\Delta l - \Delta\delta\right)}{A_b} \tag{3.2}$$

where: Δl is the length of rockbolt element section;

A_b is the cross-sectional area and $A_b=\pi r_b^2$.

Substituting Eq.(3.1) to (3.2) gives,

$$\Delta\sigma_b = \frac{2\tau\left(\Delta l - \Delta\delta\right)}{r_b} \tag{3.3}$$

If $\Delta\delta << \Delta l$, Eq.(3.3) could be simplified as,

$$\Delta\sigma_b = \frac{2\tau\Delta l}{r_b} \tag{3.4}$$

The bond stress versus slip displacement curve can be described using a trilinear bond-slip model proposed by Benmokrane et al. (1995). As shown in Figure 3-2(c), a trilinear bond-slip model consists of an ascending branch up to the peak stress at (τ_{max}, $\Delta\delta_1$), followed by a softening branch down to (τ_{res}, $\Delta\delta_2$), and a horizontal branch representing the non-zero residual frictional strength (τ_{res}) after complete debonding. The mathematical expression of the trilinear bond-slip model is expressed as,

$$\tau = k\Delta\delta + c_b \tag{3.5}$$

where: $\Delta\delta$ is the slip between the bolt and rock, k and c_b are constants which can be given as (Ma et al., 2016),

when $0 \le \Delta\delta < \Delta\delta_1$: $\quad k = k_1 = \dfrac{\tau_{\max}}{\Delta\delta_1},\ c_b = c_1 = 0,$ (3.5a)

when $\Delta\delta_1 \le \Delta\delta < \Delta\delta_2$: $\quad k = k_1 = \dfrac{\tau_{res} - \tau_{\max}}{\Delta\delta_2 - \Delta\delta_1},\ c_b = c_2 = \dfrac{\tau_{res}\Delta\delta_2 - \tau_{\max}\Delta\delta_1}{\Delta\delta_2 - \Delta\delta_1}$ (3.5b)

when $\Delta\delta \ge \Delta\delta_2$: $\quad k = k_3 = 0, c_b = c_3 = \tau_{res}$ (3.5c)

where, k_1, k_2 and k_3 are the bond stiffness at stage 1, stage 2 and stage 3 respectively; $\Delta\delta_1$ and $\Delta\delta_2$ are the slips corresponding to the maximum bond strength and the residual bond strength, respectively.

To ensure the uniformly distribution of the bond stress at the interface, the section length of rockbolt element Δl should be less than $8r_b$ (Blanco Martin et al., 2013). Using Eqs. (3.4) and (3.5), the relationship between the axial stress $\Delta\sigma_b$ and slip

displacement $\Delta\delta$ could be determined and can be further used to represent the bond-slip model of a rockbolt element.

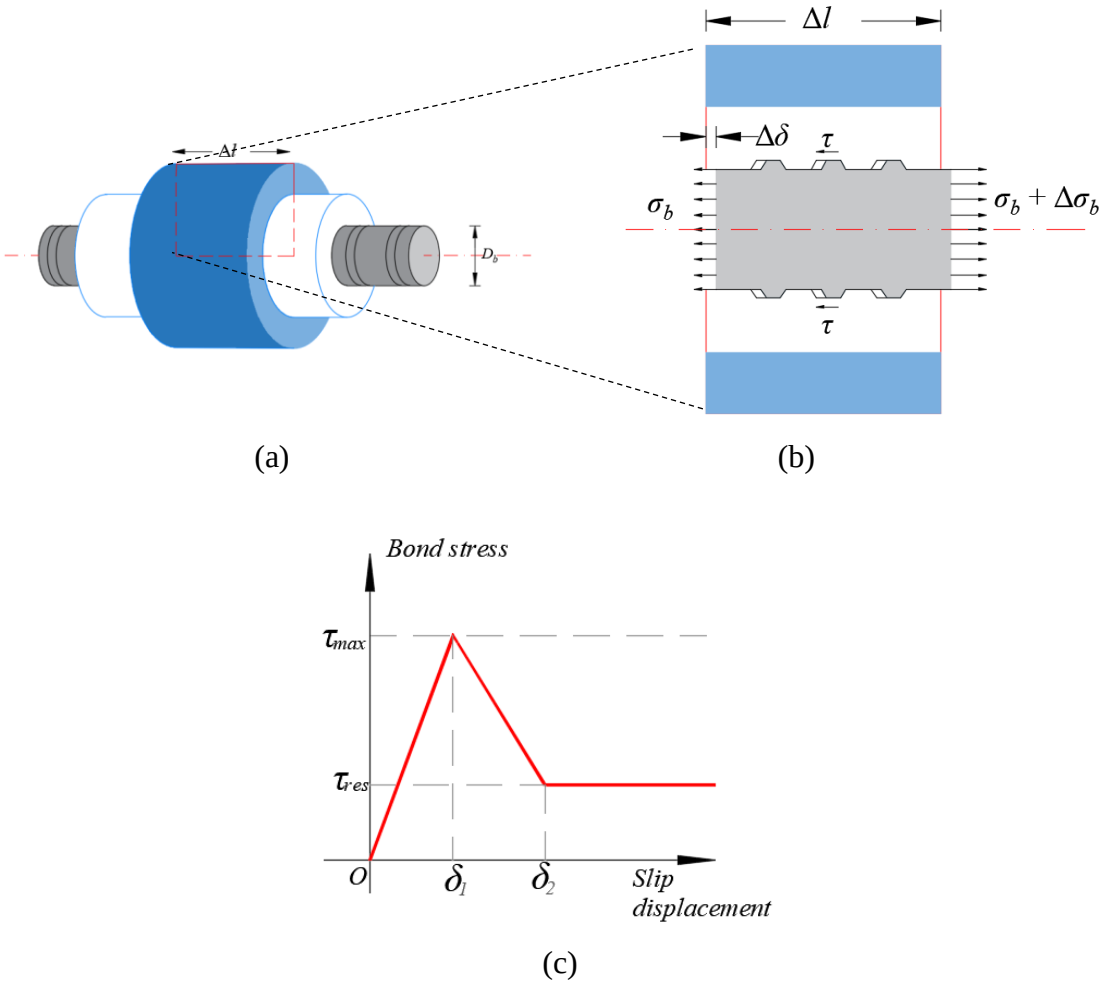

Figure 3-2 Sketch of a CMC element for (a) one element, (b) axisymmetric view, and (c) a trilinear bond-slip model to simulate the bond stress versus slip displacement curve

3.3 Crack propagation in 2D-DDA

To simulate the crack propagation in rock-like materials, artificial joints have been introduced to divide a continuous domain into small blocks in 2D-DDA (Lin et al. 1996; Ning et al., 2010; Jiao et al., 2012). In this study, the flat joint contact model (Potyondy and Cundall, 2004; Zhang and Wong, 2014; Zhang and Zhang, 2017) is introduced in the 2D-DDA code to present the force versus displacement behavior of an artificial joint. Blocks A and B as shown in Figure 3-3(a) are co-edged by an

artificial joint with a length of L. The joint aperture in the plane, w, is assumed to approach zero in the model, while the joint aperture in the out-of-plane direction is assumed as t = 1 unit. There are forces and moments arising at the co-edge once a relative deformation occurs between the two blocks. By using the normal spring and shear spring to represent the contacts as shown in Figure 3-3(b), the force and moment at the joint can be calculated as:

$$\Delta R_n = k_n \Delta d_n \tag{3.6}$$

$$\Delta R_s = -k_s \Delta d_s \tag{3.7}$$

$$\Delta M_s = -\frac{k_n L^2}{12} \Delta \theta_s \tag{3.8}$$

where ΔR_n and ΔR_s are increments of normal and shear forces at the artificial joint, respectively; k_n and k_s are normal and shear stiffness of the contact spring, respectively; Δd_n and Δd_s are increments of normal and shear displacements, respectively; $\Delta \theta_s$ is increment of shear rotation angle.

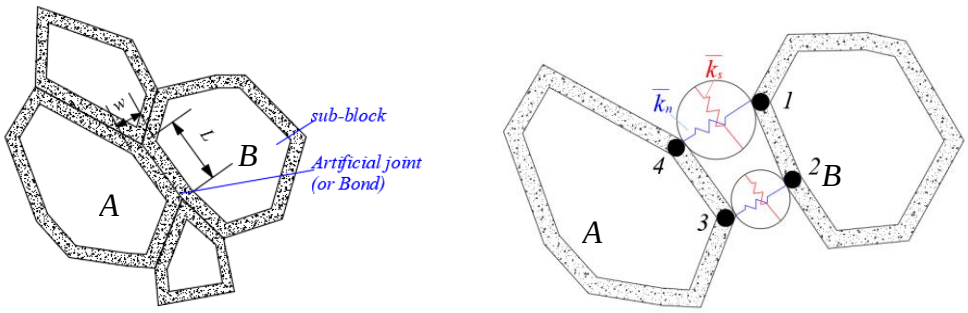

(a) Sub-blocks (b) Contacts

Figure 3-3 Contact at an artificial joint in a 2D-DDA model

The tensile stress σ_n and shear stress τ_s acting at an artificial joint can be calculated as:

$$\sigma_n = \left(-k_n d_n + k_n \theta_s \frac{L}{2} \right) \Big/ L \tag{3.9}$$

$$\tau_s = \left| k_s d_s \right| / L \tag{3.10}$$

The fracturing of an artificial joint is determined by Mohr-Coulomb failure criteria. The artificial joint opens to being a real one if $\sigma_n > \sigma_t$ or $\tau_s > \tau_{s,max}$ where σ_t is the tensile strength and $\tau_{s,max}$ is the shear strength and could be calculated as $\tau_{s,max} = \sigma_n \times \tan\varphi + c$. The properties of an artificial joint are assigned initially with the friction

angle φ, cohesion c and tensile strength σ_t. Once the artificial joint opens, its properties are resigned with the residual friction angle φ', residual cohesion c' and residual tensile strength σ_t', and usually $c' = 0$, $\sigma_t' = 0$.

3.4 Numerical Modelling

3.4.1. 2D-DDA models

The numerical analyses are carried out to simulate the bonding behavior of the rockbolt element using a direct shear model. As shown in Figure 3-4, the rock, mortar and bolt blocks with width of 80 mm are modeled from top to bottom with their heights of 4.0 mm, 12.0 mm and 12.0 mm, respectively. The left and right boundaries of the rock block are restrained by horizontal rollers. A normal stress p is applied on the top surface of the rock block. The mortar block is divided into many sub-blocks and connected using artificial joints. To simulate the geometry of the rib configuration of the CMC element, the rockbolt block is designed with the rib height h = 2.0 mm, rib face angle α = 30° and rib spacing s = 17.8 mm. The rockbolt is pulled horizontally at the right end of the rockbolt block with a constant speed v = 0.01 mm/s and restrained the vertical movement by a series of rollers. The horizontal movement of the bolt block at its right end is recorded as the slip displacement. As the force components along x-axis are in equilibrium, the bond stress could be calculated as:

$$\tau = \frac{r_b}{\Delta l}\sigma_{xx} \tag{3.11}$$

where r_b is the height of rockbolt block and Δl is the length of bond interface.

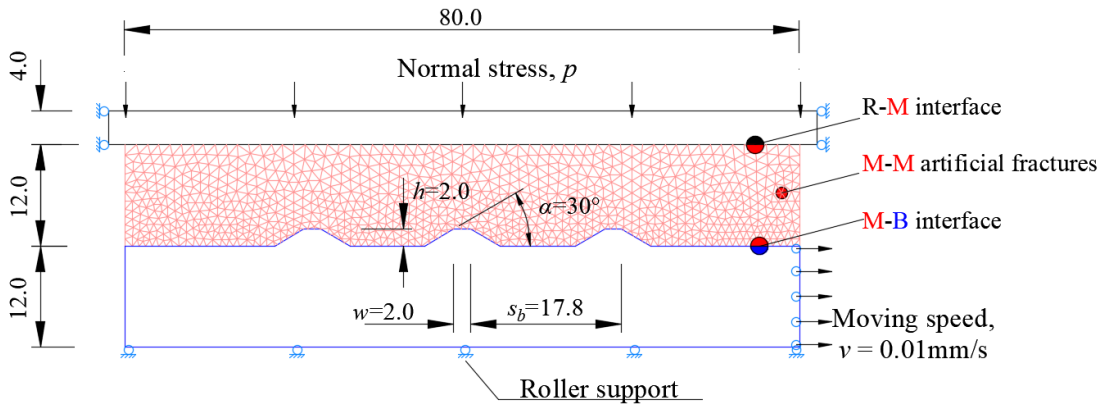

Figure 3-4 Numerical model of the CMC rockbolt element in 2D-DDA (unit: mm)

3.4.2. Determination of the properties of artificial joint in mortar

The crack propagations in the artificial joints are simulated using the flat joint contact model. The mortar properties in the DDA model are determined by comparing with the unconfined compression (UC) tests conducted by Yokota et al. (2018). In their study, the early curing staged mortar (right after 24 hr) has an average unconfined compression strength (UCS) of 10.1 MPa and an average Young's modulus of 3.4 GPa. The specimen failure involves slip and shear rupture.

The UC test of the above mortar sample is simulated using 2D-DDA with a blocky model composed by 1815 sub-blocks as shown in Figure 3-5(a). One rigid block on the top surface of the specimen is used to apply a constant downwards movement at a speed of 0.1 mm/s to simulate the loading in UC test. The right and left sides of the rigid block are restrained on the horizontal movement. Another block is attached at the bottom of the specimen to simulate the rigid base of the UC test. The vertical displacement of point *M1* at the top rigid plate is recorded as the displacement, while the vertical stress of point *M2* at the bottom plate is used to represent the stress. During the simulation, the Young's modulus, the uniaxial compression strength and the final shear rupture from the lab test were used to calibrate the mortar parameters. The final stress-strain curve obtained from the numerical analysis is shown in Figure 3-5(c), as well as the percentages of broken bonds during the test. It shows the crack is initiated at the vertical stress about 60% of UCS, followed by a sharply increases when the stress approach to UCS. As approximately 80% of the broken bonds are caused by shear failure, it shows the mortar sample has relatively low shear resistant (Shang et al., 2018). The stress contour of mortar specimen at failure is shown in Figure 3-5(b). The parameters used in DDA calculation are listed in Table 3-1. The determined properties of the mortar block are summarized in Table 3-2.

Table 3-1 Parameter setting of 2D-DDA calculation

Step time, g_2	0.0005
Max. disp. ratio, g_1	0.0002
Normal spring stiffness, k_n	5×10^8 N/m
Successive over-relaxation (SOR) factor	1.4

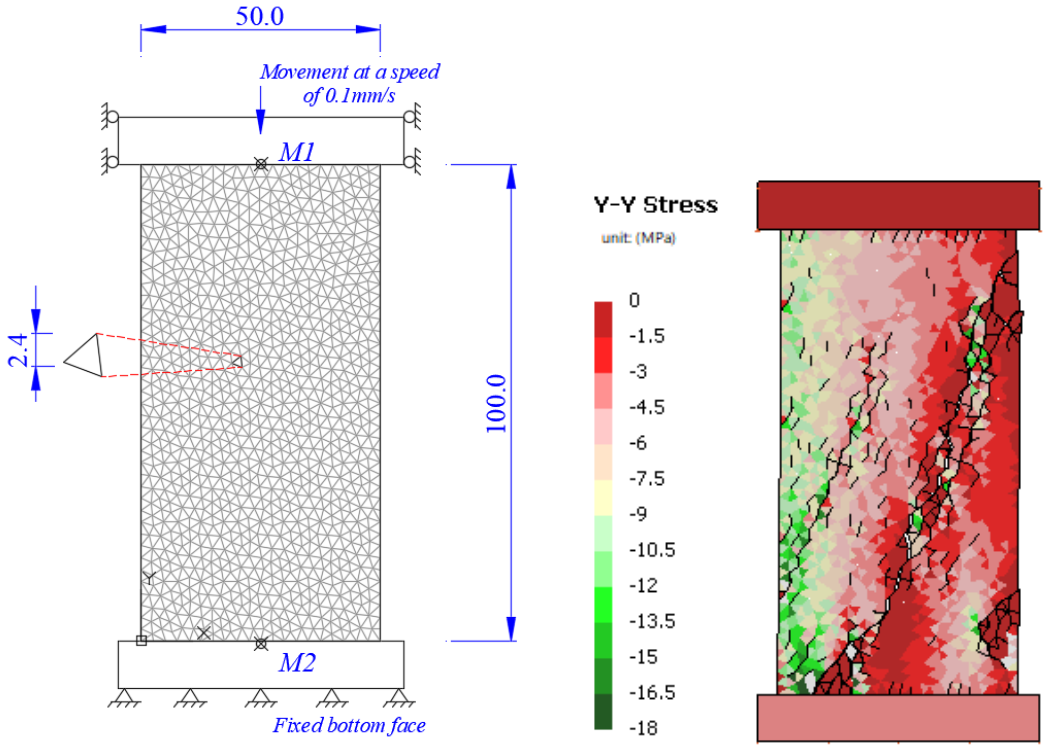

(a) (b)

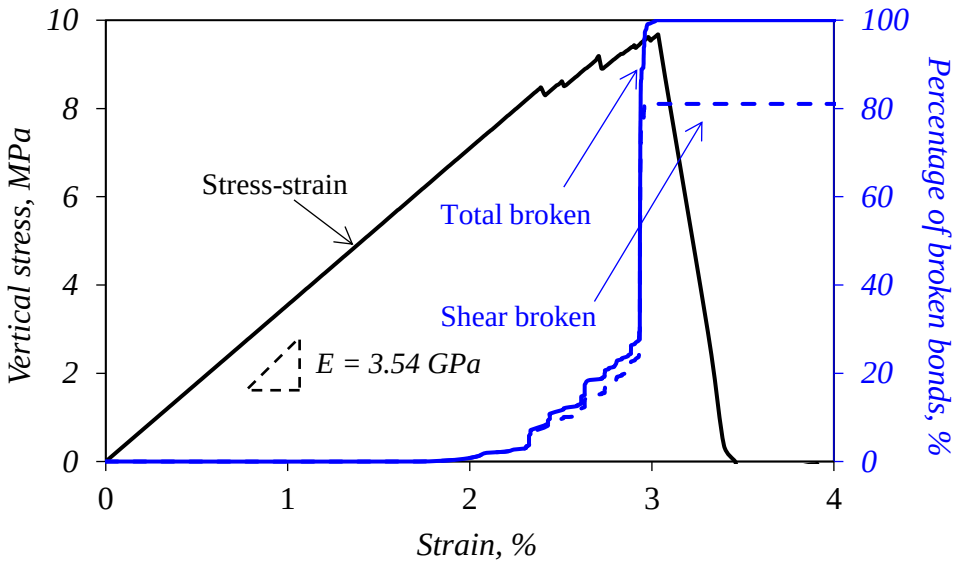

(c)

Figure 3-5 Simulation of the UC test of the motor specimen to determine the properties of motor (a) numerical model (unit: mm), (b) vertical stress contours of the specimen at failure, and (c) stress-strain curve and the relative percentage of broken bonds

3.4.3. Determination of the frictional properties at the M-B interface

A series of direct shear tests were carried out by Yokota et al. (2018) to determine the frictional properties at the M-B interface. The schematic diagram of the direct shear test is shown in Figure 3-6(a). The mortar and steel cube with dimensions of 80 × 80 × 12 mm^3 are placed in the upper and lower shear boxes, respectively. Both the contact surfaces of mortar and steel cube are flat. A normal stress p = 2.0 MPa is applied onto the upper loading plate. The shear box is pushed horizontally with a constant speed of 0.01 mm/s. The bond stress is calculated as the axial force F divided by the surface area of steel cube (80 × 80 mm). The horizontal movement of the shear box is recorded to represent the slip displacement at the interface and to determine the bond stress-slip displacement curve.

The direct shear test is simulated using 2D-DDA to obtain the joint parameters at the M-B interface as shown in Figure 3-6(b). The mortar is divided into sub-blocks assigned with the material parameters determined in Section 3.4.2 as shown in Table 3-2. A rigid plate is placed next to the mortar block to restrain its horizontal movement. One more horizontally fixed rigid plate is placed on the surface of mortar block to apply the normal stress p = 2.0 MPa. The bottom steel plate is pushed with a constant speed of 0.01 mm/s to simulate the direct shear test procedure. The properties of the friction parameters at the M-B interface are determined using trial-and-error method by comparing the calculated bond stress versus slip displacement curve and that from direct shear test. The final stress-strain curve obtained from the numerical analysis and that from the direct shear test are shown in Figure 3-6(c). It shows a reasonable agreement between the two results. The determined the friction parameters along the M-B interface are listed in Table 3-2.

Table 3-2 Physical parameter setting of the rockbolt element model

Blocks	E (GPa)		Density ($\times 10^3$ kg/m^3)		Poisson ratio	
Rock (R)	25.6		2.13		0.26	
Mortar (M)	5.0		1.96		0.27	
Rockbolt (B)	200.0		7.80		0.30	
Joints	Friction angle (°)		Cohesion (MPa)		Tensile strength (MPa)	
	Initial	After fracturing	Initial	After fracturing	Initial	After fracturing
M-B	30	20.0	3.0	0	1.0	0
M-M	40	21.5	6.0	0	4.0	0

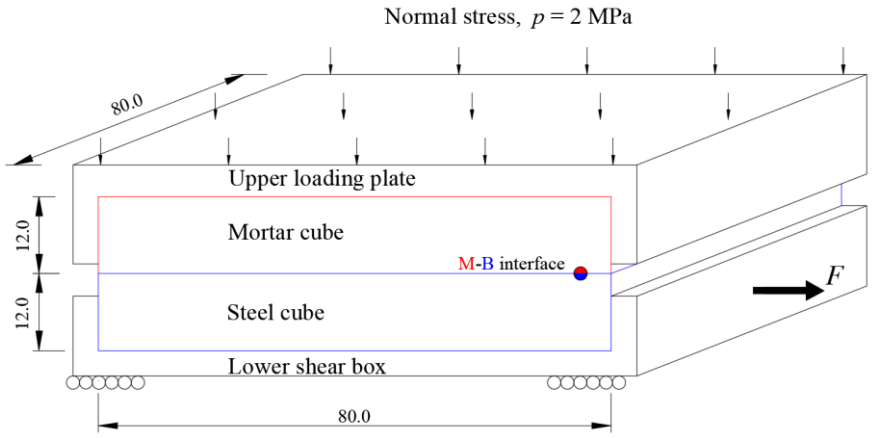

(a)

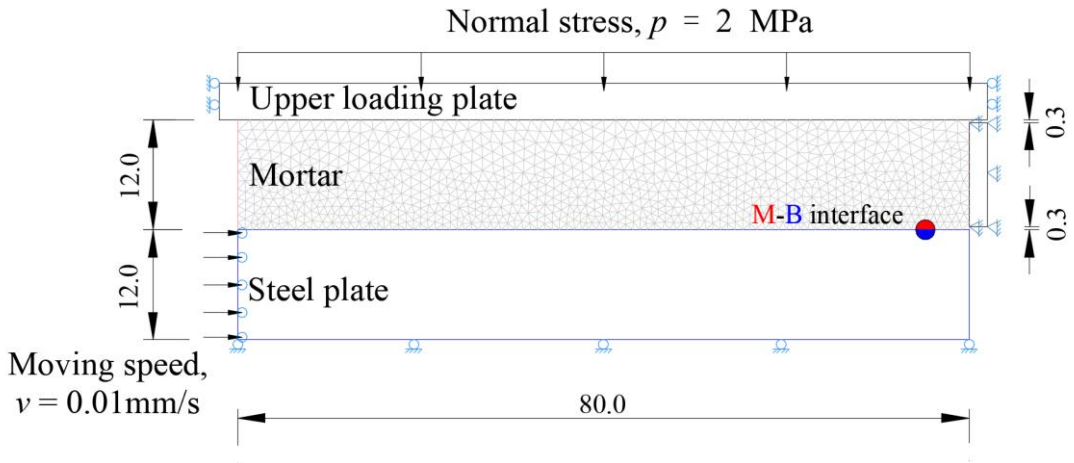

(b)

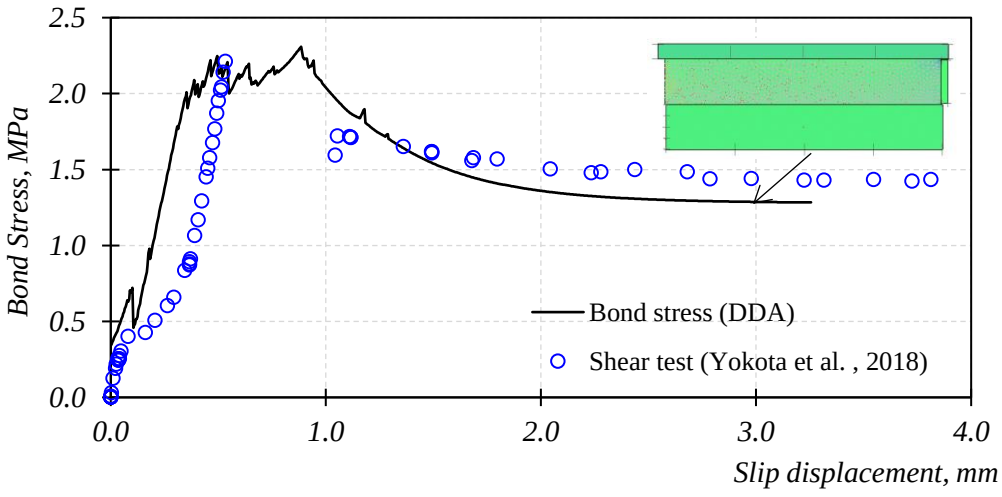

(c)

Figure 3-6 Simulation of the direct shear test using 2D-DDA (a) schematic diagram of the lab test (unit in: mm), (b) numerical model (unit in: mm) and (c) comparisons of the bond stress versus slip displacement curves

3.5 Numerical Results

The bond stress versus slip displacement curve of the CMC rockbolt element with rib face angle α = 45° and rib spacing s = 17.8 mm under a normal stress p = 2 MPa is plotted in Figure 3-7. Based on the progressive fracture development and the displacement accumulation, the curve can be classified into three stages. Stage 1 starts from the initial loading to the time when the bond stress is less than the maximum bond stress τ_{max} which can be further classified into the initial elastic stage (stage 1-1) and the crack initiation stage (stage 1-2). In the initial elastic stage, there are no broken bonds observed. Once there are broken bonds, stage 1-2 starts. The broken bonds are firstly observed at the rib surface, such as the fracture developed at the point *A* ($\Delta\delta$ = 0.06 mm) in the bond stress versus slip displacement curve as shown in Figure 3-8(a). The bond stress continues increasing with the accumulated slip displacement. Near the end of stage 1, the cracks have grown from the rib tips at an average angle of 60° with respect to the moving direction, such as fracture developed at the point *B* ($\Delta\delta$ = 0.3 mm) in the bond stress versus slip displacement curve as shown in Figure 3-8(b). Three local fractures generate from three rib tips towards the R-M surface, dividing the mortar area into four parts. There is approximately 60% of the total cracks occurring during stage 1. After the maximum bond stress τ_{max}, the bond stress decreases with the accumulated slip which is denoted as stage 2 in the bond stress versus slip displacement curve as shown in Figure 3-7. More cracks generate and connect among the three local fractures, further dividing the mortar into smaller parts (see Figure 3-8(c)). The new generated rupture surface in mortar block is at an average angle of 34° with respect to the moving direction of the bolt block. The number of new cracks in this stage accounts for about 25% of the total cracks.

The bond stress becomes stable with the residual bond strength τ_{res}, and the following stage is defined as stage 3 where very few new cracks are generated. The model fails in wedge failure mode (see Figure 3-8). The bond stress versus slip displacement curve could be fitted using the trilinear bond-slip model. As shown in Figure 3-7, the obtained parameters are k_1 = 9.0 MPa/mm, k_2 = -2.5 MPa/mm, k_3 = -0.2 MPa/mm, τ_{max} = 3.4 MPa and τ_{res} = 2.4 MPa.

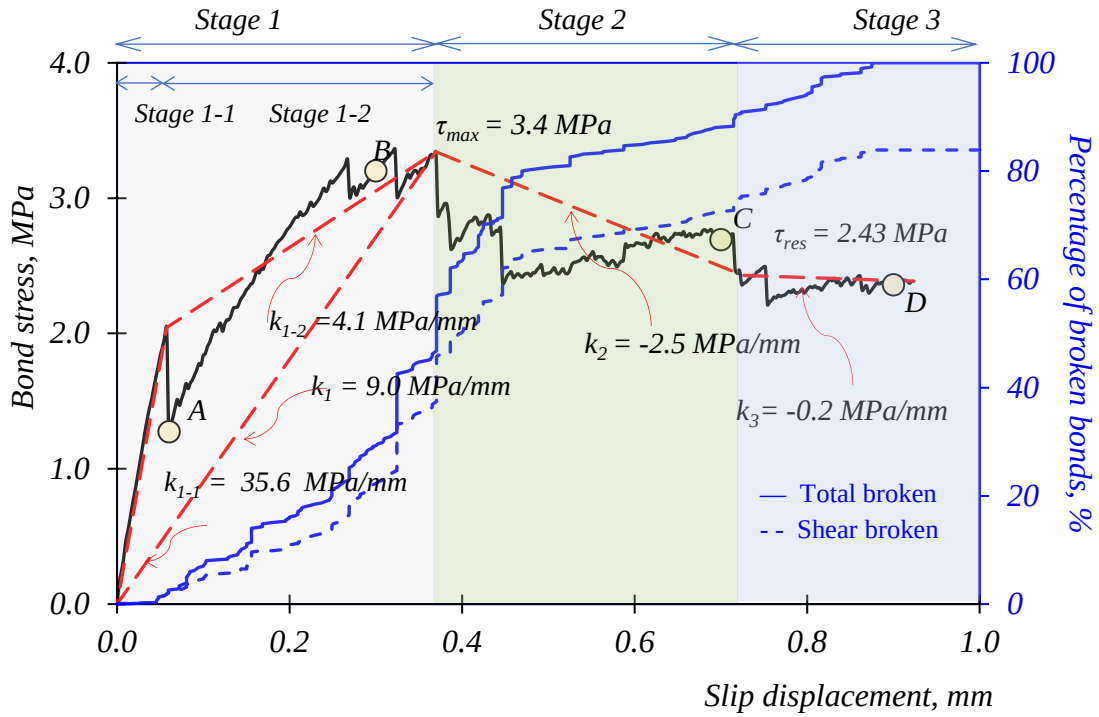

Figure 3-7 Simulated bond stress-slip displacement curve of the CMC element with rib face angle α = 45° and rib spacing s = 17.8 mm under p = 2 MPa

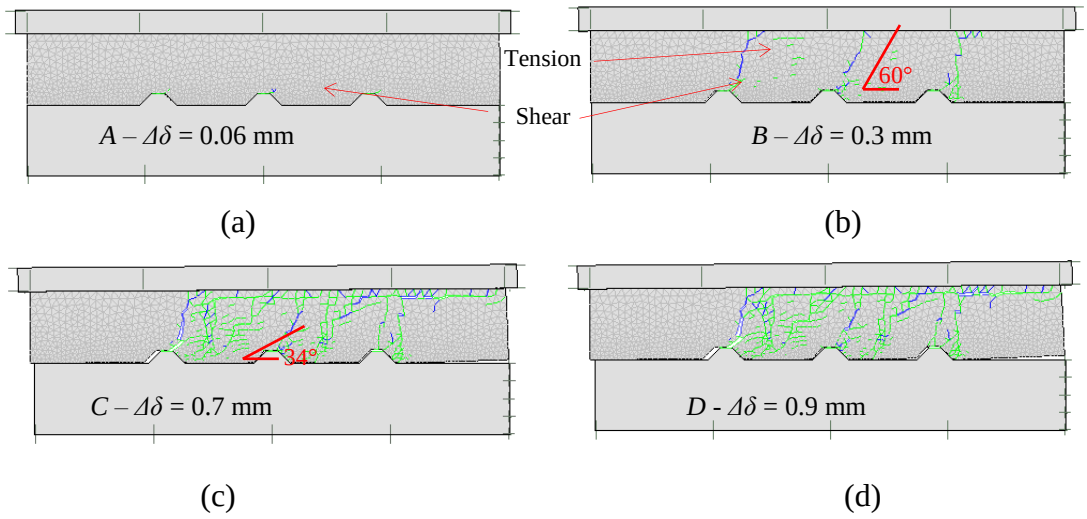

Figure 3-8 Crack propagations in mortar of the CMC rockbolt element with rib face angle α = 45° and rib spacing s = 17.8 mm under p = 2 MPa at the slip displacements of (a) $\Delta\delta$ = 0.06 mm, (b) $\Delta\delta$ = 0.3 mm, (c) $\Delta\delta$ = 0.7 mm and (d) $\Delta\delta$ = 0.9 mm

3.6 Parametric studies

To identify the major factors that affect the bond strengths of the CMC element, parametric studies are carried out. The height and width of the rock, mortar and bolt blocks are fixed as shown in Figure 3-4. The studied variables are the rib face angles α, the rib spacing s, and the normal stress p.

3.6.1. Effects of the rib face angle

The rockbolt blocks with rib spacing s = 17.8 mm and rib face angles α = 30°, 60° and 90° are analysed to investigate the effect of the rib face angle on the bond-slip models under the normal stress p = 2 MPa. The bond stress versus slip displacement curves for the CMC rockbolt elements with different rib face angles are plotted in Figure 3-9. The accumulated percentages of the broken bonds during the slip progress are also included. In the case of α = 30°, the bond stress versus slip displacement curve (see Figure 3-9(a)) shows the bond stress increases linearly with respect to the slip displacement at beginning. In addition, the curve has no softening branch. One possible reason is that the moving of the rockbolt element is sliding along the M-B interface. This can be verified using the crack propagation contours as shown in Figure 3-10(a) and (b). It shows the dilation happens along the M-B interface and very few cracks generated in the mortar block. Thus, the bonding effects of the CMC element with rib face angles of less than 30° are not effective under the normal stress of 2 MPa.

The bond stress versus slip displacement curves of the CMC element with rib face angles of 60° and 90° are shown in Figure 3-9(b) and (c), respectively. The obtained curves are similar to that of the rib face angles α = 45° (see Figure 3-7). The inclination angles of the initial cracking in the mortar from rib surface of the CMC elements with rib face angles α of 60° and 90° are slightly increased (see Figure 3-10(c) and Figure 3-10(e)), but those generating in stages 2 are not much different (see Figure 3-10(d) and Figure 3-10(f)). The bond stress versus slip displacement curve could be fitted using the trilinear bond-slip model. The obtained parameters are summarized in Table 3-3. It can be seen that the CMC element with rib face angles α of 90° has a slightly higher maximum bond stress. However, the other parameters are similar. Thus, if change the rib face angle of a CMC element from 45° to 90° under normal stress p = 2 MPa, the changes of the parameters of the bond-slip models are limited.

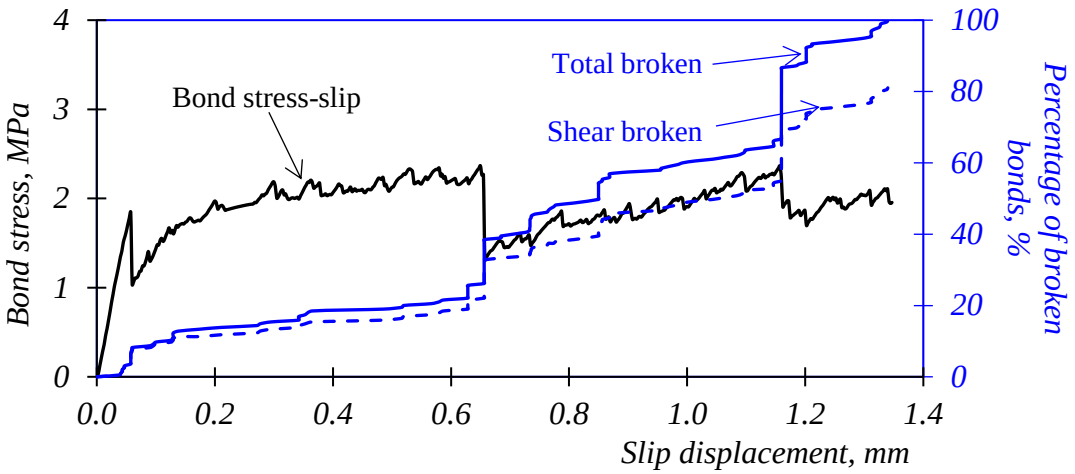

(a)

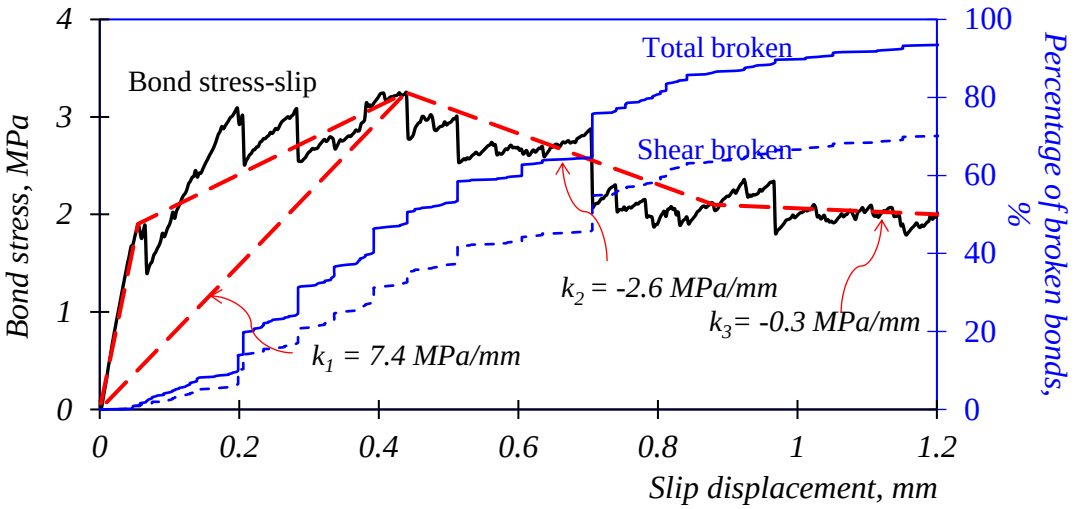

(b)

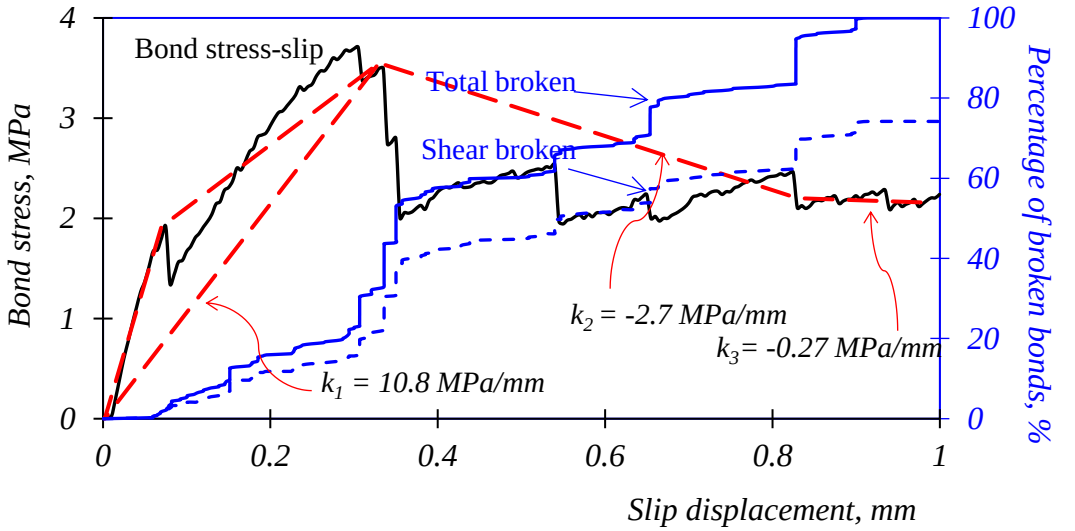

(c)

Figure 3-9 Effects of the rib face angles on the bond stress-slip displacement curves when (a) α = 30°, (b) α = 60° and (c) α = 90°

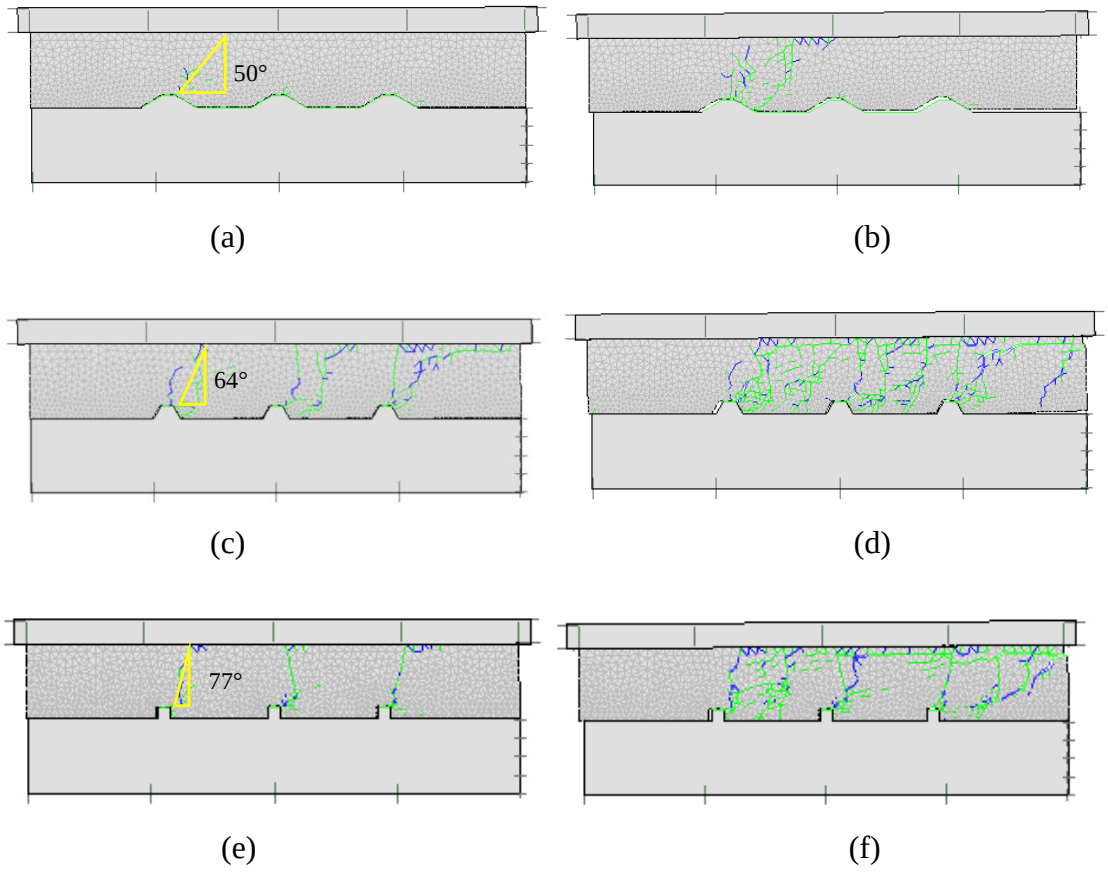

Figure 3-10 Effects of the rib face angles on the crack propagations when (a) α = 30°, $\Delta\delta$ = 0.3 mm, (b) α = 30°, $\Delta\delta$ = 0.8 mm, (c) α = 60°, $\Delta\delta$ = 0.3 mm, (d) α = 60°, $\Delta\delta$ = 0.8 mm, (e) α = 90°, $\Delta\delta$ = 0.3 mm and (f) α = 90°, $\Delta\delta$ = 0.8 mm

Table 3-3 Parameters defining the trilinear bond-slip models under p = 2 MPa

Rib spacing, s	Rib face angle, α	$k_{1\text{-}1}$, MPa/mm	$k_{1\text{-}2}$, MPa/mm	*Average* k_1, MPa/mm	k_2, MPa/mm	k_3, MPa/mm	τ_{max}, MPa	τ_{res}, MPa
17.8mm	30°	32.1	-	-	-	-	2.36	1.81
	45°	35.5	4.2	9	-2.6	-0.2	3.34	2.23
	60°	34.6	3.5	7.4	-2.6	-0.3	3.25	2.10
	90°	30.0	6.2	10.8	-2.7	-0.27	3.55	2.16
35.6mm	30°	32.1	-	-	-	-	1.84	1.81
	45°	32.0	2.80	5.4	-2.2	-0.27	3.34	2.28
	60°	34.7	2.01	5.0	-1.9	-0.2	3.20	2.00
	90°	29.0	2.75	5.3	-2.1	-0.3	3.60	2.26

3.6.2. Effects of the rib spacing

The rockbolt blocks with rib spacing s = 35.6 mm and rib face angles α = 30°, 60°, and 90° are analysed to investigate the effect of the rib spacing. The normal stress p is 2 MPa. The bond stress versus slip displacement curves of the CMC rockbolt element with rib face angles α = 30° and rib spacings s = 17.8 and s =35.6 mm are plotted in Figure 3-11(a). It can be seen that the rib spacing has no much influences on the bond stress versus slip displacement curves at the initial elastic stage (stage 1-1 as defined in Figure 3-7). With the accumulated slip displacement, the bond stress versus slip displacement curves show their differences. The larger the rib spacing of a rockbolt element, the lower the bond stress the element could sustain at the same slip displacement. As shown in Figure 3-12(a), the crack propagations and the stress contours at the slip displacements $\Delta\delta \approx$ 1.0 mm show that the failure mode of the element is the sliding along M-B interface and the cracks are only occurring near the end rib. The bond stress versus slip displacement curves of the CMC rockbolt elements with rib spacing s = 17.8 and 35.6 mm, and rib face angles α = 45°, 60° and 90°, are plotted in Figure 3-11(b) - (d), respectively. It can be seen that the simulated bond stress-slip displacement curves of the rockbolt element are similar as that of the CMC element with rib spacing s = 17.8 mm and rib face angle α = 45° as shown in Figure 3-7. The rib spacing has less influence on the bond stress versus slip displacement curves at the initial elastic stage. Compared with the bond stress versus slip displacement curves of rockbolt elements with rib spacing s = 17.8 mm, the curves of rockbolt element with rib spacing s = 35.6 mm delay the crack development. The bond stress versus slip displacement curves could be fitted using the trilinear bond-slip models (see Table 3-3). The bond stiffness at stage 1-2 for the rockbolt element with rib spacing s = 35.8 mm are approximately 57% lower than that of rockbolt element with rib spacing s = 17.6 mm which results in the average bond stiffness at stage 1 are approximately 67% of the latter one. The bond stiffness at stage 2 for the rockbolt element with rib spacing s = 35.8 mm is also lower than that of rockbolt element with rib spacing s = 17.6 mm, while the maximum and the residential shear strengths are almost the same.

The crack propagations and stress contours of rockbolt elements with rib spacing s = 35.6 mm pulled at $\Delta\delta \approx$ 1.0 mm are shown in Figure 3-12. For the case of rib face

angles α = 45° as shown in Figure 3-12(b), the crack grows from the two rib tips towards the R-M interface with an inclination about 40°, dividing the mortar into 3 parts. More cracks are generated in mortar near the M-B interface resulted in wedge failure mode. The crack propagations at failure in the mortar block are similar for the rockbolt element with varied rib face angles α = 60° and 90° as shown in Figure 3-12(c) and Figure 3-12(d), respectively.

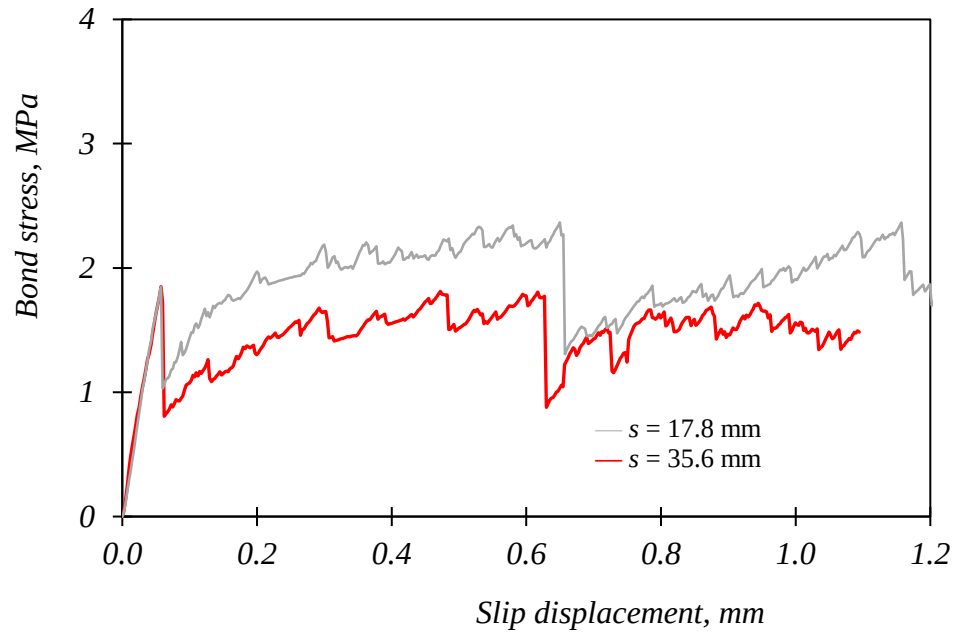

(a)

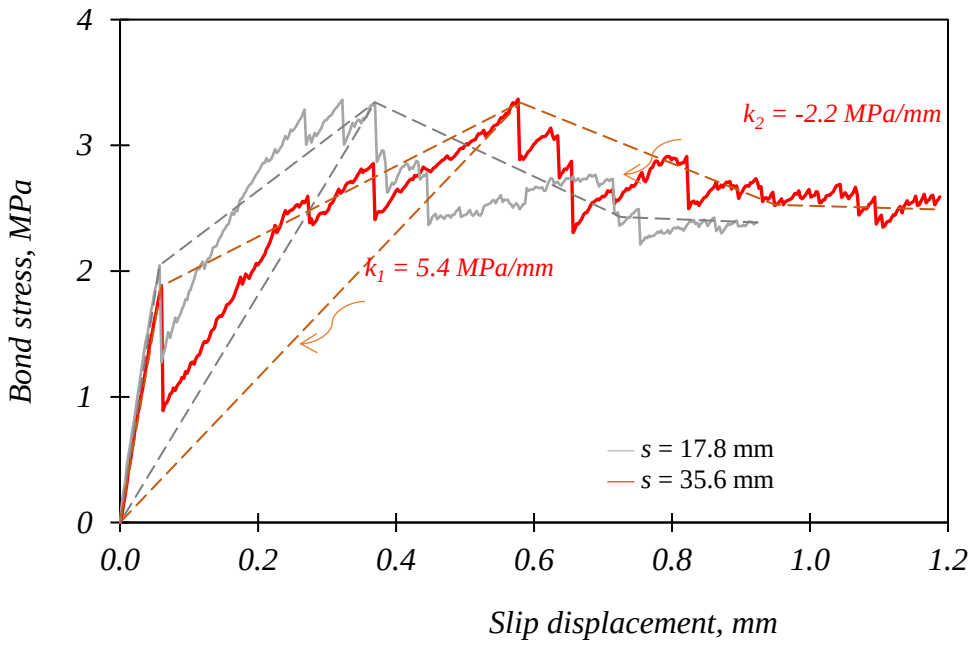

(b)

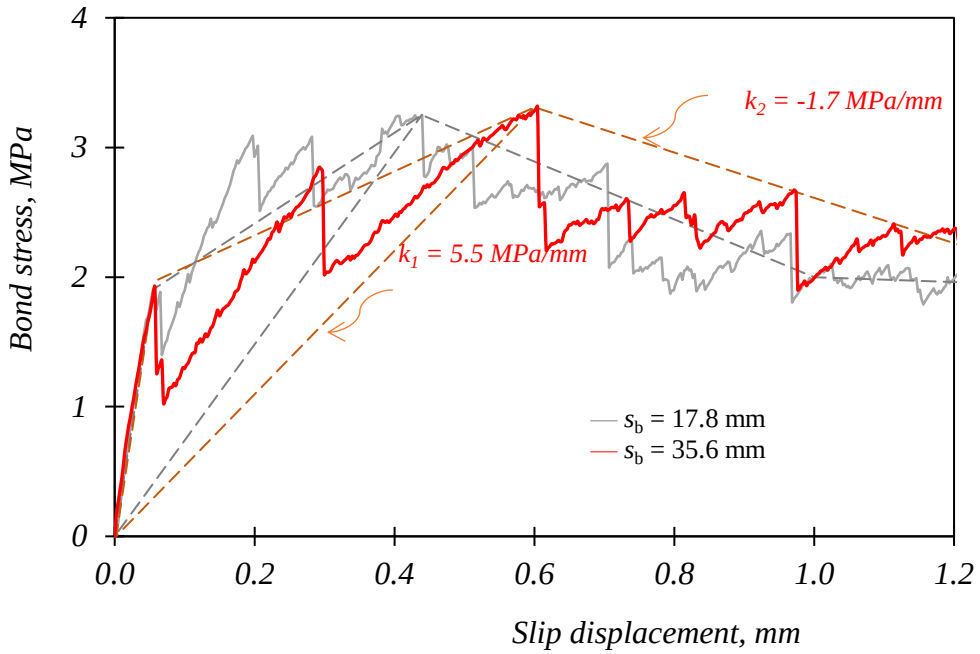

(c)

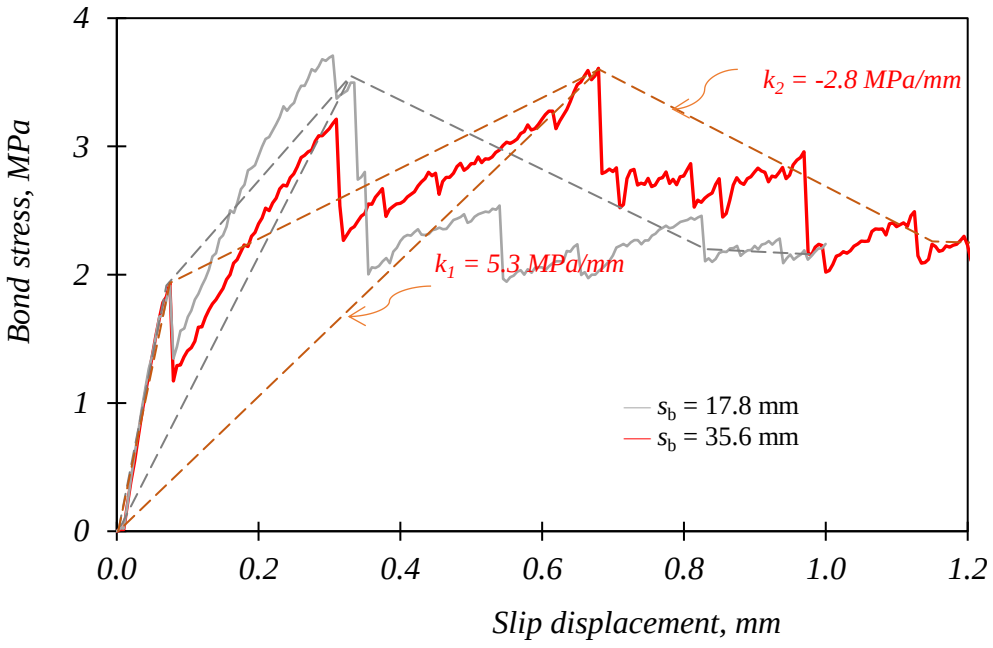

(d)

Figure 3-11 Effects of the rib spacings on the bond stress versus slip displacement curves when (a) $\alpha = 30°$, (b) $\alpha = 45°$, (c) $\alpha = 60°$ and (d) $\alpha = 90°$

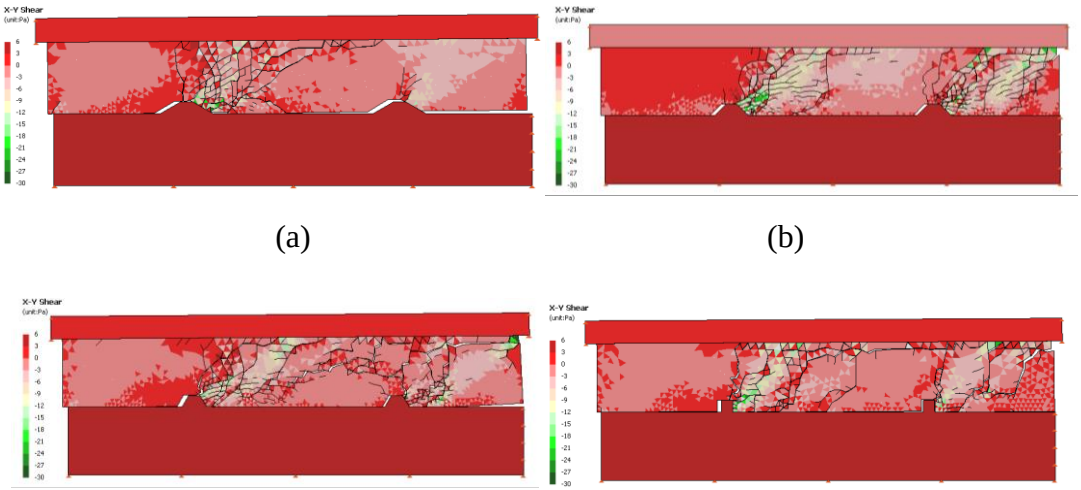

(a) (b)

(c) (d)

Figure 3-12 Effects of the rib spacing s on the fracturing in mortar block at slip displacement $\Delta\delta \approx 1.0$ mm when (a) α = 30°, (b) α = 45°, (c) α = 60° and (d) α = 90°

3.6.3. Effects of the normal stress

The rockbolt element with rib spacing s = 17.8 mm and rib face angles α = 30°, 45°, 60° and 90° under different normal stress p = 1 MPa, 2 MPa and 4 MPa are simulated to investigate the effects of the normal stress. The simulated bond stress versus slip displacement curves are shown in Figure 3-13. As expected, both the bond stiffness and the bond strength are increasing with the increase of normal stress. For the case of rockbolt blocks with rib spacing s = 17.8 mm and rib face angles α = 30° under normal stress p = 4 MPa as shown in Figure 3-13 (a), the element could be restrained, but the differences between the maximum bond strength and residual bond strength are little. The bond stresses versus slip curves of the rockbolt element with rib face angle α = 45°, 60° and 90° are shown in Figure 3-13(b), (c) and (d), respectively, the maximum bond strengths are still much higher than their residential bond stresses.

The crack propagation contours of rockbolt element with rib spacing s = 17.8 mm pullout at $\Delta\delta \approx 1.0$ mm are shown in Table 3-4. It can be seen that the higher the normal stress, the more cracks are propagated in the mortar. This explains why both the bond stiffness and the bond strength are increasing with the increase of normal stress. It also shows that the inclination of the macro-fracture from the rib tips is

increasing with the increase of normal stress. The cracks at failure propagated in the mortar block of rockbolt element with rib face angle of α = 60° and 90° are evenlt parallel to the M-B interface when the normal stress is high (i.e., p = 2 and 4 MPa).

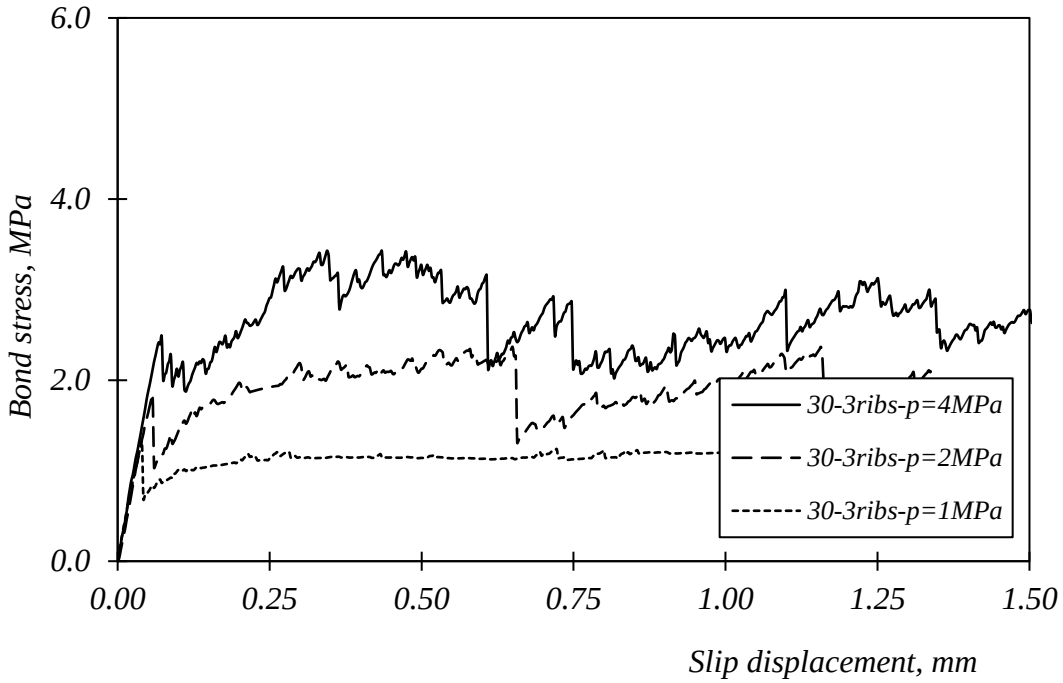

(a)

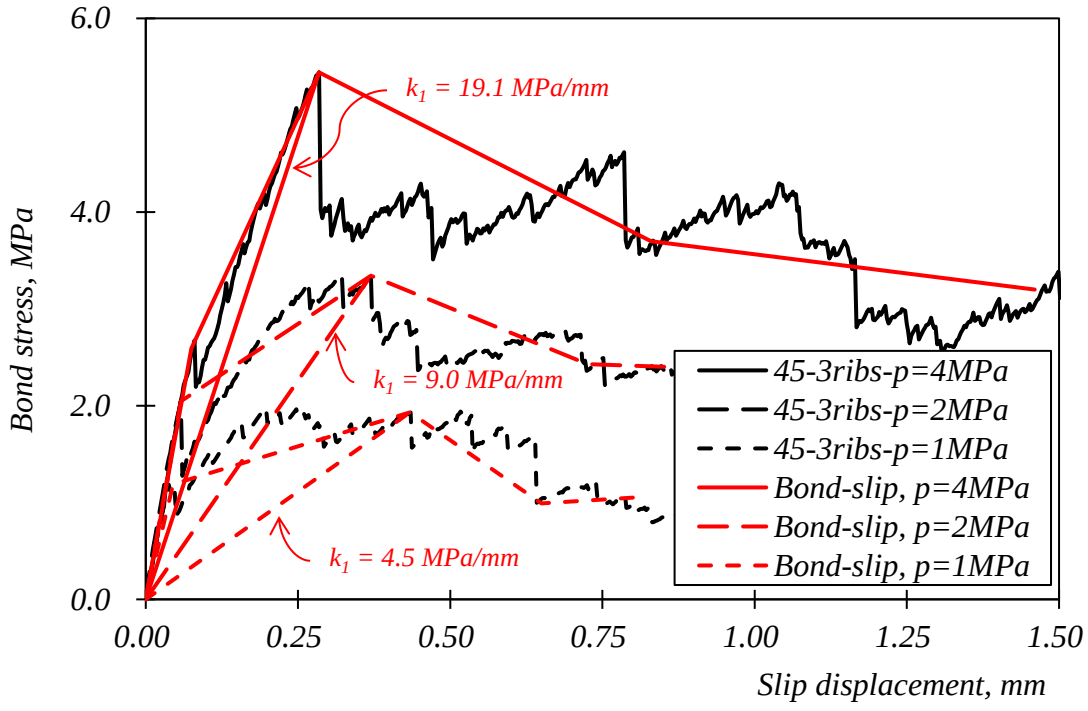

(b)

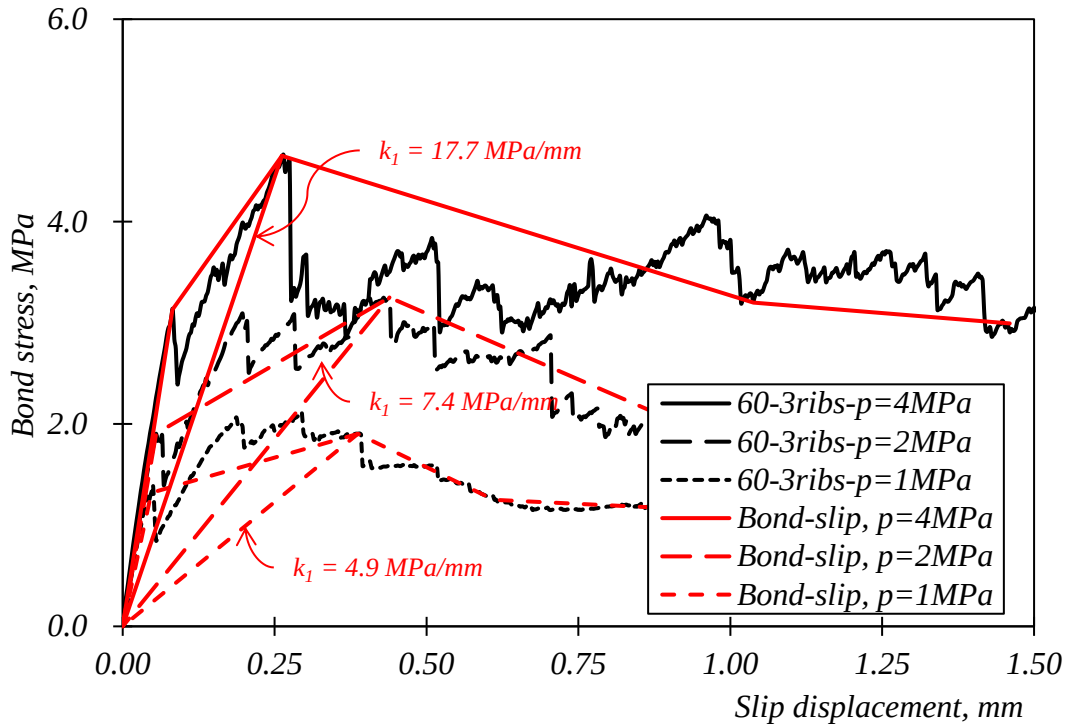

(c)

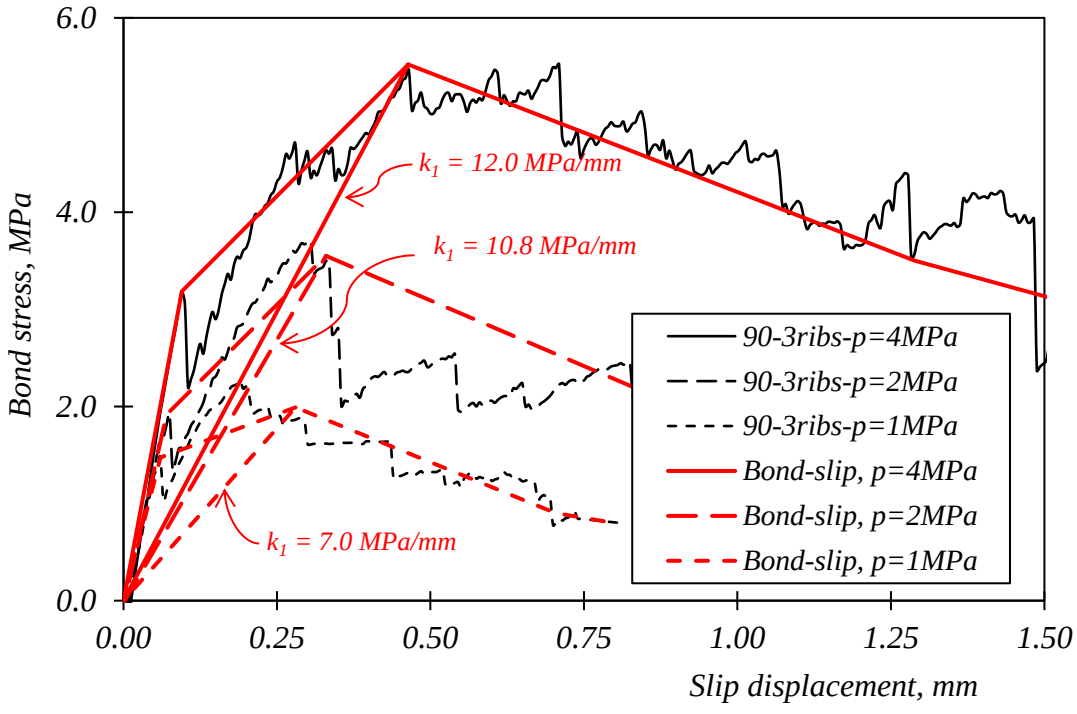

(d)

Figure 3-13 Effects of the normal stress p in different rib faces angles (a) α = 30°, (b) α = 45°, (c) α = 60° and (d) α = 90°

Table 3-4 Effects of the normal stress on crack propagations in the mortar of CMC rockbolt element with rib spacing s = 17.8 mm and different rib face angles at the slip distances $\Delta\delta$ = 1.0 mm

α	p = 1 MPa	p = 2 MPa	p = 4 MPa
30°		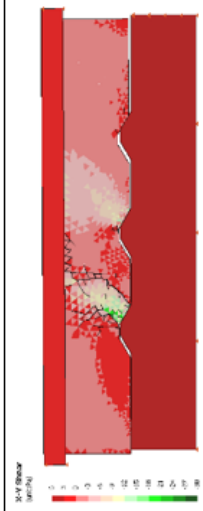	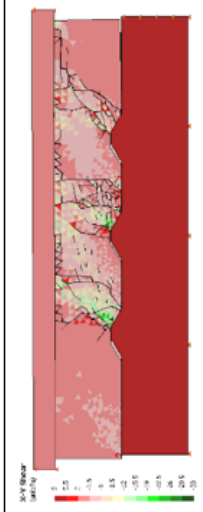
45°	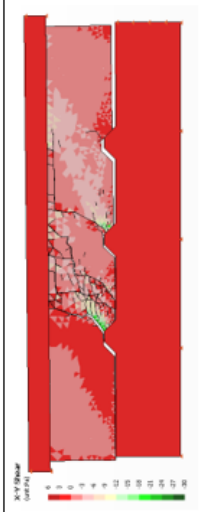	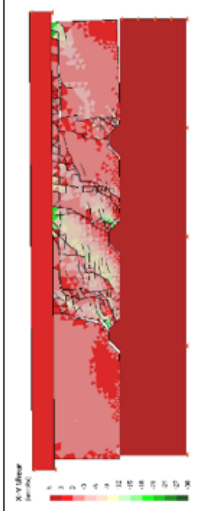	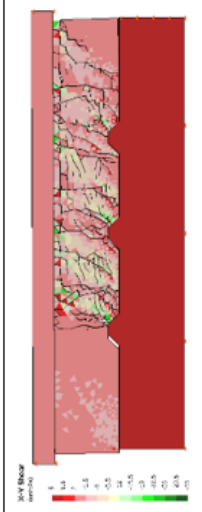
60°	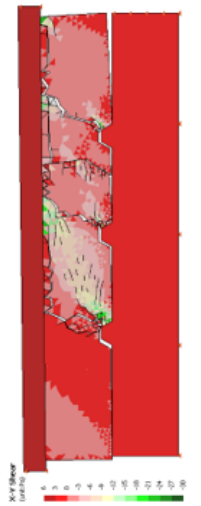	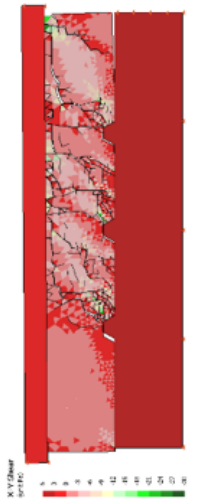	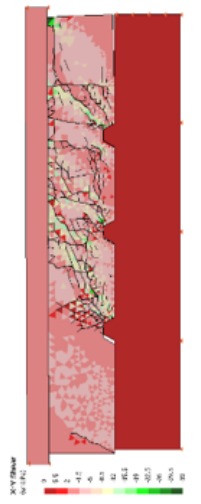
90°	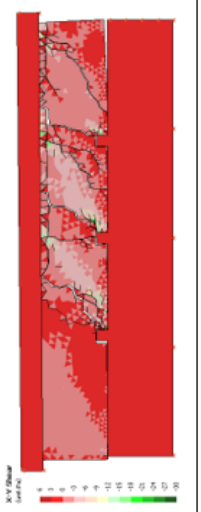	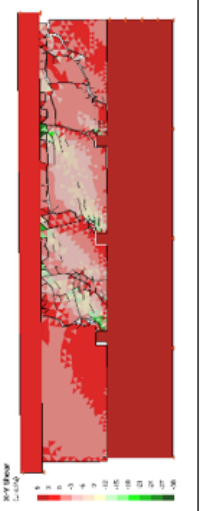	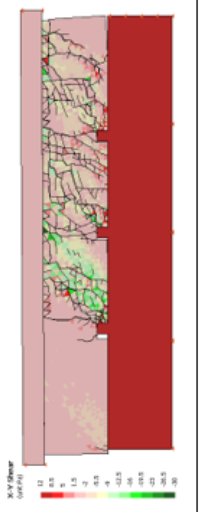

The effects of the rib face angle and the rib spacing of the rockbolt profile configuration on the pullout performance of the rockbolt are summarized in Table 3-5. Under the lower normal stress, the effect of the CMC rockbolt element with rib face angles of less than 30° is not effective. If the normal stress is high, the rib face angle doesn't have much influences on the pullout performance of the rockbolt. The rib spacing is one of the key parameters controlling the bond stiffness. The confining conditions are the most important parameters affecting the bond-slip behaviour of a rockbolt element. The higher the normal stress, the higher the bond stiffness and the bond strength of the rockbolt and more cracks are propagated in the mortar block.

Table 3-5 Results of case studies

Bolt profile Configuration / Load transfer capacity parameters		Rib face angle from 30° to 90°	Rib spacing, from 17.8 to 35.6 mm	Normal stress increase
Bond stiffness before cracking, $k_{1\text{-}1}$		No much effects		Increase
Average bond stiffness in stage 1, $k_{1,ave}$		Slightly increase	Decrease	Increase
Max. bond strength, τ_{max}		No much effects	No much effects	Increase
Bond stiffness in stage 2, k_2		No much effects	Slightly decrease	Decrease
Res. bond strength, τ_{res}		Slightly increase	No much effects	Increase
Crack propagation in mortar	Inclination of the crack growing from rib tips	Slightly increase	Decrease	Increase
	Inclination of the rupture surface	No much effects	Decrease	Decrease
	Main failure modes	Wedge failure, but tend to parallel shear slip if the normal stress increases	Wedge failure and dilational slip	Parallel shear slip
Note: The effects of the rib face angle will influenced by the normal stress scales.				

The fully grouted rebar could be considered as combinations of CMC rockbolt elements. Once the bond-slip model of the rockbolt element is obtained, the performance of rockbolt could be simulated by discrete rockbolt element. An application example is shown in Section 4.4.2. It should be noted that the above bond-slip models are drawn by assuming the rockbolt and mortar were well bonded, thus, no crack propagations are observed at the rockbolt and mortar interface in the above simulations. The bond-slip models should also be adopted for the rockbolt element under similar conditions.

3.7 Conclusions

In this chapter, 2D-DDA is used to investigate the pullout performance of the CMC rockbolt element. The CMC element is modeled as three components, i.e. the rock, the rockbolt and the mortar. The material properties of mortar blocks are adopted from the experimental results proposed by Yokota et al. (2018), and the frictional properties along rockbolt – mortar interface are calibrated with their experimental results. The flat joint contact model is introduced into the 2D-DDA code to simulate the force versus displacement behaviour of an artificial joint. The results show that a bond stress versus slip displacement curve of the CMC element is generally exhibiting three stages which are distinguished by five key parameters, i.e., the bond stiffness in three stages (k_1, k_2, and k_3), the maximum bond strength τ_{max}, and the residual bond strength τ_{res}.

Parametric studies have been carried out to investigate the effects of the normal stress and the rib profiles on the bond stress versus slip displacement curves and the fracturing modes in mortar. It is found that the normal stress plays an important role in the bond-slip modeling. The bond stiffness k_1, the maximum bond strength τ_{max} and the residual bond strength τ_{res} are increasing with the increase of normal stress. A larger rib spacing will result in a lower bond stiffness when other parameters are kept the same. Under a lower normal stress, the interlock of the CMC rockbolt element with rib face angles of less than 30° is not effective because the rockbolt elements are pulled out at the rib faces and less cracks are generated in the mortar blocks.

CHAPTER 4. DEVELOPMENT OF A ROCKBOLT MODEL IN 2D-DDA AND ITS VERIFICATIONS

Based on the load transfer theory, a rockbolt model is developed in 2D-DDA. The rockbolt model is characterized by a relatively large displacement at rock joints. Generally, the rockbolt is represented by several rockbolt elements. For each element, the axial behaviour, bond behaviour and shear behaviour are introduced. Based on the load transfer at the bond of a rockbolt element, the reinforcement of rockbolts could be simulated.

4.1 Introduction

As reviewed in Chapter 2, a reinforcement system can be considered as the combination of four components in a conceptual view (see Figure 4-1): rock, internal fitting (or bond), rockbolt and external fitting. If tension occurs in the rockbolt rod, it will be transferred to the rock by bond. The bond is referring to the bond resistance along contact surface defined by two springs. In this chapter, a new developed rockbolt model based on this conceptual view is introduced. Some verification works will also be carried out based on the experimental results.

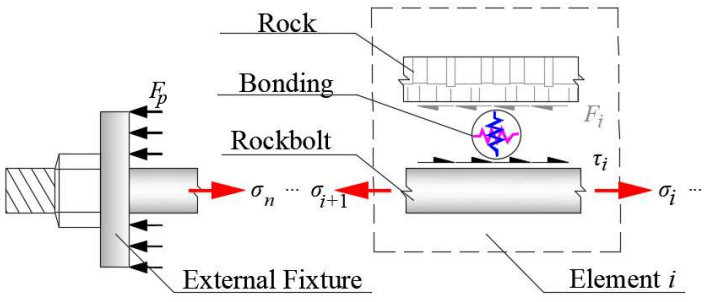

Figure 4-1 Sketch of the components of the proposed rockbolt model (Nie et al., 2014a)

4.2 Development of the rockbolt model

4.2.1. Implementation of the rockbolt model in 2D-DDA

A rockbolt model is proposed as a bar element with its direction of extension from the free end to the other end where a faceplate is usually attached. To be integrated with the block system, a rockbolt model is divided into several segments according to the block boundaries. Each segment contains several rockbolt elements, while each element is containing a pair of bolt nodes (Nie et al., 2014a, b). To consist with the bond-slip models deduced from Chapter 3, the length of the rockbolt element is set as 0.1 m (except those near joints whose lengths might be determined by the hinge length). For example, a rockbolt is going through three rock blocks A, B and C as shown in Figure 4-2. Thus, this rockbolt is divided into segments *A*, *B* and *C* accordingly. Take *Segment C* as an example, it contains four rockbolt elements, i.e. *Elements 1* to *4*. One rockbolt element, such as *Element 1*, is a bar element. It contains two rockbolt nodes, such as *bolt node 1* and *bolt node 2*. To record the relative movement between rock and rockbolt, there is a rock node which is initially with same position as the bolt nodes, such as the *rock node i'* is initially with the same position as *the bolt node i*. Once the block moves, the relative movements between two nodes are recorded as slip displacement which cause the rockbolt extension later. Thus, the tensile force/shear force will restrain the block movement. This simulates the load transfer in a rock and rockbolt system.

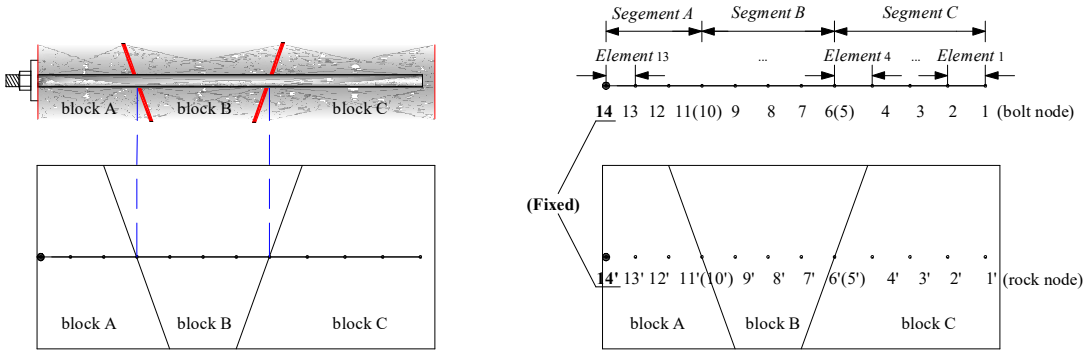

(a) Rockbolt element in rock block (b) Nodes in the rockbolt and the related rock nodes

Figure 4-2 Rock block and rockbolt model in 2D-DDA program (Nie et al, 2014a)

4.2.2. Analytical solutions of a rockbolt model

The mathematical algorithm for a rockbolt element has been introduced in Section 2.1.2. It is assumed that only the slip at the interface of rockbolt and rock is considered. Thus, the slip displacement is determined as $\Delta U_{rx} - \Delta U_{bx}$. By assuming a linear relationship between the bond stress and the slip displacement, the increase of bond stress $\Delta\tau_i$ could be calculated as:

$$\Delta\tau_i = k\left(\Delta U_{rx} - \Delta U_{bx}\right) \tag{4.1}$$

where: k –bond stiffness at the interface, unit in Pa/m; $k = k_1$, before decoupling happens, $k = k_2$, once the accumulated shear stress at the anchorages is beyond the maximum shear strength or the relative displacement is greater than δ_1 but less than δ_2, and $k = k_3$, for the low frictional slipping along interface if relative displacement is greater than δ_2,

ΔU_{rx} – displacement of the rock;

ΔU_{bx} – displacement of the rockbolt.

The axial stress in the rockbolt element i induced by bond slip is written as:

$$\Delta\sigma_i = \frac{\Delta\tau_i l_i}{A_b}\pi D_b \tag{4.2}$$

where: A_b – cross-sectional area of the rockbolt,

$\Delta\sigma_i$ – incremental axial stress, and

l_i – length of rockbolt element i.

Assuming the stress-strain relationship of the rockbolt is in linear elastic, thus,

$$\Delta\sigma_i = E_b\varepsilon_i = E_b\frac{dU_{bx}}{dx} \tag{4.3}$$

The governing equation of a rockbolt element is:

$$\frac{d^2\left(U_{bx}\right)}{dx^2} = -\frac{\tau_i}{E_b A_b} \tag{4.4}$$

$$\text{or} \quad \frac{d^2\left(\Delta U_{bx}\right)}{dx^2} - \frac{k}{AE}\left(\Delta U_{rx}\right) = \frac{k}{AE}\left(\Delta U_{bx}\right) \tag{4.4a}$$

Eq.(4.4) could be rewritten as:

$$\frac{A_b E_b}{x_i - x_{i-1}}\left(U_{bx}^i - U_{bx}^{i-1}\right) + \frac{A_b E_b}{x_{i+1} - x_i}\left(U_{bx}^i - U_{bx}^{i+1}\right) = k\left(\frac{x_{i+1} - x_{i-1}}{2}\right)\left(U_{rx}^i - U_{bx}^i\right) \tag{4.5}$$

If the rockbolt is fixed by faceplate, then,

$$T_n = \frac{A_b E_b}{x_{n-1} - x_n}\left(U_{bx}^{n} - U_{bx}^{n-1}\right) \tag{4.5a}$$

If the rockbolt end is free, we have

$$\frac{A_b E_b}{x_n - x_{n-1}}\left(U_{bx}^{n} - U_{bx}^{n-1}\right) = k\left(\frac{x_n - x_{n-1}}{2}\right)\left(U_{rx}^{n} - U_{bx}^{n}\right) \tag{4.5b}$$

The increment of the restrain force provided by rockbolt at the rockbolt node i (i = 1, …, n-1) ΔP_i could be calculated as:

$$\Delta P_i = k l_i \left(U_{rx}^{i} - U_{bx}^{i}\right) \tag{4.6}$$

By defining the angle between the rockbolt direction and x-axis as θ, the variations of point loads to the rock block induced by the restrain of rockbolt at a time step could be calculated as:

$$\begin{bmatrix} F_x \\ F_y \end{bmatrix} = \Delta P_i \begin{bmatrix} \cos\theta \\ -\sin\theta \end{bmatrix} \tag{4.7}$$

where F_x and F_y are the point loads at the horizontal and vertical direction, respectively.

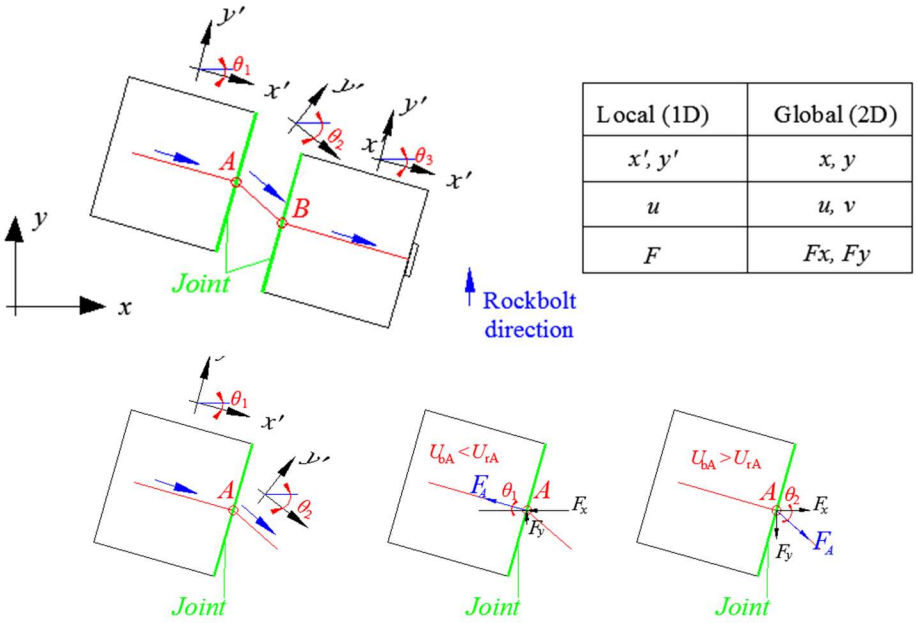

Figure 4-3 Transformation from 1D bar element to 2D space

The extension directions of rockbolt elements are assumed as constant, i.e., the same as the ones under the initial loading. However, the directions may change at the joint place, such as the extension direction at node A may follow θ_1 or θ_2. If $U_{bA} < U_{rA}$, that is the bolt is under unloading condition, θ_1 is chosen. On the other hand, if $U_{bA} > U_{rA}$, that is the bolt is under extension, θ_2 is chosen.

4.2.3. Axial behaviour

A rockbolt is usually made of steel bar. An elastic, linear strain-hardening steel model is adopted to simulate the axial behaviour of the rockbolt model. As shown in Figure 4-4(a), the rockbolt deforms according to elastic modulus E_b if the stress is less than the yield stress σ_Y. Once the stress is beyond the yielding stress (point D), the rockbolt is in linearly plastic range. At the stage of initial yield, if the loading continues to increase, the rockbolt element deforms according to tangent modulus E_T. The rockbolt will be broken by tension if the accumulated plastic strain is beyond the predefined extreme strain ε_{ext} as shown as point M. If the element is unloaded (see Figure 4-4(b)), the rockbolt will deform with the elastic modulus of E_b. These parameters are easily derived from the tensile experiments of rockbolt.

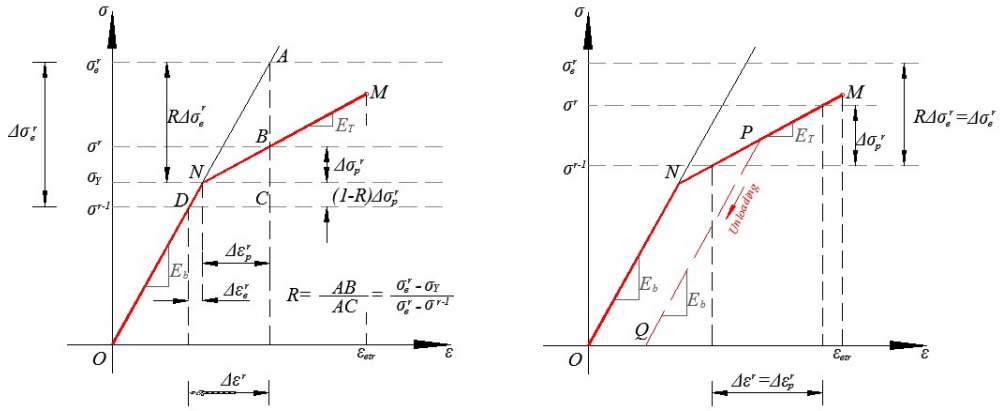

Figure 4-4 Stress-strain curves for the elastic, linear hardening rockbolt material (modified after Owen and Hinton, 1980)

4.2.4. Bond behaviour

The bond between rock and rockbolt is represented by a normal spring k_n and a shear spring k, as shown in Figure 4-1. The bond slip model during relative displacement is

following the trilinear model as shown in Figure 4-5. Calculation of the relative displacement or slip is based on the analytical solution in Section 4.2.2. Under a small slip distance, the bond stress is increasing with the slip distance in a ratio of k_1. Once the bond stress achieves the maximum bond stress, τ_{max}, the bond stress will decrease with the slope k_2. Once the bond stress is reduced to the residual bonding stress, τ_r, the bonding stress keeps nearly constant if the slip continues. The maximum bonding strength (τ_{max}) and residual bonding strength (τ_r), are functions of the confining pressure on the rockbolt element with respect to the normal spring k_n. In a DDA block system, the confining pressure is calculated as a stress component of the rock block with direction normal to the rockbolt extension direction. By adopting various bond slip models, different types of rockbolt elements (i.e., CMC, CFC and DFMC) could be simulated. Figure 4-6 shows four types of rockbolt which will be discussed in the later sections.

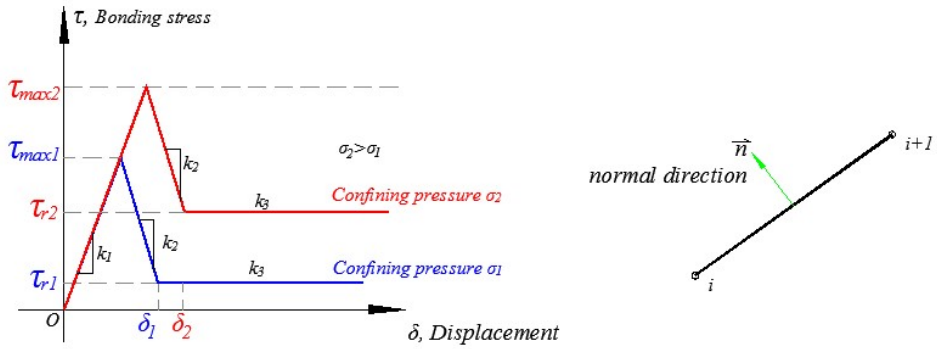

Figure 4-5 Trilinear model used to present bonding behaviour

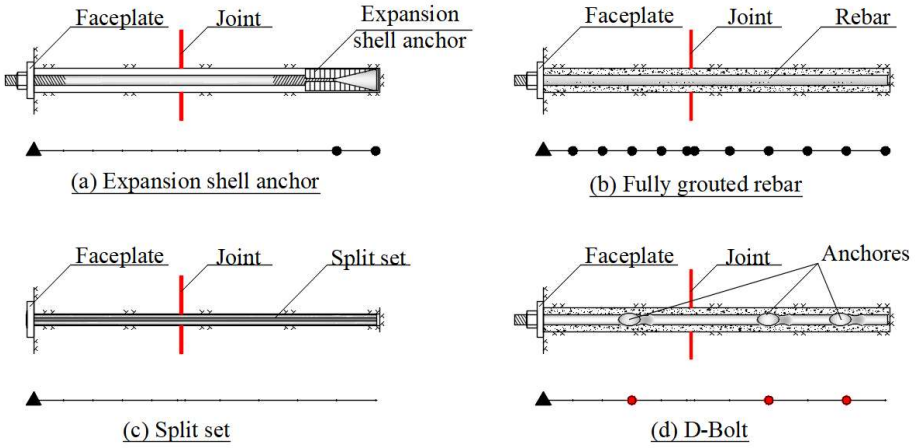

Figure 4-6 Numerical models for four types of rockbolts (Nie et al., 2014a)

4.2.5. Shear behaviour

When a fully grouted rockbolt in rock is subjected to shear loading, two plastic hinges might form at both sides of the joint plane as shown in Figure 4-7. By assuming the intersection between the rock joint and the rockbolt element at the middle of the rockbolt elements, the length of the rockbolt element through rock joint is $2l_e$ where l_e is hinge length of rockbolt. If there is no experimental data, the hinge length le is often taken as 1.0 ~ 2.0 D_b (Gerdeen et al. 1981; Grasselli 2005; Jalalifar and Aziz 2010). Under the action of shear loading, the axial load N, shear load F_s and bending moment M are generated in the fully grouted rockbolt.

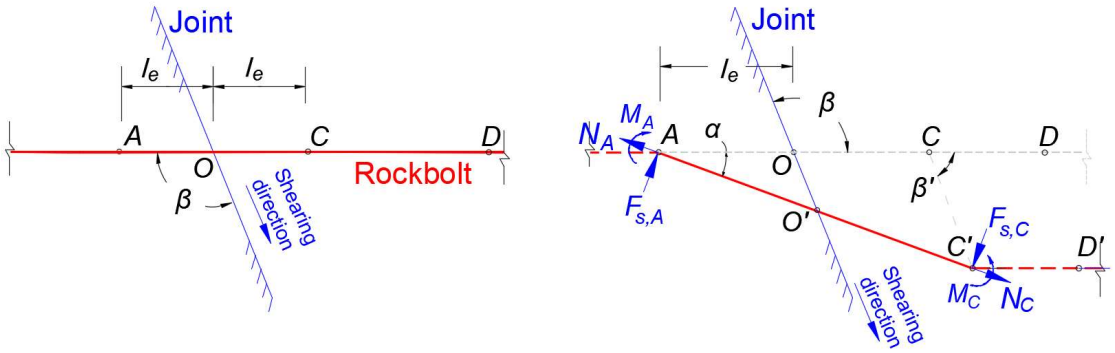

Figure 4-7 Simplified rockbolt element subjected shear movement

An example of a rockbolt through a rock joint with direction angle of θ, and incline angle between rock joint and rockbolt of β is presented in Figure 4-10. The analytical solution to consider the effects of combined tension and shear loading onto the yield performance of rockbolt is given by Li et al. (2015) and shown as:

$$\begin{bmatrix} \frac{l_e}{E_b A_b} & 0 & 0 \\ 0 & \frac{l_e^3}{3E_b I_b}+\frac{\kappa l_e}{G_b A_b} & \frac{l_e^2}{2E_b I_b} \\ 0 & \frac{l_e^2}{2E_b I_b} & \frac{l_e}{E_b I_b} \end{bmatrix} \begin{Bmatrix} N_o \\ F_{so} \\ M_o \end{Bmatrix} - \begin{Bmatrix} 0 \\ \frac{q_0 l_e^4}{360E_b I_b}+\frac{\kappa q_0 l_e^2}{12G_b A_b} \\ \frac{q_0 l_e^3}{60E_b I_b} \end{Bmatrix} = \begin{Bmatrix} U_b \\ U_s \\ \alpha_o \end{Bmatrix} \tag{4.8}$$

where: N_o – axial load,

F_{so} – shear load,

M_o – bending moment,

G_b – the shear modulus of the rockbolt,

I_b – the inertia moment of the cross section of the rockbolt element,

κ – a concentration coefficient of the shear stress distribution at the cross section which is equal to 4/3 of the solid cross-section,

U_b – axial extension,

U_s – lateral deflection, and

α_o – deflection angle.

For a symmetrical homogenous beam element with very small diameter, the bending moment M_o could be neglected. The force equilibrium at the rockbolt gives axial load N_o and shear load F_{so} at a point O as:

$$N_o = \frac{E_b A_b}{l_e} U_b \tag{4.9}$$

$$F_{so} = \frac{240\kappa G_b A_b E_b^2 I_b^2 - 40 G_b^2 A_b^2 E_b I_b l_e^2}{\left(6E_b I_b \kappa l_e - G_b A_b l_e^3\right)\left(13 G_b A_b l_e^3 + 30\kappa E_b I_b\right)} U_s \tag{4.10}$$

The relationship of the rockbolt deformation along its tangential and axial directions is written as (Li et al., 2015):

$$U_s = \frac{\sin\beta}{\cos\left(\beta+\alpha_o\right)} U_b \approx \frac{\sin\beta}{\cos\beta - \alpha_o \sin\beta} U_b \tag{4.11}$$

where: U_s and U_b – the rockbolt deformations along its tangential and axial directions, respectively.

The force equilibrium on point A as shown in Figure 4-10 gives axial load N_A, shear load F_{sA} and bending moment M_A at point A, as:

$$N_A = \frac{E_b A_b}{l_e} U_b \tag{4.12}$$

$$F_{sA} = K_s U_s \tag{4.13}$$

$$M_A = F_{sA} l_e \tag{4.14}$$

where: K_s is shear stiffness of the rockbolt element which could be calcualted by:

$$K_s = \frac{240\kappa G_b A_b E_b^2 I_b^2 - 40 G_b^2 A_b^2 E_b I_b l_e^2}{\left(6E_b I_b \kappa l_e - G_b A_b l_e^3\right)\left(13 G_b A_b l_e^3 + 30\kappa E_b I_b\right)} \tag{4.15}$$

The increase of axial load ΔN_A, shear load ΔF_{sA} and bending moment ΔM_A at the rockbolt element in a time-step could be given as:

$$\Delta N_A = \frac{E_b A_b}{l_e} \Delta U_b \tag{4.16}$$

$$\Delta F_{sA} = K_s \Delta U_s \tag{4.17}$$

$$\Delta M_A = \Delta F_{sA} l_e \tag{4.18}$$

The increase of the normal stress induced by bending moment acting at point A of rockbolt element $\Delta\sigma_M$ is:

$$\Delta\sigma_M = \frac{\Delta M_A D_b}{2I_b} \tag{4.19}$$

Combining Eqs. (4.2) and (4.19) gives the normal stress increase of rockbolt acting by combined tension and shear loading as:

$$\Delta\sigma_A = \frac{\Delta N_A}{A_b} + \frac{\Delta M_A D_b}{2I_b} \tag{4.20}$$

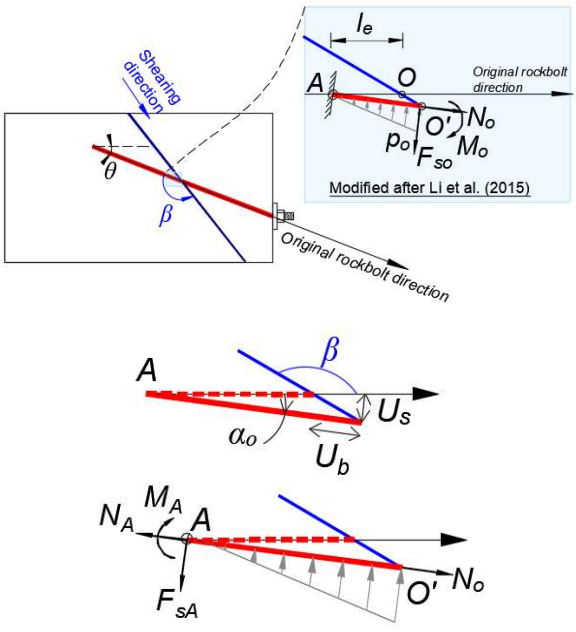

Figure 4-8 A free body diagram of a rockbolt installed through a joint

For short span beams carrying large concentrated load, the reduction from shear is significant (SSJ 1996). The Von Mises yield criterion is usually used to describe the short span beam and shown as (see Figure 4-9):

$$\left(\frac{\sigma_A A_b}{N_y}\right)^2+\left(\frac{F_{sA}}{F_{s,\max}}\right)^2=1 \tag{4.21}$$

where: N_y – yield axial load of the rockbolt element in pure tension, and $F_{s,\max}=N_y/\sqrt{3}$.

It is assumed that the shear force and moment of rockbolt element do not increase with respect to the increasing of shear displacement once the rockbolt element is yielded. The normal stress versus axial strain is still linear with tangent modulus of E_T. As shown in Figure 4-9, the yield criterion is of the short span beam is,

$$\left(\frac{\sigma_A A_b}{N_f}\right)^2+\left(\frac{F_{s,y}}{F_{s,\max}}\right)^2=1 \tag{4.22}$$

where: $F_{s,y}$ – the yielded shear load of a rockbolt element, and

N_f – ultimate axial load of rockbolt element in pure tension.

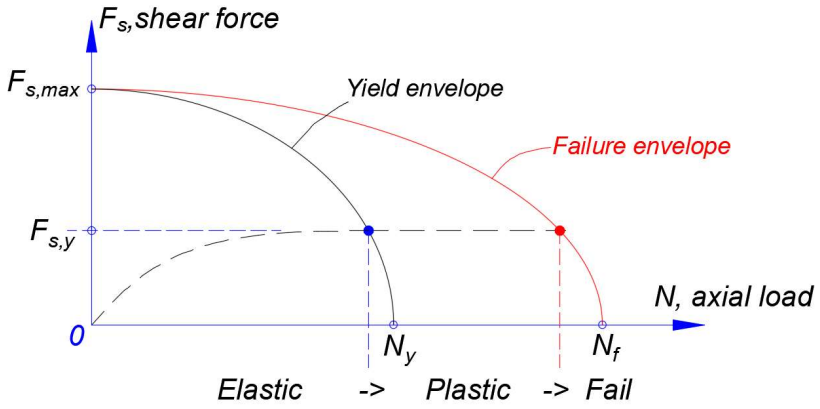

Figure 4-9 Loading state judgement using shear stress versus axial load curves

The variations of point loads to the rock block induced by the restrain of rockbolt under the combined tension and shear loads at a time step could be calculated as:

$$\begin{bmatrix}F_x\\F_y\end{bmatrix}=\Delta P_i\begin{bmatrix}\cos\theta\\-\sin\theta\end{bmatrix}+\Delta F_{sA}\begin{bmatrix}\sin\theta\\\cos\theta\end{bmatrix} \tag{4.23}$$

The point loads as shown in Eq. (4.23) will be added to the submatrix of point loading as shown in Eq. (2.37) to simulate the reinforcement effect of rockbolt to the rock

blocks. An example of the rockbolt element geometry in 2D-DDA is shown in Figure 4-10.

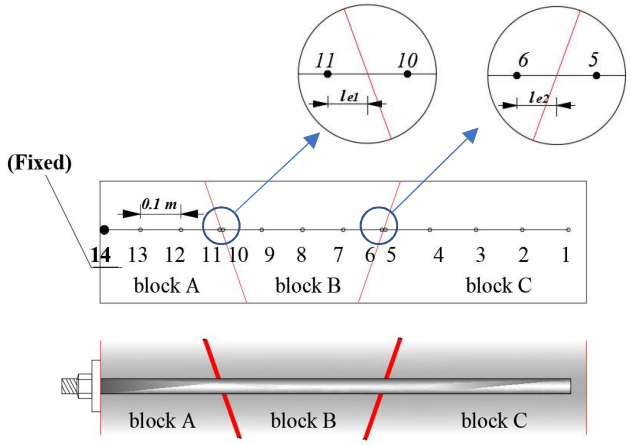

Figure 4-10 An example of a rockbolt element in 2D-DDA

4.2.6. Programming

The development rockbolt model used in 2D-DDA requires several input parameters as shown in Table 4-1. It includes four parts:

A. Rockbolt system installation parameters,

B. Axial behaviours,

C. Bond behaviour, and

D. Shearing behaviour.

The parameters are usually determined by best fitting experiments tests, such as pull-out tests. The default values are also listed based on previous experimental tests (Rong et al., 2004; Stillborg, 1986).

The newly developed rockbolt model is integrated with 2D-DDA program to apply the restrains for rock block movements. By considering axial behaviour, bond behaviour and shear behaviour, the restrains are calculated in each time step, as shown in Figure 4-11. Based on the calculations, the proposed model could present four major failure modes of rockbolt: (1) decoupling along the interface, (2) tensile failure, (3) faceplate failure and (4) shear failure. Once type (2) or/and (4) failure occurs, the force restrains are not applied to the rock blocks any more.

The changes made in flowchart of 2D-DDA codes are shown in Figure 4-12. The rockbolt models in tunnels start to apply restrains to the rock blocks movement if the pre-defined time or step is achieved (sub-function *dccable*). It is usually activated after excavation or core replacement functions (sub-function *df29*). There could be several rockbolt groups which are installed in different time/step. The restrains made by rockbolts are designed as point loads applying on rock blocks (sub-function *df15c*). After each round of open-close iteration, the slip distances are updated (sub-function *df25*), followed by the calculation of the restrained loading (sub-function *dfcable*) which is going to be applied in the next time step.

Table 4-1 Rockbolt model properties

Category	Input parameters	Unit	Default
A. Rockbolt system installation	Installation time/step	step or time	-
	Rockbolt type	-	Fully rockbolt rebar
B. Axial behaviour	Elastic modulus, E_b	Pa	200e9
	Yield stress, σ_y	Pa	382e6
	Tangent modulus, E_T	Pa	4e9
	Extreme strain, ε_{ext}	-	15%
C. Bond behaviour	1st bond stiffness k_1	Pa/m	54e9
	2nd bond stiffness k_2	Pa/m	6e9
	3rd bond stiffness k_3	Pa/m	5e6
	Max. bonding strength (no confining effect), τ_{max}	Pa	5.24e6
	Residual bonding strength, τ_r	Pa	0.5e6
D. Shearing behaviour	Shear stiffness, K_s	N/m	Eq. 4.15
	Ultimate shear force, $F_{s,max}$	N	Eq. 4.21

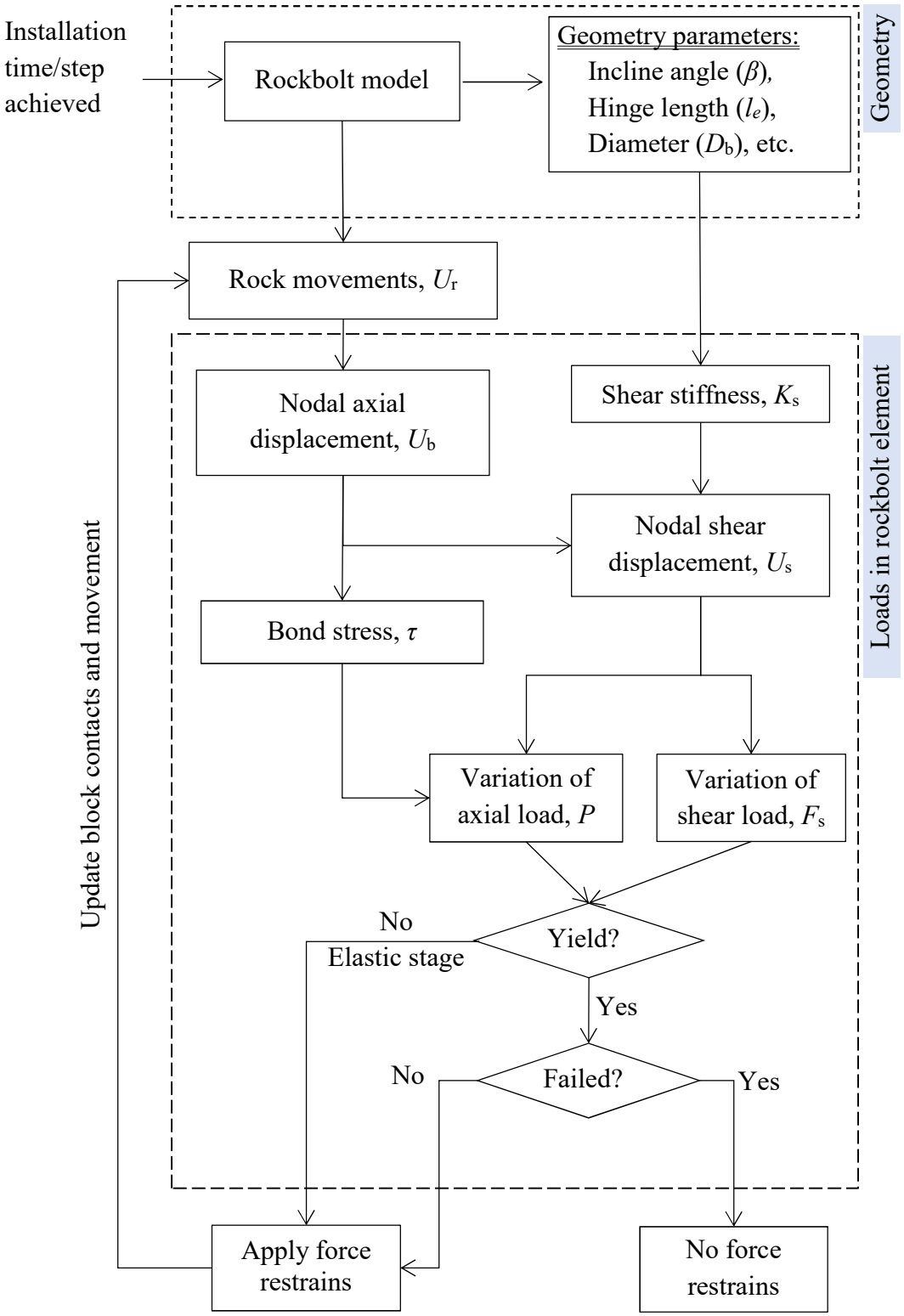

Figure 4-11 Flowchart of the calculation of rockbolt forces

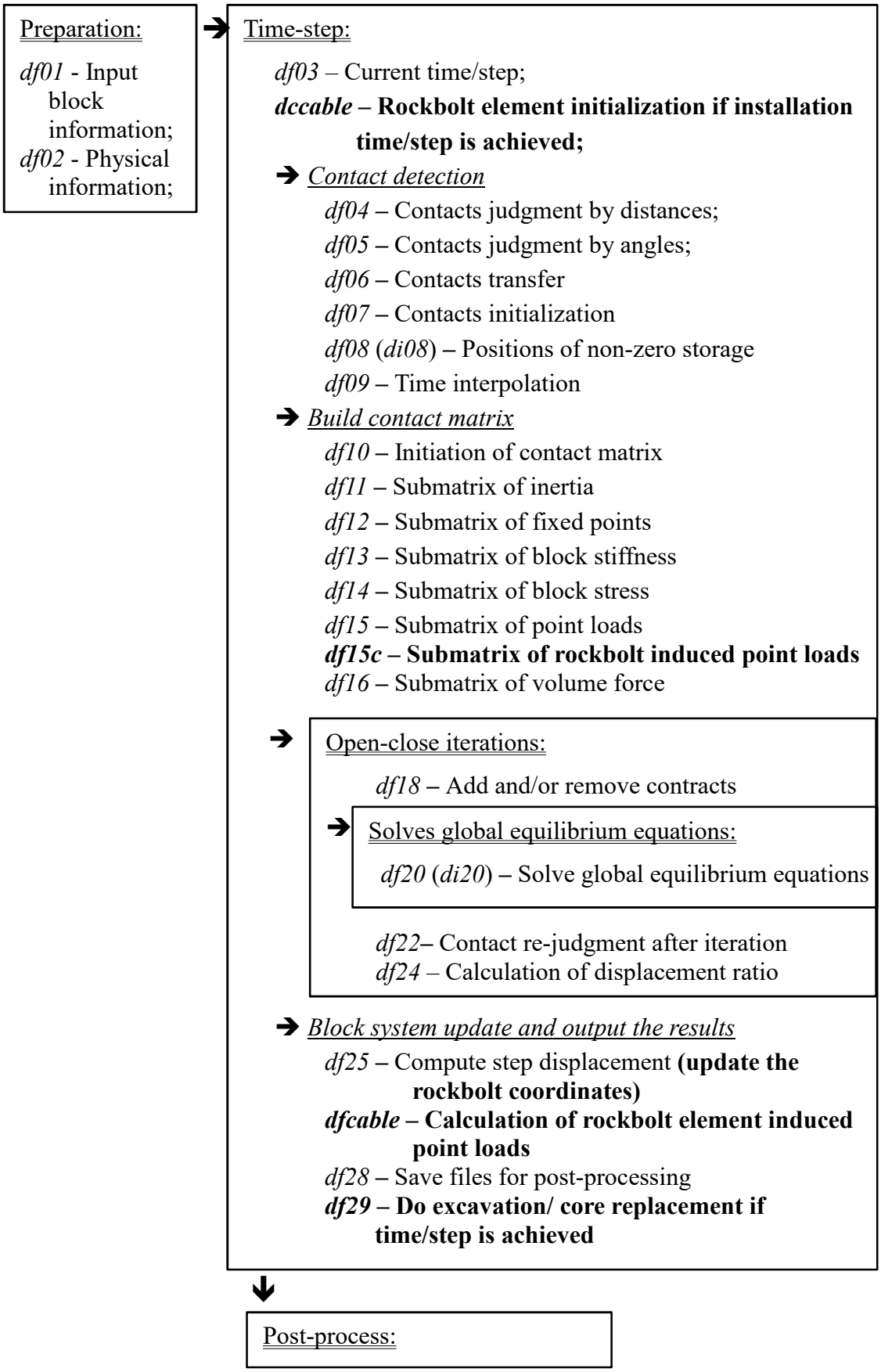

Figure 4-12 Revised flowchart of 2D-DDA codes by integrating with rockbolt models

4.3 Verification of the rockbolt model by experimental results

4.3.1. Verifying bond behaviour by pull out test

The pullout model tests conducted by Rong et al. (2004) are adopted to evaluate the accuracy of the present fully grouted rockbolt model. The maximum applied pullout load in the test was 300 kN, inducing only necking at the head of rockbolt. The dimensions and boundaries of the model in 2D-DDA is shown in Figure 4-13(a). The rockbolt is divided into 10 elements each of which is 0.1 m long. The diameter and length of the rockbolt are 32 mm and 1 m, respectively. The parameters of the trilinear bond-slip model presented by Ma et al. (2014) are used: τ_{max} = 5.24 MPa, τ_{res} = 0.524 MPa, δ_1 = 0.096 mm and δ_2 = 0.816 mm as shown in Figure 4-13(b). The elastic modulus of the steel rebar E_b = 210 GPa before yield and E_T = 4.2 GPa after yield as shown in Figure 4-13(c). More details of the parameters used in the 2D-DDA model are summarized in Table 4-2.

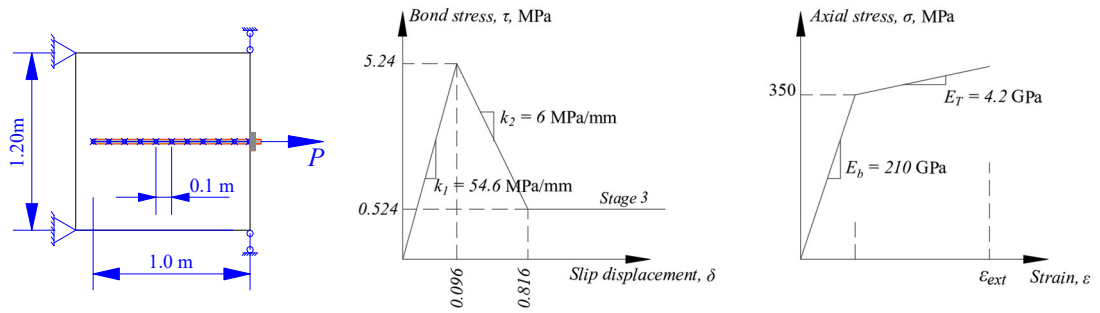

(a) (b) (c)

Figure 4-13 The parameters of rockbolt model used in 2D-DDA (a) Dimensions and boundaries of the model, (b) Bond-slip model and (c) Axial model of the rebar

The axial loads versus displacement curves from the 2D-DDA simulation and model test results are shown in Figure 4-14. It can be seen that the simulation results match reasonably well with the model test data and the analytical method proposed by Ma et al., (2014). In the present simulation, the first three nodes of rockbolt near loading position are deboned when the axial force is 300 kN, and the extreme strain is achieved at an axial load of 340 kN when five nodes are decoupled. The axial force and bond stress distributions along the rockbolt from present simulation and model test results are compared and shown in Figure 4-15(a) and (b), respectively. The pullout

loads used in the simulation are 50 kN, 100 kN, 200 kN and 300 kN, respectively. It is found that good agreements between the numerical results and the proposed model has reasonable accuracy for the simulation of fully grouted rockbolt problems.

Table 4-2 Parameters used in 2D-DDA to simulate the pullout test

Item	Parameter	Value	Item	Parameter	Value
DDA setting	Dynamic factor	0 (static)	Bolt	Diameter, d_b (mm)	32
	Step max. displacement ratio, g_2	0.001		Tangent modulus, E_T (GPa)	4.2 ($\approx E_b/50$)
	Upper limit of time interval, g_1	0.0005		Yield strength, σ_Y (MPa)	360
	SOR factor	1.4		Extreme strain, ε_{ext} (%)	1.6
	Normal spring stiffness, k_n (N/m)	3×10^9		Maximum bond strength, $F_{s,max}$	5.24e6
	k_n / k_s	2.5		Residual bond stress, $F_{s,res}$	0.524e6
	Block unit weight, $\times 10^3$ kN/m^3	26		Sliding bond node, k_3 (Pa/m):	1e5

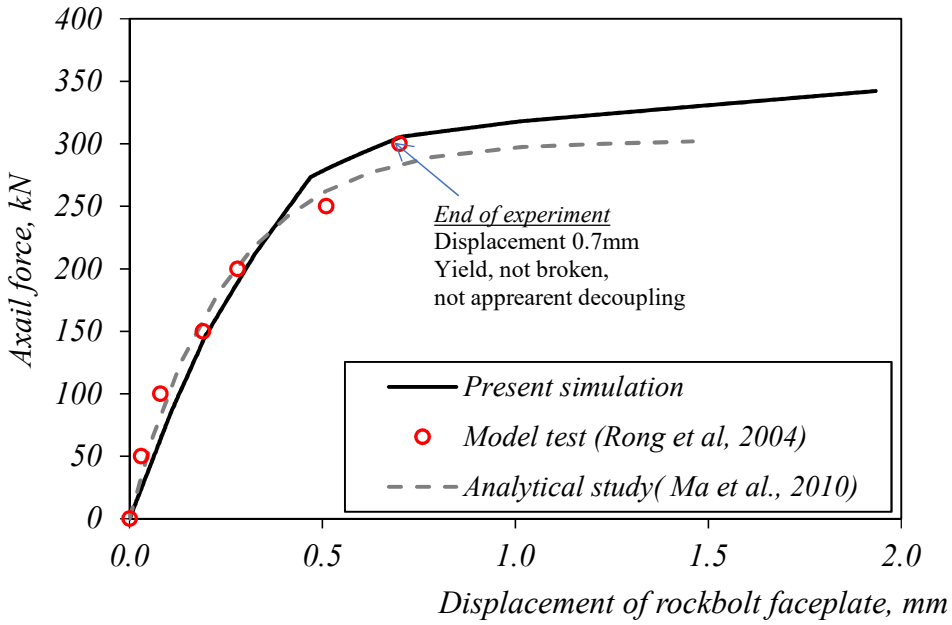

Figure 4-14 Comparisons of the axial load versus displacement curves from present study and model test conducted by Rong et al.(2004)

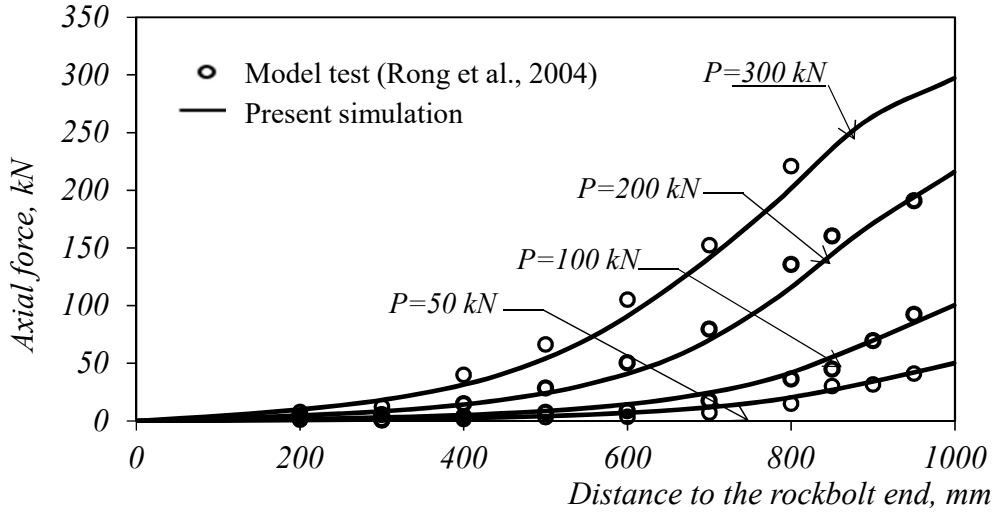

(a)

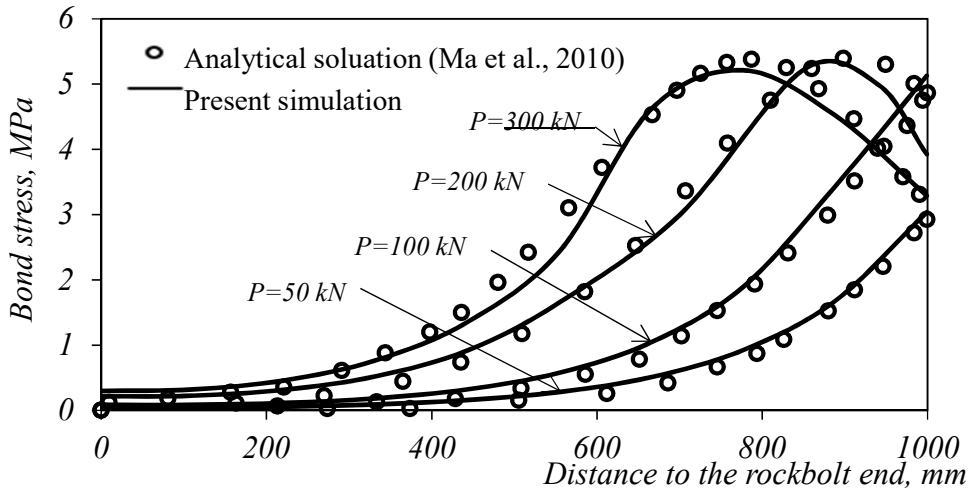

(b)

Figure 4-15 Comparisons of (a) the simulated axial force distribution with the results of model test conducted by Rong et al. (2004) and (b) the simulated bond stress distribution with the analytical solutions by Ma et al. (2010)

4.3.2. Verifying shear behaviour by shear test

The shear behaviour of fully grouted rebar has been tested in laboratory (Chen and Li, 2015). The corresponding 2D-DDA model are shown in Figure 4-16(a). The bottom block is fixed, while the upper block can only move along the horizontal direction. An rockbolt is installed to connect two rock blocks with angle β. A faceplate is attached at the top end, while the other end at the bottom block is free. According to the block boundary, the rockbolt is divided into two segments equally in length. In each segment, the rockbolt model is divided into several elements each of which is 0.1 m except the

elements next to the joint where the hinge length l_e is used to locate the rockbolt/rock nodes. The bond-slip model is assumed as a trilinear model shown in Figure 4-16(b). An elastic, linear strain-hardening steel model is adopted to simulate the rockbolt material (see Figure 4-16(c)). The detailed parameter settings of rock, rockbolt and DDA calculations are listed in Table 4-3. Three shear tests with shearing angle β = 90°, 120° and 140° are simulated. Another simulation of pull-out test is also conducted for comparison purpose. As shown in Figure 4-17, the rockbolt fail at the elements adjacent to joint in all four cases. The curves of the total loads versus displacement from the 2D-DDA simulation results are shown in Figure 4-18. It should be noted that the total force is defined as the squared sum of normal and shear forces, while the total displacement is the horizontal movement of the upper block (Chen and Li, 2015).

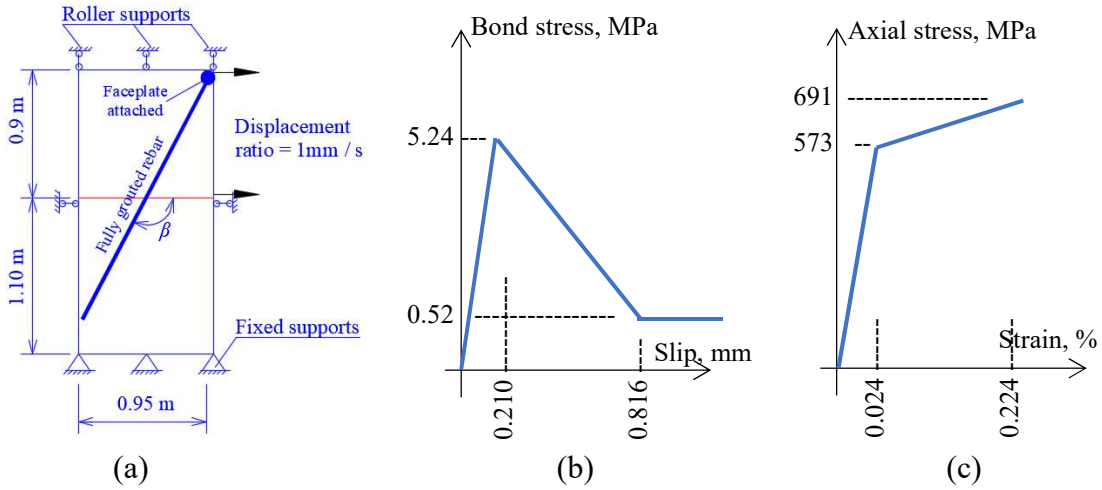

Figure 4-16 DDA model setting of the shearing tests (a) DDA model, (b) bond–slip model and (c) material model

Table 4-3 Parameters setting in the simulation of shear tests

Item	Parameter	Values	Item	Parameter	Values
Rock	Elastic modulus E_r, GPa:	30	Rockbolt	Diameter D_b, mm	20
	Poisson ratio, v	0.25		Elastic modulus E_b, GPa	210
	Unit weight, $\times 10^3$ kN/m^3	26.0		Yield axial force, kN	180
DDA calculation	Step max. displacement ratio	0.0004		Ultimate axial force, kN	217
	Upper limit of time interval	0.0002		Hinge length l_e, mm	30 (~1.5D_b)
	SOR factor	1.4		Shear stiffness K_s, MN/m	66.3

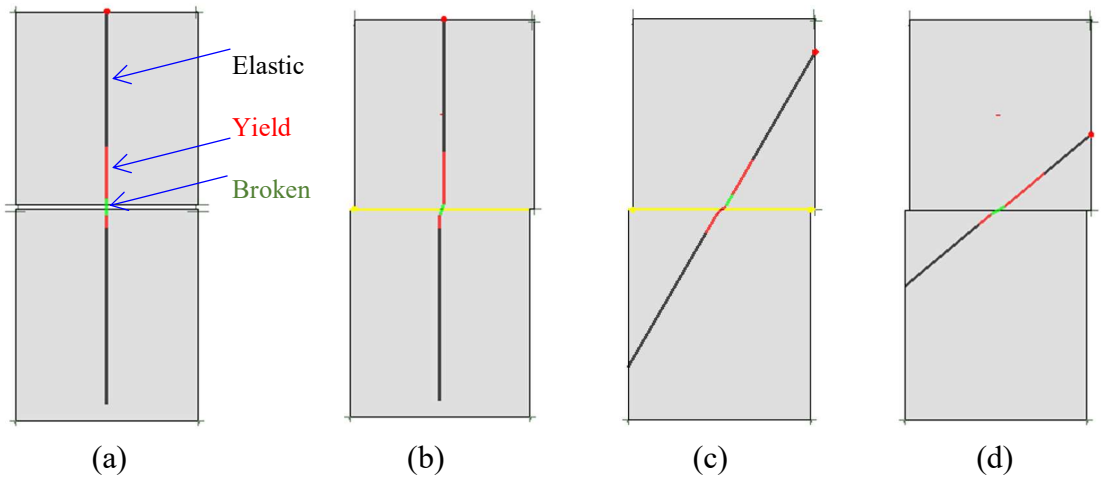

Figure 4-17 Failures of the rockbolts in numerical simulations (a) Pull-out test and shear tests at angles of (b) β = 90°, (c) β = 120° and (d) β = 140°

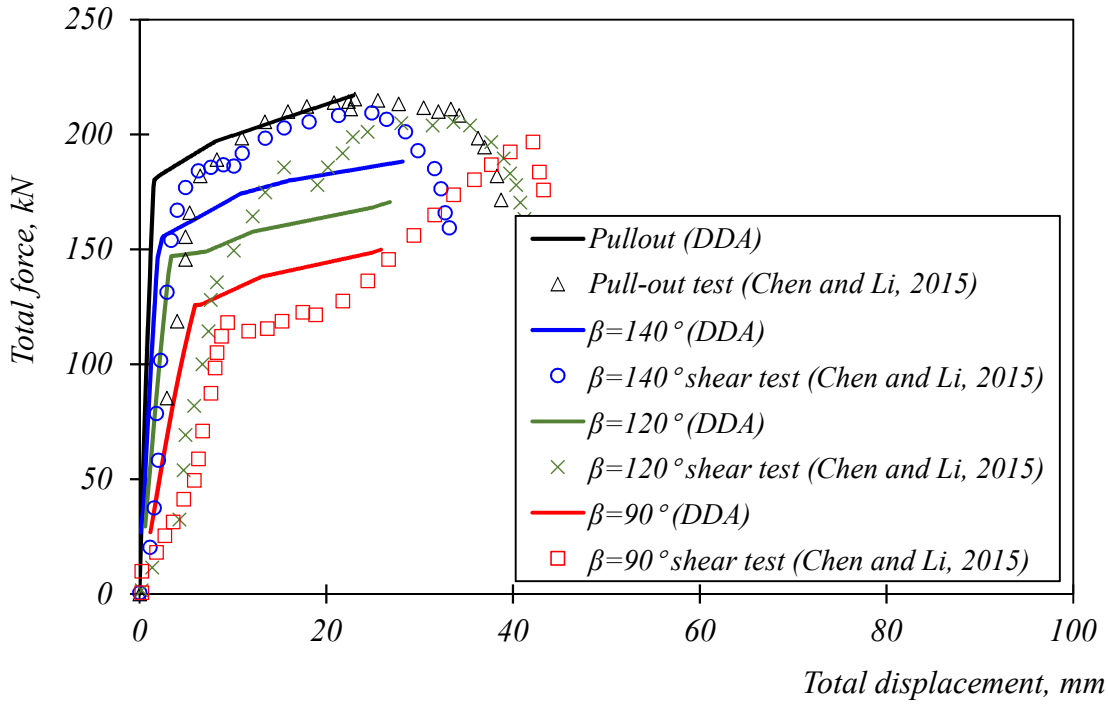

Figure 4-18 Comparisons of load-displacement curves between experiments and numerical simulations

Table 4-4 lists the comparison between the numerical and experiment results. In terms of the yielding and failure forces, the simulation results of pullout test provide good agreement with the experiment results as the errors are 1.0% and 0.7% respectively. The total loads of the rockbolts either at yielding or at breaking moments of shear tests

are lower than those in the pullout test. In the simulation of shear test with a shear angle $\beta = 90°$, the rockbolt yields at the lowest force of 115 kN. The error between the numerical result and the experiment result is about 2.7%. The rockbolt fails at the lowest total load. The error is about 23.9% compared with the experiment result. Both the yield and fail forces are increasing with the increase of shear angles. In cases of $\beta = 120°$ and $\beta = 140°$, the errors of resulted yielding forces in the simulations of shear tests are 1.9% and 5.0%, respectively, while those of failure forces are 17.5% and 11.6%, respectively. The results show that the proposed rockbolt model could catch the load variation during pulling and shearing. However, the simulations have limitations that they do not well catch the slopes of the increasing force with respect to the displacement in elastic. As listed in Table 4-4, the largest error occurs in the simulation of shear test with a shear angle $\beta = 90°$. The error becomes less if the shear angle increases. This is mainly because the displacement caused by yielding of grout is not considered in the current model.

Table 4-4 Comparisons between numerical simulations and the experiment results

Items		A. Pull-out	B. $\beta = 90°$	C. $\beta = 120°$	D. $\beta = 140°$
Yielding axial force, kN	Experiment	181.86	118.13	149.45	165.92
	DDA results	180.05	114.93	146.64	157.60
	Error, %	-1.0%	-2.7%	-1.9%	-5.0%
Ultimate axial force, kN	Experiment	215.38	196.70	205.49	209.34
	DDA results	216.97	149.66	169.63	185.07
	Error, %	0.7%	-23.9%	-17.5%	-11.6%
Rotation angle α, °	DDA results	0.0	18.5	14.3	10.5

As shown in Figure 4-19(a), the shear force varies with the shear displacement in different response to the shear angle. The shear force in the case of $\beta = 90°$ is larger than the other two cases, causing a larger rotation of rockbolt element at joint (see Figure 4-19(b)). At the failure point, the rockbolt element rotated about 27° in the case of $\beta = 90°$ and about 13.9° in the case of $\beta = 140°$. Therefore, the deduction of the load carrying compacity during shearing is mainly induced by the combination work done by the axial load and shear load at the joint.

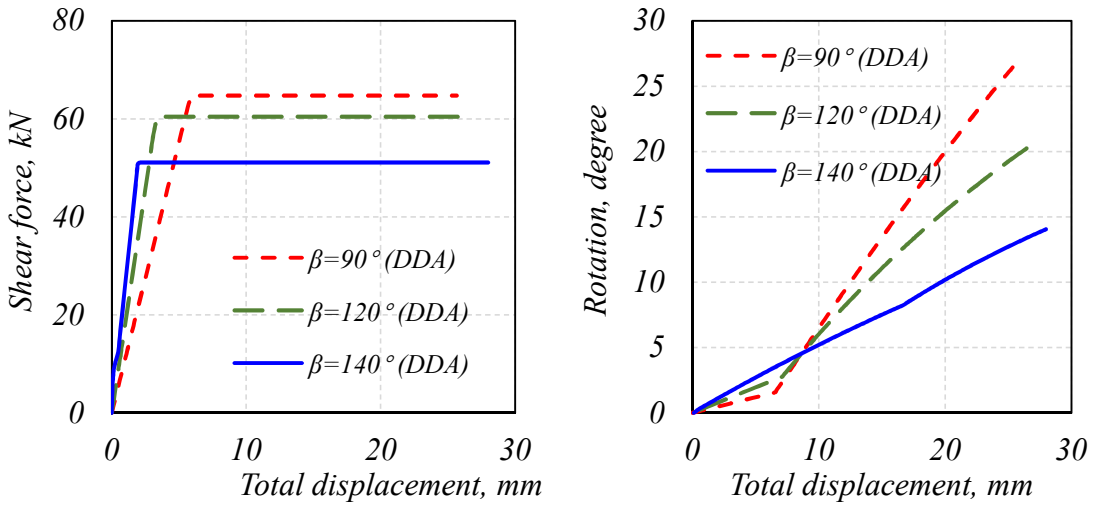

(a) Shear force histories (b) Rotations

Figure 4-19 Simulated shear behaviour of rockbolt elements at joints

4.3.3. Verifying axial behaviour by pull out tests

As shown in Figure 4-20(a), the pullout test done by Chen and Li (2015) are adopted to verify the axial behaviour of the developed rockbolt model. To simulate this kind of rockbolt elements, different bond slip models are assigned to them. As shown in Figure 4-20(b) and (c), the models of fully grouted rebar and D-bolt are considered respectively. The 2m rockbolt is divided into two segments according to the joint between two rock blocks. Each segment has 7 rockbolt elements (8 pairs of nodes) each of which is 0.14 m long. There is one more rockbolt element connecting two segments with length of 0.04 m (assuming the potential hinge length is 0.02 m).

For the fully grouted rebar, the nodes are all assigned by anchored nodes. However, for the D-bolt, the nodes are assigned by sliding nodes as the smoothing parts except the 2nd, 4th and 12th nodes from the rockbolt end which are assigned by special anchored nodes with higher bonding stiffness and bond strength than the anchored nodes. Therefore, there are four kinds of nodes in the model: (1) fix node where the faceplate is attached, (2) sliding node as a rockbolt element featured with low bond stiffness, (3) anchored node is a rockbolt element with trilinear bond behaviour as shown in Figure 4-13(b), and (4) special anchored node is a rockbolt element with strong bond behaviour. The detailed parameter settings are shown in Table 4-5.

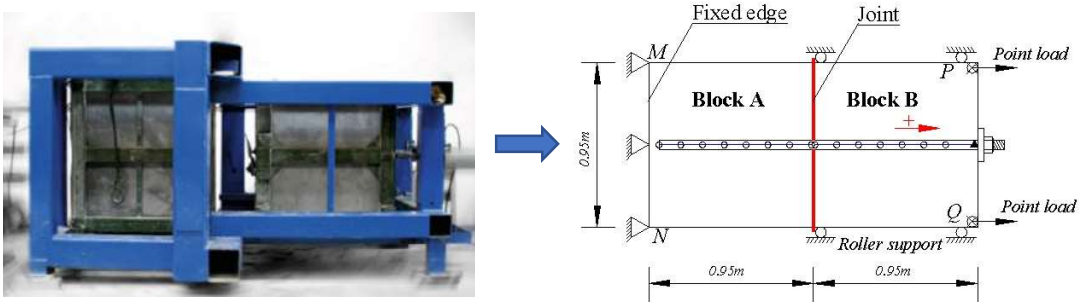

(a) Simplified pullout test model (after Li et al., 2010)

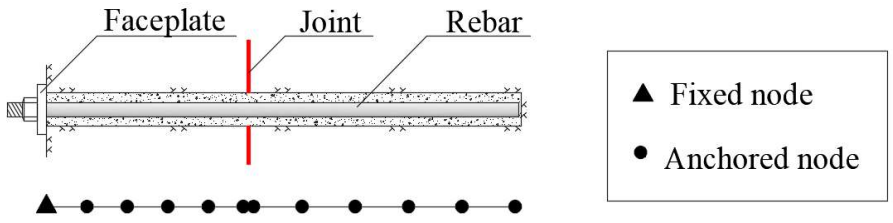

(b) Model of the fully grouted rebar

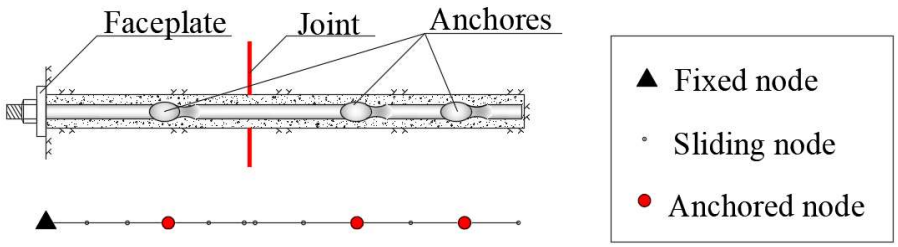

(c) Model of the D-bolt

Figure 4-20 Sketches of the pull-out test and the various rockbolt models

Table 4-5 Parameter settings in pullout models

Rockbolt parameters		Bonding models	
Diameter, d_b (mm)	20	Sliding nodes	k_1 = 1 MPa/mm
Young's modulus, E_b (GPa)	210	Anchored nodes (Rong et al, 2004)	k_1 = 54 MPa/mm k_2 = 6 MPa/mm
Tangent modulus, E_T (GPa)	1 ($\approx E_b/200$)		τ_{max} = 5.24 MPa τ_r = 0.524 MPa
Yield strength, σ_Y (MPa)	520	Special anchored nodes (for D-bolt, assumed)	k_{1s} = 80.0 MPa/mm
Extreme strain, ε_{ext} (%)	16		τ_{max} = 20 MPa

Figure 4-21 shows a comparison of the simulated load-deformation curves and the experimental results from the pullout tests. It indicates a reasonable agreement of the axial behaviours between the simulation and experiment results. The differences of the initial slope of the curves may be due to the assumed linear stress-strain relationship adopted in the numerical models.

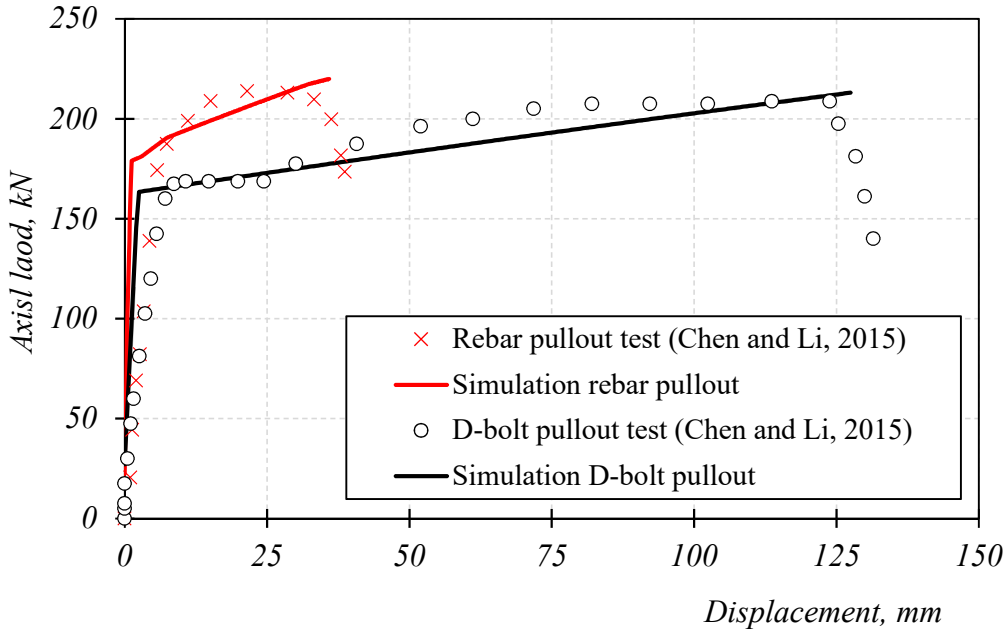

Figure 4-21 Comparisons of load-deformation curves between experiments and numerical simulations of pullout tests

The comparison shown graphically in Figure 4-21 indicates the fully grouted rebar model reaches to high load carrying capacity earlier than the D-bolt, but fails at a much lower displacement. By examining the axial stresses and bond stresses along the rockbolts (see Figure 4-22 (a)), the loads are concentrated in the central 4 elements when a pullout load of 100 kN is applied. Before failure, the central 4 elements are yielded (see Figure 4-22 (b)), and decoupling process has helped to defuse the load laterally. This indicates the deformation occurs in the central 4 elements mainly. On the other hand, the rockbolt elements between two special anchored nodes (8 elements) are sustaining the pullout load in different loading scales (such as pullout load of 100 kN and 200 kN in Figure 4-22(c) and (d) separately). It indicates the D-bolt is equally loaded in these elements, causing larger deformability. Thus, the deformability of the D-bolt is relying much on the performance of the special anchored points.

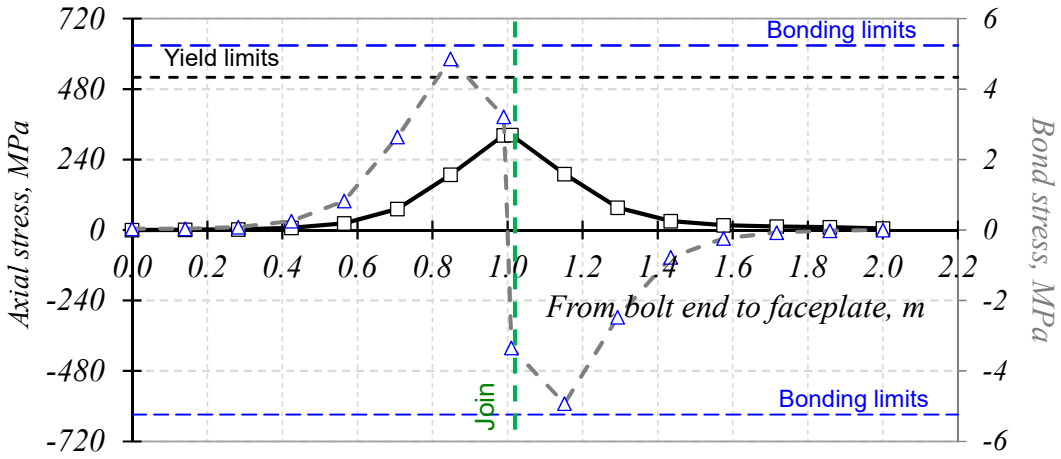

(a) Fully grouted rebar at pullout load of 100 kN

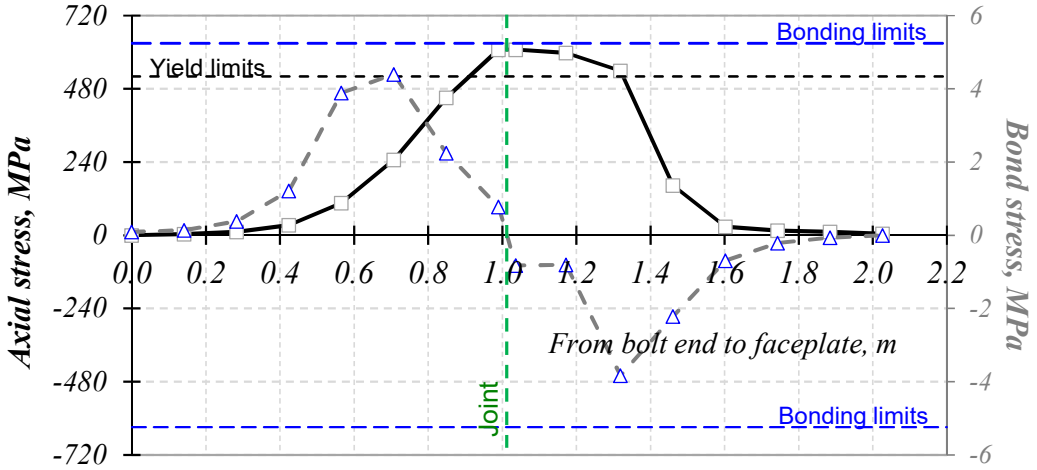

(b) Fully grouted rebar at pullout load of 200 kN

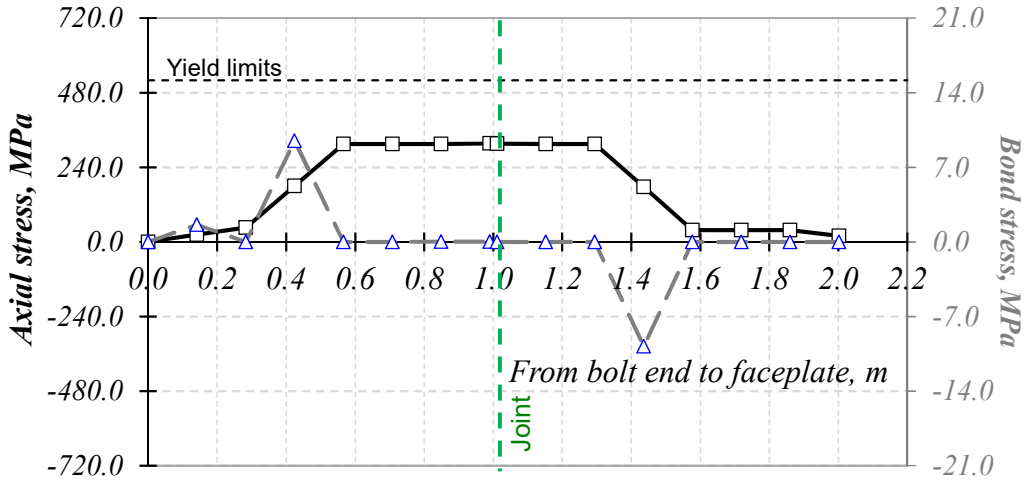

(c) The D-bolt at pullout load of 100 kN

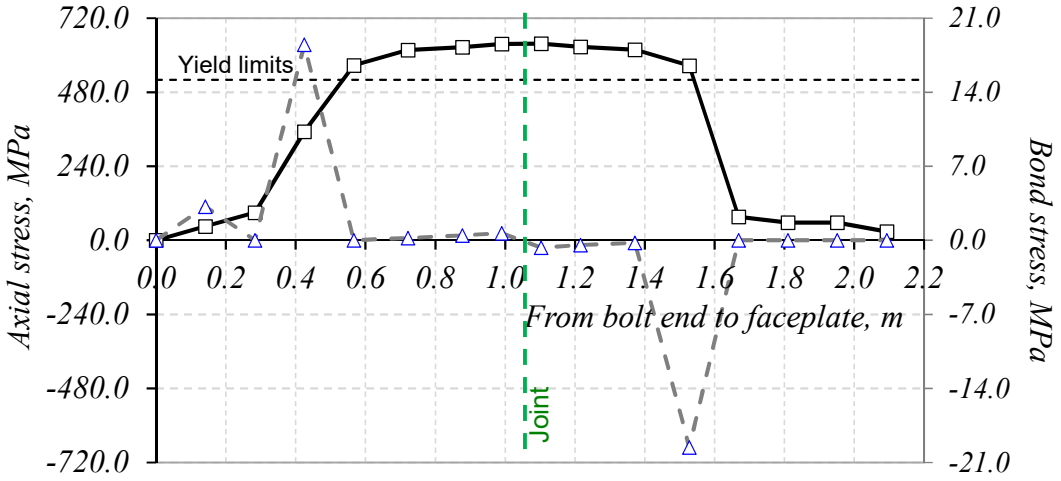

(d) The D-bolt at pullout load of 200 kN

Figure 4-22 Stress distributions along the length of rockbolt models

4.4 Parameters for rockbolt design

Table 2-4 has proposed the main parameters for a rockbolting design. In the following, numerical simulations are conducted to study the influences of the design parameters on the load-displacement of a single rockbolt under pulling/shear condition, such as, the rockbolt type, the embedded length, the installation angles, the rock properties, etc.

4.4.1. 2D-DDA models

As shown in Figure 4-23, a rockbolt gets through two deformable rock blocks. Block B is fixed at the left-side edge and can only deform horizontally by the constrains of vertical rollers. Block A can move horizontally by applying horizontal movement at its right-side edge, or have vertical displacement if there are any vertical movements applied on its top-side edge. The co-edge between blocks A and B is set as a frictionless joint. A fully grouted rebar is simulated using the developed rockbolt model. A faceplate is attached as the right end, while its left end is free to move. The nodes are numbered from the faceplate to the free end as 1 to n (n is varying in the parameter studies according to the different embedded length adopted). The performance of the rockbolt is tested by considering four different embedded lengths conditions, namely, l_0 = 0.5 m, 0.8 m, 1.0m, 1.2 m and 1.6 m. The rockbolt could be pulled if Block A moves horizontally or be sheared at angle β = 90° if Block A moves

vertically. The deformability of two rock blocks are also considered in two conditions, such as E_r = 30 GPa and E_r =0.3GPa. The elastic modulus of the rockbolt material is assumed as E_b = 210 GPa before yielding, E_T = 1 GPa after yielding. The yield force and the extreme plastic strain are 180 kN and 15%, respectively.

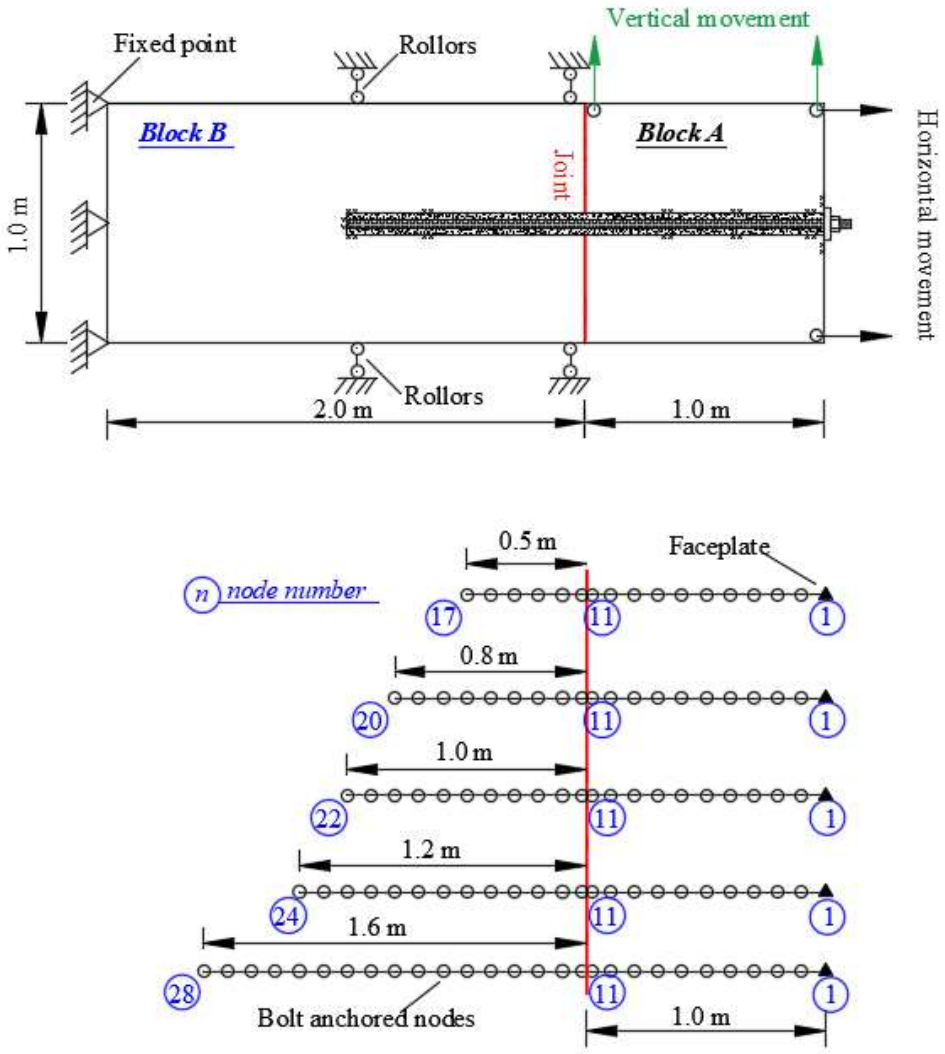

Figure 4-23 2D-DDA model of a rockbolt pullout/shear test

As shown in Figure 4-24, for a rockbolt model with an embedded length of 1.0 m in Block B, the simulated yield pulling force (F_y) and ultimate tensile force (F_{ult}) at the joint are 180 kN and 217 kN, respectively. Block A has been moved 23mm towards right when the rockbolt failed. In the following, the nodal force distributions along the rockbolts are examined to understand the load-displacement curve of the simulated tests.

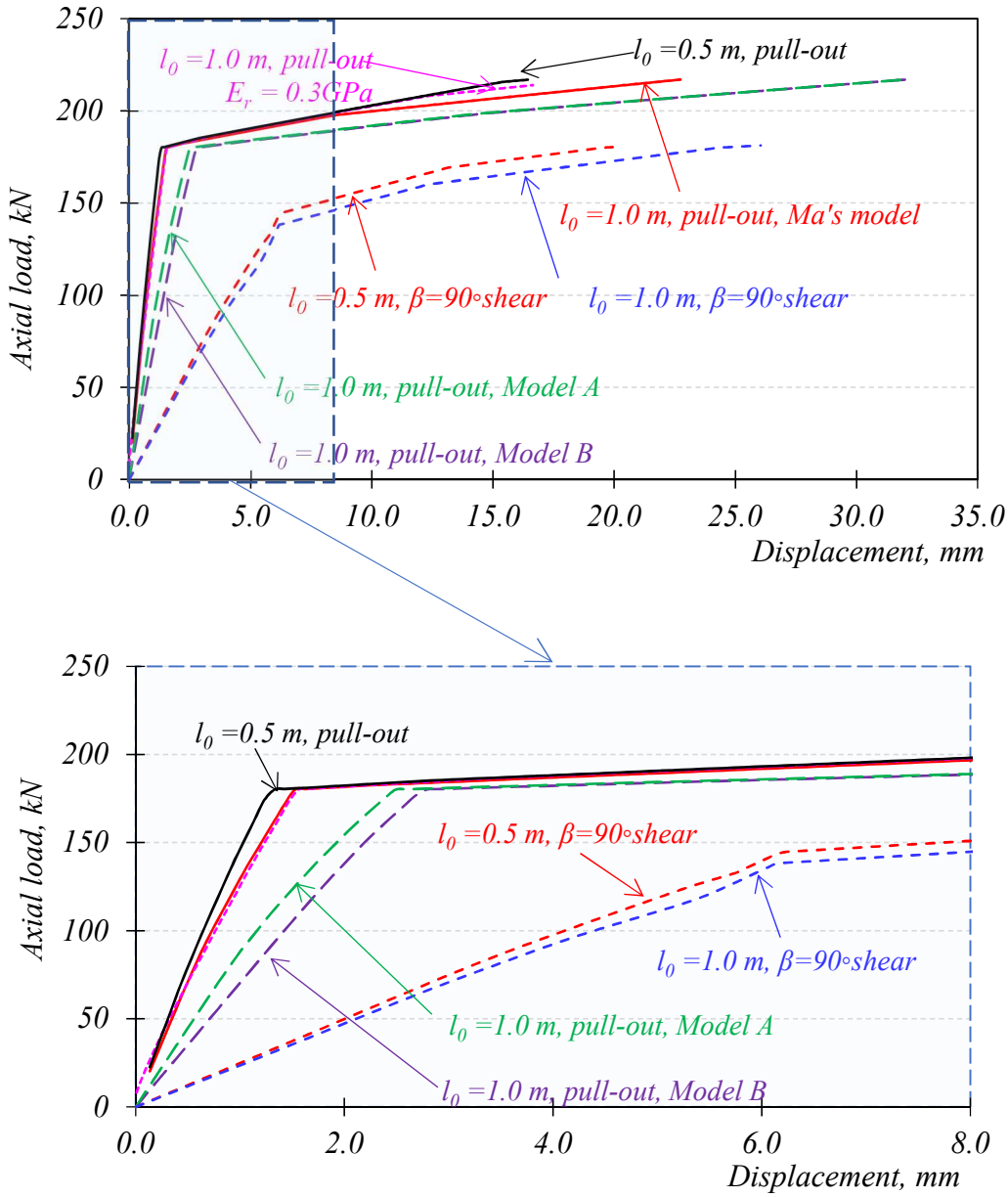

Figure 4-24 Comparisons of the simulated load-displacement curves

4.4.2. Effects of the types of rockbolt

In Chapter 3, the bond-slip model of the rockbolt elements have been studied. In fact, different types of rockbolt element could be represented by using various bond-slip models at the rockbolt and rock interface. Section 4.3.3 has showed an example of the application of the rockbolt model to simulate the fully grouted rebar and the D-bolt. Here, two kinds of fully grouted rebar are adopted to study the influence of the bond-slip models on the load transfer mechanism of a rock/rockbolt system. The two bond-slip models from previous section (see Fig. 3-11(b)) are adopted, including Model A

as the simplified bond – slip model of a rockbolt element with rib angle α = 45°, rib spacing s_b = 17.8 mm and confining pressure p = 2 MPa, and Model B as the bond – slip model of a rockbolt element with rib angle α = 45°, rib spacing s_b = 35.8 mm and confining pressure p = 2 MPa. The bond stiffness of Model B at stage 1 and stage 2 are lower than those of Model A. Both models have the same maximum and residual bond stresses. Another trilinear bond-slip model proposed and verified by Ma et al. (2014) is also included in the simulation (short as Ma's model) for comparison. The bond-slip models are shown in Figure 4-25. For the rockbolt material, the elastic modulus is assumed as E_b = 210 GPa before yielding, E_T = 1 GPa after yielding. The yield force and the extreme plastic strain are 113 kN (≈ 360 MPa) and 10%, respectively.

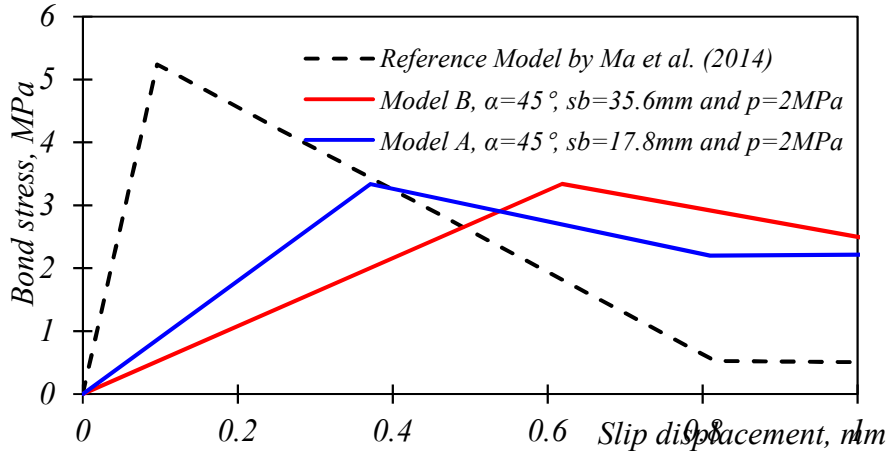

Figure 4-25 Simplified bond-slip models

The obtained axial load versus displacement curves of the pull-out tests are shown in Figure 4-24. All three rockbolt models have similar load capacity in the elastic stage. The rockbolt with Ma's model reaches the yielding point at first, followed by the rockbolt with bond-slip Model A and then that with Model B. Thus, the rockbolt with Ma's model is more rigid than the other two. Considering the deformability of the rockbolt, the simulation result of the rockbolt using Ma's model has the lowest displacement when the rockbolt has broken due to tension. The displacements at the tensile broken of the rockbolts using Model B and Model A are almost the same.

The distributions of the nodal bond stresses along the rockbolt at the pullout loading of 108 kN (0.6 × yielding force) are selected, as shown in Figure 4-26(a), to analyze the load transfer between rockbolt and rock blocks. It can be seen that there are no

decoupling occurs along the rockbolts simulated using Model A and Model B. One decoupled node is found at the rockbolt element near the joint when the rockbolt element is simulated using Ma's model. The nodal bond force distributions of the bonded nodes along the rockbolt could be curve fitted using exponential model $y = A \times \exp(Bx)$ (Li and Stillborg, 1999). The nodal bond force is calculated as the product of bond stress multiplied by the average length of rockbolt element nearby. It shows the smaller the bond stiffness k_1, the larger the values of the parameter A. The exponential models of the nodal axial forces along the rockbolt are presented in Figure 4-26(b). It also shows the parameter A is increasing with decreasing of the bond stiffness k_1. The load transfer capacity along the rockbolt is influenced by the bond stiffness k_1 and the maximum bond strength τ_{max}. The decoupling process will extend inside of the rockbolt if the pull-out loads increases. Before the tension failure, the distributions of the axial forces and the bond stresses along the rockbolt elements are presented in Figure 4-27(a) and (b), respectively. It shows there are 2 decoupled nodes when analyzed using the rockbolt with Ma's model, and 4 decoupled notes when using Model A, and 3 decoupled notes when using Model B. The curve fitting parameters of the exponential models are summarized in Table 4-6, presenting the mechanical coupling at the interface between rock and rockbolt for engineering practice using similar rockbolt elements.

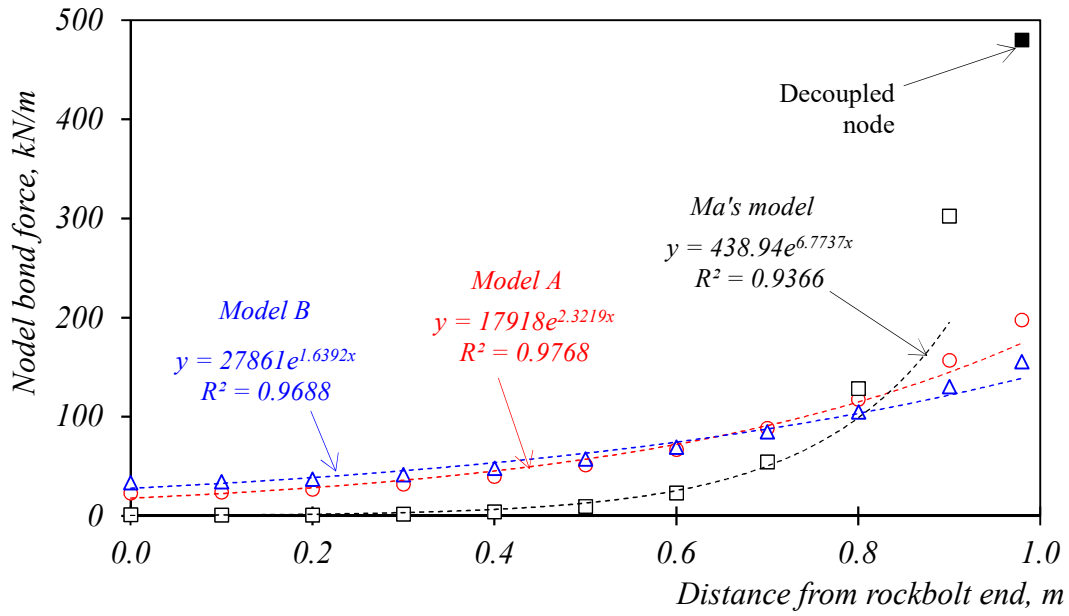

(a)

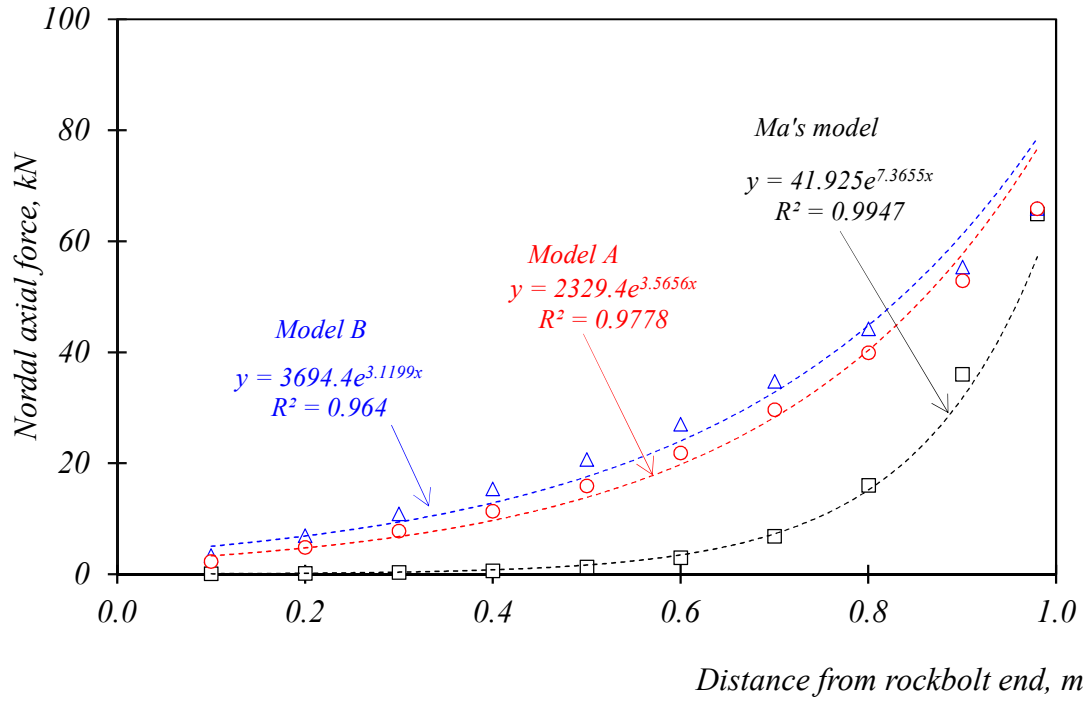

(b)

Figure 4-26 (a) Nodal bond force and (b) nodal axial force along the rockbolts at the pull-out loading of 108 kN

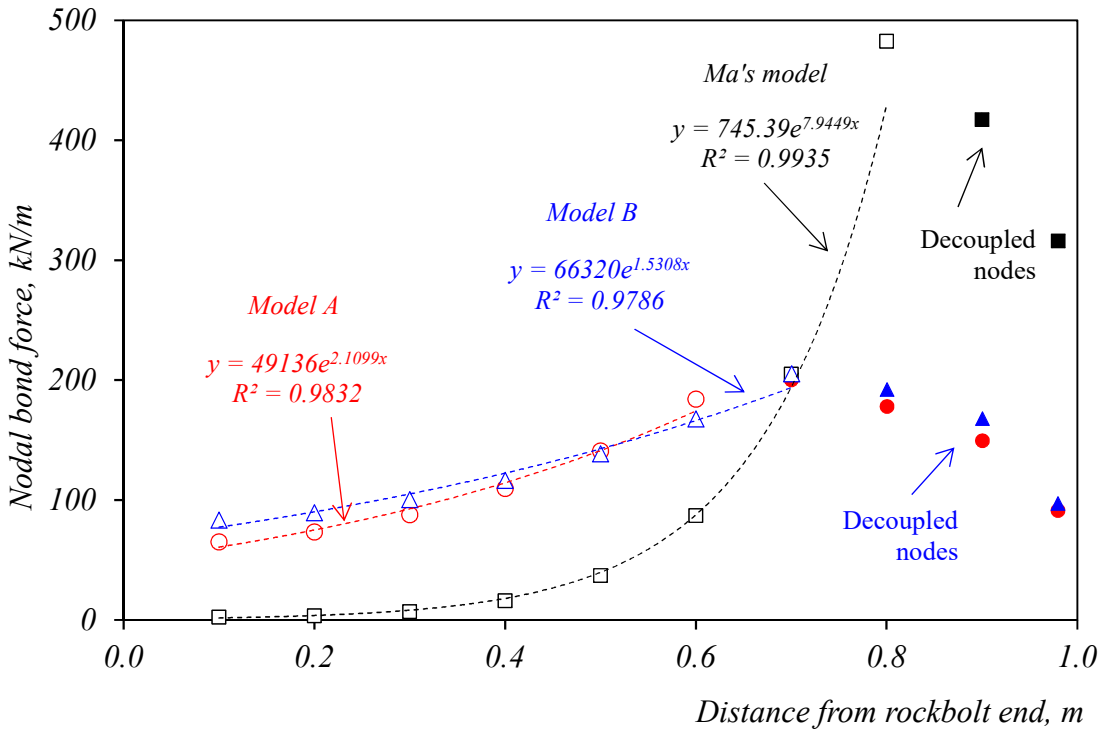

(a)

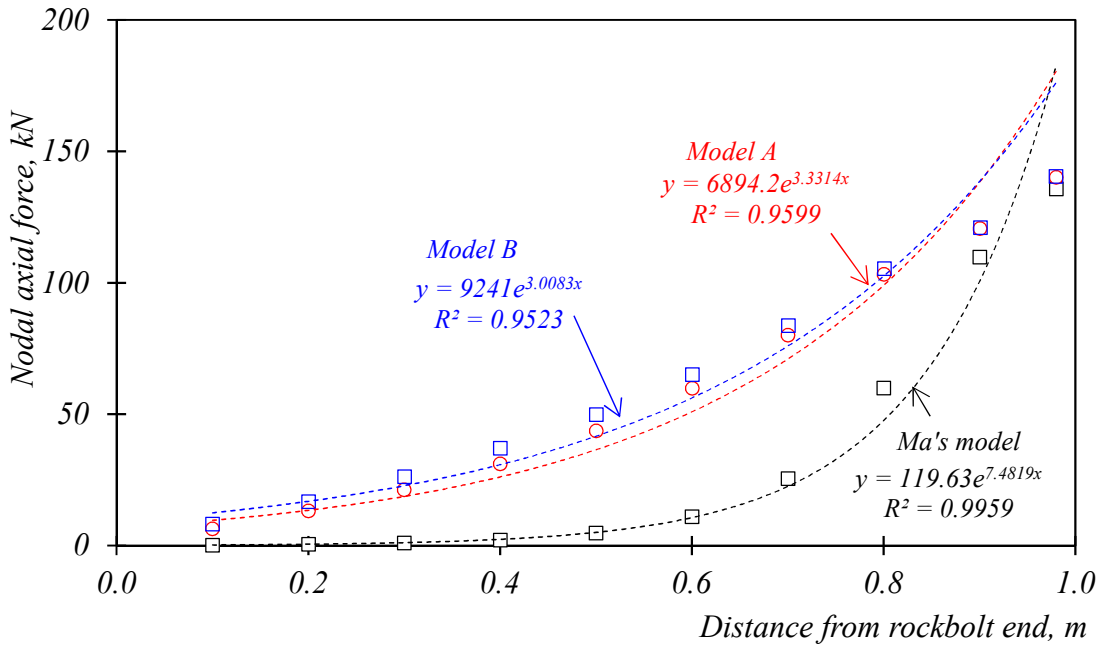

(b)

Figure 4-27 (a) Nodal bond force and (b) nodal axial force along the rockbolts at the extreme loading

4.4.3. *Effects of the embedded length*

The effects of the embedded lengths are examined using the pull-out simulations. Figure 4-24 compares the load-displacement curves in cases of l_0 = 1.0 m and 0.5m. The displacement at tension fail in the case of l_0 = 0.5 m is only 70% of that of l_0 = 1.0 m indicating a reduction in the deformability of the rockbolt if a shorter embedded length is adopted. This could be explained using the nodal axial loading distributions along the rockbolt. Figure 4-28(a) presents the loading conditions when the pullout force is 104 kN. As the head of rockbolt are fixed by a faceplate, there are no much differences in the load distributions along the rockbolt elements in Block A. However, for the rockbolt model with the embedded length l_0 = 0.5 m, all the anchorage points of the rockbolt in Block B are activated, transferring the axial loads through bonds to the rock block B (see Figure 4-29a). When the rockbolt is close to failure, the anchorage points in Block B are easily decoupled at the interface (see Figure 4-29(b)). The bonding conditions of the rockbolts become strong in the case of $l_0 \geq$ 1.2 m. Thus, the reinforcement effort provided by a rockbolt in short embedded length ($l_0 <$ 1.2 m) should be re-estimated.

Table 4-6 Parameters of three bond-slip models and the fitted exponential models

	Items	Ma's model	Model A	Model B
Bond-slip model parameters	Bond stiffness at stage 1, k_1	*54 MPa/mm*	*9.0 MPa/mm*	*5.4 MPa/mm*
	Max. bond strength, τ_{max}	*5.24 MPa*	*3.34 MPa*	*3.4 MPa*
	Bond stiffness at stage 2, k_2	*6 MPa/mm*	*2.6MPa/mm*	*2.2 MPa/mm*
	Residual bond stiffness, τ_{res}	*0.524 MPa*	*2.23 MPa*	*2.28 MPa*
	Bond stiffness at stage 3, k_2	*0.1 MPa/mm*	*0.2 MPa/mm*	*0.2 MPa/mm*
Exponential models: $y = A \times \exp(Bx)$ at pull-out loading = 108 kN	Numbers of the decoupled nodes in Block B	1	0	0
	Bond forces (bonded rockbolt elements)	*A = 438.9*	*A = 17918*	*A = 27861*
		B = 6.774	*B = 2.322*	*B = 1.639*
		$R^2 = 0.937$	$R^2 = 0.977$	$R^2 = 0.969$
	Axial forces	*A = 41.9*	*A =2329.4*	*A = 3694.4*
		B = 7.365	*B = 3.566*	*B = 3.120*
		$R^2 = 0.995$	$R^2 = 0.978$	$R^2 = 0.964$
Exponential models: $y = A \times \exp(Bx)$ at pull-out loading = 108 kN	Numbers of the decoupled nodes in Block B	2	4	3
	Bond forces (bonded rockbolt elements)	*A = 745.4*	*A = 49136*	*A = 66320*
		B = 7.945	*B = 2.110*	*B = 1.531*
		$R^2 = 0.994$	$R^2 = 0.983$	$R^2 = 0.979$
	Axial forces	*A = 119.6*	*A = 6894.2*	*A = 9241*
		B =7.482	*B = 3.331*	*B = 3.008*
		$R^2 = 0.996$	$R^2 = 0.960$	$R^2 = 0.952$

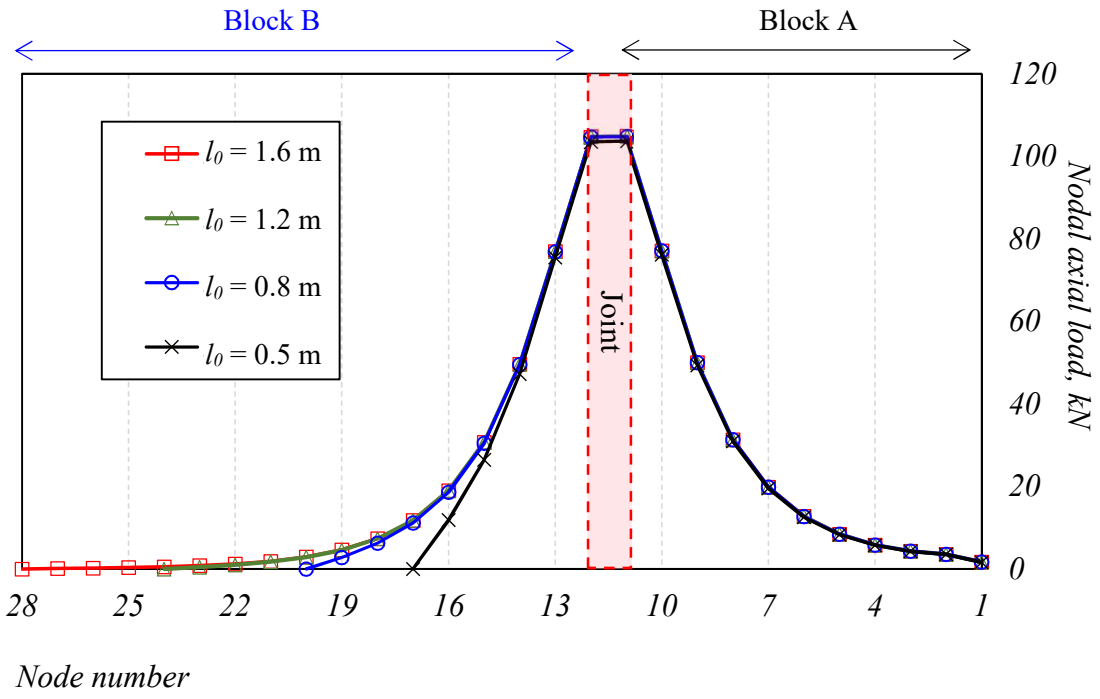

(a)

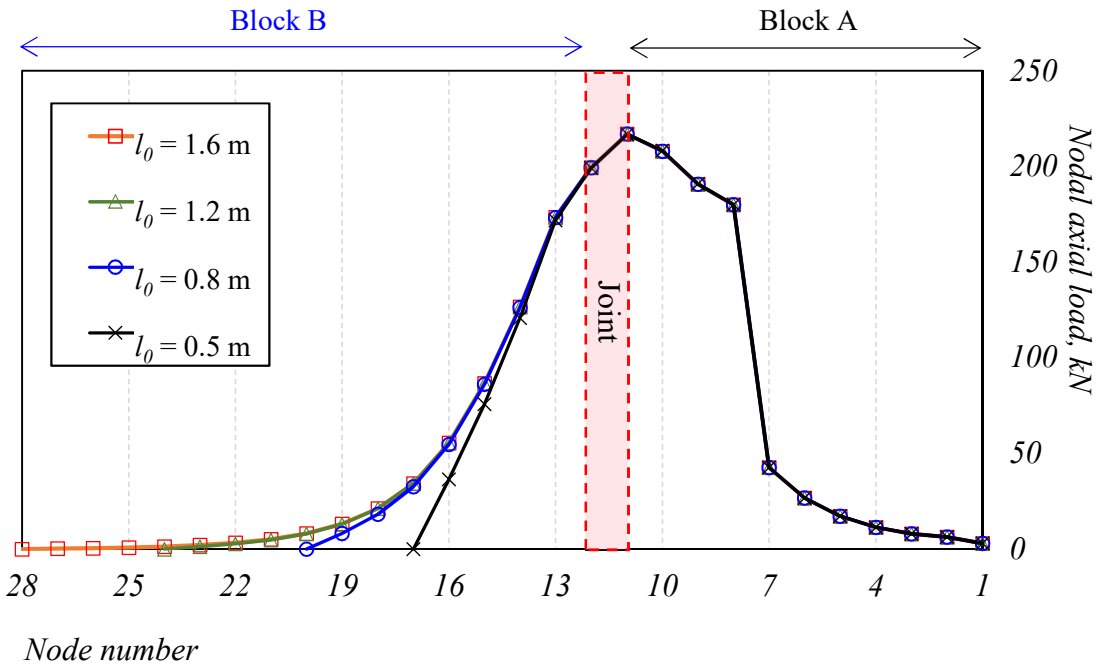

(b)

Figure 4-28 Simulated nodal axial loads along the rockbolt models when the tensile loads at joint are (a) 60% of F_y and (b) F_{ult}

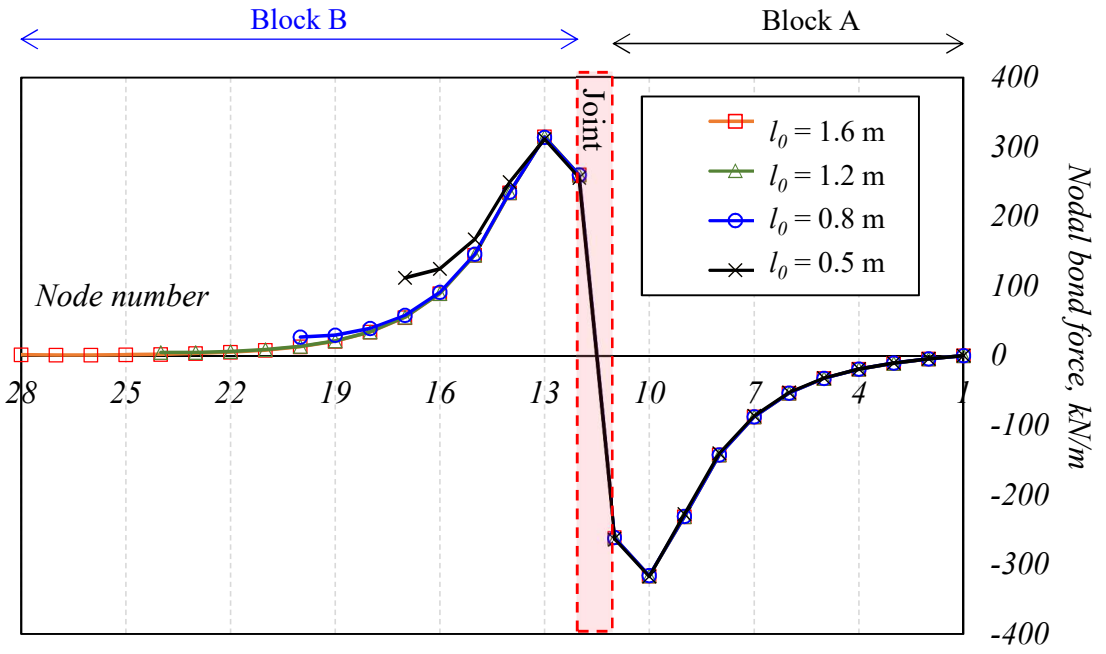

(a)

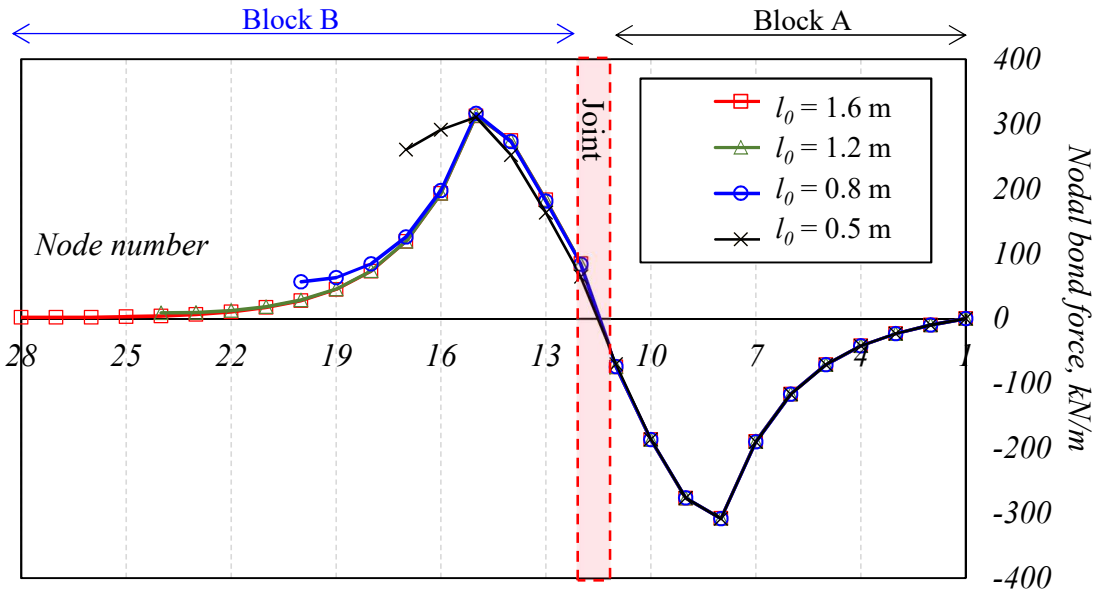

(b)

Figure 4-29 Simulated nodal bond forces along the rockbolt models when the tensile loads at joint are (a) 60% of F_y and (b) F_{ult}

4.4.4. Effects of the shear angle

The deduction of the load carrying compacity during shearing is mainly due to the combination work done by the axial load and shear load at the joint, as discussed in Section 4.3.2. By examining the nodal axial loads along the rockbolt, the load distributions are almost the same as shown in Figure 4-28(a) and Figure 4-30(a) when the rockbolts are behaving in elastic. However, the maximum axial load is observed at an inner element from the joint in shear test when the rockbolts are yield. Compared with Figure 4-28(b) and Figure 4-30(b), the axial load at the node at the right of the joint is reduced significantly, and much less reinforcement could be provided by the relative rockbolt element under shear conditions.

4.4.5. Effects of the rock deformability

The main reason why the deformability of a rockbolt reduces in soften rock mass comes from the contribution of deformation in rock blocks. As shown in Figure 4-31, at the initial loading, the deformation occurs in the movable rock block causing a uniformly distributed axial stress along the rockbolt in Block A. At the same time, the embedded end of the rockbolt is slightly loaded. Once the joint opens, the axial load of the rockbolt at the joint starts to concentrate and activates the anchorages at the embedded end. The failure occur at the joint, but compared with the axial load distribution of rockbolt in rock mass with E_r = 30 GPa, the deformability of rockbolt reduces due to the initially deformation with the deformable rock blocks whose E_r = 0.3 GPa (see Figure 4-24).

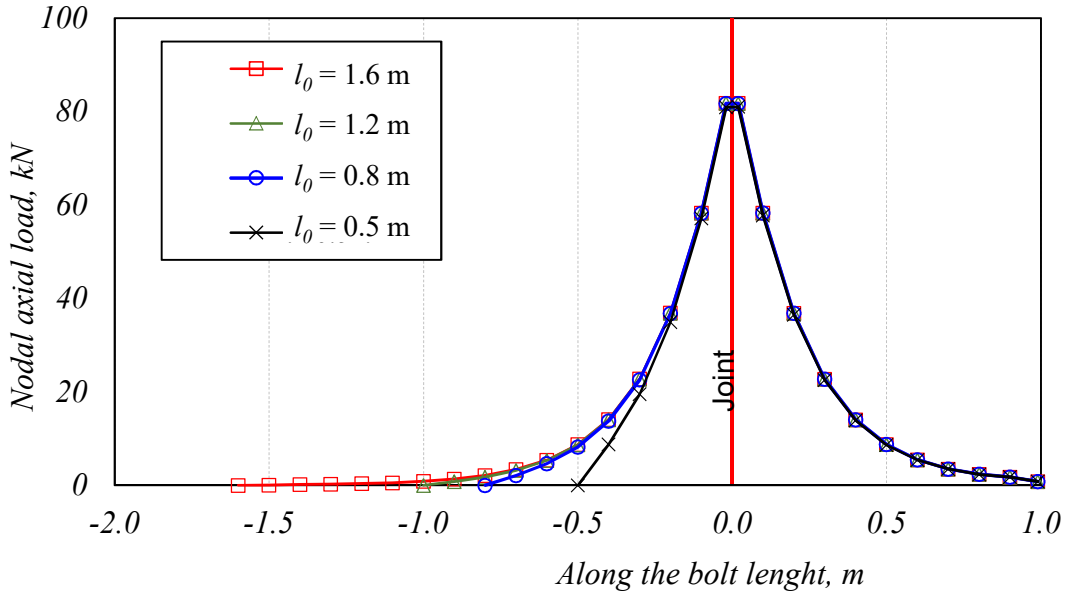

(a)

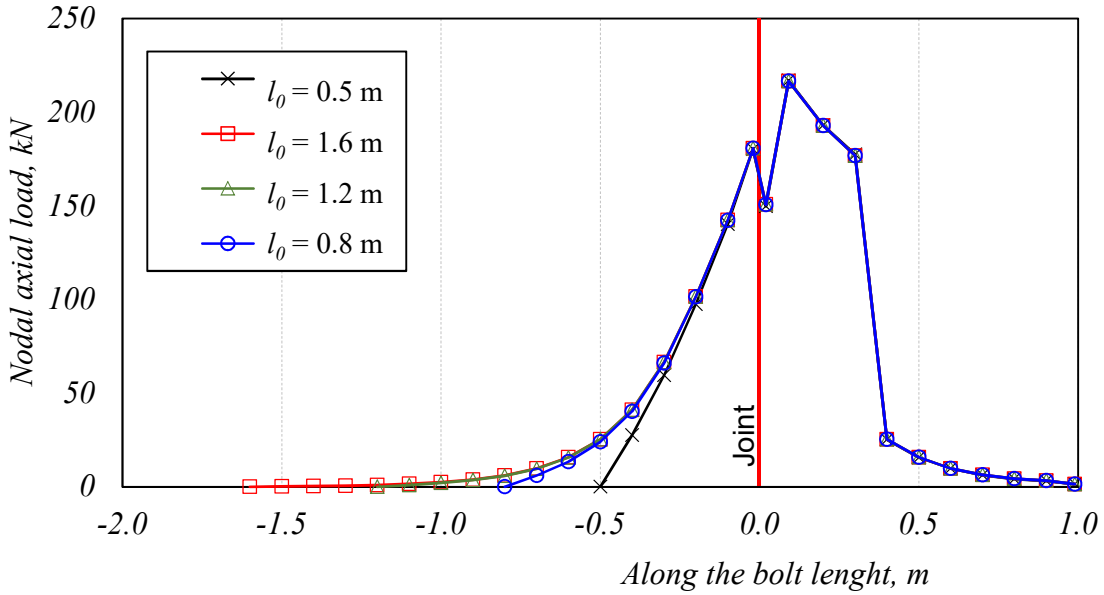

(b)

Figure 4-30 Simulated nodal axial loads in the shear tests of rockbolt with shear angle $\beta = 90°$ when the loads at joint are (a) 60% of F_y and (b) F_{ult}

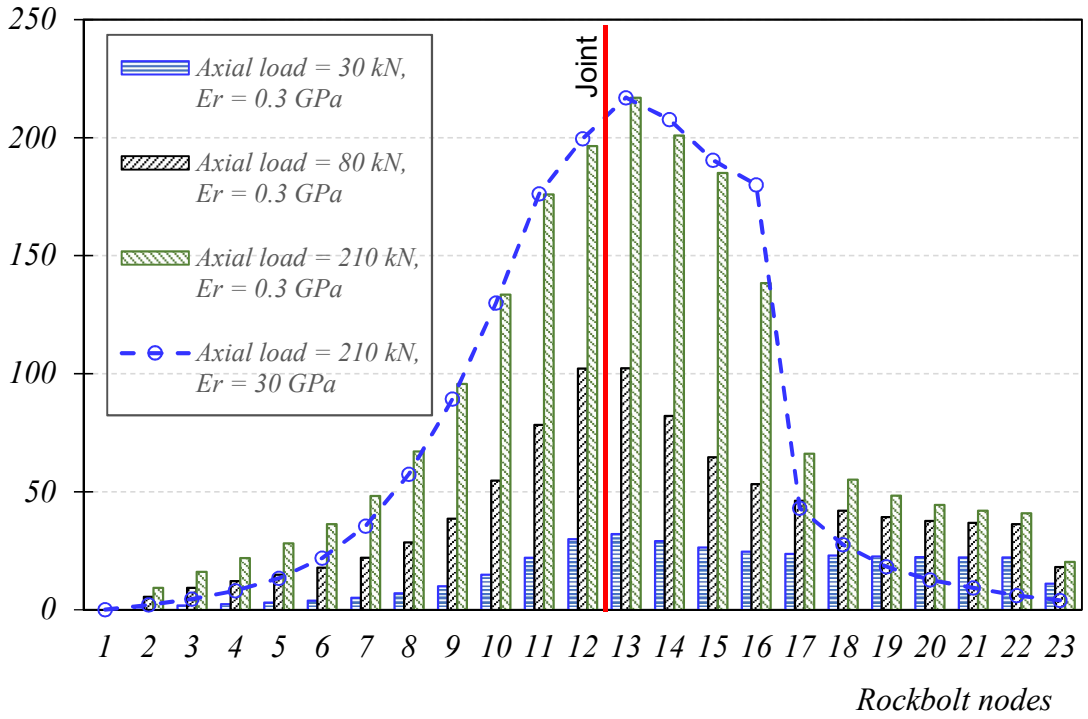

Figure 4-31 Axial loads variations in case of deformable rock blocks

4.5 Conclusions

In this chapter, a rockbolt model is developed in 2D-DDA based on the load transfer theory. A rockbolt is divided into several segments according to rock block boundaries. Each segment has a number of rockbolt elements. Three major behaviours of rockbolts, including axial behaviour, bonding behaviour and shear behaviour, are considered in this model. By varying these three major behaviours, different kinds of rockbolt could be simulated.

To integrate the rockbolt model under 2D-DDA frame work, several sub-functions are developed. The rockbolt applies their restrains as point loads in the system. There will be limited or no restrains if the rockbolt is yielding or failed. In such a way, the rockbolt could be installed in groups at different times/steps.

In summary, the proposed rockbolt models could present four major failure modes of rockbolt, i.e., decoupling along the interface, tensile failure, faceplate failure and shear failure. Verifications of the proposed rockbolt model have been carried out.

(1) The bond behaviour is verified using pullout tests. The simulation results show good agreements between the proposed rockbolt model and experiments results. The rockbolt model can reveal the decoupling along the interface, tensile failure of rockbolt elements, faceplate failure under pulling out load.

(2) By comparing with shear tests, the simulation results show reasonable agreements in the reduction of reinforcement effects. The shear failure of the rockbolt element at joint are presented.

(3) The axial behaviour is verified using pullout tests results. Two types of rockbolts are simulated under pullout condition. The simulated load-deformation curves show good agreements with the experimental ones. It also confirms the larger deformability of the D-bolt compared with the fully grouted rebar as a result of equally loaded rockbolt elements between special anchored nodes.

(4) Based on the above verifications, it can be concluded that the rock-rockbolt reaction could be simulated with the proposed rockbolt model. In the following chapter, these verified rockbolt models are adopted to simulate rock-rockbolt interaction in various rock conditions.

(5) The bond-slip model controls the load transfer between rock and rockbolt. By fitting the nodal axial forces and nodal bond force distributions along the rockbolt using the exponential model, the results show the parameters of the exponential models are heavily influenced by the bond stiffness k_1 and the maximum bond strength τ_{max}. The curve fitting parameters of the exponential models can be used for engineering practice under similar conditions.

(6) Using the given bond-slip models in the previous studies, parameter studies show that the anchorage the rockbolts become strong enough for the case of $l_0 \geq 1.2$ m. On the other hand, the reinforcement effort provided by a rockbolt with a short-embedded length ($l_0 < 1.2$ m) should be re-estimated.

(7) The installation angle will influence the load-displacement of a rockbolt as the combination work done by the axial load and shear load at the joint may reduce the load carrying compacity of the rockbolt.

CHAPTER 5. SIMULATION OF THE REINFORCED ROCK UNIT IN JOINTED ROCK MASS

The load carrying capacity of a rockbolt can be evaluated using reinforced rock unit (RRU). Generally, the RRU is a model considering the rockbolt as a suspension device transferring loads in rock strata. In jointed rock mass, the RRU has to be considered with regards to the loading scale and the condition of rock mass discontinuities. In this chapter, a parametric study has been carried out using the newly developed rockbolt element in 2D-DDA. The results are used to the estimation of RRUs in jointed rock mass and the corresponding loads in rockbolt element.

5.1 Introduction

The reinforced rock unit model is a modified rockbolt suspension theory by considering the rockbolt as a suspension device transferring the weight of the weaker rock strata to the stronger strata. As the rock at the end of the rockbolt may be fractured, the rockbolt can only influence the rock mass located between the fracture plane and the head of rockbolt (Li, 2006). This part of the rock is often called Reinforced Rock Unit (RRU) (Lang and Bischoff, 1982; Choquet and Hadjigeorgiou, 1993). A typical example for a rockbolt to supply local support in homogeneous rock mass is shown in Figure 5-1. The boundary of the RRU of the rockbolt is usually assumed in a cone shape with the apex angle of β, which is also denoted as the reinforcement angle (Hobst and Zajíc, 1983; Nie et al., 2016). The maximum axial stress of the rockbolt is determined by the properties of rock mass and the installation method as shown in Table 5-1. For the rockbolt installed in a homogeneous rock mass in line grid with spacing of S, see Figure 5-1b, the maximum axial stress of the rockbolts is also influenced by the interaction between rockbolts as summarized in Table 5-1. Calculation methods for maximum axial stress

of the rockbolts installed in squared grid with spacing of *S*, see Figure 5-1c, are summarized in Table 5-1. For the rockbolt installed in the irregular and dense irregular jointed rock mass, the properties of joints also influence the maximum axial stress of the rockbolt, see Table 5-1. However, to the best knowledge of the author, there are still not enough studies to analyse the relationships between fully grouted rockbolt and jointed rock mass.

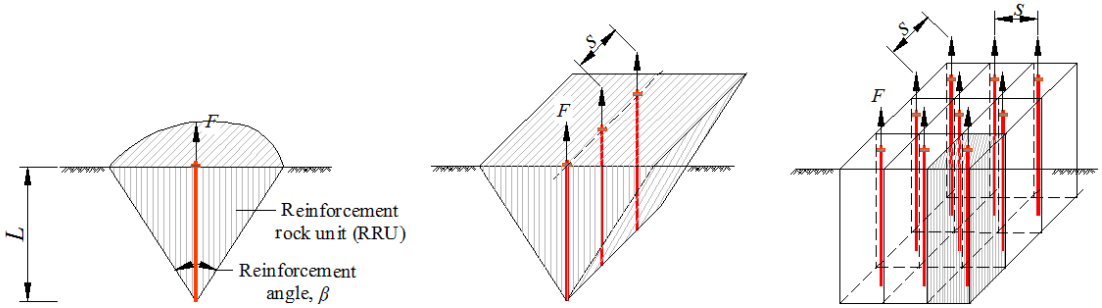

(a) RRU of a rockbolt (b)RRU of a line of rockbolts (c) RRU of rockbolt grid

Figure 5-1 Sketches of RRUs of rockbolts in homogeneous rock mass (after Hobst and Zajic, 1983)

Table 5-1 The maximum axial stress of the rockbolt installed in different rock mass (modified after Hobst and Zajìc, 1983)

Type of Rock Mass	Single rockbolt	Line Grid	Square Grid	Notes
Homogeneous	$\sigma = \frac{\sqrt{2}\pi\tau_{ult}L^2}{s_f A}$	$\sigma = \frac{2\sqrt{2}\tau_{ult}SL}{s_f A}$	$\sigma = \frac{4\tau_{ult}LS}{s_f A}$	$\beta = 90°$
Irregular jointed	$\sigma = \frac{\pi\gamma L^3 \tan^2\varphi}{3 s_f A}$	$\sigma = \frac{S\gamma L^2 \tan\varphi}{s_f A}$	$\sigma = \frac{\gamma L S^2}{s_f A}$	$\beta = 2\varphi$
Dense irregular jointed	$\sigma = \frac{\pi\sigma_h L^2 \tan^2\varphi}{3 s_f A}$	$\sigma = \frac{S\sigma_h L \tan\varphi}{s_f A}$	$\sigma = \frac{4S\sigma_h L \tan\varphi}{s_f A}$	$\beta = 2\varphi$
Note:	τ_{ult} – shear strength of rock mass; φ – the friction angle of discontinuity; σ – maximum axial stress of the rockbolt; σ_h – lateral field stress; L – the rockbolt length; s_f – the safety factor; A – the area of rockbolt cross-section; S – the spacing of the rockbolt.			

5.2 2D-DDA model

Numerical analyses have been conducted to analyse the performance of a single rockbolt installed in a jointed rock mass. The numerical model used in 2D-DDA software is shown in Figure 5-2. The rock mass is 2.5 m deep and 10 m wide with grid of rock blocks size in 0.1 × 0.1 m^2. The left, right and bottom boundaries of the rock mass are fixed in a rigid box. Two joint sets are dominant in the model. The primary joint set is persistent to simulate the continuous joints or rock laminations with dip angle of α, and the second joint set is non-persistent and perpendicular to the primary one. The rock block is simulated as a linear elastic material with density of 2600 kg/m^3, Young's modulus of 0.3 GPa and Poisson's ratio of 0.25. All the joints follow the Mohr-Coulomb law with friction angle of 20° and cohesion of zero.

The rockbolt is 1.0 m long and fully embedded into the rock mass. The rockbolt is divided into several segments according to the block boundaries. A rigid block, as block *A* shown in Figure 5-2, with a height of 0.1 m and a width of 0.2 m are attached on the head of the rockbolts to simulate the faceplate and apply pullout loads. The details of the parameters used in the 2D-DDA model are summarized in Table 5-2. The numerical analyses are divided into three steps. The first step is to build the initial equilibrium between the gravity and deformation of rock blocks. The second step is to install the rockbolt into the rock mass in the designed positions. The third step is to apply pullout loads onto the faceplate with a constant speed of 1 mm/s.

Table 5-2 Parameters used in 2D-DDA to simulate the pullout test

Item	Parameter	Value	Item	Parameter	Value
DDA setting	Dynamic factor	static	Bolt	Diameter, d_b (mm)	32
	Step max. displacement ratio, g_2	0.001		Tangent modulus, E_T (GPa)	4.2 (≈E_b/50)
	Upper limit of time interval, g_1	0.0005		Yield strength, σ_Y (MPa)	360
	SOR factor	1.4		Extreme strain, ε_{ext} (%)	1.6
	Normal contact spring stiffness, k_n (N/m)	3×10^7		Maximum shear strength (Pa)	5.24e6
	k_n/ k_s	2.5		Residual shear stress (Pa)	0.524e6
	Block unit weight, $\times10^3$ kN/m^3	26		Sliding bond node, k_3 (Pa/m):	1e5

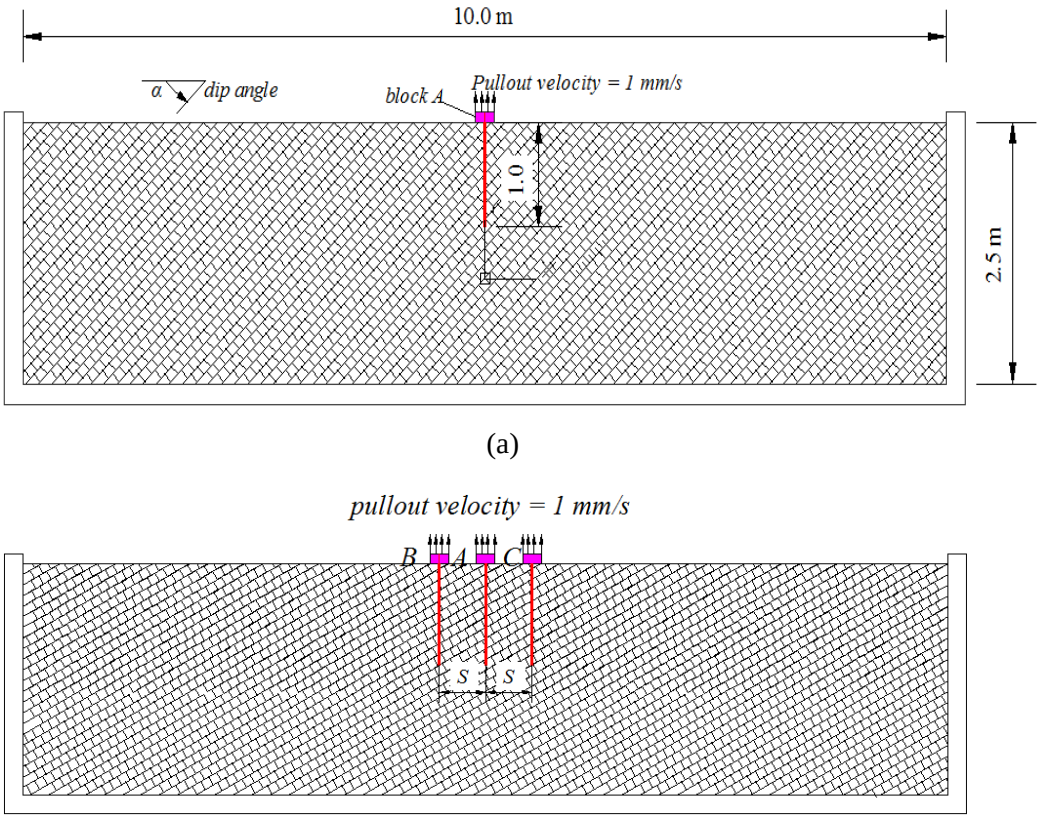

Figure 5-2 DDA models of pulling rockbolt

5.3 RRU of single rockbolt

5.3.1. Influence of the joint orientation

Five jointed rock mass models containing the primary discontinuous with dip angles α = 0°, 30°, 45°, 60° and 90° are used in the simulation to investigate the influences of the joint orientations to the rockbolt. The pullout resistances versus displacements of rockbolt curves are plotted in Figure 5-3. For the rock model with primary joint dip angle α = 0°, the pullout resistance increases substantially before pullout resistance of 21.5 kN with respect to the increasing of displacement. Here, the threshold is denoted as the critical pullout resistance when rockbolt displacement reaches 1 mm as the increase ratio of pullout load with displacement becomes smaller after that. With the increase of dip angle from 0° to 45°, the critical pullout load increases from 21.5 to 41 *kN*. However, when dip angle increases to 90°, the critical pullout resistance decreases to 5.8 kN. This implies that the pullout resistances are heavily affected by the discontinuities of jointed rock mass.

The simulated displacement contour maps of the jointed rock blocks are summarized in Table 5-3. The RRU region was determined as the rock domain which were moved with the rockbolt continuously. The displacements of rockbolt faceplate U_A are 5, 10 and 20 mm, respectively. For rockbolt displacement U_A = 5 mm, only surrounding rock blocks are moved together with rockbolt. With the increase of the rockbolt movement, more rock blocks are moved together with rockbolt, see U_A = 10 mm. The RRUs are heavily influenced by the joint orientations and featured with triangular cross sections. For the rock model with primary joint dip angle α = 0°, the RRU has a reinforced angle β = 53° and the RRU area s = 0.495 m^2. With the increase of dip angle α, the area of RRU increase to the peak values s = 1.009 m^2, when α = 45°. For dip angle α increasing from 45 to 90°, the reinforcement angle β is decreased from 90° to 0° and the RRU area changes from 1.009 to 0.100 m^2.

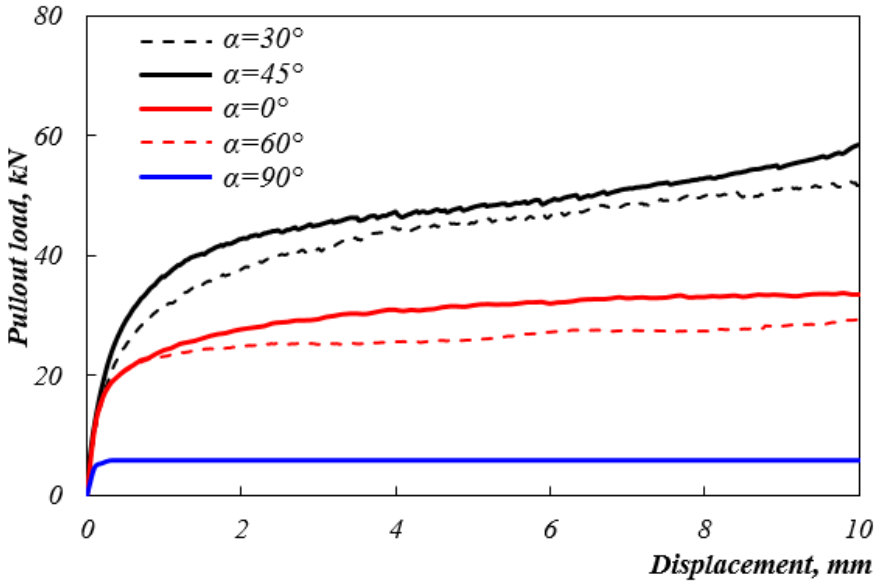

Figure 5-3 Effects of the rock joint orientations on the pullout resistance of rockbolt (for E_r = 0.3 GPa, φ = 20°, L = 1.0 m and α = 0˚, 30˚, 45˚, 60˚ and 90˚, respectively)

These observations can be explained by the load transfer process between the rockbolts and the rock blocks. Figure 5-4 shows the contour of the major principal stresses of the rock blocks when the faceplate was pullout 10 mm from the original place. To reduce the influence from the initial principal stresses induced by gravity σ_0, the major principal stresses σ_1 are normalized as σ_1/σ_0 in the contour maps where a warmer colour represents

a larger increasing ratio and a cooler colour presents a larger decreasing ratio. The contour of the major principal stress for the rock mass with the dip angle α = 0° is symmetric along the rockbolt axis because the rock structures are symmetric. There are increasing transverse stresses in the adjacent rock blocks resulting from the compressions in RRU. For the rock mass with dip angles α = 30°, 45°, and 60°, the rock blocks along the persistent joint or lamination direction (right sides of rockbolts in Figure 5-4(b) – (d)) have slightly smaller changing ratios than those along the non-persistent one (left sides of rockbolt in Figure 5-4(b) – (d)) because of the influence from the asymmetry rock orientations. For dip angle α = 90°, the RRU is in a column and disturbs little amount of rock blocks nearby as shown in Figure 5-4(e).

Table 5-3 Displacement contours in rock blocks during rockbolt pullout process

α	U_A = 5 mm	U_A = 10 mm	U_A = 20 mm	RRU
0°	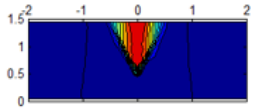	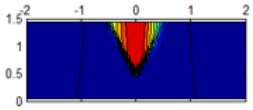	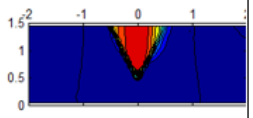	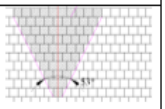 β = 53° s = 0.495 m^2
30°	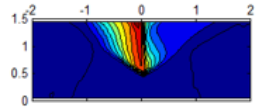	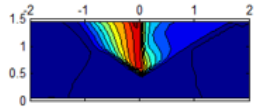	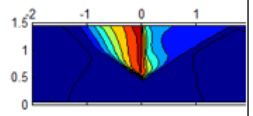	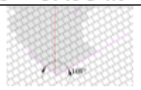 β = 108° s = 0.725 m^2
45°	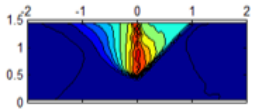	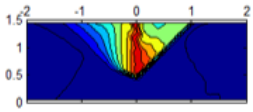	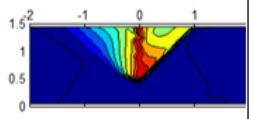	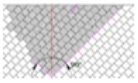 β = 90° s = 1.009 m^2
60°	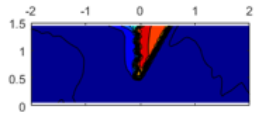	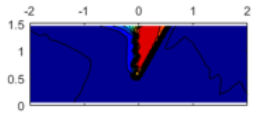	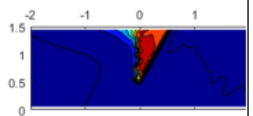	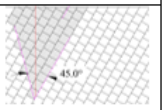 β = 45° s = 0.353 m^2
90°	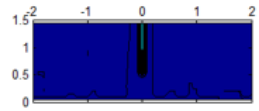	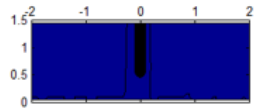	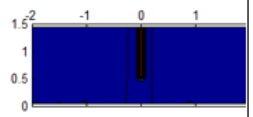	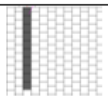 β = 0° s = 0.100 m^2
Contour unit: mm		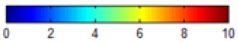	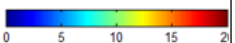	

The upward deformation of ground surface during the pullout process of rockbolt is shown in Figure 5-5 where *x*-coordinate is the distance from rockbolt and *y*-coordinate is the upwards displacement of the rock blocks. Generally, the upward deformation of

ground surface increases with respect to pullout distance U_A. The rock block at the surface of rock mass with $x = 0$ has the same magnitude as U_A because it is grouted to the rockbolt. For the case of $\alpha = 0°$, the surface movements of the rock mass are symmetrically distributed along the axis of the rockbolt as shown in Figure 5-5(a). The ground surface has small deformation when $|x| > 0.5$ m. The influence range of the rockbolt on the upward deformation of the ground surface is about 2.0 *m*. For the rock mass with the dip angle $\alpha = 30°$, 45°, and 60° as shown in Figure 5-5(b) – (d), respectively, the deformations of ground surface are not symmetric but dependent on the angle between the rockbolt and the persistent joint. For the rock mass with the dip angle $\alpha = 90°$ as shown in Figure 5-5(e), the deformation of the ground surface is limited to the rock blocks where the rockbolt was penetrated through.

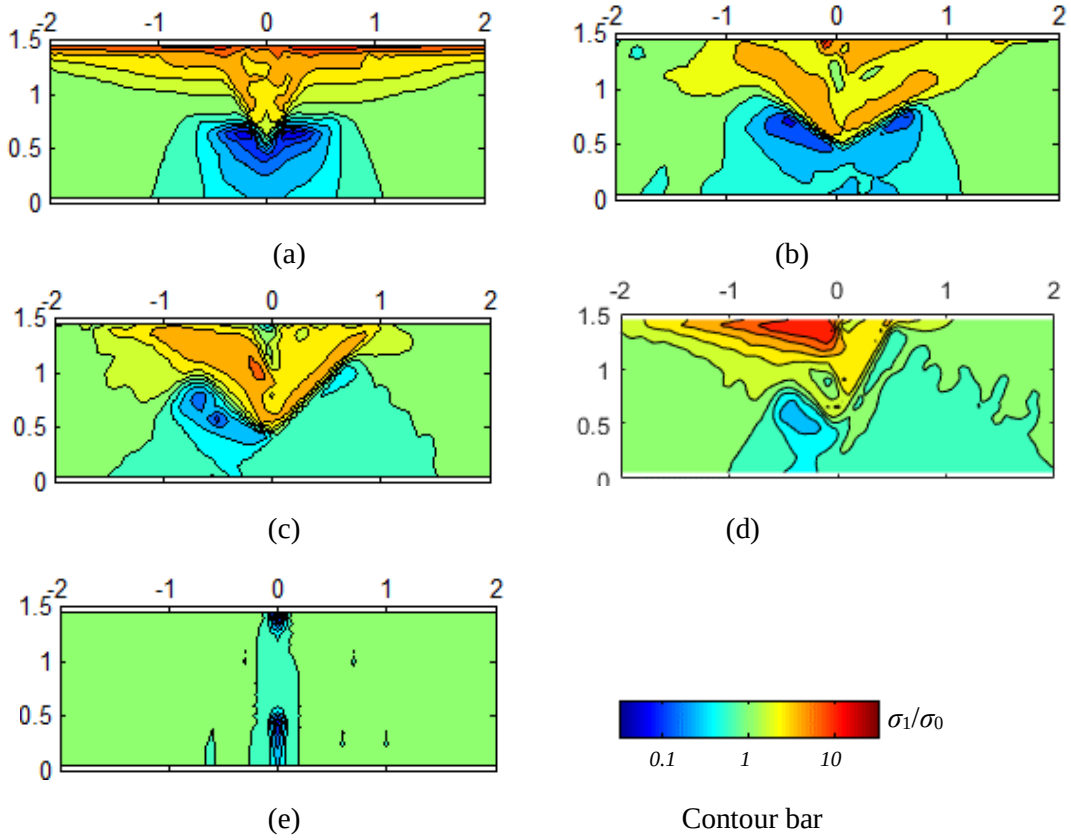

Figure 5-4 Contours of normalized major principal stresses σ_1/σ_0 in rock mass for U_a = 10 mm, E_r = 0.3 GPa, $\varphi = 20°$, L = 1.0 m and (a) $\alpha = 0°$, (b) $\alpha = 30°$, (c) $\alpha = 45°$, (d) $\alpha = 60°$, and (e) $\alpha = 90°$

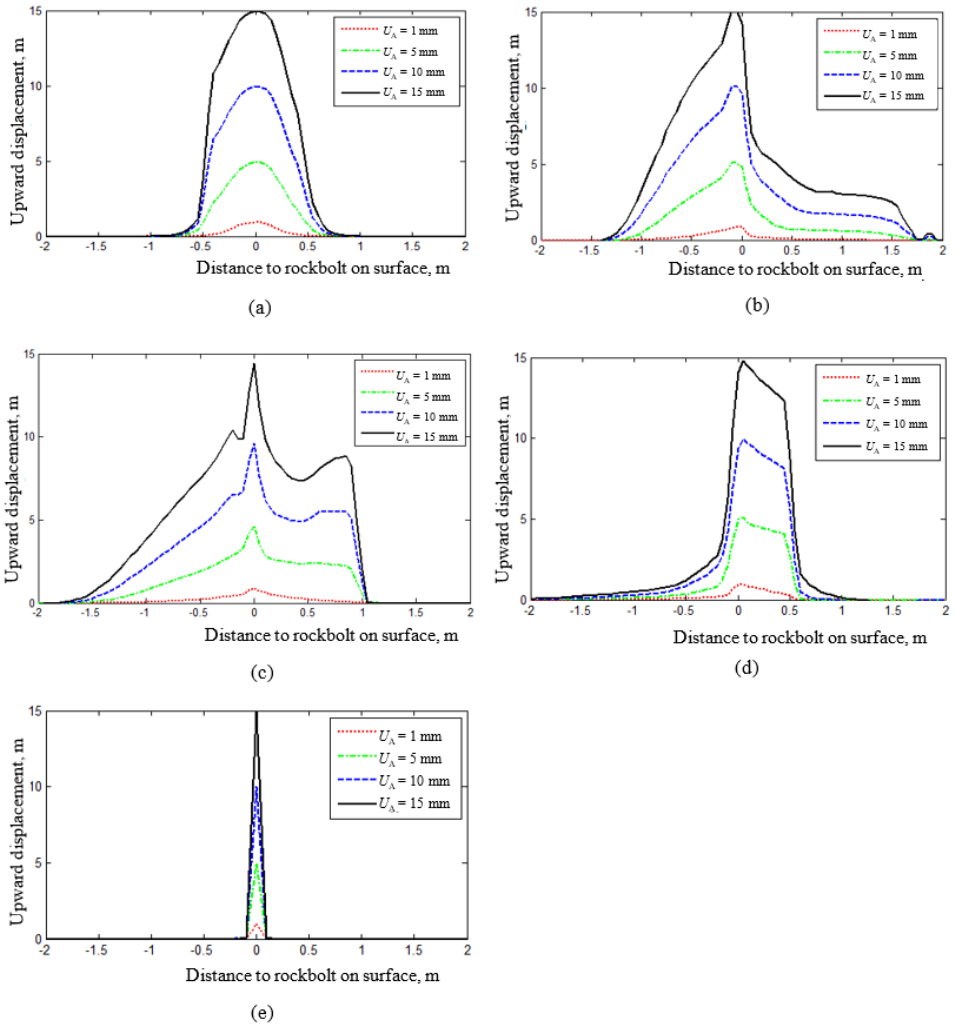

Figure 5-5 Deformation at the rock surface during the pullout process of rockbolts for E_r = 0.3 GPa, φ = 20°, L = 1.0 m and (a) α = 0°, (b) α = 30°, (c) α = 45°, (d) α = 60°, and (e) α = 90°

5.3.2. *Influence of the friction angle and Young's modulus of rock mass*

In order to evaluate the influence of frictional angle on the area of RRU and the axial load carrying capacity of the rockbolt, cases with the friction angle of 20° and 40° are analyzed using 2D-DDA. The other basic parameters are the same as those discussed in Section 5.3.1. Figure 5-6(a) shows the variation of the RRU areas with respect to the dip angle of rock mass. The ratios of increase of the RRU areas are 14%, 23%, 6% and 9% for the dip angles α = 0°, 30°, 45° and 60°, respectively. However, for the dip angle of 90°, the effects of the friction angle on the areas of RRU are limited. Similar observations are also obtained when comparing the results of axial loads of rockbolts as

shown in Figure 5-6(b). To evaluate the inflluence of elastic modulus of rock mass on the area of RRU and the axial load of rockbolt, cases with the elastic modulus of rock mass of 0.3 and 30 GPa and friction angle of 20° are analyzed using the numerical method. The RRU areas and axial load carrying capacity of rockbolt versus dip angles plots are shown in Figure 5-6(a) and (b), respectively. It can be seen that the ratios of increase of the RRU areas are less than 10% for the dip angles ranging from 0° to 60°, and zero for dip angle α = 90°. Similar observations are also obtained for the axial load carrying capacity of rockbolts as shown in Figure 5-6(b). It can be concluded from this parametric study that the increase of friction angle and elastic modulus of the rock mass can increase the axial load and RRU area of rockbolt, especially for the low-angle laminated rock blocks, such as the dip angle ranging from 0° to 45°.

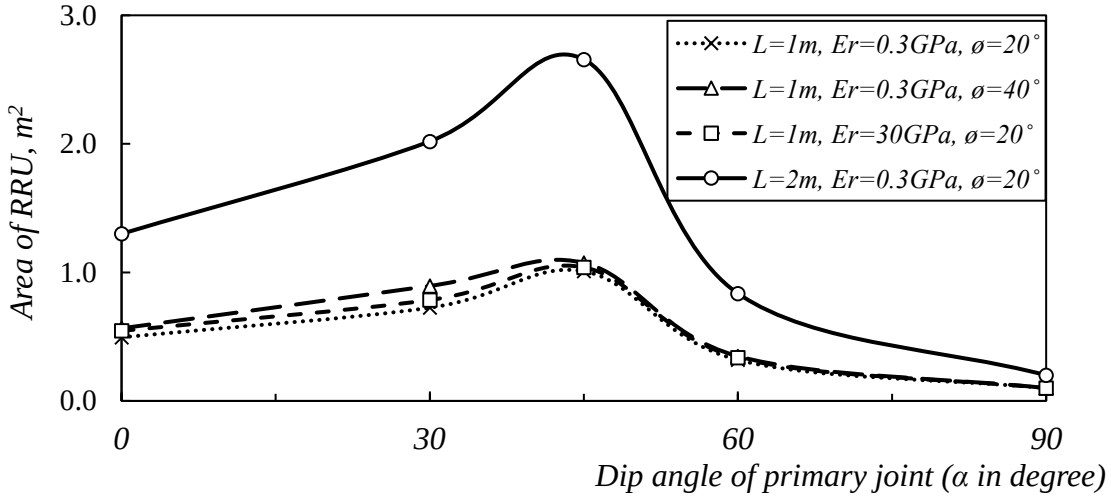

(a) Area of RRU

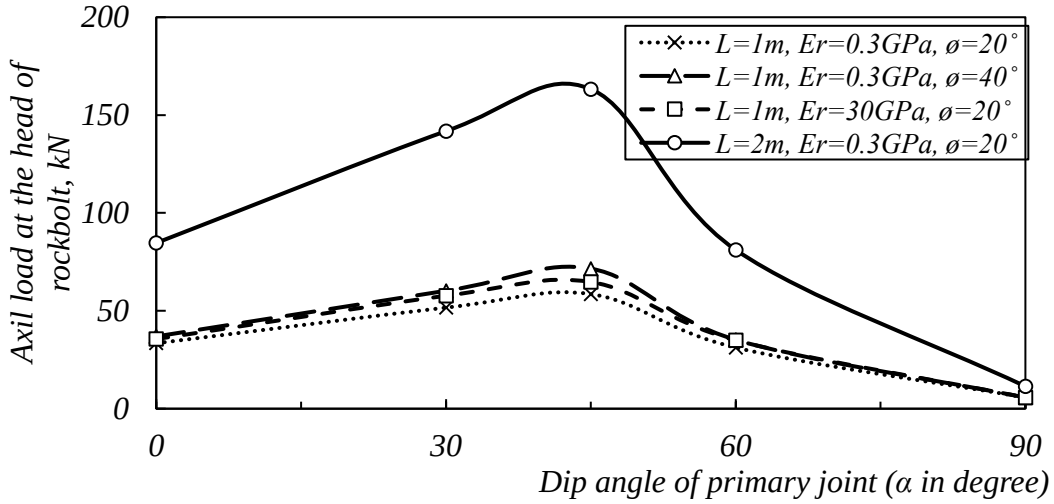

(b) Axial load on the head of rockbolt

Figure 5-6 Parametric studies on the key influence parameters

5.3.3. Influence of the rockbolt length

The rockbolts with their lengths of 1 and 2 *m* installed in rock mass with the elastic modulus of 0.3 and 30 GPa and friction angle of 20° are analyzed. Figure 5-6(a) shows shows that the ratios of increase of the RRU areas are 130%, 202%, 266% and 84% for the dip angles = 0°, 30°, 45° and 60°, respectively. However, for the dip angle of 90°, the area of RRU only increases 20%. Mathematically, the RRU area should increase 300% for triangle shape and 100% for column shape when the length of rockbolt is doubled. One of the possible reasons for the lower ratios is that the rock joints restrict the load transfer from rockbolt to the surrounding rocks. Figure 5-6(b) shows the variations of the axial loads of rockbolts with respect to the rockbolt lengths. The axial loads increase 153%, 175%, 179% and 160% for the dip angles of 0°, 30°, 45° and 60°, respectively, but 100% for the dip angle of 90°. It can be concluded from this parametric study that increasing the length of the rockbolt is one effective method to increase the load transfer capacity and RRU area, especially for the low-angle laminated rock blocks, such as the dip angles ranging from 30° to 45°.

5.4 Grouped rockbolts

Parametric studies are also conducted to investigate the group effect of the rockbolts installed in grid spacing. The numerical model is shown in Figure 5-2(b). Three rockbolts named as *A*, *B* and *C* are installed in the rock mass and are fully penetrated the rock mass. Three grid spacings $S = 0.3L$, $0.5L$ and $0.8L$ are used in the simulation where L is the length of rockbolt. Five jointed rock mass models containing primary joints with dip angles of α = 0°, 30°, 45°, 60° and 90° are used to investigate the influences of the rock lamination orientations on the grouped rockbolts. The pullout speed during the simulation is kept as 1 mm/s.

Table 5-4 summarizes the influence of the rock lamination orientations α and the grid spacing of grouped rockbolts S on the displacement contour of rock blocks when the rockbolts are pullout 10 mm from their original locations. The RRUs are also calculated and shown in Table 5-4. It can be seen that the RRUs are heavily influenced by the rock orientations and the grid spacing of the rockbolts. The smaller the spacing S, the larger overlap between the RRUs is generated. The RRUs have less overlap when the rockbolt installed in spacing of $0.8L$ in the rock mass with dip angle α = 0° and 60° but still have

relative larger overlap in rock mass with dip angle α = 45°. This phenomenon can also be observed from the uplift deformation of the rock surface as shown in Table 5-5.

Table 5-4 Displacement contour of rock blocks when U_A = 10 mm

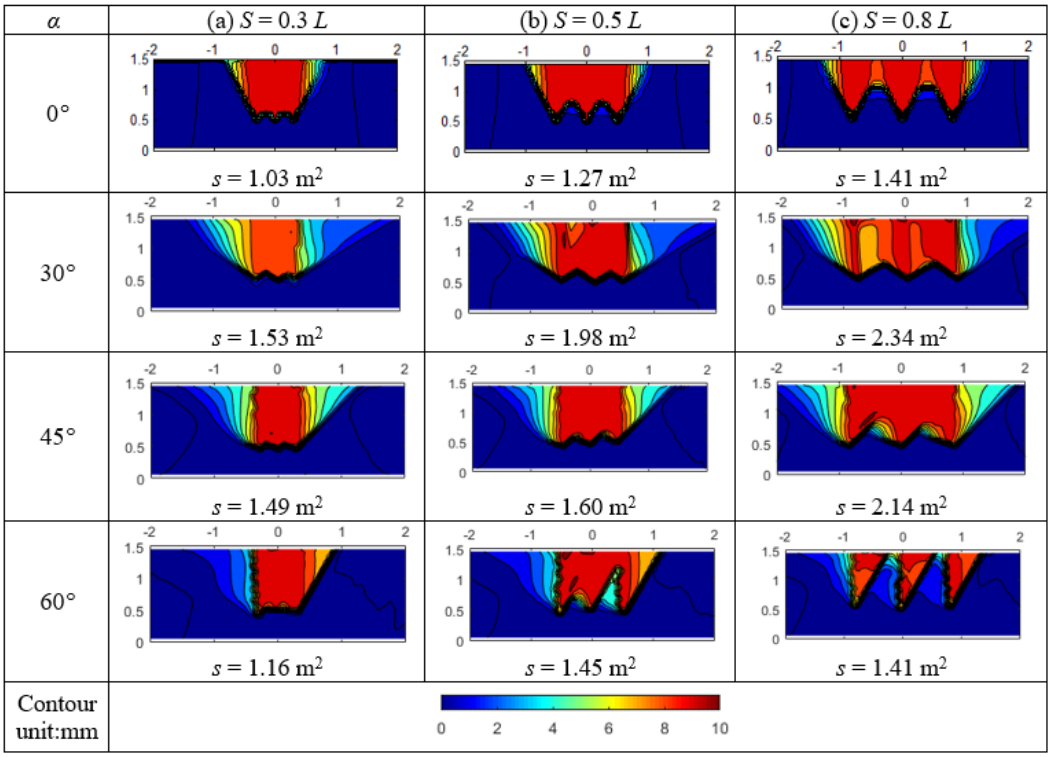

Figure 5-7(a) shows the axial loads versus displacement curves of the rockbolts installed at spacing of 0.3*L* in rock mass with dip angle α = 0°. It shows that the axial loads of the rockbolt *B* and *C* increase with respect to the displacement. However, the axil load in rockbolt *A* increases with the displacement at the beginning of loading test, but decreases slowly after a peak value. Similar observations are also obtained for the case of *S = 0.5L* as shown in Figure 5-7(b). However, for the case of *S = 0.8L*, all the axial loads of the three rockbolts increase with respect to their displacement except those of the middle rockbolt are slightly smaller (see Figure 5-7(c)). One reason for this observation is the group effects of rockbolts installed in a grid. In the grouped rockbolt, the reinforced rock blocks nearby the middle rockbolt may also be reinforced by the lateral rockbolts which are consistent with the observation in the overlap area of the RRUs as shown in Table 5-4. In such cases, the overlap of RRU may be presented as a function of grid spacing of rockbolts (see Figure 5-7(d)). To investigate the interaction of RRUs as a function of grid spacing, the axial load developments of the middle rockbolt in other laminated rock models are presented in Figure 5-8.

Table 5-5 Deformation of rock surface

α	(a) S = 0.3 L	(b) S = 0.5 L	(c) S = 0.8 L
0°	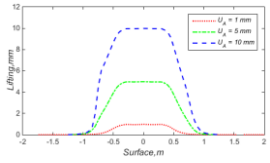	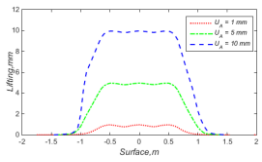	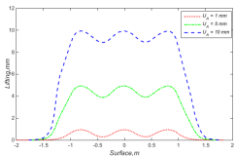
30°	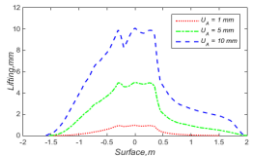	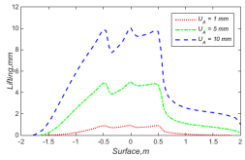	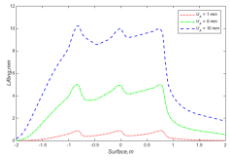
45°	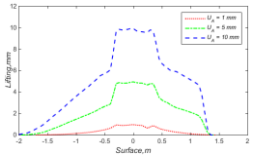	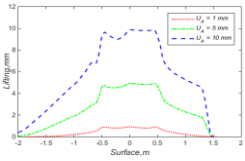	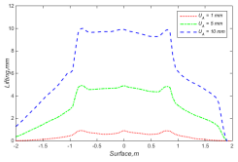
60°	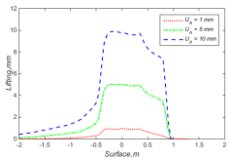	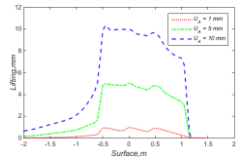	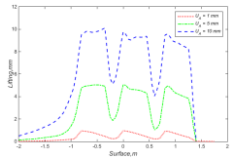
90°	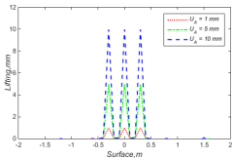	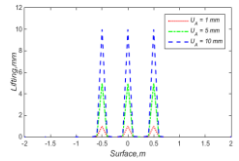	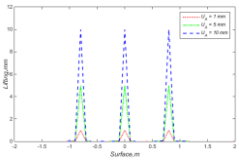

Figure 5-8 shows the axial loads versus displacement of the middle rockbolt in laminated rock models with dip angles α = 0°. It can be seen that the peak values of the axial load of the middle rockbolt are heavily influenced by the grid spacing, decreasing in value as grid spacing increases. For the grid spacing of 0.8L, the axial load in middle rockbolt versus displacement curve is similar to that of single rockbolt. This can be explained as the group effect of the three rockbolts is ignorable. However, decreasing the grid spacing to 0.5L and 0.3L, the axial loads in the middle rockbolt is significantly smaller than that of single rockbolt. Similar observations were also obtained from the axial loads versus displacement curves of the middle rockbolt installed in the jointed rock models with dip angles α = 30°, 45° and 60° as shown in Figure 5-8(a) – (c), respectively. However, the grid spacing has no obvious influence on the axial loads versus displacement curves of the rockbolt installed in the laminated rock models with

dip angles α = 90°, see Figure 5-8(d). This is because there are little interactions between the rockbolts or among the induced RRUs.

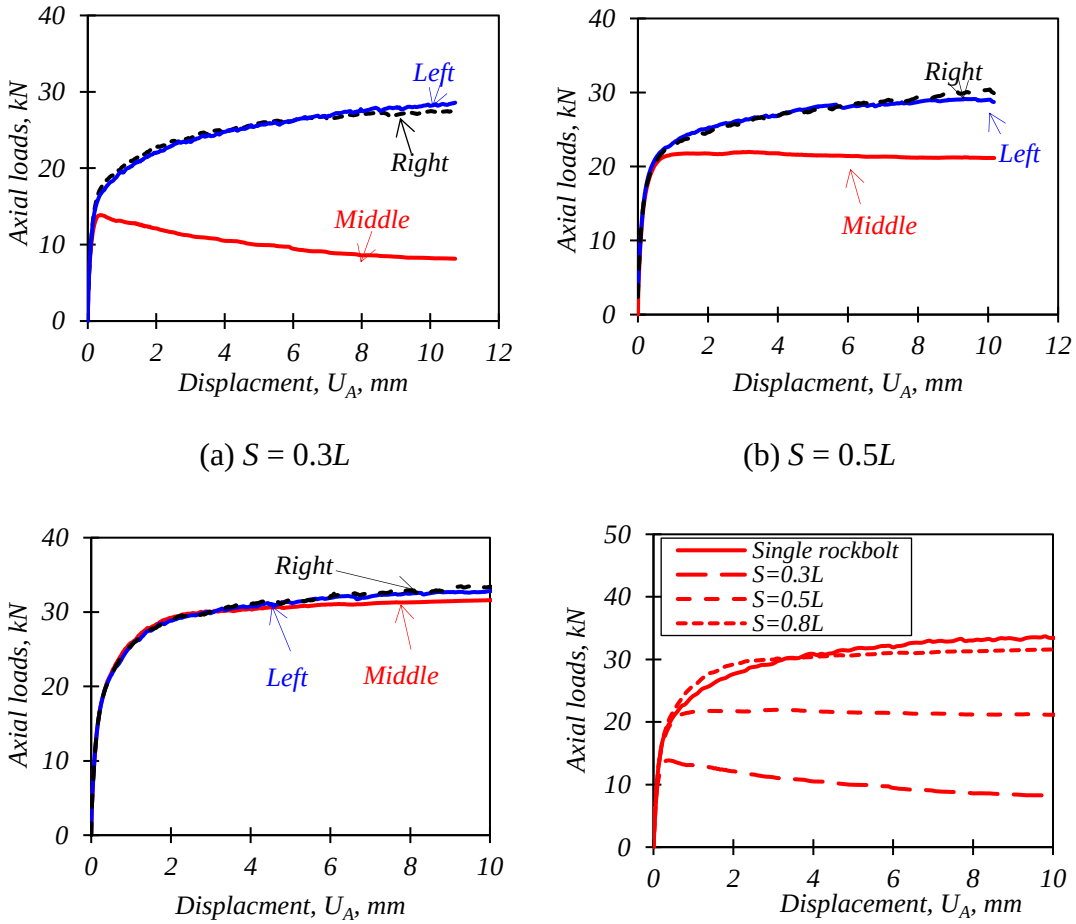

(a) S = 0.3L (b) S = 0.5L

(c) S = 0.8L (d) Comparisons of axial loads

Figure 5-7 Axial loads *vs.* displacement curves for the rockbolt in jointed rock mass with dip angle of 0°

By selecting the axial loads in the middle rockbolt at the displacement U_A = 10 mm from Figure 5-8 and comparing their values with those of single rockbolt, the percentages of the axial load reduction in the middle rockbolt can be derived and plotted in Figure 5-9. For α = 0°, the axial load in the middle rockbolt is reduced by as higher as 24.65% and 63.29% for grid spacing S = 0.3L and 0.5L, respectively. However, for α = 45°, these values are reduced to 10.61% and 30.1% for grid spacing of 0.3L and 0.5L, respectively. It can also be seen that the axial load in the middle rockbolt installed with grid spacing of 0.8L are very close to single rockbolt for α > 60° or α < 30°.

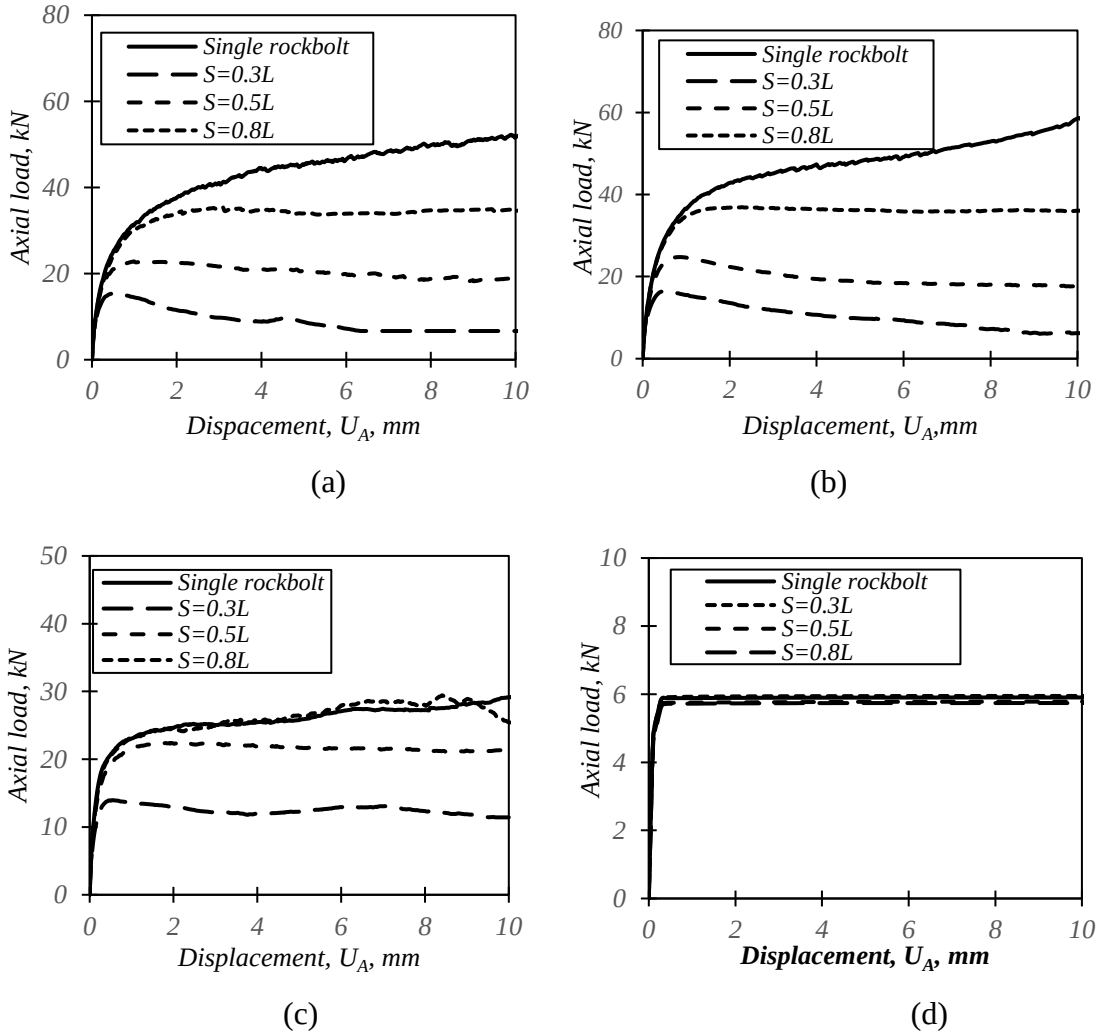

Figure 5-8 Axial loads of the middle rockbolt in cases of primary joints with dip angles of (a) 30°, (b) 45°, (c) 60° and (d) 90°

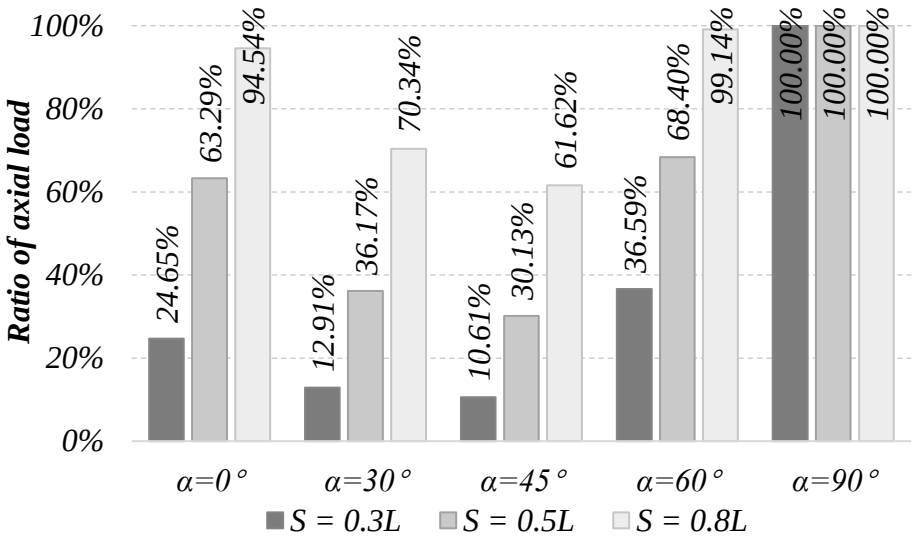

Figure 5-9 Percentages of the axial loads of middle rockbolts

5.5 Discussion

The rockbolt model is implemented into the 2D-DDA code to analyse the single and grouped rockbolts installed in jointed rock mass. The performances of the rockbolts are evaluated by pulling them out from five jointed rock mass models with the primary joints in dip angles of 0°, 30°, 45°, 60° and 90°. The RRU is used to define the influenced rock region affected by the pulling of the rockbolt. Based on current study, the traditional method to calculate the area of RRU by assuming it is cone-shaped with isosceles right angle is not always accurate especially for the jointed rock mass conditions. The cross-sections of the RRU are influenced by the loading scale and the condition of rock mass discontinuities. Take models with reinforcement angle less than 90° for example, the RRU areas are much smaller than those estimated by the traditional method which may overestimate the reinforced area of the rockbolts.

To evaluate the cross-section of RRUs of grouped rockbolts, an overlap ratio r_1 is defined as:

$$r_1 = \left[1 - \frac{\left(RRU_g - (n-1)\times RRU_i\right)}{RRU_i}\right]\times 100\% \tag{5.1}$$

where n is number of rockbolts in the rockbolt group (here n = 3), RRU_g and RRU_i is the RRU area of the grouped and individual rockbolts, respectively.

Figure 5-10 shows the calculated overlap ratio versus dip angle curves for the rockbolts installed in grid spacing S = 0.3L, 0.5L and 0.8L, respectively. It shows that the smaller the grid spacing of the rockbolts, the larger the overlap ratio is generated, see *S = 0.3L*, which indicates that the capacity of rockbolt has not been fully utilized. The overlap ratio is also influenced by the rock properties. For the same grid spacing but dip angle α from 0° to 45°, the overlap ratios increase slowly till their peak value. However, for the dip angle α from 45° to 90°, the overlap ratio decreases very quickly till close to zero, see α=90°, where there is no overlap among rockbolts for all spacings. It can be concluded that the maximum spacing of the grouped rockbolt has to take into consideration the rock joints orientations.

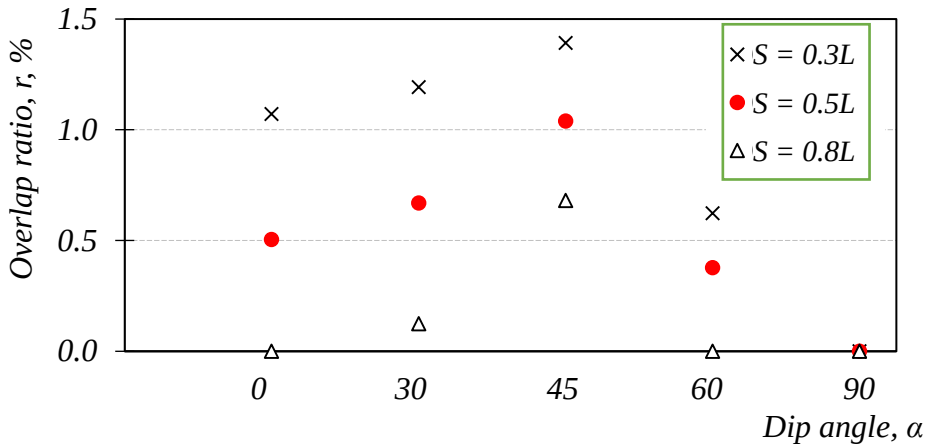

Figure 5-10 Overlap ratio of the RRUs

Based on this study, the free body diagram of the RRU can be simplified as shown in Figure 5-11 by considering the effect of the rock joints orientations. Equilibrium of the force along the vertical direction yields the following equations:

$$P = kW$$
$$k = 1 + \sin\alpha_1 \cos\alpha_1 \tan\varphi_1 + \cos^2\alpha_2 \tan\varphi_2 \tag{5.2}$$

where W is the dead weight of RRU, α is the dip angle of RRU boundaries and φ is the friction angle at the boundaries.

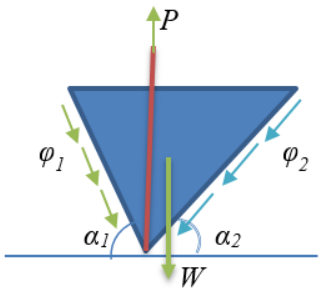

Figure 5-11 Illustration of the relationship between RRU and axial load

In the simulated rock model, the load transfer capacity of a rockbolt is depending on the resistance of the rock mass and affected by the discontinuities in rock masses. As the results of single rockbolt pullout shown in Figure 5-12(a), a larger RRU results in a larger axial load. Considering the cases with same joint properties, linear regression is carried out and show in Figure 5-12(b). The result shows that the axial load is about 1.4 times of the dead weight of RRU which may be caused by the friction. In field, the rate

k may vary in different conditions, such as the complex ground, the displacement ratio, etc.

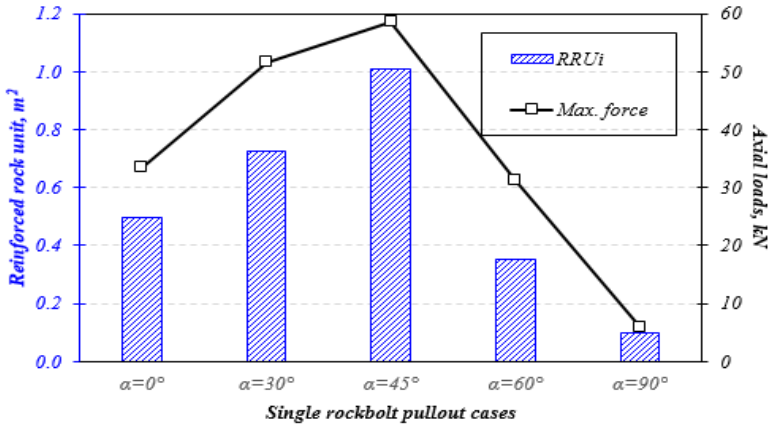

(a) Comparisons of common cases

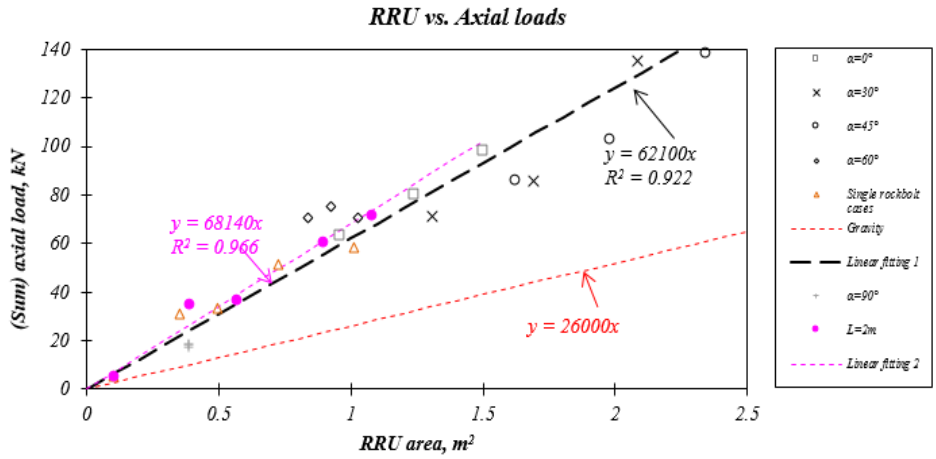

(b) Linear regression of the relationship between RRU area and axial load

Figure 5-12 Comparison of the RRU areas with the maximum axial loads of rockbolt at U_A = 10 mm

5.6 Pressure arch estimation using RRUs

5.6.1. 2D-DDA model

Numerical studies are conducted to investigate the formation of pressure arch by considering different RRUs in jointed rock mass. The sketch of the models used in 2D-DDA is shown in Figure 5-13. The laminated rock mass is considered with an inclination angle of 0º (see Figure 5-13(a)) and 90º (see Figure 5-13(b)), respectively. The numerical model is 11.75 m wide and 3.25 m high modelled by 280 blocks with size of

0.4 × 0.4 m^2. Two perpendicular joint sets are setup in the model. Five 3-m-long rockbolts, named as RB1 to RB5, are preinstalled into the rock mass. The lateral sides of the model are restrained using two rigid blocks as shown in Figure 5-13(a). Linear pressure q_2 are applied on rigid blocks towards each other to simulate the in-situ horizontal stress. The top blocks of the model are restrained by one row of rigid block elements. The line pressure q_1 is applied on the blocks downwards to simulate the in-situ vertical stress. Three blocks are used to constrain the bottom movement. The two blocks on the right and left ends are fixed during the simulation, while the middle long block is used to maintain the in-situ stress during stress balance stage and removed at the excavation stage. In the numerical modelling, the initial in-situ stress state is achieved at 1.0 s after the initial loadings are applied. After another 1.0 s balance time, the middle long block is removed. It should be noted that the shear resistance along discontinuities is assumed to be purely frictional. The cohesion and tensile strength of the discontinuities are neglected in the simulations.

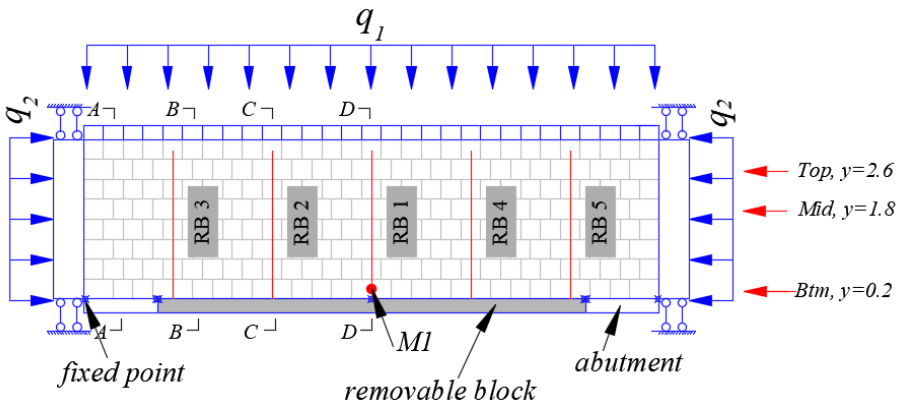

(a)

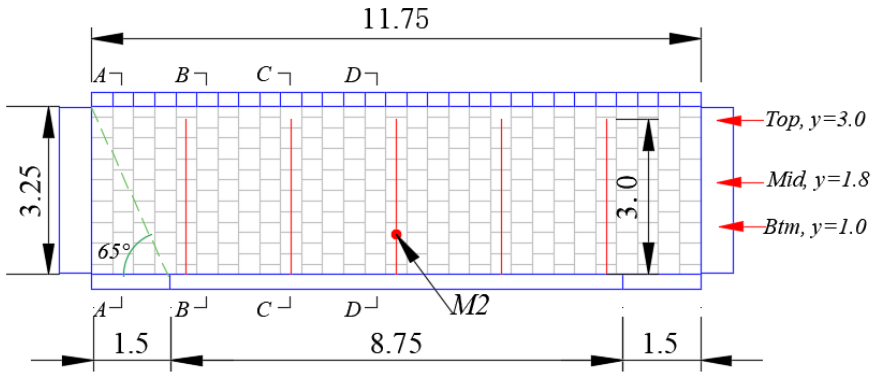

(b)

Figure 5-13 DDA models for pressure arches in layered rock with inclined angles of (a) α = 0° and (b) α = 90°

5.6.2. *Influence of the horizontally persistent joints*

(1) Natural pressure arch

The in-situ stress ratio k is defined as the ratio between horizontal and vertical pressure, q_2/q_1. Figure 5-14(a) shows the simulation results of the vertical displacement of point *M1* near the middle of the excavation boundary (see Figure 5-13(a)) with respect to the different in-situ stress ratios. It can be seen that the larger the k value, the smaller the vertical displacement at point *M1*, and a more stable natural pressure arch might be induced. For the cases of k = 2.0 and 3.0, point *M1* is movable after excavation. But, *M1* become stable after some adjustments for the cases of k = 3.5, k = 4, and k = 6. The displacement at point *M1* is lowest for the case of k = 6.0. Figure 5-14(b) shows the simulated contour maps of the horizontal stress, σ_{xx}, with respect to different in-situ stress ratios. Generally, the pink contours determine the range of the pressure arch. The simulation shows the pressure arch is not observed graphically in the studied domain if k = 3.0, resulted in the crush of the model. It means the displacement at point *M1* could not be controlled. However, the contour maps show that the pressure arches could be observed for the cases of k = 4 and k = 6 and the height of the former one is higher than that of the latter one. The results could illustrate the phenomena that the higher stress ratio k, the displacements of the immediate roof are controllable as the heights of the pressure arch are lower.

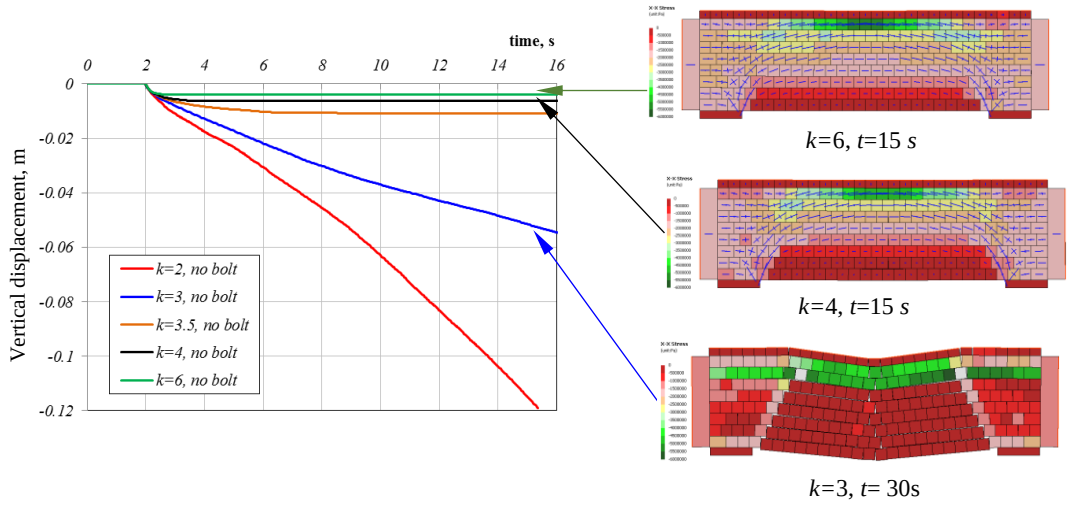

(a) (b)

Figure 5-14 Effect of the in-situ stress ratios on (a) the vertical displacement of *M1*, and (b) the contour maps of the transverse stresses

(2) Artificial pressure arch

A so-called artificial pressure arch will be formed after rock excavation due to the reinforcement provided by the rockbolts. The in-situ stress ratio *k* of 4.0 and 2.0 are used in the simulation. Figure 5-15(a) shows the simulation results of the vertical displacement of the same point *M1* with respect to the different number of rockbolts and in-situ stress ratios. It can be seen that the roof may have some displacement when *k* = 2.0 even 5 rockbolts are installed in the rock mass. For the case of in-situ stress ratio *k* = 4.0, the displacement of *M1* after installed 5 rockbolts are much more stable than no rockbolts. The vertical displacement at point *M1* is slightly smaller for the case of 1 rockbolt than that for the case of 2 rockbolts. This is because the rockbolt go through the block in the former case where *M1* located. Furthermore, it also indicates that the location of rockbolt may also influences the formation of pressure arch.

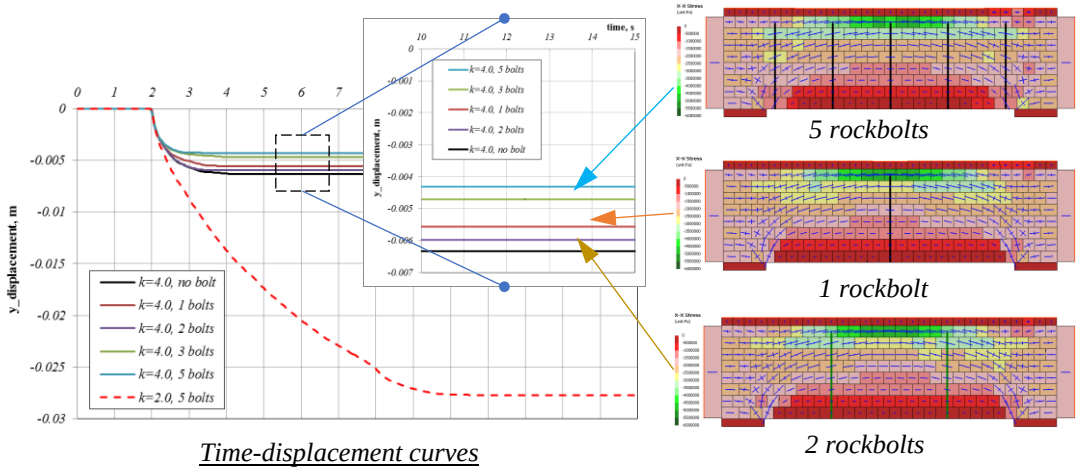

Figure 5-15 Effect of the number of rockbolts on (a) the vertical displacement of *M1* and (b) contour maps of the transverse stresses

Four vertical cross-sections, marked as A, B, C and D in Figure 5-13(a), from left abutment to midspan are used to investigate the distributions of the stresses and displacements of rock blocks in the pressure arch. The distributions of the *x* - (horizontal) and *y* - (vertical) stresses and *y* - (vertical) displacements of the rock blocks in the pressure arch are shown in Figure 5-16. It can be seen that the rock blocks are under compression in *x*- direction ($\sigma_{xx} < 0$) but the values become more unevenly distributed when approaching to midspan. Above the abutment (cross section A), the distribution

of σ_{xx} is in rectangular with its pressure of 2 MPa that is the same as the applied pressure. When approaching to the midspan (from cross-section B to D), σ_{xx} decreases at the roof and increases with the depth far away from the roof resulting in trapezoidal distributions with a higher maximum σ_{xx} near the top edge and a lower σ_{xx} near the bottom edge. The σ_{xx} at the midspan (cross section D) is not linear but in parabolic shape, which means the pressure arch is moving to the depth. Connecting the points with σ_{xx} = 2.0 MPa in the four cross sections, it gives parabolic curves in convex shapes. The heights of the intersections are also shown in Figure 5-16(a). It can be seen that the heights are proportional to the displacements of *M1*. The heights for the case without rockbolt is 17.7% higher than the case of 5 rockbolts. The lower value of the heights means a more reliable pressure arch will be generated.

The *y* stress σ_{yy} distributions along the four cross-sections are shown in Figure 5-16(b). The stress concentration at the cross-section B has the highest level σ_{yy} which is about threefold applied loading of 0.5 MPa. When approaching to the midspan (from cross-section B to D), σ_{yy} decreases along the whole cross section. At the cross-section D, the distribution of σ_{yy} is not linear. For the cases of no rockbolt and 2 rockbolts are installed, only the top end of the blocks are compressed, while the bottom rocks are in zero stress (σ_{yy} = 0) or even in tension (σ_{yy} < 0). When the rock blocks are reinforced by 3 or 5 rockbolts, more rock blocks on the top are compressed.

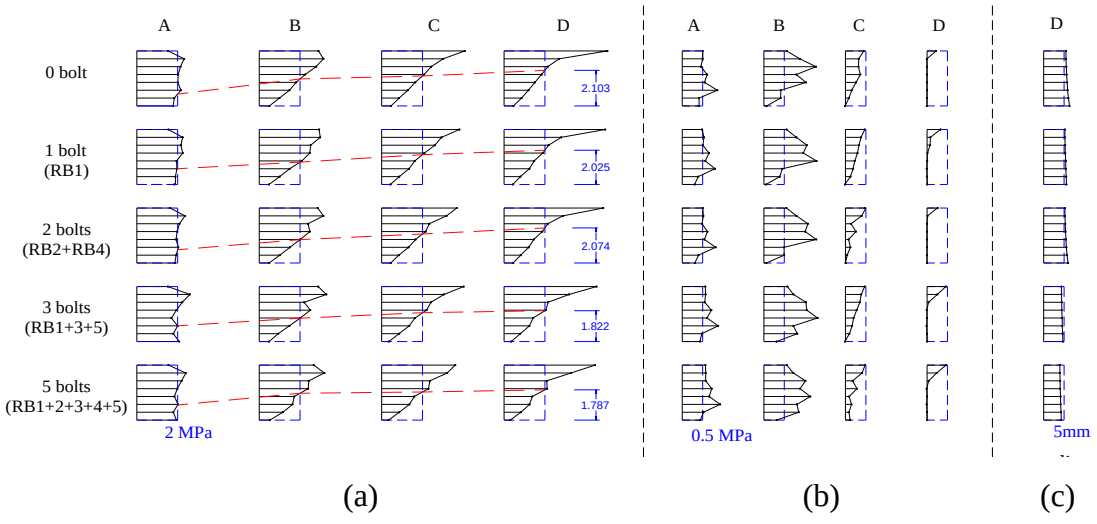

Figure 5-16 Distributions of stresses and displacements in rock blocks along vertical cross sections (a) *x*-stress, (b) *y*-stress and (c) *y*-displacement

5.6.3. *Influence of the vertically persistent joints*

(1) Natural pressure arch

Four cases are designed to investigate the formation of natural pressure arches in cases of the in-situ stress ratio k = 2.0, 3.0, 4.0 and 6.0. The vertical displacements of *M2* are measured to see the stability of roof, as shown in Figure 5-17(a). When k = 6.0, the natural arch is well established and no rock blocks from roof falls. On the other hand, even the vertical displacement of *M2* indicates a stable roof at k = 4.0, several blocks fall down. When k decreases, more blocks in the roof become moveable, such as the whole model may collapse in case of k = 2.0. The x-stress contours (see Figure 5-17(b)) show that there is no pressure arch formed in case of k = 2. Compared with the displacement in the horizontal jointed rock mass, the present models show the vertically persistent joints are unfavorable for roof stability.

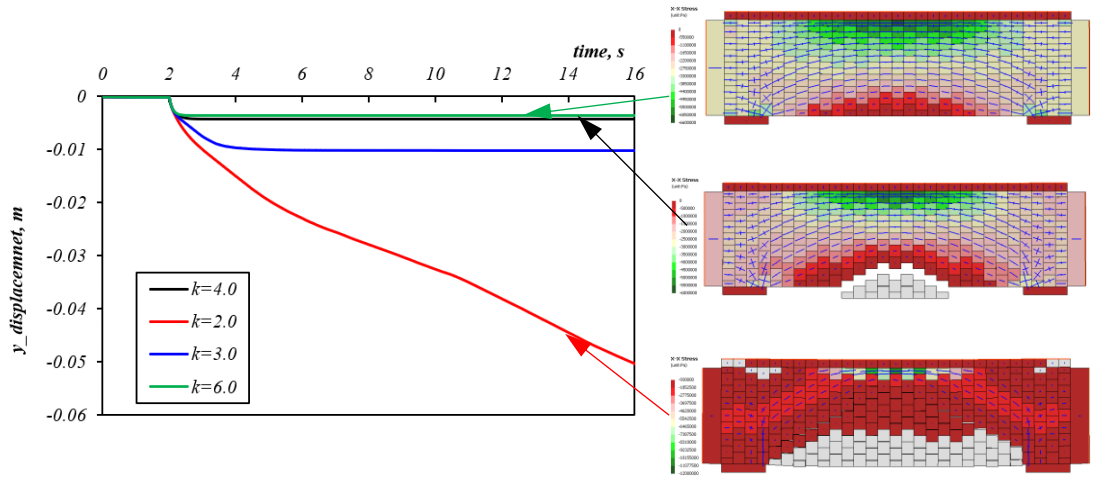

(a) (b)

Figure 5-17 Effect of the stress ratios on the vertical displacement of *M2* in verticlly jointed rock mass (a) Displacement histories of measuring point *M2* and (b) Contour maps of the stress ratio k = 6.0, 4.0 and 2.0

(2) Artificial pressure arch

Figure 5-17 has showed the loss of local stability in the middle roof in case of stress ratio k = 4.0. The moveable roof blocks are not well stabilized even some rockbolts are added in the same model as shown in Figure 5-18. The rockbolts only reinforce the rock blocks which the rockbolts are getting through indicating very limited reinforced unit of

single rockbolt. Taking the displacements at *M2* as examples, the case with installation of 5 rockbolts has the smallest displacement at *M2*, but the loose roof may expand to lateral blocks showing unfavorable reinforce forces for artificial arch formation. In contrast, the displacements are doubled when 2 rockbolts are installed compared with the displacement of *M2* in natural arch formation. But the whole roof is more stable as less moveable rock blocks than that with 5 rockbolts. The distributions of the stresses and displacements along four vertical cross sections, marked as A, B, C and D from left abutment to midspan, are showing in Figure 5-19.

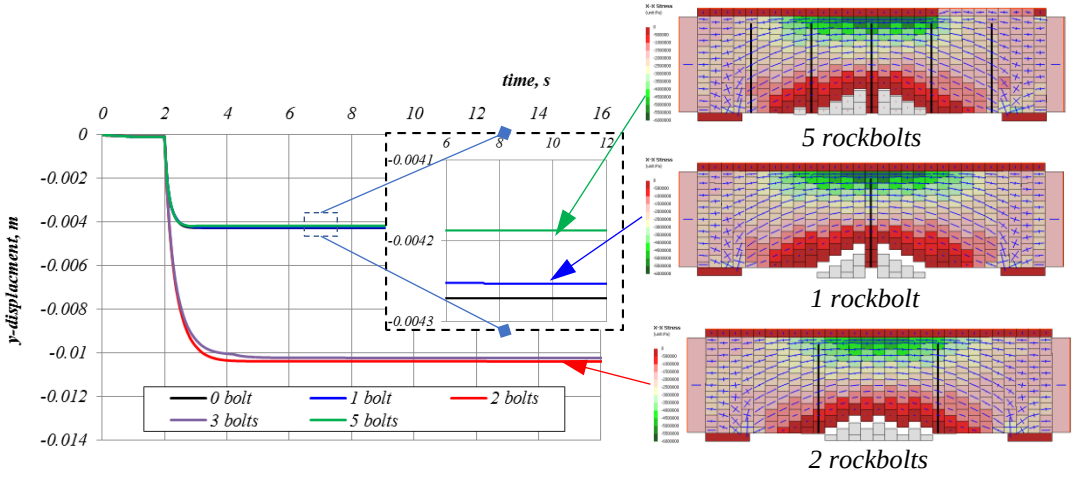

Figure 5-18 Vertical displacement of *M2* in cases of artificial roof arches formed in vertically jointed rock mass (a) Displacement histories of measuring point M2; (b) Contour maps of the transverse stresses in cases of 5 rockbolts, 1 rockbolt and 2 rockbolts are installed

Considering the variation of σ_{xx} along four vertical sections, they are generally varying from rectangular distribution along section A to trapezoid distribution along section B, followed by triangular distributions along C and D. That is to say, σ_{xx} is increasing when x approaches to midspan at the top edge and is decreasing at the bottom edge. But the increaments may vary in different cases. Connecting the points with σ_{xx} = 2.0 MPa in four cross sections, the depths are reversely proportional to the displacements of *M2*. The depth in the case of 2 rockbolts installed is the smallest value in all five cases. The distributions of σ_{yy} along four cross sections from left abutment to midspan are varying from trapezoid along A to triangular distributions along D (except for the 5 rockbolts

case). This is because σ_{yy} has concentration near the bottom edge at abutment, but the σ_{yy} concentration is limited and not affecting section B and other sections.

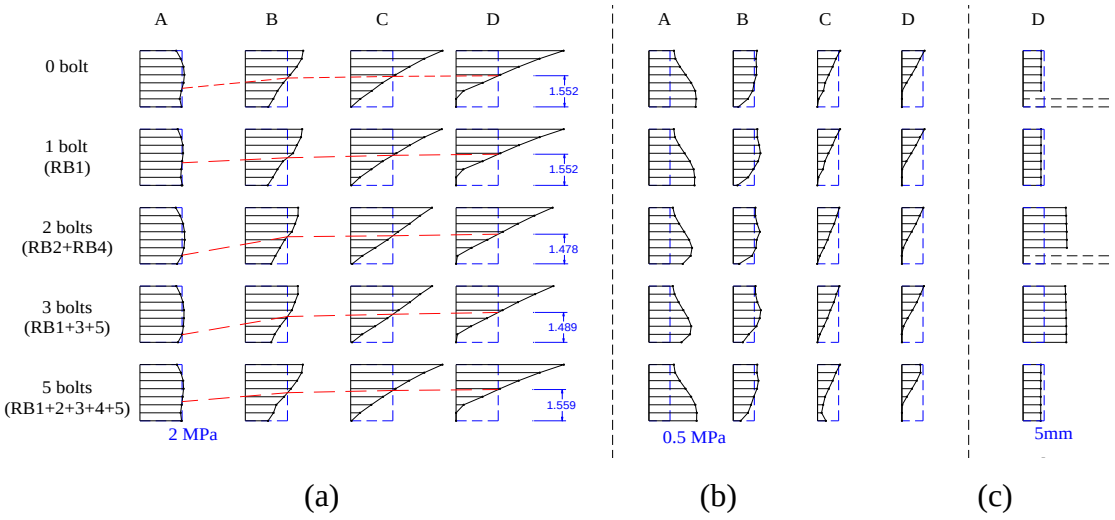

Figure 5-19 Changes in the stresses and vertical displacements in various rockbolts reinforced conditions (a) *x*-stress, (b) *y*-stress and (c) *y*-displacement

5.6.4. Discussion and limitation

Figure 5-20 plots the axial loading along the rockbolt with indication of the influence area of single rockbolt as same as the areas showing in pullout test (Table 5-3). It can be seen that the supposed RRU of rockbolt in horizontally laminated rock mass is much larger than that in vertically laminated rock mass under the same number of rockbolts reinforcement condition. In horizontally laminated rock mass, two rockbolts are vertically installed with a spacing of 4.0 m on the roof, both rockbolts have low axial forces of 4.0 kN evenly distributed along the whole rockbolts (see Figure 5-20a). The influence areas are not overlapped indicating only local reinforcement are achieved by each rockbolt, such as the local stress variation. When 5 rockbolts are installed with a spacing of 2.0 m (see Figure 5-20b), the axial forces are unevenly distributed along the rockbolt RB3 and RB2. The rockbolt RB3, located near the left abutment, has a yield axial force at the rockbolt elements embedded in the immediate roof and very low axial force (near 0) at the rest parts of rockbolt elements embedded in the deep roof. RB2 has similar axial loading distribution as RB3. The axial forces of RB1 located at the midspan are in tension along the rockbolt. The maximum axial force along RB1 is only 15 kN, located at a joint with a depth of 0.8 m from roof. By the reinforcement of 5 rockbolts,

the influence areas of five rockbolts are overlapping to each other resulted in a stiff rock roof arch. In vertically laminated rock mass, the rockbolts are under evenly tension along the whole length with axial loading of 20.0 kN evenly distributed along the whole rockbolts, when two rockbolts are installed with a large spacing of 4.0m (see Figure 5-21(a)). The columns of each rockbolt stabilize the rock blocks which the rockbolt get through. In five rockbolts cases (see Figure 5-21(b)), even RB3 bears large tensile force at the elements in roof, and it does not help to change the stresses of roof too much due to its limited reinforcement area. As the numerical models in the examples were designed under specified geology conditions, the comparisons between the RRUs and the pressure arches were only for illustration purpose. In the future, more detailed work should be carried out to explore the relationship between RRU and the geometry of pressure arch, as well as the possible loading on the rockbolt.

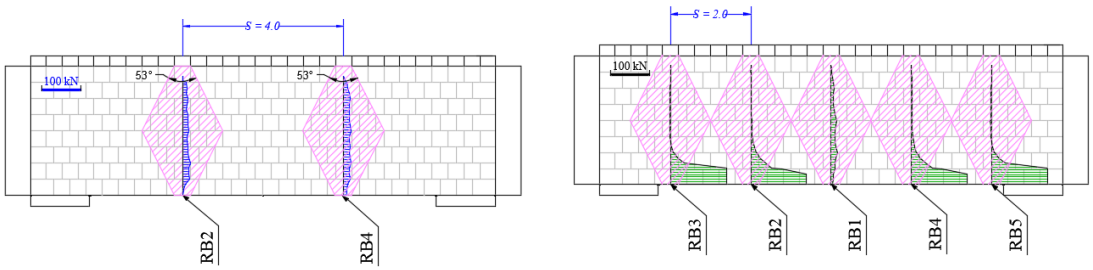

(a) (b)

Figure 5-20 Axial load of the rockbolt and its sketched RRU in the horizontally laminated rock blocks (a) two rockbolts and (b) five rockbolts

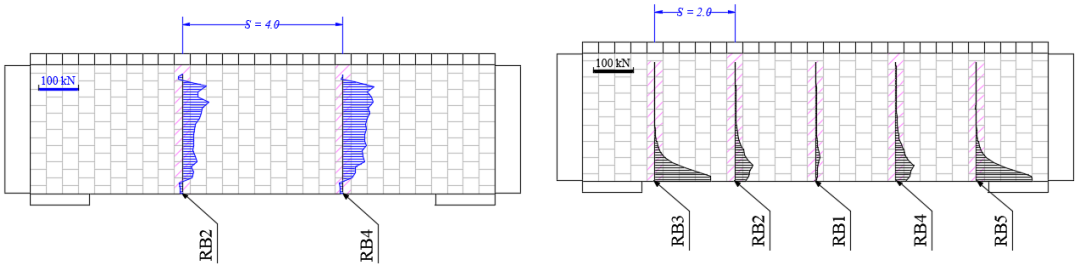

(a) (b)

Figure 5-21 Axial load of the rockbolt and its sketched RRU in the vertically laminated rock blocks (a) two rockbolts and (b) five rockbolts

5.7 Conclusions

A fully grouted rockbolt model is implemented into 2D-DDA to analyse the performance of the rockbolts installed in jointed rock mass. The reinforcement area of the reinforcement rock units (RRU) is evaluated by pulling rockbolts out from five different jointed rock models.

For a single rockbolt, the pullout resistances are heavily affected by the discontinuities of jointed rock mass. With the increase of dip angle from 0 to 45°, the critical pullout resistance increases from 21.5 to 41 kN. However, when dip angle increases to 90°, the critical pullout resistance decreases to 5.8 kN. The RRUs are heavily influenced by the discontinuity orientations with triangular cross sections. Mathematically, the RRU area should increase 300% for triangle-shaped cross section and 100% for column-shaped when the length of rockbolt is doubled. However, the ratios of increase of the RRU areas are 130%, 202%, 266%, 84% and 20% for the dip angles of 0°, 30°, 45°, 60° and 90°, respectively. This is because the rock joints restrict the load transfer from rockbolt to the surrounding rocks. The changing of principal stress shows the elongation of the rockbolt induces compression in RRU. For the special model with discontinuity dipping at 90°, the RRU of a single rockbolt is limited to a column of rock blocks.

For grouped rockbolts, the traditional method to calculate the area of RRU by assuming it is cone-shaped with isosceles right angle is not always accurate especially for the complex joint conditions. The RRUs are heavily influenced by the rock orientations and grid spacing of the rockbolts. The smaller the spacing S or the rock mass with dip angle closer to 45°, the larger overlap between the RRUs is generated which indicates that the capacity of rockbolt has not been fully utilised. For the same grid spacing but dip angle α from 0° to 45°, the overlap ratios increase slowly till their peak value. However, for dip angle α from 45° to 90°, the overlap ratios decrease very quickly till zero. For α = 90°, there is no overlap among RRUs for all spacings. The maximum grid spacing of the grouped rockbolt must take into consideration the rock joints orientations.

CHAPTER 6. STABILIZATION OF ROOF WEDGE USING ROCKBOLTS

Unstable wedges might be exposed on the roof of the underground excavation. The design parameters of the rockbolt are usually determined by the weight of the unstable blocks. More advanced research should be carried out to investigate the rockbolt designs if the deformations induced by the re-adjustment of the stress field in the rock is comparable to those induced by the weight of loosen rock blocks. In this chapter, 2D-DDA is used to evaluate the rockbolt design to stabilize roof wedges for underground opening. To represent a deformable rock mass under stresses, the joint relaxation method is adopted in the 2D-DDA models.

6.1 Introduction

For tunnels excavated in jointed rock mass, rock wedges formed by intersecting structural discontinuities may fall from the roof or slide out of the sidewalls as shown in Figure 6-1(a). As there might be no restraints from the boundary, the rock wedge in the tunnel roof may fall as soon as its base is fully exposed by the excavation of opening (Hoek et al., 1995). The falling of the roof wedge will reduce the restraints and interlocks in the surrounding rock mass. Unless proper supports are used to reinforce the loose wedges, the stability of the surrounding rock may deteriorate rapidly.

The spot rockbolt and sparsely spaced pattern rockbolt are recommended in the empirical methods in jointed rock mass to stabilize the rock wedges. The rockbolts for wedge stabilization are usually designed based on the deadweight of the rock wedge (Li, 2017; Low and Einstein, 2013). This is because the major driving force of the wedge falling is its deadweight, especially if the tunnel is excavated in hard jointed rock mass under the low field stress state. The design parameters of the rockbolt include the bolt

strength, length, diameter, spacing, patterns, and so on. The recommendations and suggestions for the design parameters are summarized in Table 2-4.

In practice, the relative locations of the rockbolt to the major joints are also important for the effectiveness of the rockbolt supports. The embedded length (l_0), which is defined as the length of rockbolt in the stable rock behind the wedge, is one of critical parameters. As shown in Figure 6-1(b), the embedded length changes with the relative location of the rockbolt to the wedge boundaries. It should be sufficient long to ensure the anchorages in the stable interior rock. Otherwise, the rockbolt would be pulled out easily. For the fully grouted rockbolt, the required embedded length is usually about 1.2 m (Li et al., 2016). The angle between the rockbolt and the joint is another important factor. As shown in Figure 6-1(c), the rockbolts may be subjected to tension and/or shear loads depending on the angle of rockbolt installation. The shear components may reduce the load capacity of the rockbolt (Chen and Li, 2015).

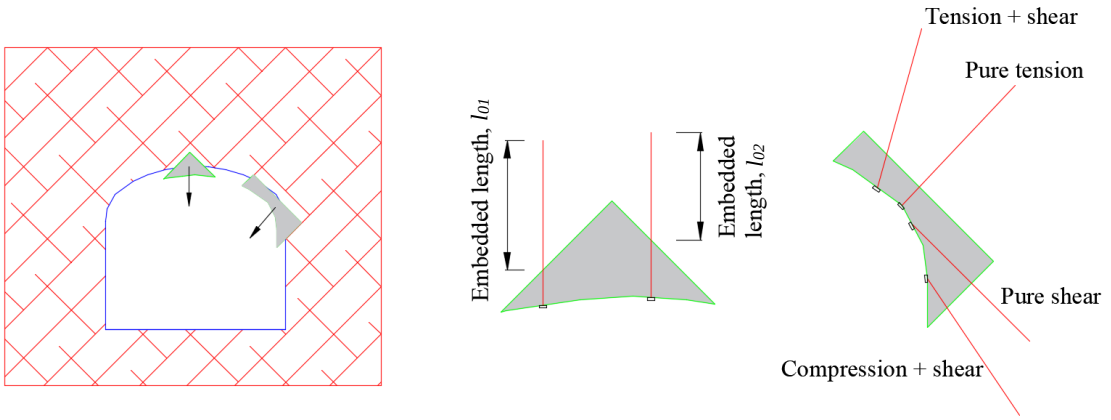

(a) (b) (c)

Figure 6-1 Examples of the definitions of rockbolting design parameters in wedge problems (a) sketch of unstable wedges formed in an underground opening, (b) changes of embedded lengths and (c) changes of response modes of rockbolts

The stable state of rock wedge might change during the stress re-adjustment in the surrounding rock mass during the excavation process (Dwivedi et al., 2014). The rock wedge may be partly loaded by surface forces caused by the residual internal pressure (Wittke, 2014). To estimate the magnitudes of the surface forces, the joint relaxation

method is suggested by introducing the joint stiffness and wedge displacement caused by joint deformation (Sofianos, 1986; Nomikos et al., 2002; Nomikos et al., 2006). Using the above method, the required support forces from rockbolts are calculated as the difference between the deadweight of rock wedge and the vertical deriving force (Brady and Brown, 2006). The calculation often involves sensitivity studies to find out the influences of each significant parameter on the displacement after relaxation. It will be more efficient if a numerical method could be used (Nomikos et al., 2006).

Verification studies on the stability of rock blocks using 2D-DDA have been conducted by MacLaughlin and Doolin (2006) and Jiao et al. (2014). They have concluded that the solutions of the 2D-DDA matched the limit equilibrium solution with high precision. As the 2D-DDA method uses an incremental solution procedure, the balanced contact forces could be presented in the simulation progress. The stress variations after excavation could also be presented in the simulation of rock tunnelling (Tsesarsky and Hatethodzor, 2006). By using 2D-DDA method, it is possible to assess the force-displacement relationships of rock blocks in the simulations and compose ground reaction diagram to predict the interaction between rock wedge and rockbolt (Windsor, 1997; Aydin et al., 2014 and Nie et al., 2018a).

In this chapter, the stability of the rockbolt reinforced rock wedges in tunnel roof reinforced is analysed using 2D-DDA. The change of stress state in the surrounding rock blocks after excavation is represented using the joint relaxation method. Parameter studies are carried out to investigate the effects of the horizontal pressure, the spacing between rockbolts and the installation angle on the reinforcement effort of the rockbolts for the rock wedge stabilization. A case study is also conducted to illustrate the usage of the proposed method.

6.2 2D rock wedges stability in tunnel

For 2D problems, the geometry of rock wedge is assumed not to be changed in the direction perpendicular to the discontinuity (Wittke, 2014). It is also assumed that the forces acting on the wedge allow the movement only parallel to the discontinuity. The rock block is generally subjected to its own weight, surface forces, and some support load. The water pressure is not considered in this study.

6.2.1. 2D-DDA model

A symmetric wedge block is used to simulate the unstable rock wedge as shown in Figure 6-2(a). It has a height of 2.0 m and a semi-apical angle of 30°. The surrounding rock mass are simulated using two blocks each of which with a height of 6.0m and a width of 5.0 m. The joints between the wedge and two surrounding rock blocks are purely frictional. The engineering properties of these three blocks are the same, i.e. density ρ = 2.6 $\times 10^3$ kg/m^3, elastic modulus E = 30 GPa and Poisson's ratio v = 0.1. Two rigid blocks are added at the two sides to provide the horizontal confining pressure. Roller supports are applied at the bottom of the rock blocks to restrain their vertical movements.

The numerical analysis is conducted in three steps. The first step is to apply lateral confining pressure p progressively onto the two lateral rigid blocks to achieve the initial equilibrium stress state. The second step is to remove the roller at the central bottom of rock wedge to simulate the excavation process. During this process, the deformation of the joint defining the rock wedge is taken account. As shown in Figure 6-2(b), the contact forces at points A to D between the rock wedge and the surrounding rock blocks are recorded. It should be noted that points A and B are used to separate the contacts of the top vertex to the right and left joints, respectively. The third step is to add two symmetrical rockbolts into the model right after the second step to support the rock wedge. As shown in Figure 6-2(c), the length, embedded length, inclined angle and spacing of rockbolt are denoted as L_b, l_0, θ and s_b, respectively. To provide enough anchorage force, the embedded length of a rockbolt is designed as l_0 = 1.2 m as suggested by empirical method given by Li (2017a). The rockbolt model used in Section 4.3.2 is employed here. The length of the rockbolt element in the rock is set as 0.1 m, while that near the rock joint is set as $2l_e$. The parameter setting is listed in Table 6-1.

6.2.2. Model verification

To verify the accuracy of the wedge model without rockbolt, the simulation result is compared with that from analytical solution given by Brandy and Brown (2006). Before relaxation progress as shown in Figure 6-3(a), the force equilibrium in the vertical direction gives the vertical deriving load P of the rock wedge as:

$$P = 2N_0 \sec\varphi \sin(\varphi - \alpha) \tag{6.1}$$

where: P – Vertical deriving load;

N_0 – Surface forces normal to the joint, assume $N_0 = N_{0,1} = N_{0,2}$;

S_0 – Surface forces tangent to the joint; and $S_0 = S_{0,1} = S_{0,2}$;

α – Wedge semi-apical angle of joint, $\alpha = \alpha_1 = \alpha_2$, and

φ – Friction angle of joint, $\varphi = \varphi_1 = \varphi_2$.

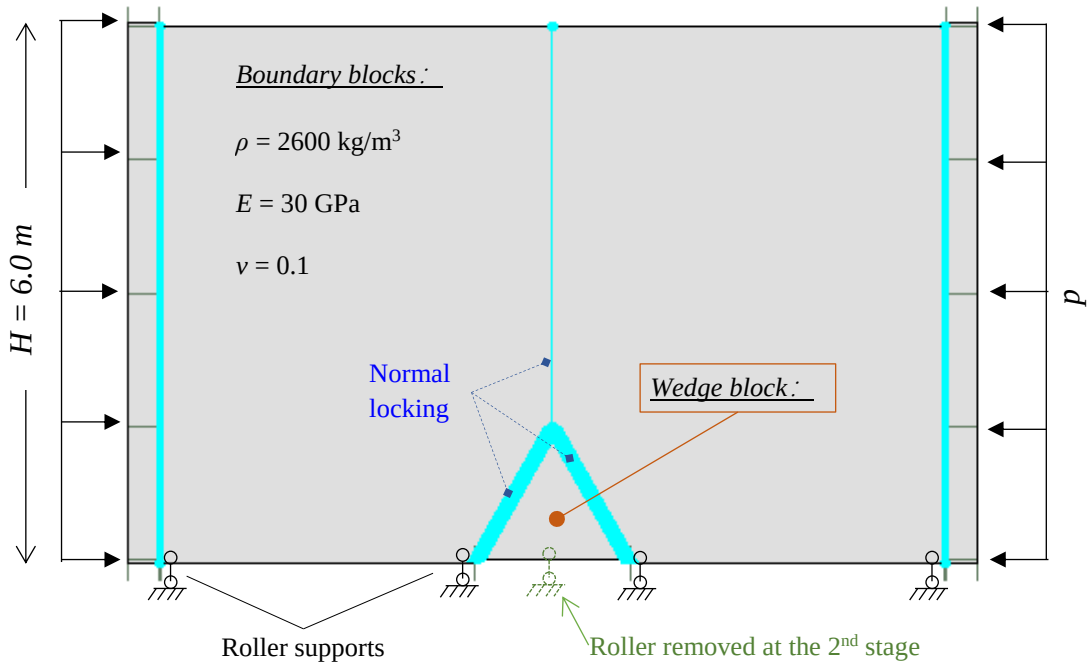

(a)

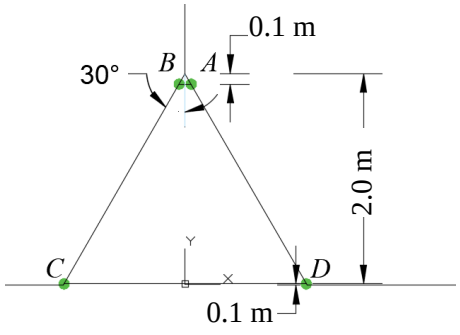

(b)

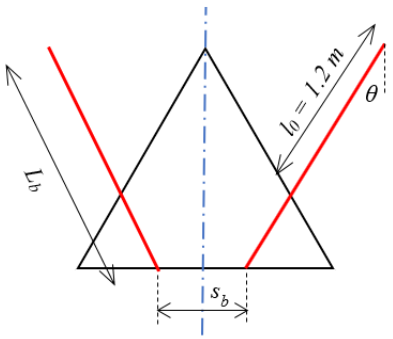

(c)

Figure 6-2 2D-DDA model for a symmetric wedge with straight wedge free face (a) geometry model, (b) contacts at the wedge block and (c) parameters of rockbolts

Table 6-1 Parameters setting in the numerical simulation

Item	Parameter	Values	Item	Parameter	Values
Rock	Elastic modulus E_r, GPa:	30	Rockbolt	Diameter D_b, mm	20
	Poisson ratio, v	0.1		Elastic modulus E_b, GPa	210
	Unit weight, $\times 10^3$ kN/m^3	26.0		Yield axial force, kN	180
DDA calculation	Step max. displacement ratio	0.0004		Ultimate axial force, kN	217
	Upper limit of time interval	0.0002		Hinge length l_e, mm	30 (~1.5D_b)
	SOR factor	1.4		Shear stiffness K_s, MN/m	66.3

By introducing the joint stiffness $\bar{k}_n$ and $\bar{k}_s$ as shown in Figure 6-3(b), the limiting vertical load P_l is calculated as:

$$P_l = 2\frac{M}{D} H_0 \sin(j - a) \tag{6.2}$$

where: H_0 – The horizontal force before joint relaxation, $H_0 = N_0^2 + S_0^2$.

D and M are constants which are calculated as:

$$D = \bar{k}_s \cos\alpha \cos\varphi + \bar{k}_n \sin\alpha \sin\varphi \tag{6.2a}$$

$$M = (\bar{k}_s \cos^2\alpha + \bar{k}_n \sin^2\alpha) \tag{6.2b}$$

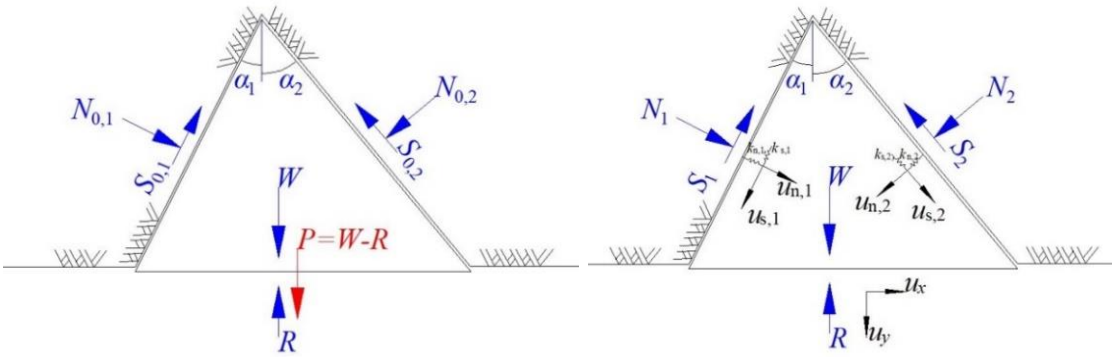

(a) (b)

Figure 6-3 Free-body diagrams of a 2D roof wedge in (a) rigid joint condition and (b) relaxed joint condition

Comparing P_l with the wedge weight W, the stability of the roof wedge could be estimated by assessing the support force R and potential displacement or displacement

u_y caused by joint relaxation. Some results are summarized in Table 6-2. It shows the rock wedge could be self-supported after relaxation if $P_l \geq W$. Assuming $H_0 = pH$, where p is the horizontal pressure, and substituting it to Eq. (6.2) gives the critical horizontal confining pressure p_{cr} as:

$$p_{cr} \geq \frac{WD}{2MH\sin(\varphi-\alpha)} \tag{6.3}$$

Assume the joint has an area of A, the reaction forces due to the joint deformation could be calculated as

$$R_n = \bar{k}_n A d_n \tag{6.4}$$

$$|R_s| = \bar{k}_s A |d_s| \tag{6.5}$$

where: d_n and d_s – normal and shear deformation of a joint, respectively;

R_n and R_s – normal and shear reaction forces, respectively, and

$\bar{k}_n$ and $\bar{k}_s$ –joint stiffness at the normal and shear directions, respectively.

Based on the analytical solution, the horizontal pressure, p_{cr}, versus friction angle, φ, are plotted in Figure 6-4. It shows for a certain rock wedge, the critical horizontal confining pressure p_{cr} should vary with the ratio of normal and shear joint stiffness. The ratio of joint stiffness on the critical horizontal confining pressure could also be considered as:

$$\frac{\bar{k}_n}{\bar{k}_s} = \frac{R_n/d_n}{R_s/d_s} \approx \frac{k_n}{k_s} \tag{6.6}$$

Here, the shear contact stiffness k_s is assumed as $0.4k_n$. During the simulation, the boundary of joint will be pushed back as no-penetration and no-tension are allowed between blocks in 2D-DDA. In the following, three normal contact spring stiffness k_n are adopted in the numerical simulations to analyse the critical horizonal confining pressure after joint relaxation, i.e., $k_n = 3\times10^9$, 30×10^9 and 300×10^9 N/m, or $1.3\,E_r\times L$, $13\,E_r\times L$ and $130\,E_r\times L$, where E_r is the Young's modulus of the rock block and L is the length of the line across which the contact springs are attached. The dimension of the joint out-of-plane is assumed as 1 unit. The results of numerical analysis agree reasonable with those obtained by analytical solutions, especially for the simulation using normal contact stiffness $k_n = 3\times10^9$ N/m. The mismatch between the two results

is because the unsymmetrical contacts forces are generated during the simulation. This could be further explained using the numerical models with friction angle φ = 40° and three contacts.

Table 6-2 Roof wedge stability based on the analytical solutions

Case	Semi-apical angle, α	Internal horizontal force, H_0	Stability assessment		
			P_l	Support force, R	Displacement, u_y
A	φ close to α and $\alpha \leq \varphi$	Low	$0 < P_l \leq W$	Any decrease of φ and decrease of H_0 will result in the increase of required support forces.	Potentially stable if sufficiently support provided.
B	$\alpha \leq \varphi$	Low	$P_l > W$	No or less support required (for safety).	Potentially stable.
C	$\alpha \leq \varphi$	High	$P_l > W$	No support required if the displacement is allowable; Require reinforcement to increase the joint stiffness if the joint displacement is large.	Potentially stable after a large amount of joint relaxation.
Note:	• A larger P_l indicates a more stable condition. • u_y affected by H_0 and the joint stiffness, and • H_0 creates confining on the rock wedge				

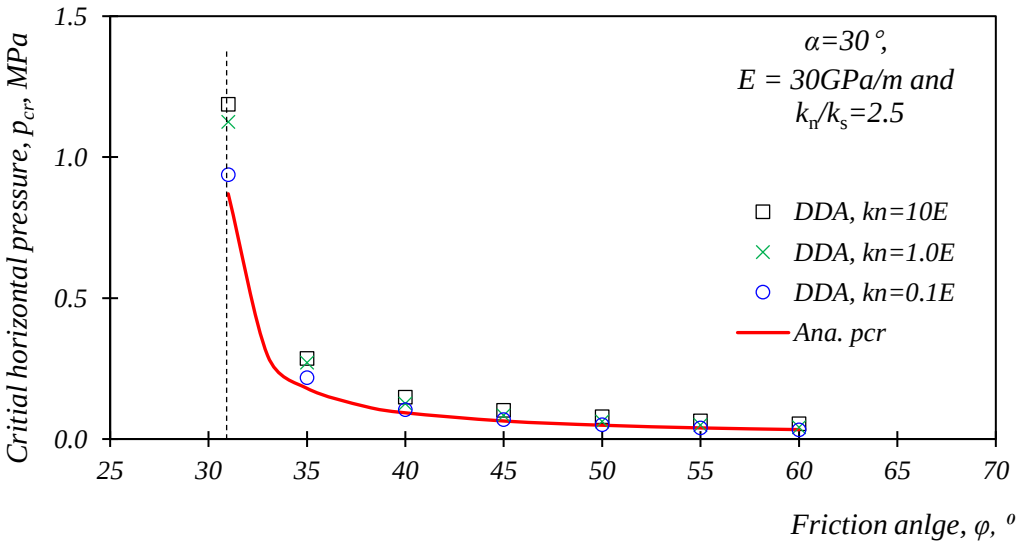

Figure 6-4 Comparisons between the simulated critical horizontal pressures and the analytical solutions at different friction angles

As shown in Figure 6-5, the magnitudes of the displacements in the 2nd step decrease with the increase of contact stiffness. The model with a normal contact stiffness as k_n = 3×10^9 N/m shows progressive displacement before the new balance achieves. The normal contact forces of the wedge to the boundary blocks in the two simulation steps are also investigated. The normal contact force versus the time step curves at the contact points *A* to *D* are plotted in Figure 6-6(a). Even the load is supposed to be applied linearly with time step at the 1st step, the obtained curves are not purely linear. The contact forces are symmetrically distributed. The differences between upper contact points (*A* and *B*) and lower contact points (*C* and *D*) are very little. For the case of k_n = 30×10^9 N/m (see Figure 6-6(b)), the normal contact forces increase linearly with the increase of time step during loading time. In both stages, the normal contact forces are under and symmetric solution. However, the contact forces of the upper contacts (*A* and *B*) are less than those of the bottom contacts (*C* and *D*). In case of k_n = 300×10^9 N/m (see Figure 6-6(c)), the differences between the normal forces at upper contact points (*A* and *B*) and those at bottom contact points (*C* and *D*) become larger. The forces at the upper contact points are only 70% of those of the bottom contacts. It also shows that the contact forces have oscillations in the simulations leading to unsymmetrical loadings at two sides of rock wedge. This might be the reason that a block model with soft contacts (i.e., k_n = (3 ~ 30) $\times10^9$ N/m or (1.3 ~ 13) $\times E \times L$) are resulted in a close agreement with the analytical solutions.

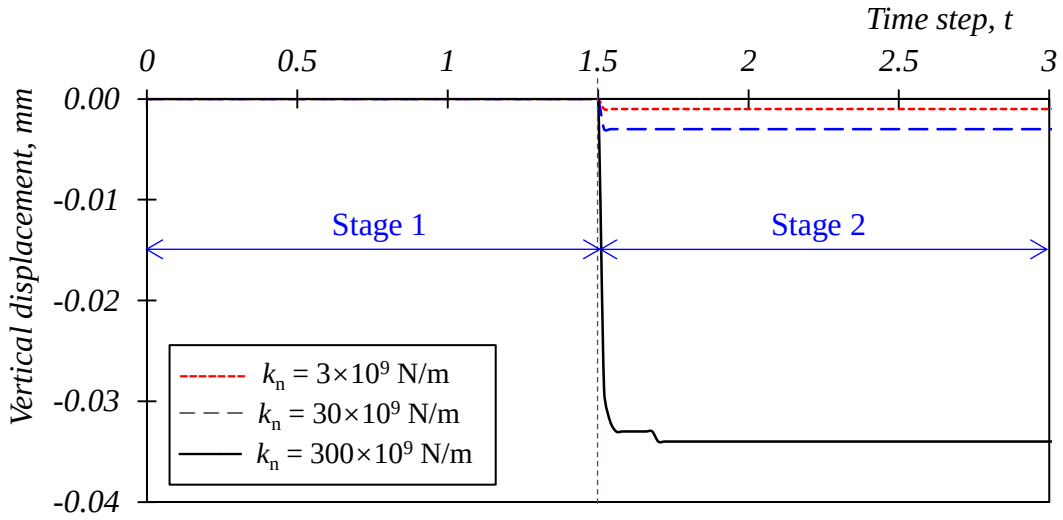

Figure 6-5 Comparisons of the vertical displacements versus time curves obtained from numerical analysis with different contact stiffness

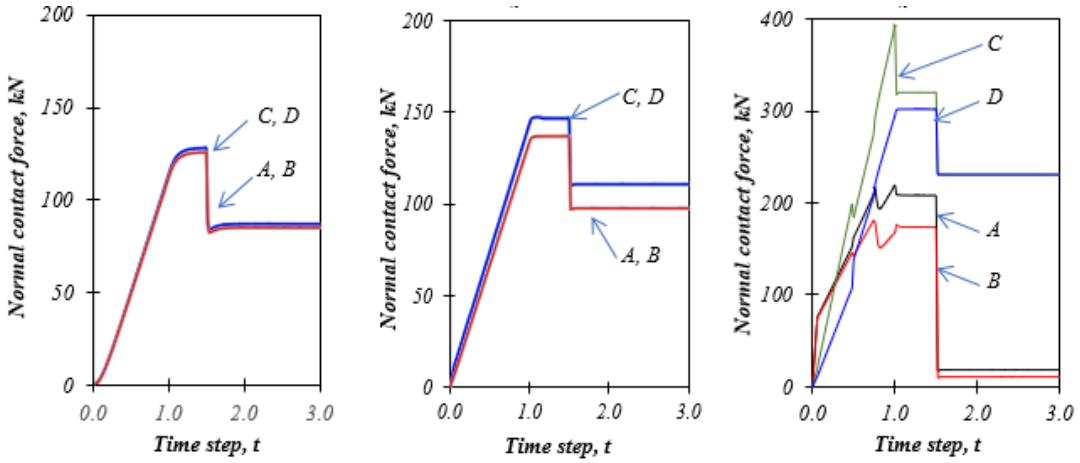

(a) (b) (c)

Figure 6-6 Comparisons of the normal contact forces versus time step curves when friction angle φ = 40° (a) the vertical displacements and the normal contact forces in the cases of (b) $k_n = 3\times10^9$ N/m, (c) $k_n = 30\times10^9$ N/m and (d) $k_n = 300\times10^9$ N/m

6.2.3. Parameter studies

Parametric studies are carried out to investigate the key parameters that might influence the reinforced effects of rockbolts when they are used to stabilize the rock wedge. The 2D-DDA model with the contact stiffness $k_n = 3\times10^9$ N/m and $k_s = 0.4k_n$ is adopted to assess the stability of rock wedge. The friction angle of the joints between the wedge and two surrounding rock blocks are assumed as 40°. The studied variables are the initial horizontal pressure (p), the spacing between two rockbolts (s_b) and the incline angles of the rockbolt with respect to the direction of rock falling (θ).

The effects of the horizontal pressure, p, are investigated by changing its magnitude and keeping s_b = 2.0 m and θ = 0°. As shown in Figure 6-7, the rockbolts are slightly loaded due to the joint displacement if the horizontal pressure $p > p_{cr}$, which means the wedge could be self-supported after stress redistribution. However, for $p \leq p_{cr}$, the wedge is unstable. The support force provided by each rockbolt is about half of the wedge weight (30 kN). The horizontal stress in the wedge after stress re-balance is about 6.2 kPa.

Three spacing between the two rockbolts are adopted to analyse the effects of the spacing, i.e., s_b = 0.5, 1.0 and 2.0 m and kept p = 80 kPa (< p_{cr} = 93 kPa) and θ = 0°.

The variations of rockbolt force in three cases are shown in Figure 6-8. In general, the axial load at the rockbolt element is decreasing with the decrease of spacing (s_b). The support force of each rockbolt when s_b = 0.5 m is about 77% of that when s_b = 2.0 m. The horizontal stress in the wedge after stress re-balance in the former case is about 27% of that of the latter case. This could be explained as the rockbolts with narrow spacing induce less deformation in the deformable wedge.

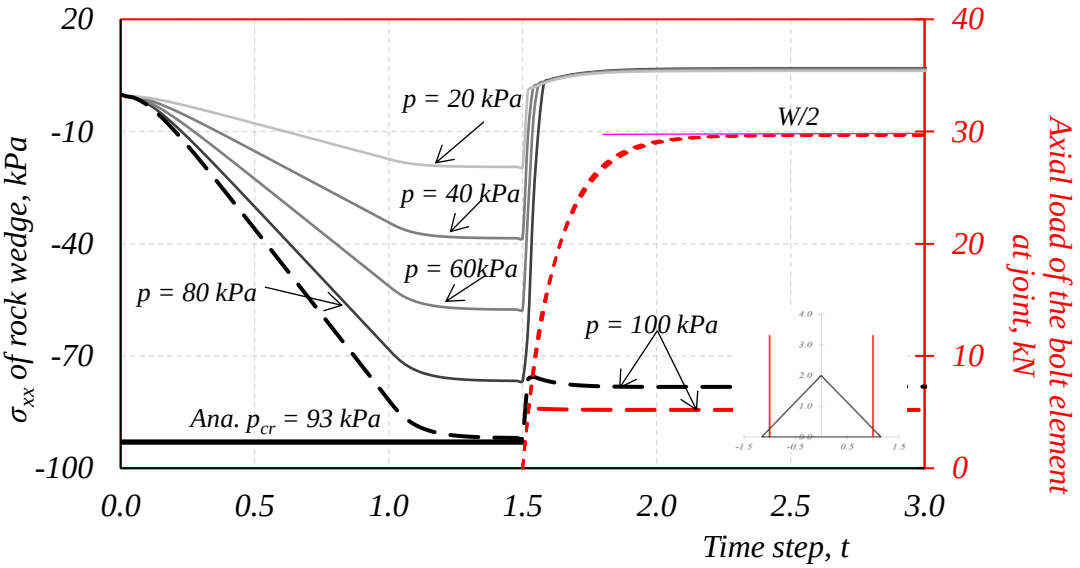

Figure 6-7 Effects of the horizontal pressure p on the reinforced efforts of rockbolts to stabilize the 2D wedge

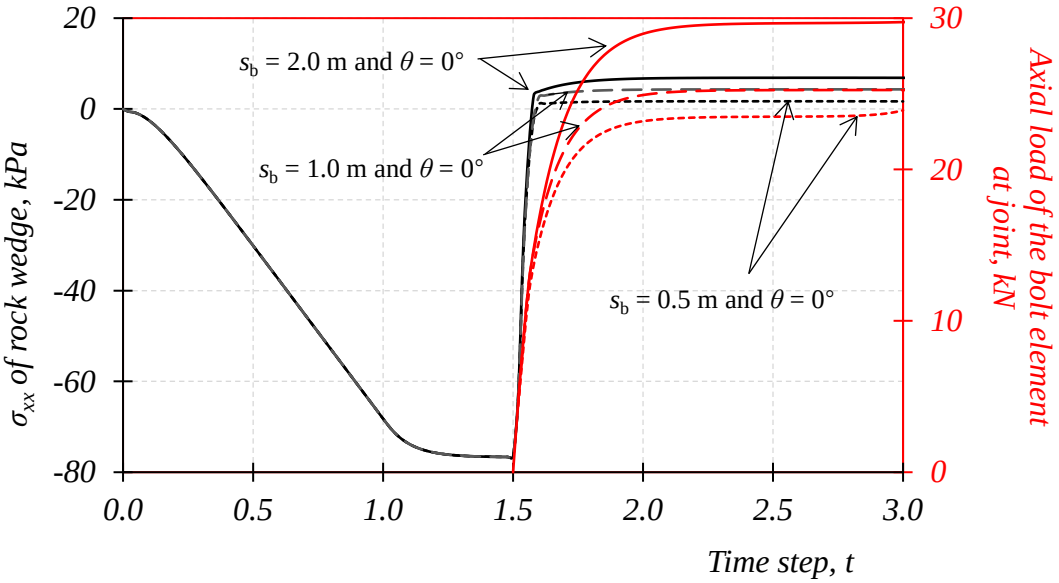

Figure 6-8 Effects of the bolt spacing s_b on the reinforced efforts of rockbolts to stabilize the 2D wedge

Two cases are analysed to investigate the effects incline angles of the rockbolt with respect to the direction of rock falling. If keep p = 80 kPa (< p_{cr} = 93 kPa) and s_b = 1.0 m, the required support force when θ = 45° will increases with a magnifying factor of sec(θ) from that when θ = 0°, as shown in Figure 6-9.

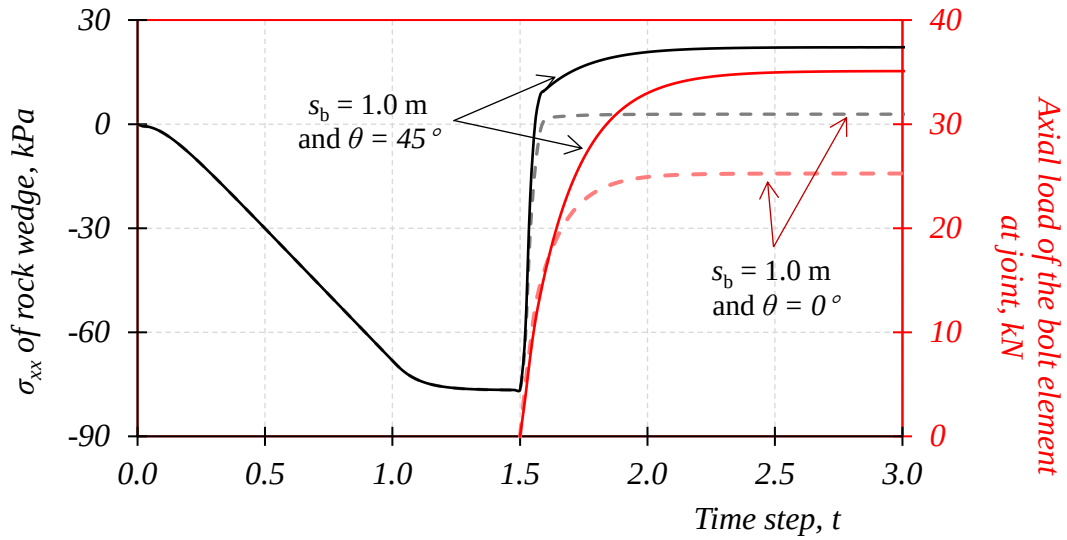

Figure 6-9 Effects of the installation angle θ on the reinforced efforts of rockbolts to stabilize the 2D wedge

6.3 Case study

The Jurong Rock Caverns (JRC) cavern was constructed beneath the seabed at the Banyan Basin in Jurong Island, Singapore, for hydrocarbons storage and located approximately 150m below ground in sediment rock. As shown in Figure 6-10, the cross-section of the storage galleries is in a horse-shoe shape with its height of 27 m and span of 20 m and excavated using the top heading and bench technique. The height of the top heading is about 9.0 m. A site investigation indicated that the ratio of maximum principal horizontal stresses to maximum principal vertical stress is approximately 2.0 (Zhou et al. 2017). The geological map showed there is one bedding plane and three joint sets on the site as shown in Figure 6-10 and summarized in Table 6-3. The rock mass was composed by dark grey mudstone interbedded with light grey sandstone. It also recorded that the bedding planes were not significant and there were other joints which were rough, dry water condition, fresh and strong. The rockbolt support method is used to restrain the unstable wedge in roof as shown in Figure 6-10. The 5.0 m long

rockbolt is installed in rectangular pattern with in-line spacing of 2.2 m and out-line spacing of 2.3 m. The shotcrete with thickness of approximately 80 mm is used to stabilize the excavation surface. One metric point in storage gallery, is selected in this study to illustrate methods of using proposed rockbolt model for rock wedge stabilization in the roof of rock cavern.

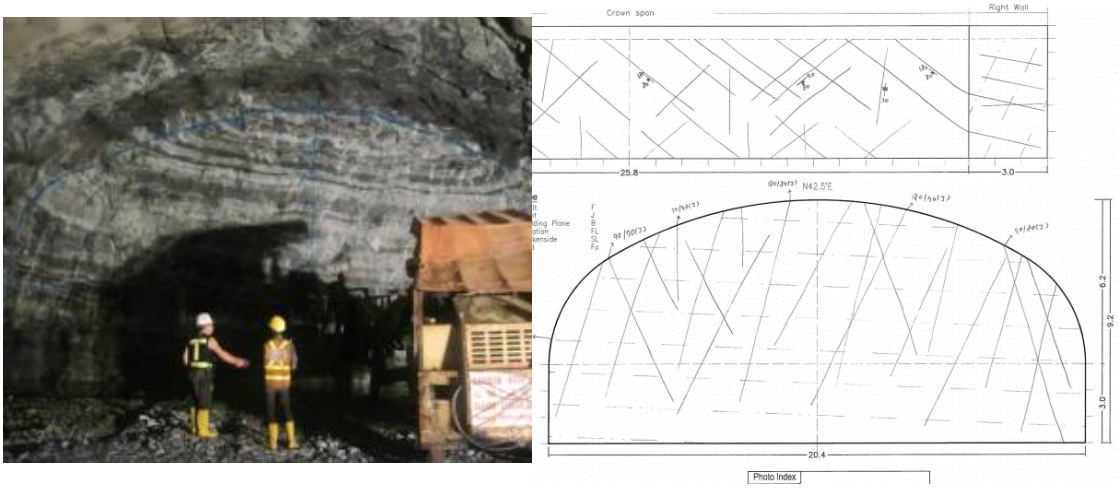

(a)

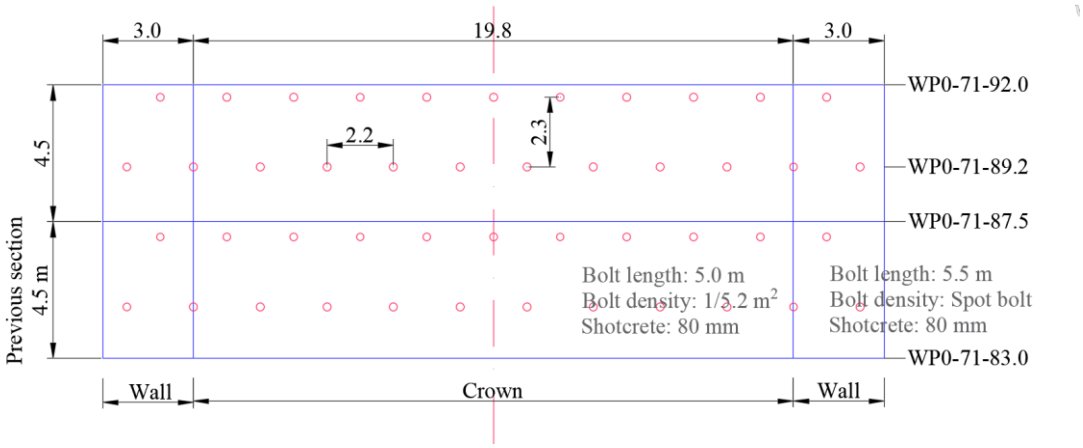

(b)

Figure 6-10 Site information after top heading (a) geological and (b)support conditions

Table 6-3 Characteristic of the discontinuities according to the site geological mapping after top heading

	Bedding	Joint 1	Joint 2	Joint 3
Dip, °	20 ~ 25	70 ~ 90	70 ~ 90	80 ~ 90
Dip direction, °	320	170 ~ 180	80 ~ 90	30 ~ 50
Friction angle (assumed), °	30	30	30	30

A spreadsheet is developed to estimate the removable key blocks in the cavern surface using key block theory proposed by Goodman and Shi (1985). Moreover, the envelopes of the possible removable pyramids at the roof and wall are projected on the cross section of the rock caverns which is also presented in the worksheet as shown in Figure 6-11. By gathering the geometry data and extending the boundaries of the envelopes, an approximated 2D blocky model could be constructed as shown in Figure 6-12(a). After invoking the 2D-DDA code, a 2D plane strain model could be adopted to simulate the wedge stability with or without rockbolts. The rock block has a Young's modulus of 12 GPa and density of 2.6 $\times 10^3$ kN/m^3. The joints are assumed with same properties as friction angle φ = 30°, cohesion c = 2MPa and tensile strength σ_t = 1MPa. According to the bolting design, two kinds of bolt arrangements are considered. Block A with an area of 10.7 m^2 on the immediate roof is chosen as the study target. According to the relative positions between rockbolts and block A, two reinforcement situations could be identified. One case, defined as Case A, is the rockbolts at metric axis WP0-71-89.2 are installed through block A as shown in Figure 6-12(b). The other case, defined as Case B, is the rockbolts at metric axis WP0-71-92.0 are installed through block A as shown in Figure 6-12(c).

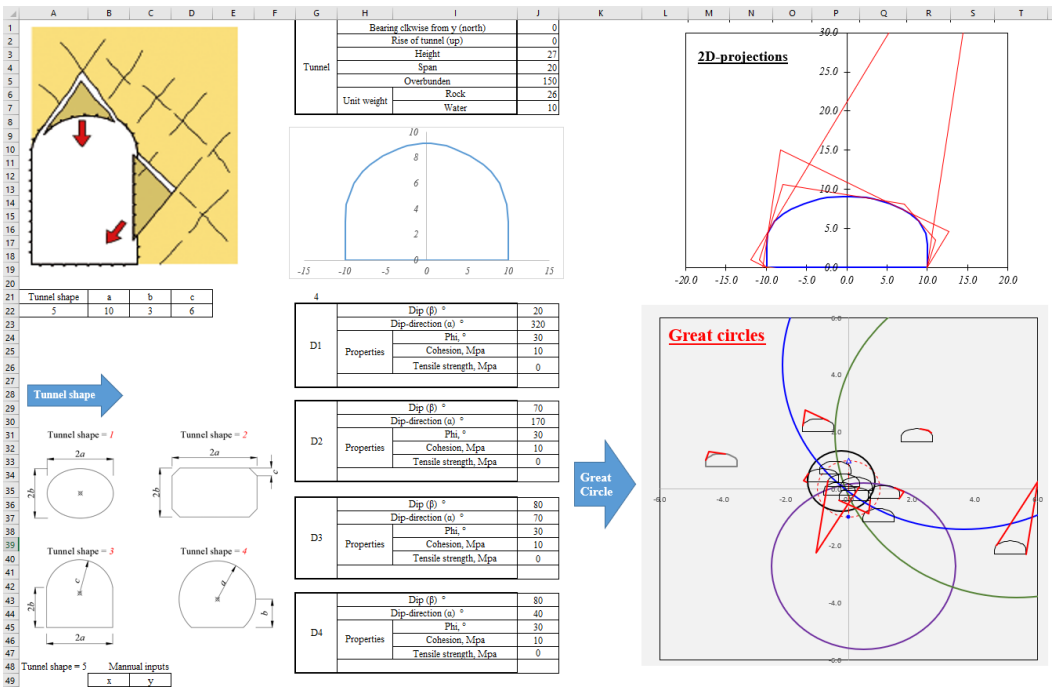

Figure 6-11 Method to estimate the removable key blocks in the cavern surface using key block theory

The simulation is conducted in three steps. The 1st step is to obtain the initial stress state. The 2nd step starts at time step t_0 = 60 when the excavation core is removed, followed by the 3rd step when the rockbolts are added in the model at time step t_b.

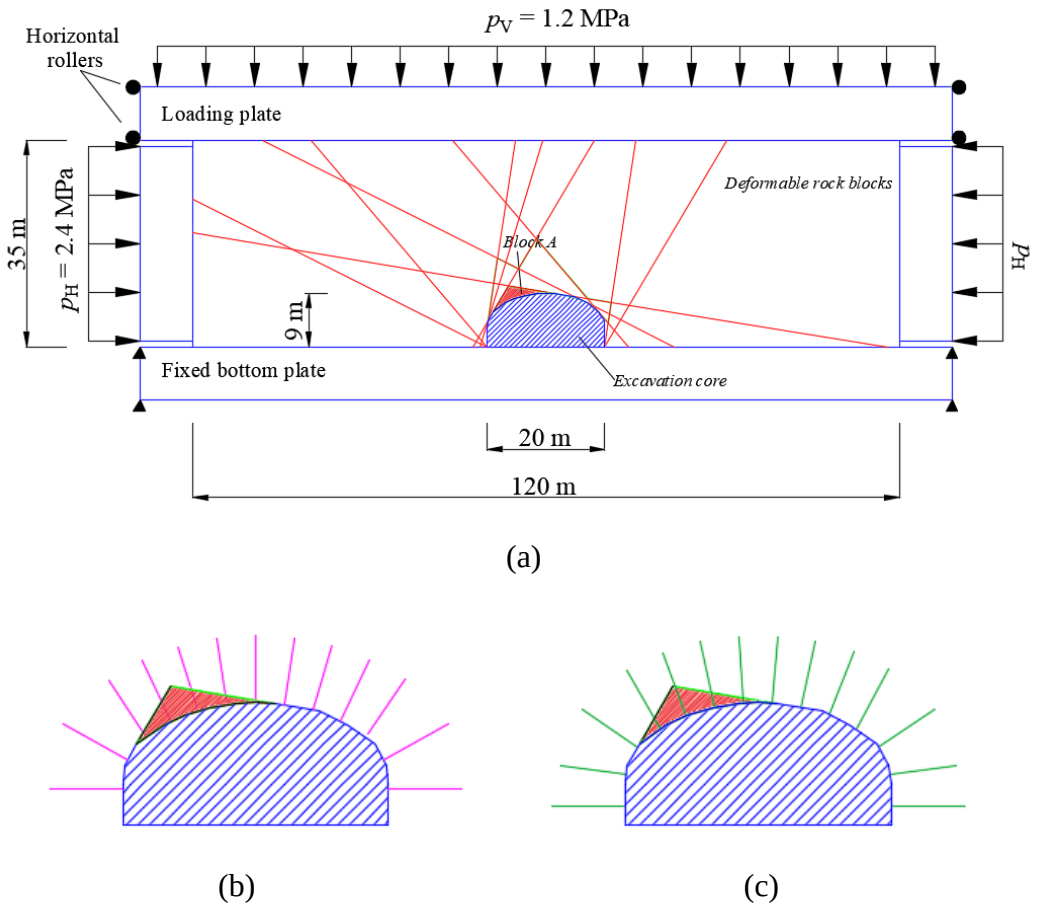

Figure 6-12 An approximated blocky model of (a) the cavern cross-section, (b) rockbolt arrangement of Case A and (c) rockbolt arrangement of Case B

Numerical studies are carried out to identify the major factors that affect the stability of block A for the case with no rockbolt reinforcement. Figure 6-13(a) plotted the vertical displacement versus time curves and the stress versus vertical displacement curves of block A for normal stiffness of the contact spring k_n = 1.2×10^9, 6×10^9, 12 ×10^9, 120 × 10^9 N/m, and $k_s = 0.4k_n$ .It can be seen that the soften contact with k_n = 1.2×10^9 and 6× 10^9 N/m will be resulted in a larger displacement after stress re-adjustment. As shown in Figure 6-13(b), the vertical stress is quickly rebalanced for k_n = 120 ×10^9 N/m, but progressively balanced for k_n < 12 ×10^9 N/m. To further explain the phenomena, Table 6-4 shows the horizontal stress contours σ_{xx} for k_n = 6×10^9 and 120 ×10^9 N/m at the step

time right after excavation, t = 60.05, and that at the step time after rebalanced, t = 100. It can be seen that the stress re-balance at block A for k_n = 120 ×10^9 N/m is much faster than that for k_n = 6 ×10^9 N/m. In the following, the simulation of k_n = 6 ×10^9 N/m is adopted to study the rockbolt performance during the stress redistribution and the wedge progressively movement.

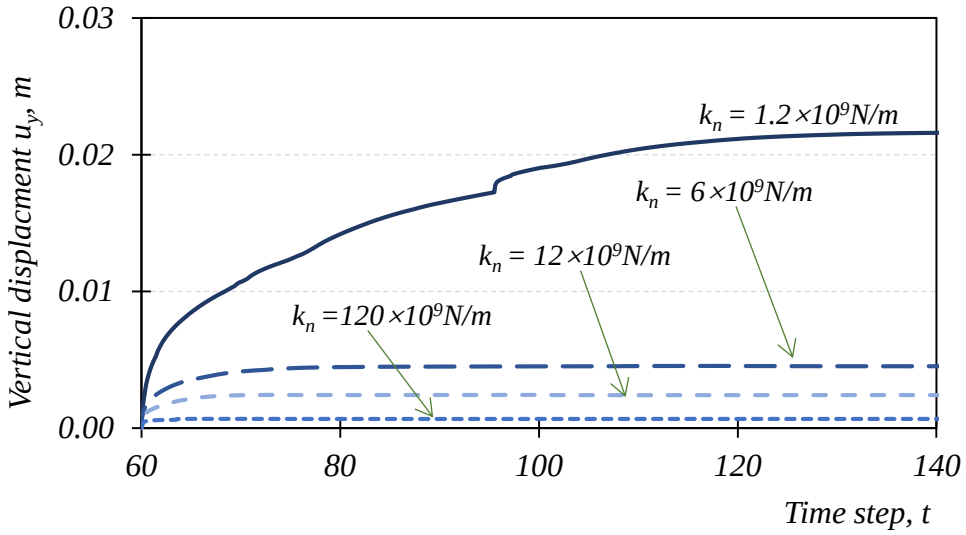

(a)

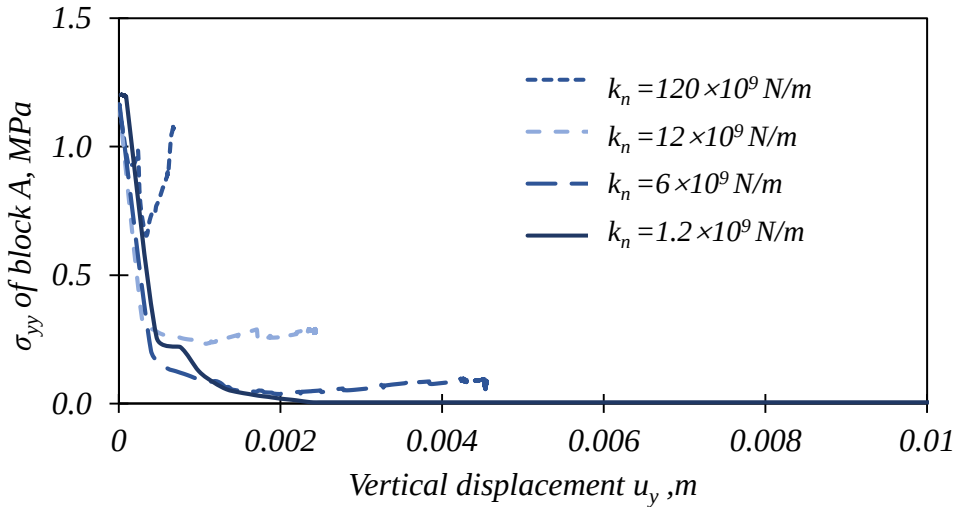

(b)

Figure 6-13 Simulated reactions of (a) vertical displacement and (b) the variations of stress versus displacement at block A under different joint relaxation situations

Numerical studies are also carried out to study the influences of rockbolting pattern and timing. For rockbolt installed in Case A and Case B as shown in Figure 6-12(b) and (c) respectively, totally five rockbolts are installed through the block A in different position. The total support forces of the five rockbolts acting on block A in the two cases are shown in Figure 6-14. It can be found the total support forces for rockbolts installed in Case A increase slowly with the time step than those for rockbolts installed in Case B at time t_b = 60. However, the ultimate support forces acting at the boundary of the block A in both cases are matched. The total support forces for rockbolts installed in Case B at step time t_b=60.05 and 61.0 are much lower than those installed at step time t_b=60. It can be concluded that the rockbolts installed at t_b=61.0 are too late.

Table 6-4 Contour maps of the horizontal stress σ_{xx} at different time step

	Installation time step = 60.05	Installation time step =100
$k_n = 120 \times 10^9$ N/m	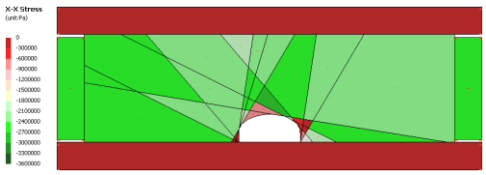	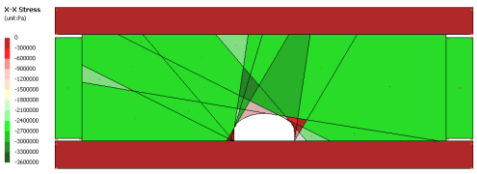
$k_n = 6 \times 10^9$ N/m	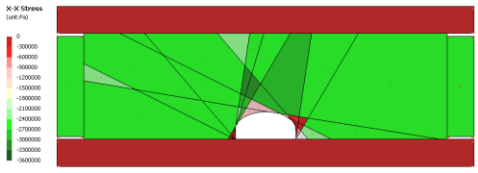	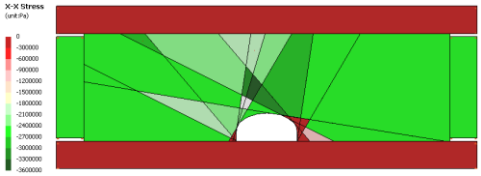
Note: Excavation occurs at step time 60.		

The installation position of the rockbolt determines the maximum axial force along the rockbolt. For rockbolt installed at step time t_b=60 in Cases B and A as shown in Figure 6-15(a) and (b), respectively, the maximum axial force always occurs in the second rockbolt from left to right. The difference of the maximum force in rockbolt installed in Case A is 13% higher than those installed in Case B. The maximum axial force along the rockbolt changes with respect to its installation time. For rockbolts installed at step time t_b=60, 60.05 and 61.0 in Case A as shown in Figure 6-14 (b), (c) and (d), the maximum axial forces at the second rockbolt from left to right are 89 kN, 43 kN and 20 kN, respectively. This is to say the maximum axial force along the rockbolt installed at step time t_b=60 reduced 345% than that installed at step time t_b=61.0.

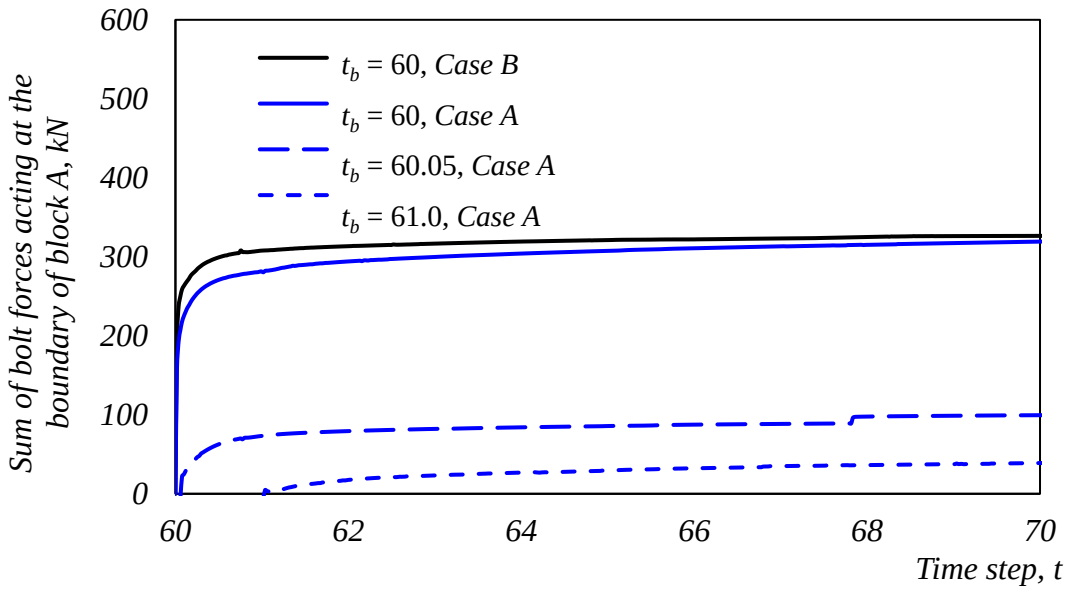

Figure 6-14 The total support force acting on block A in *Cases 5* to *9*

The installed rockbolts restrain the movement of block A. Figure 6-16 shows the numerical results of the stress versus vertical displacement curves of block A installed in Case A at step time t_b=60, 60.05 and 61.0. Results for the case of $k_n = 6\times10^9$ N/m with no rockbolt reinforcement is also plotted in Figure 6-16 for reference purpose. It can be seen that the earlier the bolting installed, the more restrains could be provided and less movement of the block A. For rockbolt installed at step time t_b=60, the displacement of block A could reduce by 0.4 mm or 9%. For the rockbolts installed at t_b = 60.05, the displacement of block A could reduce by 0.2 mm or 4%. However, for the rockbolts installed at t_b = 61.0, the rockbolt is carrying few loads and did not reduce the displacement of block A.

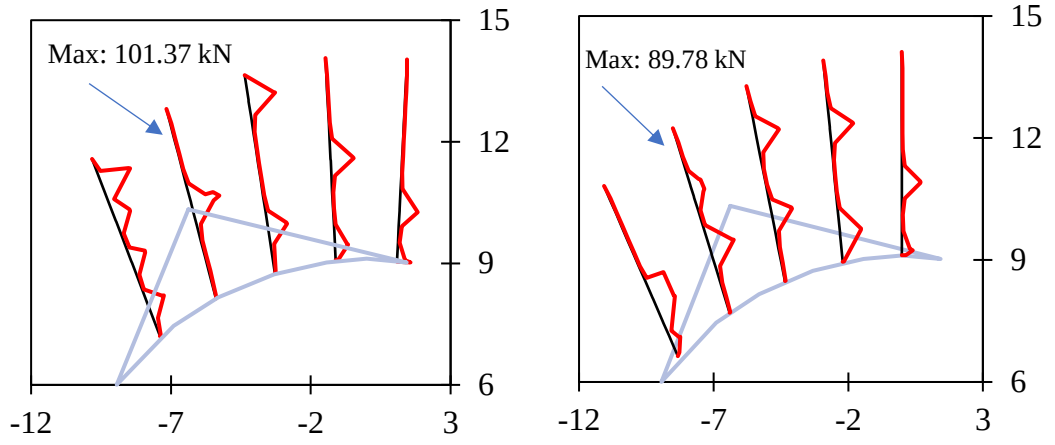

(a) t_b = 60, Case B (b) t_b = 60, Case A

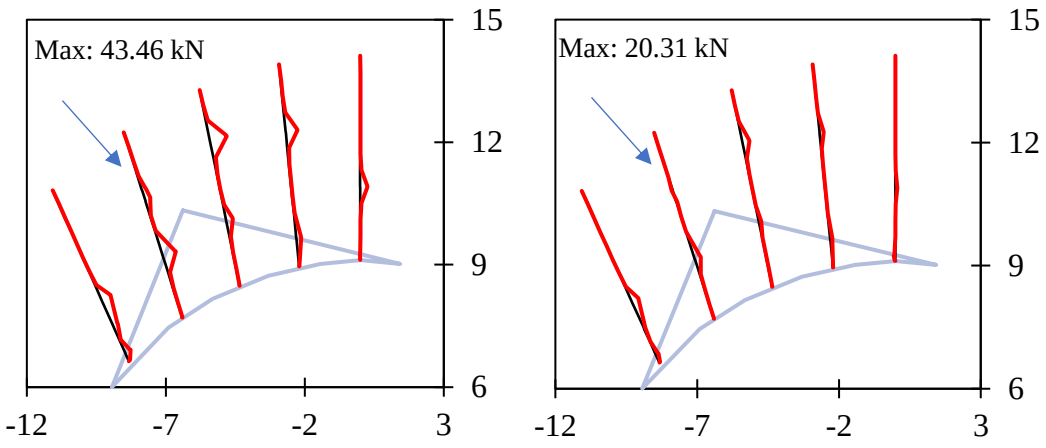

(c) t_b = 60.05, Case A (d) t_b = 61.0, Case A

Figure 6-15 Simulated axial forces along the rockbolts through block A

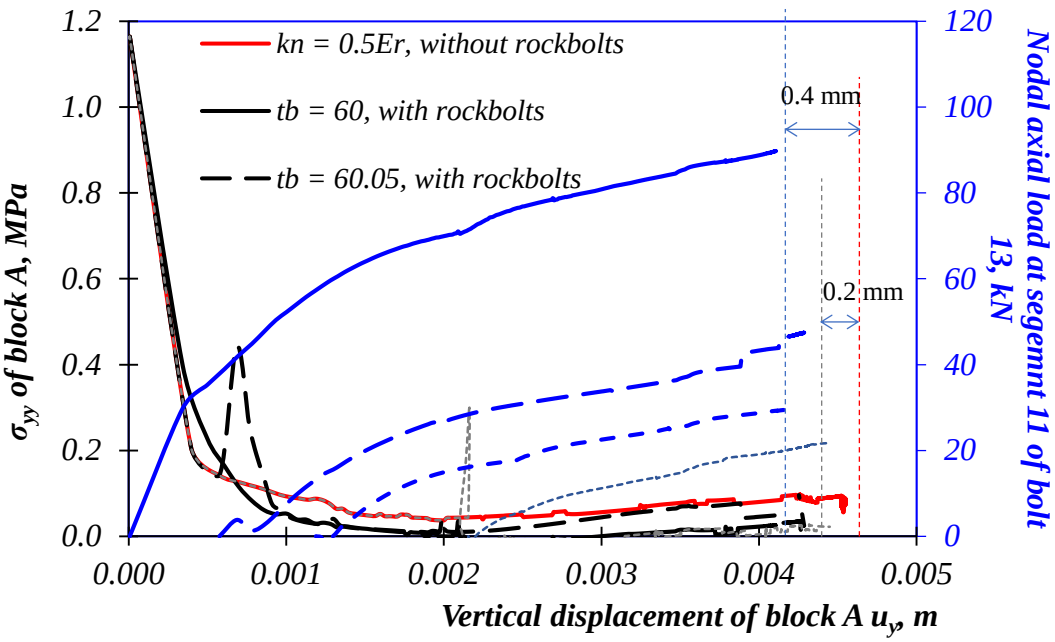

Figure 6-16 Simulated reactions of block A with varies rockbolting time

It should be noted that the proposed 2D-DDA model is constructed according to the projection of the 3D blocks on 2D tunnel cross-section based on Block Theory. The spreadsheet could quickly find the possible falling wedges and the projections of envelops. The average CPU time for the computation for the case study using 2D-DDA is about 40 min/case (on a PC of Intel Core 2 Quad CPU @ 3.0 GHz and 4.0 GB of RAM). Therefore, the proposed method provides a way to quickly access wedge stability and axial forces along rockbolt.

6.4 Conclusions

Unstable wedges might be exposed on the roof of the underground excavation. More advanced research should be carried out to investigate the rockbolt designs if the deformations induced by the readjustment of the stress field in the rock is comparable to those induced by the weight of loosen rock blocks. In this chapter, 2D-DDA is used to evaluate the rockbolt design to stabilize roof wedges in underground opening.

The joint relaxation method is adopted to represent a deformable rock mass under stresses. The results are calibrated using the analytical solutions. Parametric studies are carried out to investigate the key parameters that might influence the effects of rockbolts when they are used to stabilize the rock wedge. The results show 2D-DDA could be used to find the critical horizontal pressure to sustain the rock wedges using the contact stiffness $k_n = (3 \sim 30) \times 10^9$ N/m or $(1.3 \sim 13) \times E \times L$ and $k_s = 0.4k_n$ where E is the Young's modulus of the rock block and L is the length of the line across which the contact springs are attached. The wedge could be self-supported after stress redistribution if the horizontal pressure $p > p_{cr}$ and $\alpha \leq \varphi$. In such cases, the rockbolts are slightly loaded due to joint displacement. It also shows the bolt force slightly decreases when the spacing between two rockbolts decreases. However, the bolt force increases if there is shear components during the wedge deformation.

A case study to analyse the Jurong Rock Caverns (JRC), Singapore, is conducted to show the application of the 2D-DDA models for rockbolt design to support roof wedges. The block model is constructed based on the projection of the envelopes of possible wedges on the cavern cross-section. A spreadsheet is developed to estimate the removable key blocks in the cavern surface using key block theory. The reaction of the wedge block at the roof is used to study the reinforcement efforts provided by rockbolts. The result shows that the maximum axial force along the rockbolt is determined by the installation pattern and time of rockbolts. The stress versus vertical displacement curves showed clearly the effect of rockbolt on sustaining the movement of rock wedge. This way to create characteristic diagram could be used by the site engineers to evaluate the rockbolting design to sustain the possible roof wedges.

CHAPTER 7. PERFORMANCE-BASED SUPPORT DESIGN FOR HORSESHOE-SHAPED ROCK CAVERNS USING 2D FEM

The previous work on rock reinforcement mechanism aims to understand the rockbolt and rock mass interaction. It shows the rockbolt might be used as suspension structure to connect the loosen layers to the stable rock mass. The pattern rockbolts could be utilized to generate the artificial arch if the spacing is narrow enough. In this chapter, a support design method was proposed based on the ground reactions after excavation and support performances.

7.1 Introduction

An accurate knowledge of geological conditions is favourable for rock cavern excavation design. In the design stage, there is uncertainty due to naturally variable phenomena in time and lack of knowledge or understanding. The uncertainty also comes from the excavation which may affect the stress field and engineering properties of the surrounding rock mass. As shown in Figure 7-1, the influence zones due to excavation in rock are normally classified as Excavation disturbed Zone (EdZ), Excavation Damaged Zone (EDZ), and Highly Damaged Zone (HDZ) (Siren et al., 2015). The rock mass in the EDZ and HDZ are often fully yielded with very limited self-support capacity. The normal distance from the EDZ edge to the excavation surface is often defined as damage depth (D_p) to characterise the damage of the rock mass. Another commonly used parameter to represent the damage due to excavation is the convergence on the boundary of the excavation surface. The two parameters are often used for economic

evaluations for the rock cavern performance and supports designs (Kwon et al., 2009; Zhang and Goh, 2010; Hijazo et al., 2012; Siren et al., 2015; Feng et al., 2018).

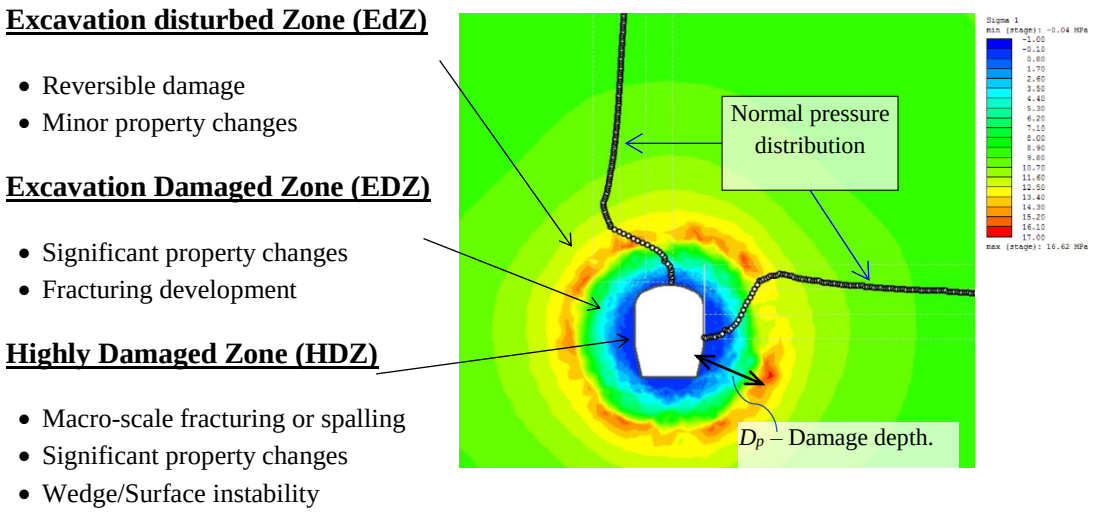

Figure 7-1 Influence zones due to excavation in rock (modified after Siren et al., 2015)

To reduce the damage depth and improve the self-support capacity of the surrounding rock mass, the sequential excavation method (SEM) is often used for excavation in rock by deliberately controlling and adjusting the stress and deformation field. One of the major steps in the SEM process is the selection of the sequential excavation parameters, such as the subdivision of cavern cross-section, the round length (or maximum unsupported excavation length), and the support installation locations (or support installation time). The sequential excavation parameters and the geological conditions determine the selection of the support systems which are usually classified using empirical methods, i.e. the RMR support system (Bieniawski, 1989) and the *Q*-system (NGI, 2015). The commonly used support system includes the rockbolt, steel set, shotcrete, concrete lining or a combination of the above.

The support system design has to consider its installation time and their interaction with the surrounding rock mass. The convergence confinement method (CCM) is a widely used method to assess the stress relaxation in the exacavation surface, the pressure on support and the progressive expansion of the EDZ at different excavation steps (Sinha, 1989; Carranza-Torres and Fairhurst, 2000; Alejano et al., 2010; Lü et al., 2011). The CCM uses characteristic curves to define the support-ground interaction. The characteristic curves include the Ground Reaction Curve (GRC), the Longitudinal

Displacement Profile (LDP) and the Support Characteristic Curve (SCC). As the stress re-distributions in the rock mass are quite complex during the excavation process, the characteristic curves in CCM are hard to be determined using analytical methods.

Numerical simulations for excavation in rock have been performed by many researchers to determine the characteristic curves (Karakus, 2007; Pellet et al. 2009). As a full 3D numerical analysis is usually too time-consuming for the preliminary support design, the suitable 2D finite element (FE) plane strain models are often used to consider the 3D excavation effects (Karakus, 2007; Cai, 2008; Janin et al., 2015; Kitchah and Benmebarek, 2016). The key difficulty in the application of the 2D model is how to determine the correspondence between the simulation stage and distance from the excavation face (Alejano et al., 2010). To solve this problem, an improved Longitudinal Displacement Profile (LDP) has been proposed by Vlachopoulus and Diederichs (2009, 2014).

In this chapter, the excavation in rock was simulated using the 2D FE plane strain models. Parametric studies were conducted to investigate the influence of SEM parameters and the geological conditions. Using the numerical results, the artificial neural network (ANN) models were built to identify the relationships among the geological conditions, the sequential excavation parameters and the cavern performances. An evaluation chart was proposed which could provide an evaluation of a support design for the rock caverns. A case study was also conducted to illustrate the process of using the proposed evaluation chart.

7.2 Theoretical background

7.2.1. Characteristic curves

The characteristic curves of CCM include GRC, LDP and SCC. The typical characteristic curves for excavation in rock are shown in Figure 7-2. The GRC gives the relationship between the pressure on ground (p_i) and the displacement at excavation surface towards the opening (displacement, u). The in-situ ground pressure before excavation is denoted as p_0. With the increase of displacement, the pressure on ground decreases linearly in elastic ground or nonlinearly in plastic ground. The point *D'* in GRC is the threshold that the rock mass starts to loosen and thus the supports have to be

installed before it. The LDP presents the relationship between the displacement (u) and the distance from the excavation face (x) which can be used to establish the displacement at excavation locations in the SEM process. The SCC is the plot of the pressure on support (p_s) versus the displacement (u) curve. The stiffness of the support determines the slope of the SCC. The SCC of the rigid Support B has higher slope than that of the flexible Support A.

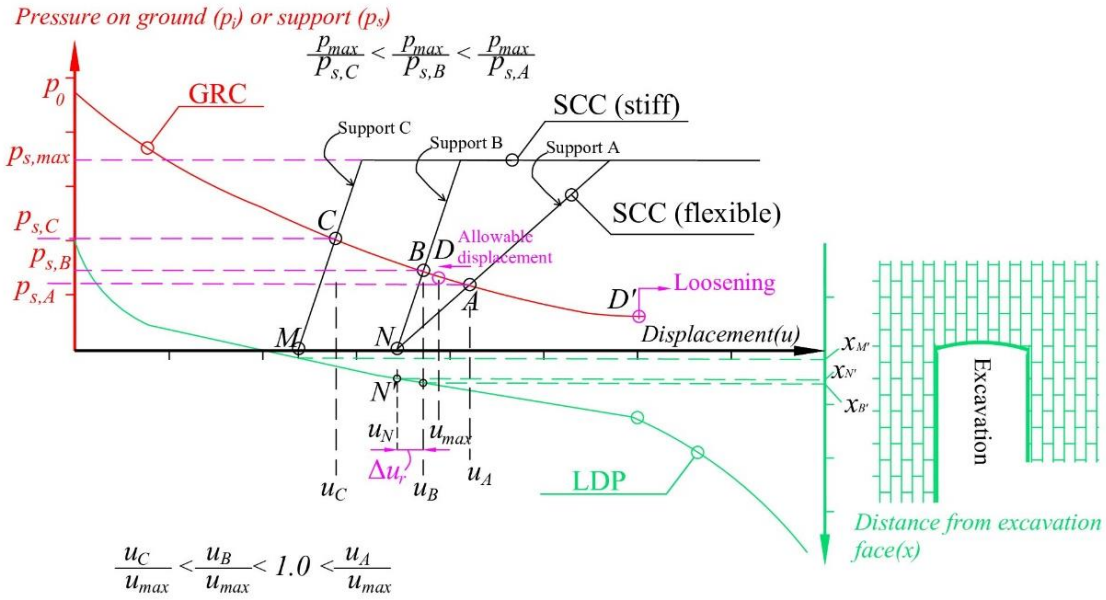

Figure 7-2 Characteristic curves for excavation in rock (modified after Lü et al., 2012)

The intersection of the SCC and displacement axis (point N) could be used to determine the installation position of the support using LDP (point N'). The intersection between SCC and GRC means the support pressure and the ground stress are balanced which could be used to determine the pressure on the supports. As shown in Figure 7-2, supports A, B, C have to sustain $p_{s,A}$, $p_{s,B}$, $p_{s,C}$, respectively. As the required pressure on support $p_{s,A}$ is the smallest among the three and much less than the support capacity $p_{s,max}$, the flexible support (Support A) installed at point N gives the highest factor of safety. The allowable displacement $u_{\max}$ is another parameter to restrain the support design which indicates that a rigid support (Support B) installed at point N' is more proper due to $u_B < u_{max} < u_A$. In this way, the characteristic curves can be used to evaluate the design of the support system.

7.2.2. Performance functions

To represent the performances, the support system has to satisfy the following three design criteria, i.e. displacement criterion, support capacity criterion and rockbolt length criterion. The performance functions (limit state functions) of the displacement criterion $g_1(\mathbf{x})$, the support capacity criterion $g_2(\mathbf{x})$ and the rockbolt length criterion $g_3(\mathbf{x})$ are shown as,

$$g_1(\mathbf{x}) = u_{\max} - u \tag{7.1}$$

$$g_2(\mathbf{x}) = p_{s,\max} - p \tag{7.2}$$

$$g_3(\mathbf{x}) = L_b - (D_p + l_0) \tag{7.3}$$

where: $\mathbf{x}$ is the vector of random variables,

$u_{\max}$ is the allowable displacement,

u is the displacement at the excavation surface to the opening,

$p_{s,max}$ is the bearing capacity of the support,

p_s is the pressure on support,

L_b is the length of rockbolt,

D_p is the damage depth of EDZ from the excavation surface, and

l_0 is the anchored length of rockbolt which is approximately 1.2 m.

The displacement coordinate of the intersection between SCC and GRC is the displacement at the excavation surface to the opening that the support system is fully functioned. However, the displacement at the installation position of support u' is different from that at the intersection of SCC and GRC. As shown in Figure 7-2, support B will provide support $p_{s,B}$ at point B with its displacement of u_B. The displacement at installation point N is u_N. The difference between u_B and u_N is the section in LDP. Therefore, the relationship between the displacements at the installation point u' and that the support system is fully functioned is:

$$u' = u - \Delta u_r \tag{7.4}$$

and

$$\Delta u_r = \frac{p_s}{K_s} \tag{7.5}$$

where p_s is the support stress and K_s is the support stiffness.

The load carrying capacity $p_{s,max}$ in Eq. (7.2) is not easy to be determined as the group effects of the support system are hard to be defined. It is usually assumed $p_{s,max}$ as the sum of the load carrying capacity of each individual support element (Hoek, 2007). The support capacities of three commonly used support systems, i.e. the steel set, the rockbolt and the shotcrete lining, and their stiffness on a circular tunnel with radius of r_0 have been proposed by Hoek (2007) and summarized in Table 7-1. The length of rockbolt L_b in Eq. (7.3) is determined by cavern span B when the rockbolt is used to suspend the failure zone to the natural arch. An empirical equation to estimate L_b (unit in: m) in moderately jointed hard rock masses has been proposed by Li (2007) and shown as:

$$L_b = 1.40 + 0.184B \tag{7.6}$$

Table 7-1 Support capacities defined by Hoek (2007)

Support elements	Parameters	Determined equations
Steel set support	Max. support pressure, $p_{max,ss}$	$p_{max,ss} = A_s\sigma_{ys} / s_l r_0$
	Stiffness, $K_{s,ss}$	$K_{s,ss} = E_s A_s / s_l r_0^2$
End anchored rockbolts in pattern	Max. support pressure, $p_{max,b}$	$p_{max,b} = T_{bf} / s_b^2$
	Stiffness, $K_{s,b}$	$K_{s,b} = E_b \pi d_b^2 / 4 L_b s_b^2$
Shotcrete linings	Max. support pressure, $p_{max,sc}$	$p_{max,sc} = \frac{\sigma_{cc}}{2}\left[1 - \frac{(r_0 - t_c)^2}{r_0^2}\right]$
	Stiffness, $K_{s,sc}$	$K_{s,sc} = \frac{E_c\left[r_0^2 - (r_0 - t_c)^2\right]}{2(1-\upsilon^2)(r_0 - t_c) r_0^2}$

Note: σ_{ys} is the yield strength of the steel, MPa; E_s is the Young's modulus of the steel set, MPa; A_s is the cross-sectional area of the section, m^2; s_l is the spacing of support along the tunnel axis; σ_{cc} is the *UCS* of the concrete or shotcrete, MPa; E_c is the Young's modulus of the concrete or shotcrete, MPa; υ_c is the Poisson's ratio of the concrete or shotcrete; t_c is the thickness of the shotcrete lining, m; d_b is the rockbolt diameter, m; s_b is the in-plane rockbolt spacing, m, here assumed $s_c = s_b$ (out-of-plane spacing), and E_b is Young's modulus of the rockbolt.

7.3 Analysis of horseshoe cavern using numerical method

7.3.1. Numerical models

A rock cavern with a horseshoe-shaped cross section (short as 'horseshoe cavern') has been successfully constructed in Singapore with span B of 20 m and height H of 27 m. The 2D FE plane strain model is conducted based on the dimensions of this horseshoe cavern using RS^2 program (Rocscience Inc., 2010), as shown in Figure 7-3(a). The height and the width of the horseshoe cavern are denoted as H and B, respectively. The distance of the cavern wall to the model boundary is set to $4H$. To study the effects of the sequential excavation, the full-face (FF) excavations and the subdivisions are considered in the numerical analysis.

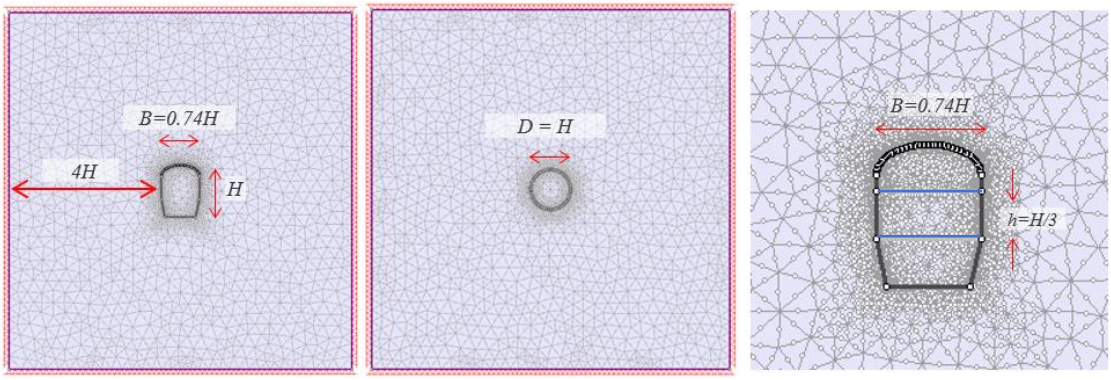

(a) (b) (c)

Figure 7-3 Numerical models using RS^2 program for (a) horseshoe cavern, (b) circular tunnel, and (c) horseshoe cavern under subdivision

The cavern is assumed under an isotropic stress state of 10 MPa (i.e., $\sigma_h = \sigma_v = 10$ MPa). Five ground classes are assumed based on Q-value, i.e., very good ($Q = 40$), good ($Q = 10$), fair ($Q = 4$), poor ($Q = 1.0$) and very poor ($Q = 0.1$). The elastic moduli of the rock mass before peak are calculated as (Bieniawski, 1984),

$$E_m = 2RMR - 100 \qquad (RMR > 50) \tag{7.7}$$

$$E_m = 10\text{^}((RMR\text{-}10)/40) \qquad (RMR \leq 50) \tag{7.8}$$

where RMR is the Rock Mass Rating (RMR) and calculated as,

$$RMR = 9.0\ln Q + 44 \tag{7.9}$$

The UCS of the rock mass is (Serafim and Pereira, 1983; Palmstrom, 2000),

$$UCS = RMR \tag{7.10}$$

The Geological Strength Index (GSI) of the rock mass is (Marinos et al., 2005),

$$GSI = RMR - 5 \tag{7.11}$$

The Hoek-Brown criterion (Hoek, 2007) is used to predict the yield of rock masses which can be written as follows,

$$\sigma_1' = \sigma_3' + \sigma_{ci}\left(m_b \frac{\sigma_3'}{\sigma_{ci}} + s\right)^a \tag{7.12}$$

where σ'_1 and σ'_3 are the maximum and minimum effective principal stresses at failure, respectively, m_b is the value of the Hoek-Brown constant m for the rock mass, s and a are constants which depend upon the rock mass characteristics, and σ_{ci} is the UCS of the intact rock samples.

For the residual properties of rock mass, such as E_m, UCS, GSI, m_i, m_b, s and a, the linear interpolation method is used to calculate their values based on the intervals of GSI proposed by Alejano et al. (2010). All the properties of the rock mass used for the numerical analysis are summarized in Table 7-2.

Table 7-2 Geotechnical parameters for numerical models

Q		0.4	1.0	4	10	40
RMR		36	44	56	65	77
Before Peak	UCS (MPa)	36	44	56	65	77
	GSI	31	39	51	60	72
	E_m (GPa)	4	7	13	30	50
	m_i	12	15	15	20	20
	m_b	0.985	1.698	2.515	4.793	7.358
	s	0.0004	0.0011	0.0039	0.0117	0.0445
	a	0.522	0.512	0.506	0.503	0.501
Residual	GSI	2.3	3.2	3.5	6.5	10
	E_m (GPa)	20	27	30	35	40
	m_i	10	10	10	10	10
	m_b	0.574	0.737	0.821	0.981	1.173
	s	0.0001	0.0003	0.0004	0.0007	0.0013
	a	0.544	0.527	0.522	0.516	0.511

The excavation effects in rock are simulated using the progressive core replacement method or stiffness reduction method proposed by Swoboda (1979). The excavation core and surrounding rock mass are initially assigned with same mechanical properties and calculated to get their initial balanced stress state. The properties of the excavation core are then replaced and assigned by softened unstressed elastic material. The surrounding rock mass will converge, while the stress filed will rebalanced. The process of replacement is repeated till the excavation core is totally removed from the model. Totally ten stages are used to simulate the excavation process. Point M1 right above the middle of the roof surface (out of excavation core) is used to record the roof displacement towards opening (u). Point M2 right below the middle of the roof surface (in the excavation core) is set to record the normal stress on the ground (p_i). The normal stress p_i versus roof displacement u is the GRC as shown in Figure 7-4.

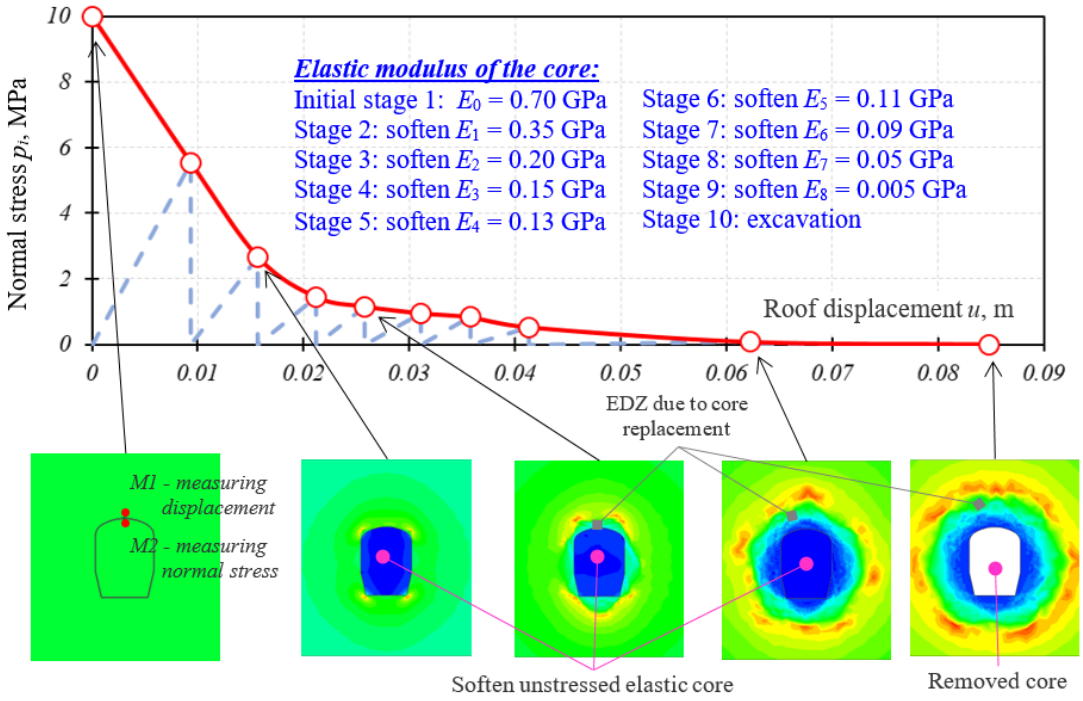

Figure 7-4 Illustration of the progressive core replacement method (span = 20 m under fair rock condition)

Another circular tunnel model with diameter $D = H$ as shown in Figure 7-3(b) is used to determine the LDP curve for horseshoe cavern by assuming it is the same as that of the circular tunnel (Vlachopoulos and Diederichs, 2014). The damage depth (D_p) of each simulation stage is recorded. The simulation stages are associated with the locations

from the excavation face along the tunnel axis based on the empirical equation (Vlachopoulos and Diederichs, 2009) as:

for $x < 0$, in the rock mass: $$u^* = \frac{u}{u_{\max}} = u_0^* \times e^x \quad (7.13a)$$

for $x = 0$, at face: $$u_0^* = \frac{u_0}{u_{\max}} = \frac{1}{3} e^{-0.15R^*} \quad (7.13b)$$

for $x > 0$, in the cavern: $$u^* = 1 - (1 - u_0^*) \times e^{-\frac{3x}{2R^*}} \quad (7.13c)$$

where R^* is the normalized plastic radius, $R^* = R_P / R_T$, R_T is the tunnel radius, R_P is the radius of plastic zone, $u_{\max}$ denotes the maximum radial displacement, u_0 is the radial displacement at the face location.

The SEM parameters and the geological conditions are essential to determine the support system in the preliminary design stage. The numerical model to analyse the effects of the subdivision is shown in Figure 7-3(c). The dimensions of the horseshoe shaped cross-section used for parametric study are scaled with the ratio *B/H* of 0.74 based on the rock cavern model as shown in Figure 7-3(a). The cavern cross-section is evenly subdivided into multiple sections based on the cavern height by assuming the height of top-heading equals to that of benching. It is assumed that the sequenced models for FF excavation are also valid to simulate the 3D subdivision excavation (Vlachopoulos and Diederichs, 2014).

7.3.2. Parametric study and characteristic curve

（1）Effects of the *Q*-value

The effects of *Q*-value on the EDZ development are investigated using the numerical analysis of the horseshoe carven with B = 20 m and H = 27 m. The roof displacements u versus the distance from the excavation face x curves (LDP) are plotted in Figure 7-5(a). It can be seen that the roof displacements increase nonlinearly with respect to the distances from the excavation face when $Q < 4$. For $Q > 10$, the roof displacement is not changing significantly along the excavation axis which indicates the ground is strong enough for self-support of the horseshoe carven. If an allowable roof displacement is set as $u_{\max}$ = 20 mm, the unsupported distance for good to very good

ground (Q > 10) could be more than 10.0 m. For a fair ground condition (4 < Q < 10), the unsupported distance is less than 6.0 m. For poor or even worse ground conditions (Q < 4), the roof displacement at the excavation face cannot satisfy the allowable value.

The damage depths versus the distances from the excavation face curves are shown in Figure 7-5(b). As expected, the smaller the Q-value, the deeper the damage depth is generated in the surrounding rock mass. The damage depth increases nonlinearly with respect to the distances from the excavation face. For the cavern span of 20 m, the rockbolt length is recommended of 5.0 m according to the support categories of the Q-system (NGI, 2015). According to Eq. (7.3), the depth of EDZ from the excavation surface is calculated as 3.8 m which can be used to separate the purposes of the rockbolt as suspension and arching. For D_p > 3.8 m, the rockbolt might not connect to the undamaged rock mass which indicates the spacing of the rockbolt has to be reduced to assist the formation of artificial arch in the surround rock mass.

The normal stress versus roof displacement curves (GRC) for the horseshoe cavern excavated in five ground classes are plotted in Figure 7-5(c). It shows the normal stresses reduce nonlinearly with respect to the roof displacements. The smaller the Q-value the larger normal stresses are generated in the surrounding rock mass and thus larger support pressures are required. Eq. (7.2) could be used to assess the support safety once the maximum support capacity of the support is known.

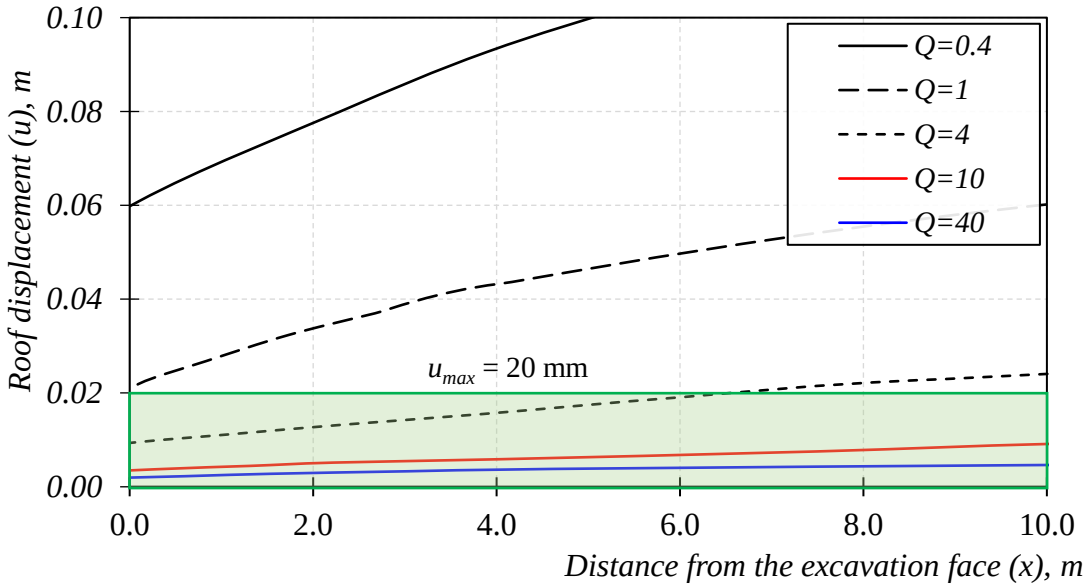

(a)

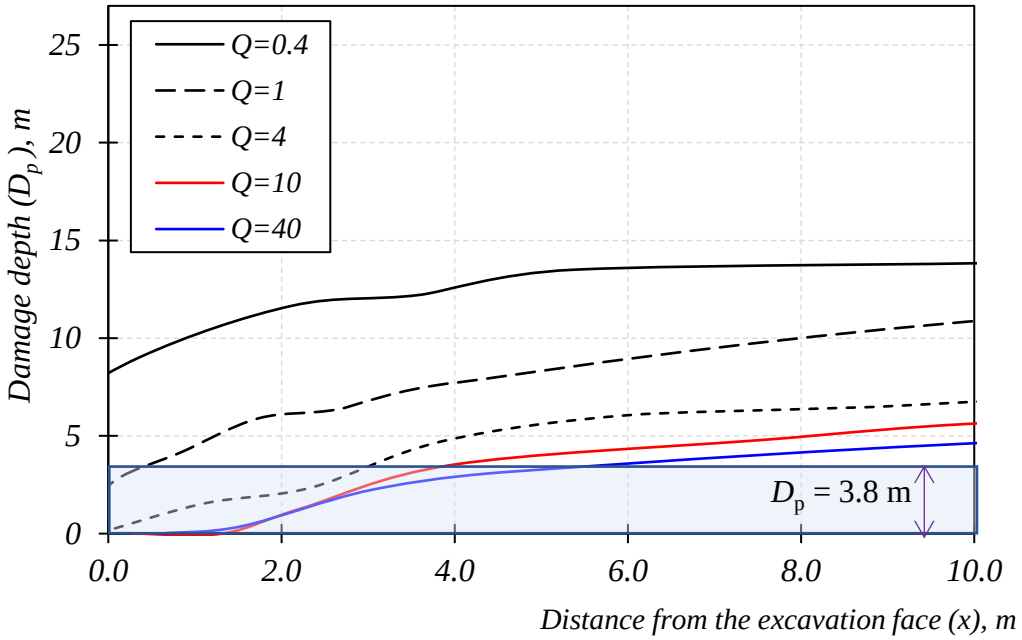

(b)

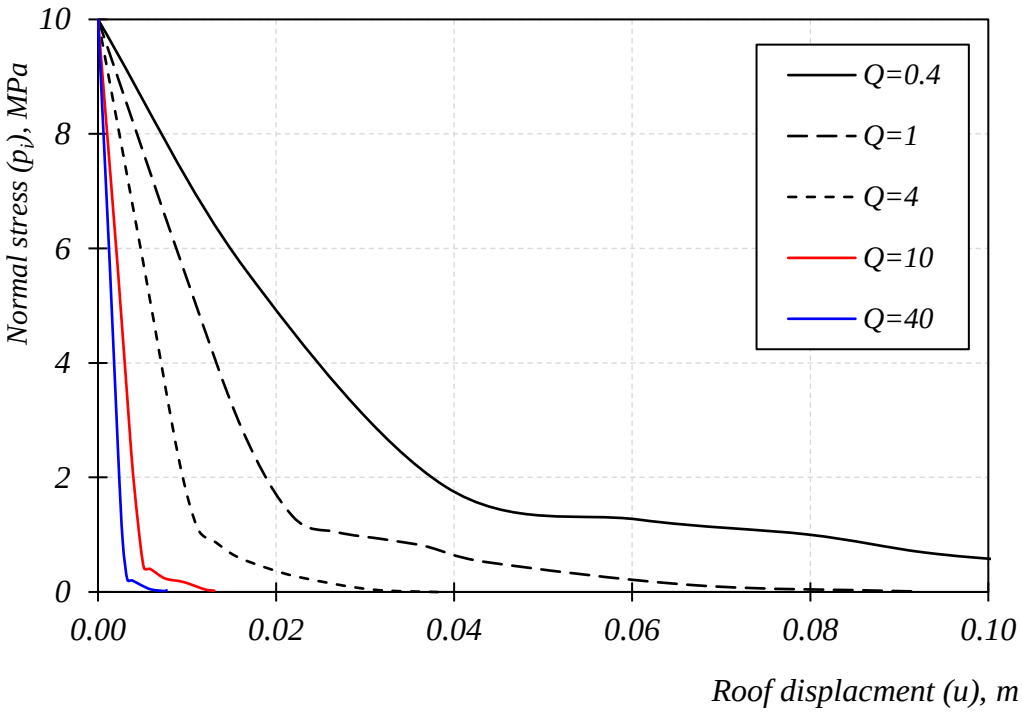

(c)

Figure 7-5 Effects of *Q*-value on the cavern performance (a) LDP, (b) damage depths at the roof from the excavation face, and (c) GRC

(2) Effects of the SEM parameters

The effects of the subdivision of cavern cross-section and the round length or the maximum unsupported excavation length are investigated. The horseshoe caverns with span B of 5 m, 8 m, 10 m, 15 m, 20 m, 25 m and 30 m excavated in five different ground conditions represented by Q-value of 40, 10, 4, 1 and 0.4 are considered. The ratios of the damage depth to span (D_p/B) versus Q-values are plotted in Figure 7-6(a) which shows nonlinear relationships. The larger the round length the larger the ratio D_p/B. The roof displacement versus normal stress curves for the subdivisions using 2-sections, 3-sections, 4-sections and full face (FF) are shown in Figure 7-6(b). It can be seen that the normal stress reduces nonlinearly with respect to the roof displacement.

However, there is no obvious relationship for the four subdivision processes. The normal stress versus u/B plots for certain subdivision excavation and Q-value could indicate the differences of the subdivision method, see FF and 3 subdivided sections excavated in rock mass with Q = 1.0 in Figure 7-6(c). More advanced function is still required to present the relationship between the SEM parameters and the cavern performance.

7.4 Prediction of cavern performance using ANN

The ANN models are built to identify the relationships among the geological condition parameters, the excavation design parameters and the cavern performances obtained from the numerical analyses. The ANN is the multi-layer feed forward back-propagation network which has been widely used in rock engineering for data analysis to find their complex relationships (Zhao and Ren, 2002; Zhao et al, 2008; Tiryaki, 2008). In this study, a 4-**n**-1 structure is used to map the relationships between a set of SEM design parameters P_i (i.e., ground class P_1, width of top heading P_2, height of top heading P_3, round length P_4) and support performance O_j (i.e., normal stress O_1, damage depth O_2 or roof displacement O_3) as shown in Figure 7-7. The **n** varies in the three models to predict the support performance O_j based on the training and testing errors.

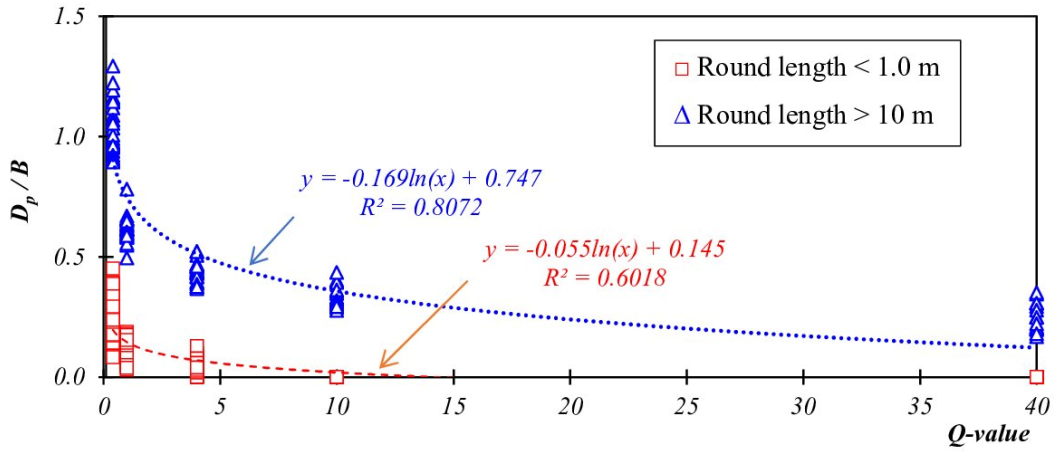

(a)

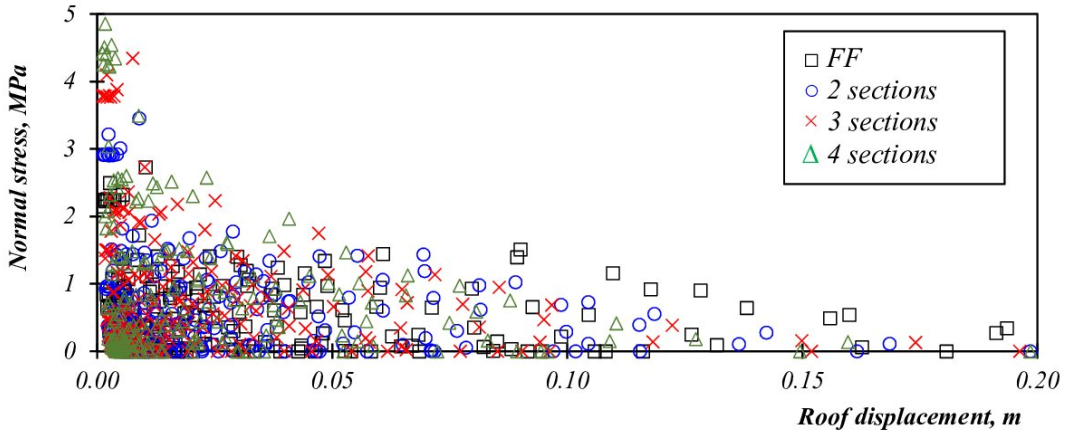

(b)

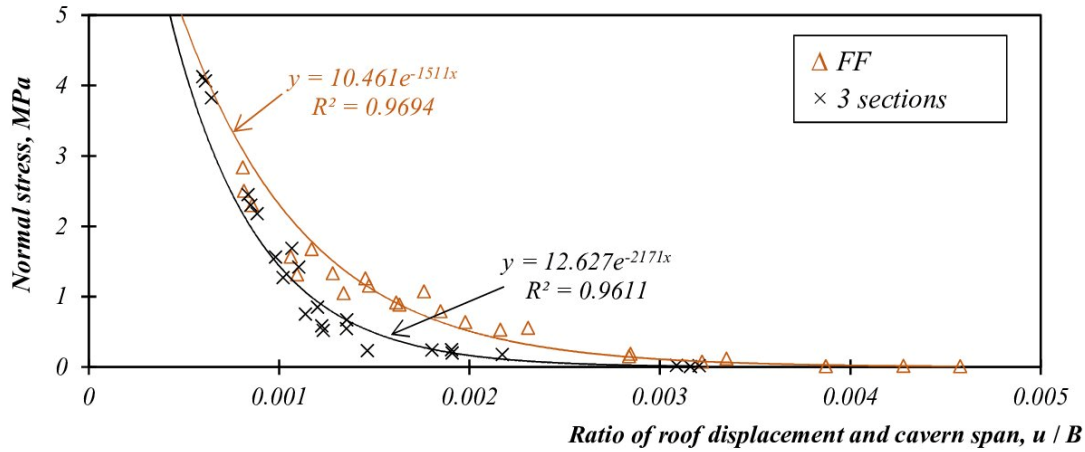

(c)

Figure 7-6 Effects of the SEM parameters on cavern performance (a) the round length, (b) the cavern size, and (c) the cavern size for 3-section excavation in case of Q = 1.0

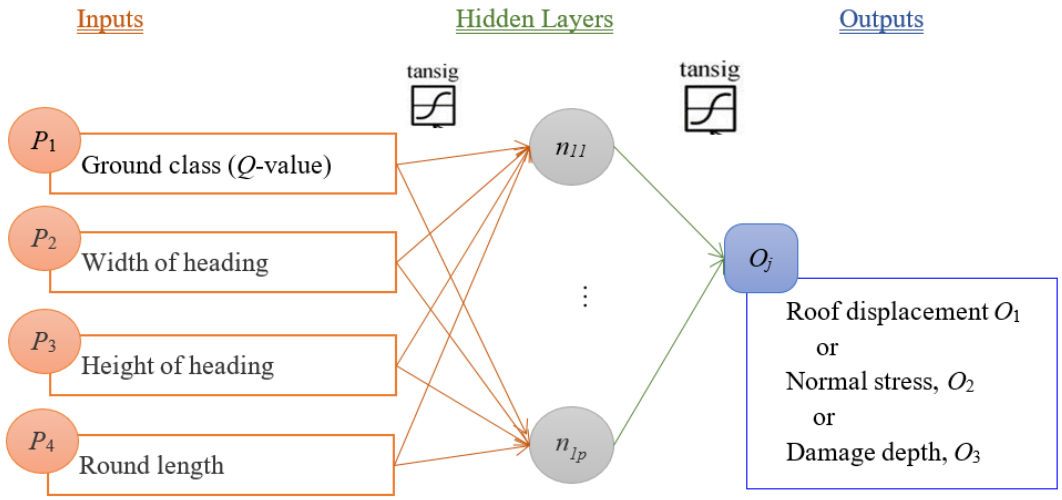

Figure 7-7 Architecture of the ANN models

The transfer function is tangent sigmoid transfer function, denoted as 'tansig' in Figure 7-7, for both the hidden layer and the output layer, which can be expressed as,

$$f\left(P_i\right)=\frac{1}{\arctan(P_i)+1} \tag{7.14}$$

where $f(P_i)$ is tangent sigmoid transfer function, P_i is the inputs, i = 1 for ground class, i = 2 for width of top heading, i = 3 for height of top heading, and i = 4 for round length.

There are 700 data generated from the numerical analysis. Approximately 70% of them are randomly chosen as training data while the rest of them are used for testing. The input P_i are normalized using the minimum and the maximum magnitudes of the parameter P_i based on the numerical results as summarized in Table 7-3. The equation to normalize parameter P_i is shown as,

$$P_i^{'}=\frac{2\left(P_i-P_{i,\min}\right)}{P_{i,\max}-P_{i,\min}}-1 \tag{7.15}$$

where $P_{i,\min}$ and $P_{i,\max}$ are the minimum and the maximum magnitudes of the parameter P_i, respectively.

The network is essentially trained using optimization methods by adapting the weights and biases of neurons and minimizing the mean square error between the predicted and the target values. The MATLAB code is attached in Appendix C. The performance of the ANN models for training the numerical results to predict the damage depth and the

normal stress are shown in Figure 7-8(a) and (b), respectively. The comparisons between target and predicted values of the damage depth and the normal stress are shown in Figure 7-9(a) and (b), respectively. The results show very good agreements between the predictions and the testing data.

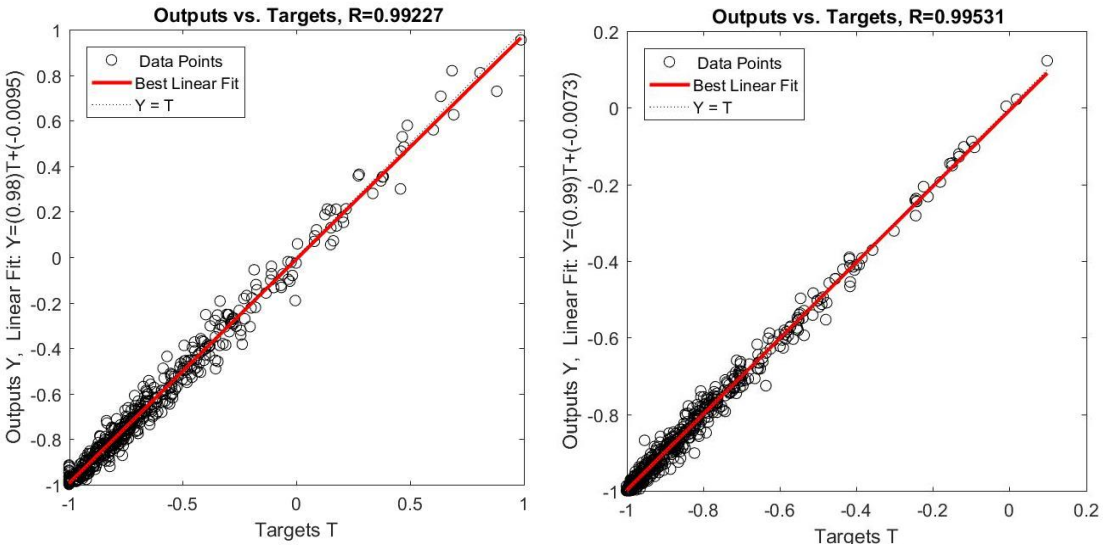

(a) (b)

Figure 7-8 Performances of the ANN models to train the numerical results to predict (a) the damage depth and (b) the normal stress

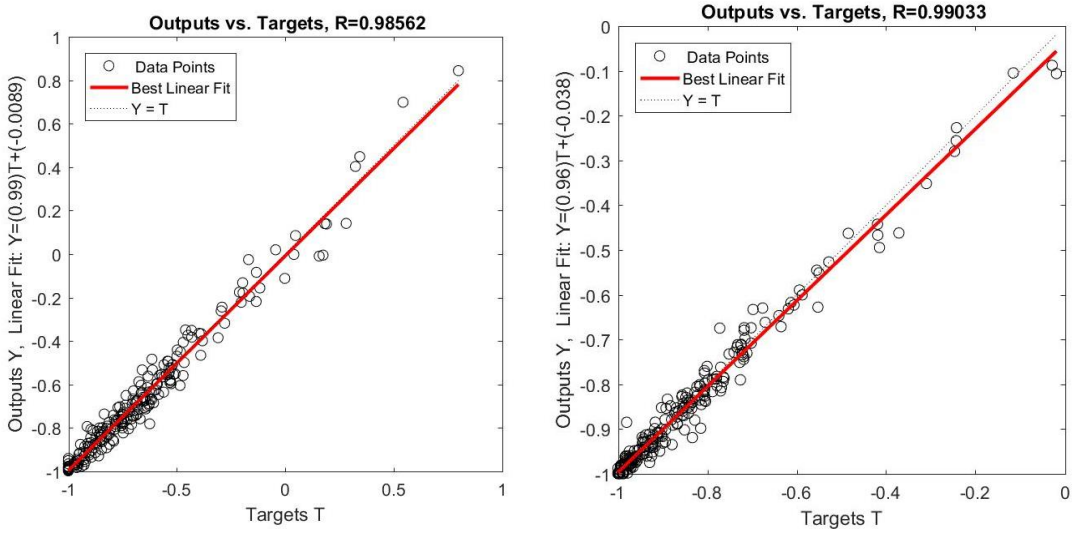

(a) (b)

Figure 7-9 Comparisons between the targets and the predicted values of (a) the damage depth and (b) the normal stress

Table 7-3 Magnitudes of P_i and O_j for normalization based on numerical results

	P_1	P_2	P_3	P_4	O_1	O_2	O_3
	Q value	Span, m	Height of top heading, m	Round length, m	Roof displacement, m	Inner pressure, MPa	Damage depth, m
Max.	40	40	54	50	0.3	10	50
Min.	0.1	3	5	0	0	0	0

7.5 Development of an evaluation chart based on ANN models

To directly use the ANN models for preliminary support design, an evaluation chart is proposed and coded using Microsoft Excel as shown in Figure 7-10. The evaluation chart contains the following five parts, the inputs of cavern geometry and ground class (A. Inputs), the prediction of cavern performance using ANN models (B. Prediction), the SEM design parameters (C. SEM Design), the support design parameters (D. Support Design), and the support performance based on the predicted results (E. Performance Functions).

The cavern geometry and ground class in part A have the maximum and minimum boundaries as summarized in Table 7-3. For part B, the proposed three ANN models are adopted to generate the response surfaces and predict the damage depth and the stress on support. Based on the above ANN models, the support performance O_j (i.e., normal stress O_1, damage depth O_2 or roof displacement O_3) are calculated as,

$$O_j = f\left[\sum_{i=1}^{n} w_{ji} P_i + b_j\right] \tag{7.16}$$

where: w_{ji} is the weights of the neuron j, and b_j is the bias of the neuron j.

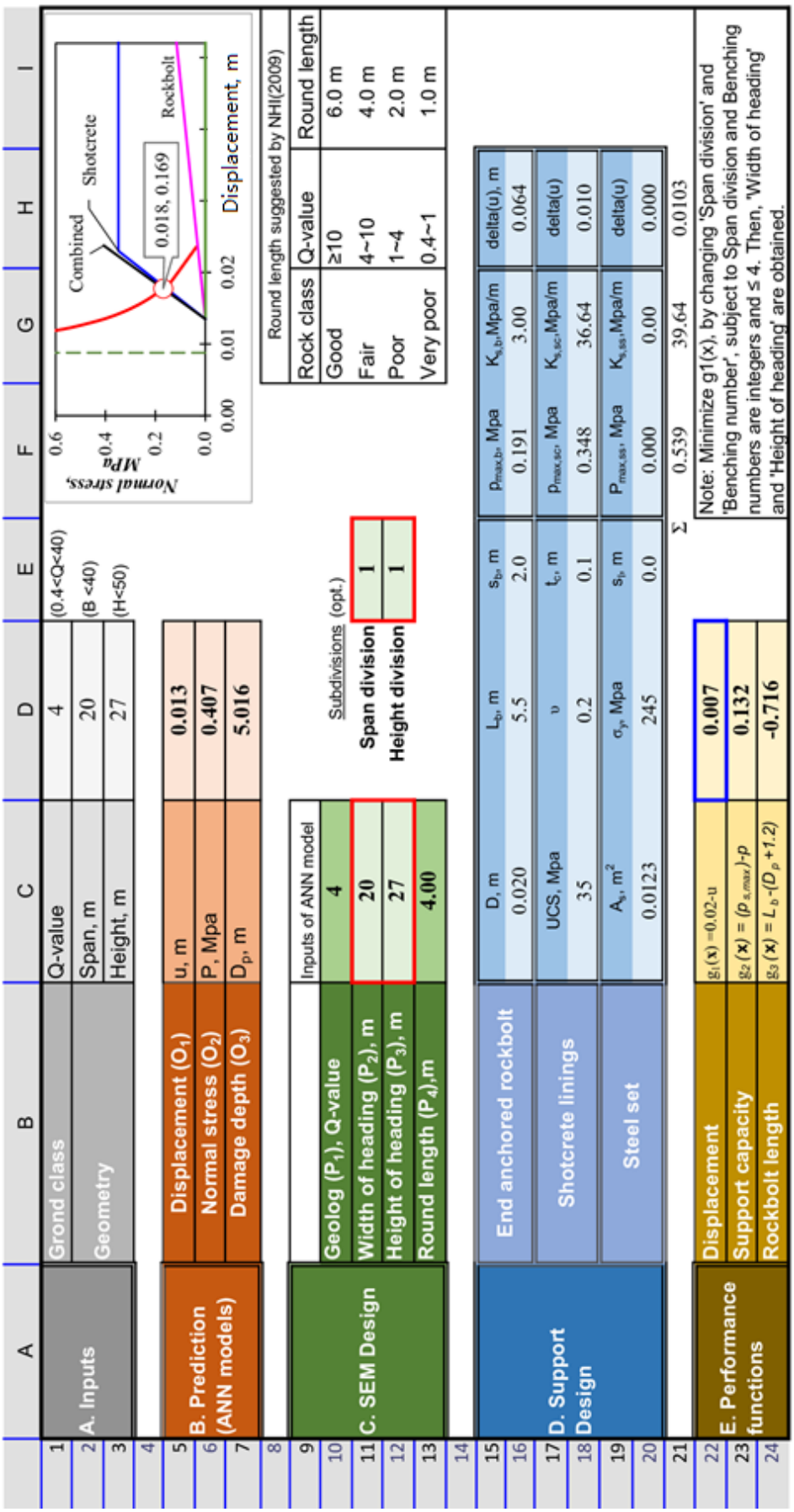

Figure 7-10 Evaluation chart for the preliminary support design

Part C lists the SEM design parameters P_i (i.e., *Q-value* P_1, width of heading P_2, height of heading P_3 and round length P_4). The width of heading P_2 and height of heading P_3 are calculated based on the divisions of span and height respectively. If no subdivision is considered, P_2 is the cavern span, and P_3 is the cavern height. The round length P_4 is set according to the NHI (2009). These parameters are the inputs for the ANN models to predict the normal stress and roof displacement to plot the GRC. In Part D, the estimations of support capacity provided by the end-anchored rockbolt, the shotcrete linings and/or the steel set are given according to Hoek (2007). Note that all three support elements are assumed to act independently, and the bearing capacity and the stiffness of the compound support system are the accumulation of their bearing capacity and the stiffness respectively (Özsan and Başarır, 2003). The SCCs of different support types are plotted with GRC to present the ground-support interaction in the diagram. The intersection between GRC and SCC indicates the displacement and the support pressure when the equilibrium is achieved. Part E gives three performance functions as shown in Eqs. (7.1) to (7.3) to indicate the support performances.

The evaluation chart could be used to estimate the support safety. A shotcrete lining with thickness t_c = 0.1 m is selected as an example. The cavern is full-face excavated in rock with UCS and E_c of 35 MPa and 35 GPa, respectively. The calculated support capacity criterion $g_2(\mathbf{x}) > 0$ means the support is suitable for the ground conditions and cavern size. As shown in Table 7-4, the shotcrete lining support with t_c = 0.1 m could only be effective in good rock conditions with $Q \geq 10$ or narrow span caverns with $B <$ 10 m. The data used to generate Table 4 are also shown in Figure 7-10 where the GRC and SCC curves are also included to illustrate the calculation process.

The evaluation chart could be used to assess the functions of the patterned rockbolt to support rock cavern. The damage depth can be predicted using the ANN model. Example of the calculated rockbolt length criterion function $g_3(\mathbf{x})$, see Eq. (7.3), is shown in Table 7-5. The functions of the patterned rockbolts for rock cavern support could be generally separated as suspension element when $g_3(\mathbf{x}) > 0$ and arching element when $g_3(\mathbf{x}) \leq 0$ (Li, 2017). Table 7-5 shows that the patterned rockbolts are suspension elements for $4 < Q < 10$ and $20 < B < 30$ m. The pattern rockbolt are arching elements for the rest cases. The rockbolt lengths are much less than the sum of damage depth and anchored length, $g_3(\mathbf{x}) < -2$ m, for $Q = 0.4$ and $B > 8.0$ m.

Table 7-4 Predictions of the support safety function $g_2(\mathbf{x})$ for shotcrete linings with thickness t_c = 0.1 m

Span, m \ Q	0.4	1	4	10
30	-1.15	-1.07	-0.14	-0.28
25	-1.12	-0.90	-0.10	-0.09
20	-0.74	-0.42	-0.09	0.07
15	-0.63	-0.38	0.03	0.25
10	-0.23	0.04	0.45	0.60
8	0.30	0.32	0.69	0.80
5	0.67	0.97	1.27	1.34

t_c = 0.1 m
UCS = 35 MPa
E_c = 35 GPa

Legend	
	$g_2(\mathbf{x}) \geq 1$
	$0 \leq g_2(\mathbf{x}) < 1$
	$-0.5 \leq g_2(\mathbf{x}) < 0$
	$g_2(\mathbf{x}) < -0.5$

Table 7-5 Predictions of the rockbolt length criterion function $g_3(\mathbf{x})$ for rockbolt support

Span, m \ Q	0.4	1	4	10
30	-7.0	-0.3	0.8	1.3
25	-5.8	-0.6	0.4	0.5
20	-5.1	-1.3	-0.7	0.0
15	-3.7	-1.2	-0.8	-0.8
10	-2.6	-1.3	-1.2	-0.9
8	-2.1	-1.0	-1.0	-0.8
5	-1.2	-0.6	-0.4	-0.5

Legend	
	$g_3(\mathbf{x}) > 0$
	$-1 \leq g_3(\mathbf{x}) < 0$
	$-2 \leq g_3(\mathbf{x}) < -1$
	$-3 \leq g_3(\mathbf{x}) < -2$
	$g_3(\mathbf{x}) < -3$

The evaluation chart could be used to optimize the subdivisions of the excavation cross section. The division of span and height would be optimized using displacement criterion $g_1(\mathbf{x})$. This could be achieved using "Solver" function by minimizing cell D22, and changing cell E11 and cell E12 with their magnitudes of integers and less than 4 (assumed the division of the segment is less than 4 parts). The width and height of heading are obtained by dividing the span based on the optimized results. As shown in Figure 7-10, cells E11 and E12 are the optimization results for the FF excavation. The width and height of heading are then obtained as shown in cells C11 and C12, respectively, in Figure 7-10. The displacement after balance is u = 0.018 m which is close to the allowable displacement u_{max} = 0.02 m. It should be noted that the evaluation chart provides an estimation of the ground-support interaction for preliminary design as the ANN models are build based on the 2D numerical modelling which might not be

exactly representing the excavation process and time effect in real 3 dimensional conditions.

7.6 A case study

The evaluation chart is applied to evaluate a real design case of Kaletepe tunnel presented by Sari and Pasamehmetoglu (2004). The highway tunnel with a wall height of 9.6 m, a width of 12.7 m and a length of 2.5 km was excavated under a hill with the maximum overburden of approximately 300 m. The test results of core specimen taken from six borehole sections and site investigations were used as the input parameters to assess the geological conditions. The support recommendation and excavation guide preliminary support design proposed by Sari and Pasamehmetoglu (2004) are shown in Table 7-6. In previous studies, the tunnel length was divided into seven sections (section 1 to 7), along its axis for the preliminary support design. Only sections 2, 5 and 7 are selected in this study to illustrate the applications of the proposed evaluation chart. An allowable displacement is assumed as u_{max} = 0.02 m. The support capacities are based on those listed in Table 7-1.

For section 2, the length and the spacing of the rockbolt are 3.9 m and 0.8 m, respectively, which are the average data given in Table 7-6. The sequential excavation method is top heading and benching. The thickness of the shotcrete lining is 0.25 m. The calculated GRC and SCC are shown in Figure 7-11(a). The intersection between SCC and GRC determines the displacement and the support pressure which are 0.024 m and 0.207 MPa, respectively. However, the displacement of 0.024 m is larger than u_{max} = 0.02 m indicating the support design should be optimized. Moreover, the SCC curve of shotcrete shows the pressure on support is much less than its bearing capacity which means the support is not utilized wisely. Figure 7-12(a) gives the calculated GRC and SCC curves of the shotcrete lining and rockbolt support with optimized design parameter, such as round length of 5 m and thickness of shotcrete lining of 0.15 m. The intersection between SCC and GRC curves shows the support system could restrain the displacement close to 0.02 m within its bearing capacity.

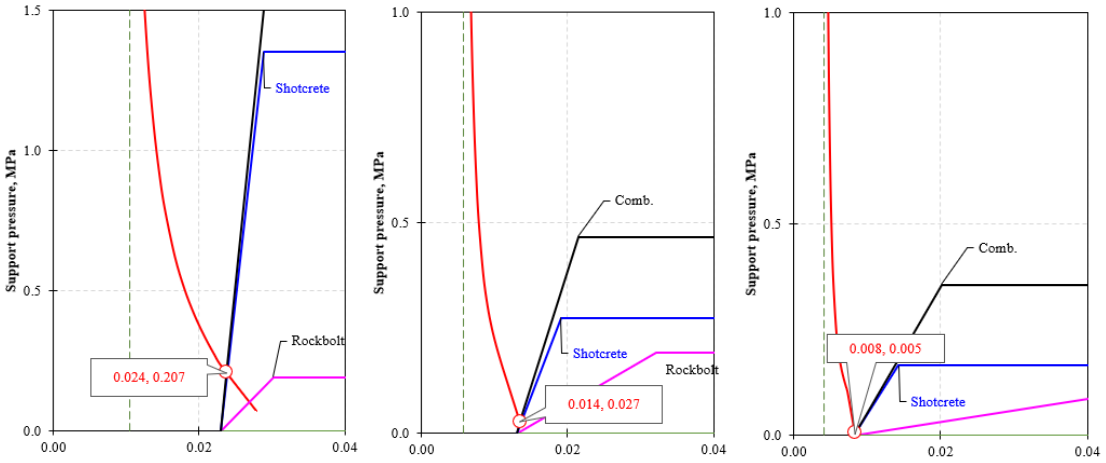

(a) (b) (c)

Figure 7-11 Calculated GRCs and SCCs using evaluation chart to assess the support designs proposed by Sari & Pasamehmetoglu (2004) for (a) Section 2, (b) Section 7, and (c) Section 5.

The GRCs and SCCs are calculated using the evaluation chart to assess the support design proposed by Sari & Pasamehmetoglu (2004) for Section 5 and Section 7. The support parameters are also given in Table 7-6. The calculated GRCs and SCCs of the support designs for Section 7 and Section 5 are shown in Figure 7-11(a) and (b), respectively. The intersections between SCC and GRC show the displacements are smaller than the allowable displacement u_{max} = 0.02 m which means the support system could satisfy the requirement. For Section 7, Figure 7-11(b) shows the shotcrete linings and the rockbolt can provide sufficient support pressure to restrain the displacement. However, the predicted support pressure is 0.027 MPa which is only 10% the bearing capacity of the shotcrete lining. Less support might be also effective, such as set the spacing of rockbolt to 2.0 m. As shown in Figure 7-12(b), the SCCs and GRCs show the support can restrain the displacement within 0.02 m. For Section 5, the intersection between SCC and GRC in Figure 7-11(c) shows the rockbolt has no effective support which means the shotcrete is strong enough to provide the support pressure. The spot rockbolt could be used to provide the support pressure as shown in Figure 7-12(c).

Table 7-6 Support design parameters (B – bolting, SL – shotcrete lining)

Proposed by		Sari and Pasamehmetoglu (2004)			Current research according to evaluation chart		
Ground condition		Section 2	Section 7	Section 5	Section 2	Section 7	Section 5
		Poor	Fair	Good	Poor	Fair	Good
SEM parameter	Round length, *m*	10	20	20	5	20	20
	Sub-division	Top heading & benching	FF	FF	Top heading & benching	FF	FF
B	Length, *m*	3.9	3.9	3.9	3.9	3.9	3.9
	Spacing, *m*	0.5 - 1.0	1 - 1.5	2.5 - 3	0.8	2	Spot bolt
SL	Thickness, *m*	0.2 - 0.3	0.05	0.03	0.15	0.05	0.03

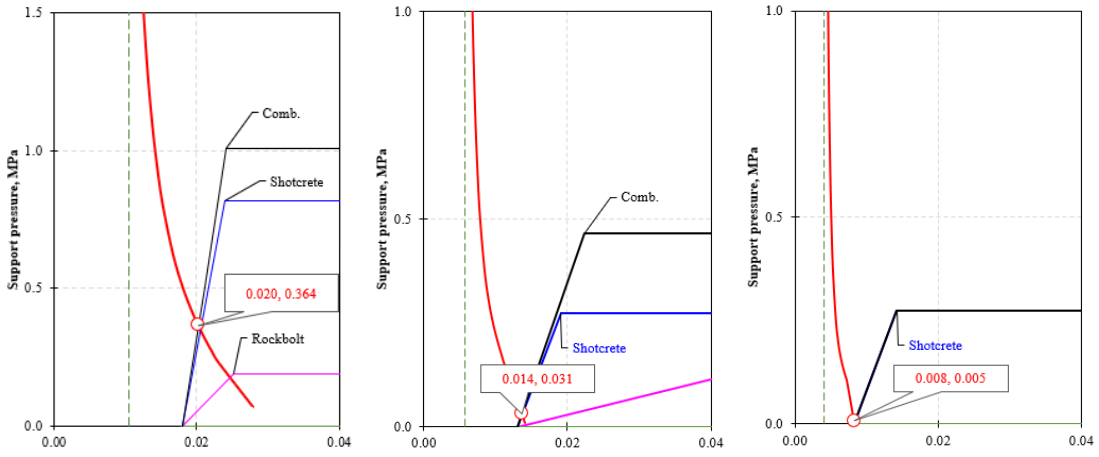

(a) (b) (c)

Figure 7-12 GRCs and SCCs to evaluate the revised support designs for (a) Section 2, (b) Section 7, and (c) Section 5.

To further evaluate the performance of the support design parameters proposed by current study and Sari & Pasamehmetoglu (2004), series of numerical simulations are carried out. The displacement contours around the excavation face without support, with support system in current study and with support system by Sari & Pasamehmetoglu (2004) are shown in Table 7-7. The maximum displacement and the damage depth of EDZ from numerical analysis and evaluation chart are also listed in the table for comparison purpose. It can be seen that the support designs proposed by current study and Sari & Pasamehmetoglu (2004) can restrain the roof displacement within u_{max} =

0.02 m. The revised support design using evaluation chart proposed in this study adopts less supports. The roof displacement and the damage depth of EDZ resulted in numerical analysis and evaluation chart are further plotted in Figure 7-13(a) and (b), respectively. The average difference between the numerical analysis and evaluation chart to calculate the maximum displacement and the damage depth of EDZ are 12% and 1.2%, respectively.

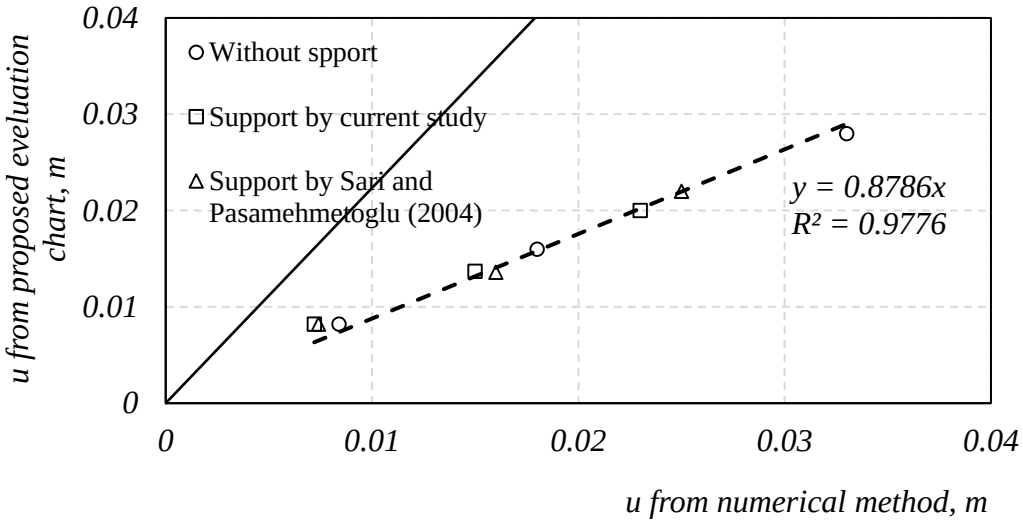

(a)

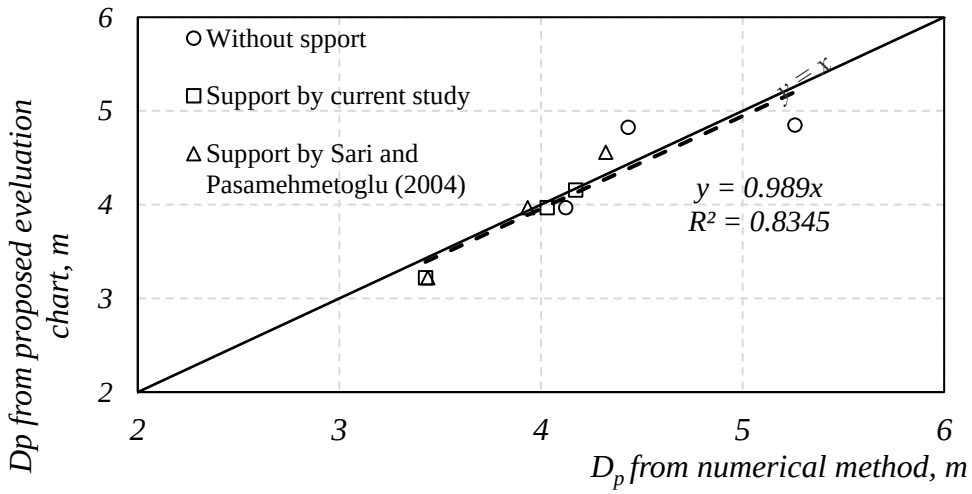

(b)

Figure 7-13 Comparisons between the results from numerical analysis and evaluation chart in terms of (a) displacement and (b) damage depth of EDZ from the excavation surface

Table 7-7 Displacement contours around the tunnel with/without supports

<table>
<tr><th></th><th>Section 2</th><th>Section 7</th><th>Section 5</th></tr>
<tr><td>Without support</td><td> 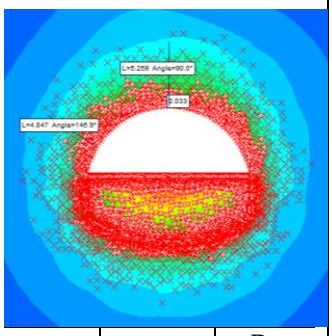
<table>
<tr><th></th><th>u_i</th><th>D_{pi}</th></tr>
<tr><td>Num.</td><td>0.033</td><td>5.259</td></tr>
<tr><td>Chart</td><td>0.028</td><td>4.849</td></tr>
<tr><td>Error</td><td>15.15%</td><td>7.80%</td></tr>
</table></td><td> 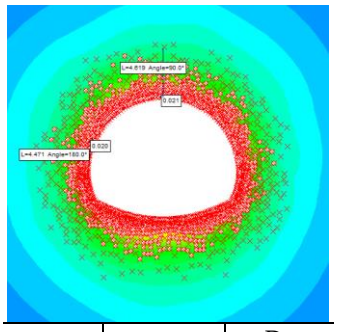
<table>
<tr><th></th><th>u_i</th><th>D_{pi}</th></tr>
<tr><td>Num.</td><td>0.018</td><td>4.432</td></tr>
<tr><td>Chart</td><td>0.016</td><td>4.823</td></tr>
<tr><td>Error</td><td>11.11%</td><td>8.82%</td></tr>
</table></td><td> 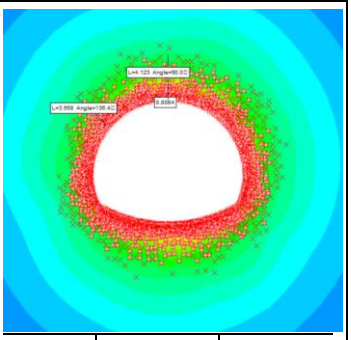
<table>
<tr><th></th><th>u_i</th><th>D_{pi}</th></tr>
<tr><td>Num.</td><td>0.0084</td><td>4.123</td></tr>
<tr><td>Chart</td><td>0.0082</td><td>3.968</td></tr>
<tr><td>Error</td><td>2.38%</td><td>3.76%</td></tr>
</table></td></tr>
<tr><td>With support as reference</td><td> 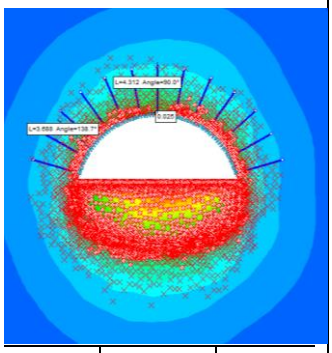
<table>
<tr><th></th><th>u_i</th><th>D_{pi}</th></tr>
<tr><td>Num.</td><td>0.025</td><td>4.321</td></tr>
<tr><td>Chart</td><td>0.022</td><td>4.558</td></tr>
<tr><td>Error</td><td>12.00%</td><td>5.48%</td></tr>
</table></td><td> 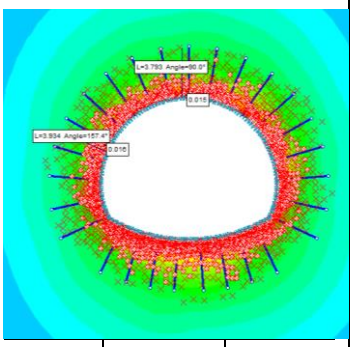
<table>
<tr><th></th><th>u_i</th><th>D_{pi}</th></tr>
<tr><td>Num.</td><td>0.016</td><td>3.934</td></tr>
<tr><td>Chart</td><td>0.0136</td><td>3.967</td></tr>
<tr><td>Error</td><td>15.00%</td><td>0.84%</td></tr>
</table></td><td> 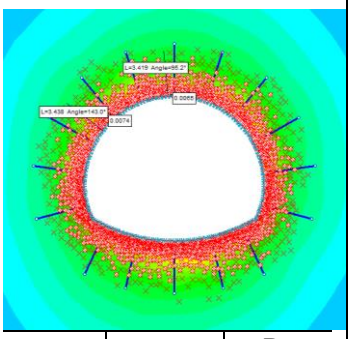
<table>
<tr><th></th><th>u_i</th><th>D_{pi}</th></tr>
<tr><td>Num.</td><td>0.0074</td><td>3.438</td></tr>
<tr><td>Chart</td><td>0.0082</td><td>3.217</td></tr>
<tr><td>Error</td><td>10.81%</td><td>6.43%</td></tr>
</table></td></tr>
<tr><td>Revised support design</td><td> 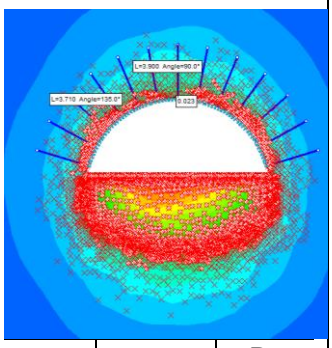
<table>
<tr><th></th><th>u_i</th><th>D_{pi}</th></tr>
<tr><td>Num.</td><td>0.023</td><td>4.171</td></tr>
<tr><td>Chart</td><td>0.020</td><td>4.155</td></tr>
<tr><td>Error</td><td>13.04%</td><td>0.38%</td></tr>
</table></td><td> 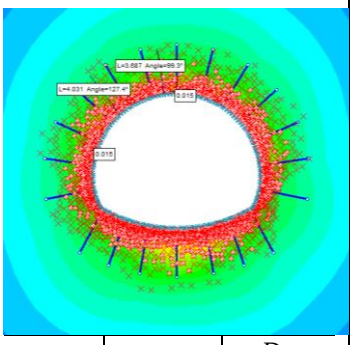
<table>
<tr><th></th><th>u_i</th><th>D_{pi}</th></tr>
<tr><td>Num.</td><td>0.015</td><td>4.031</td></tr>
<tr><td>Chart</td><td>0.0137</td><td>3.967</td></tr>
<tr><td>Error</td><td>8.67%</td><td>1.59%</td></tr>
</table></td><td> 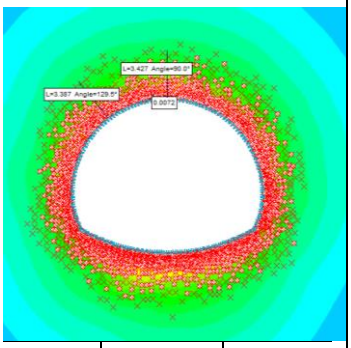
<table>
<tr><th></th><th>u_i</th><th>D_{pi}</th></tr>
<tr><td>Num.</td><td>0.0072</td><td>3.427</td></tr>
<tr><td>Chart</td><td>0.0082</td><td>3.217</td></tr>
<tr><td>Error</td><td>13.89%</td><td>6.13%</td></tr>
</table></td></tr>
</table>

7.7 Conclusions

A support design method for horseshoe-shaped rock caverns is proposed in this chapter with considerations of the progressive damage of the rock mass using the 2D numerical modelling and the artificial neural network (ANN). The excavation effects of the rock

cavern are simulated using the 2D finite element plane strain models. The performances of the rock cavern during excavation are investigated based on the convergence-confinement method (CCM).

Parametric studies are conducted to analyse the effects of the *Q*-values on the EDZ development of rock cavern with a span of 20 m and a height of 27 m under isotropic stress of 10 MPa. It is found that the roof displacements versus the distances from the excavation face curves increase nonlinearly when $Q < 4$ and change insignificantly for $Q > 10$. Furthermore, the smaller the *Q*-value the deeper the damage depth is generated in the surrounding rock mass. The spacing of the rockbolt has to be reduced for poor ground classes ($Q \leq 1$) to assist the formation of the artificial arch in the surround rock mass. The effects of sequential excavation parameters are also investigated by changing the size of rock cavern and the subdivision of cross-sections. It is found that the subdivision can reduce the range of the EDZ but there are no obvious relationships for different subdivision methods. More advanced function is still required to present the relationship between the SEM parameters and the cavern performance.

The ANN models are built using the numerical results to find the complex relationships among the rock mass condition, the sequential excavation parameters and the cavern performances. Totally 700 data are generated from the numerical analysis. Approximately 70% of the results are randomly chosen as training data and the rest of them are used for testing. Good agreements between the predictions and the targets are obtained. An evaluation chart is proposed by integrating the ANN models into the EXCEL software. The proposed evaluation chart provides an effective method to evaluate the support safety, the functions of the patterned rockbolt and the optimization of subdivisions of the excavation cross section. The evaluation chart is applied to evaluate a real case design of Kaletepe tunnel. Comparing to the preliminary design presented by Sari and Pasamehmetoglu (2004), the support designs proposed by the current study can restrain the roof displacement. It should be noted that the evaluation chart is feasible to estimate the support for the preliminary design as the ANN models are built based on the 2D numerical results which might not be exactly representing the complex excavation process and time effect.

CHAPTER 8.
CONCLUSIONS AND FUTURE WORK

8.1 Conclusions

Underground space has been increasingly exploited in recent years. The potential for instability in the rock mass surrounding the underground excavation is a threat to the lives and safety of construction workers. The rockbolt has been the primary reinforcement structure in underground tunnelling and mining. To mobilize the reinforcement efforts and improve the design of the rockbolt, the reinforcement mechanism of a rockbolt system in underground excavations is studied using 2D-DDA. The following conclusions have been made through the studies:

(1) Pullout performance of the CMC rockbolt element

The 2D-DDA method is used to investigate the pullout performance of the CMC rockbolt element which is modeled as three components, i.e. the rock, the rockbolt and the mortar. The material properties of mortar blocks are adopted from the experiment result proposed from Yokota et al. (2018). The frictional properties along rockbolt – mortar interface are calibrated with their experimental results. The flat joint contact model is introduced into the 2D-DDA code to simulate the force versus displacement behavior of an artificial joint. The results show that a bond stress versus slip displacement curve of the CMC element is generally exhibiting three stages and representing by five key parameters, i.e., the bond stiffness in three stages (k_1, k_2, and k_3), the maximum bond strength τ_{max}, and the residual bond strength τ_{res}. Parametric studies have been carried out to investigate the effects of the normal stress and those of the rib profiles on the bond stress versus slip displacement curves and fracturing modes in mortar. It is found that the normal stress plays an important role in the bond-slip modeling. The bond stiffness k_1, the maximum bond strength τ_{max} and the residual bond strength τ_{res} are increasing with the increase of normal stress. The rib spacing may

influence the bond stiffness of a bond-slip model in the way that a larger rib spacing will result in lower bond stiffness when the other parameters are the same. Under a lower normal stress, the interlock of the CMC rockbolt element with rib face angles of less than 30° is not effective because the rockbolt elements are pulled out along the rib faces and less cracks are generated in the mortar blocks.

(2) Developed rockbolt model in 2D-DDA and verified the model

The developed rockbolt element is capable to simulate different types of rockbolt under various load conditions with consideration of three behaviours: the axial behaviour, the shearing behaviour and the bond behaviour. By adopting different models, the four major failure modes of rockbolt could be simulated: (1) decoupling along the interface, (2) tensile failure, (3) faceplate failure and (4) shear failure at joint. Verifications of the rockbolt element are also carried out. The bond behaviour is verified using pullout test results. The simulation results show good agreements between the proposed model and the experiments results. By comparing with shear tests, the numerical results show good agreements in the reduction of reinforcement effects. The shear failure of the rockbolt elements at joint is also presented. The axial behaviour is verified using pullout test results. Two types of rockbolts, i.e. the fully grouted rockbolt and the D-bolt, are simulated under pullout condition. The simulated load-deformation curves show good agreements with the experimental ones. It also confirms the larger deformability of the D-bolt compared with the fully grouted rebar as a result of equally loaded rockbolt elements between special anchored nodes. By verification of the proposed model, it indicates that the proposed rockbolt model can simulate the rock reinforcement using rockbolts. Especially, it can simulate several types of rockbolt restrains of jointed rock blocks which are under large deformation conditions.

(3) Reinforced rock unit in jointed rock mass

The investigation of reinforced rock unit (RRU) of rockbolts in jointed rock mass is carried out using the newly developed rockbolt element in 2D-DDA. In jointed rock mass, the RRU should be considered with regards to the displacement and the conditions of rock mass discontinuities. In general, the RRU is cone-shaped, but its boundary may be limited by the existing joint sets, resulting in a non-triangular cross section in some

cases. A parametric study has been carried out to show that the friction of joints and the stiffness of rock blocks will affect the RRU area.

(4) Stability analysis of rockbolt reinforced rock wedge

The stability of the rockbolt reinforced roof wedges is investigated using 2D-DDA. The change of stress state in the surrounding rock blocks after excavation is reparented using the joint relaxation method. The movement of rock wedge induced by its dead weight and the re-adjusted stress in field are presented. The influences of the horizontal pressure on the wedge stability are investigated. It shows the roof wedge has potential to fall if the semi-apical angle is less than the friction angle along the wedge boundary. The critical horizontal pressure could be calculated using 2D-DDA that the wedge could be self-supported after stress redistribution if the horizontal pressure is larger than it. The results agree reasonably with the analytical solutions. The effects of the rockbolt spacing and installation angle are also presented. The results show the axial forces of rockbolt may slightly decrease when narrowing the rockbolt spacing but increase if the installation angle increase.

A case study is presented to show the application of the 2D-DDA models for the assessment of the rockbolting design to support roof wedges. Using the rock/rockbolt interaction diagrams, the results could be used by the site engineers to evaluate the rockbolting design to sustain the possible roof wedges.

(5) Performance-based support design for rock caverns

A support design method for horseshoe-shaped rock caverns is proposed with considerations of the progressive damage of the rock mass using the RS^2 and the artificial neural network (ANN). The excavation effects of the rock cavern are simulated using the 2D finite element plane strain models. The performances of the rock cavern during excavation are investigated based on the convergence-confinement method (CCM). Parametric studies are conducted to analyse the effects of the *Q*-values on the EDZ development of rock cavern. The effects of sequential excavation parameters are also investigated by changing the size of rock cavern and the subdivision of cross-sections. The ANN models are built using the numerical results to find the relationships among the rock mass condition, the sequential excavation parameters and the cavern

performances. An evaluation chart is proposed by integrating the ANN models into the EXCEL software. The proposed evaluation chart provides an effective method to evaluate the support safety, the functions of the patterned rockbolt and the optimization of subdivisions of the excavation cross section. The evaluation chart is applied to evaluate a real case design of Kaletepe tunnel. Comparing to the preliminary design presented by Sari and Pasamehmetoglu (2004), the support designs proposed by the current study can restrain the roof displacement. It should be noted that the evaluation chart is feasible to estimate of the support for the preliminary design as the ANN models are built based on the 2D numerical results which might not be exactly representing the complex excavation process and time effect.

8.2 Future work

The present work attempted to improve the rockbolt design in complex rock conditions and to have a good understanding of the reinforcement mechanism. Some recommendations and suggestions for further studies are proposed as follows.

(1) As the expansion of the underground construction, many new types of rockbolts have been developed to satisfy the support requirements. The developed rockbolt model could be used to present types of rockbolts if the bond-slip models are available for the rockbolt elements. The proposed rockbolt model can be used to simulate the loading behavior of new proposed rockbolt element, such as CFC element and DMFC element. As the current model is based on 2D numerical model which could not consider the twist failure of the rockbolt, 3D numerical model with spatial rockbolt arrangement should be developed to better understand their reinforcement effects.

(2) The current studies focus on the reinforcement effects of rockbolts. However, other structures are also used to support the underground opening, i.e. shotcrete lining, steel set, etc. The interactions mechanisms between these support structures and surrounding rock mass have not been fully understood yet. Future studies on the working principles of the combined support system should be carried out. The combined support stiffness and support capacity have to be used for support designing.

(3) One of the design principles of NATM is to take advantages of the inherent geological strength available in the surrounding rock mass to stabilize the tunnel in terms of economic consideration. The CCM method was use for preliminary designing based only limited data. The program can be improved when the working principles of the combined support system are better understood. The ground reaction curves in complex ground conditions should be studied to increase the reliability of the ANN models. Through building a more comprehensive database, the rock/support diagram could be estimated during the construction progress and help the site engineers to assess and mitigate the possible risks.

REFERENCES

Alejano, L.R., Alonso, E., Rodríguez-Dono, A., Fernández-Manín, G. (2010). "Application of the convergence-confinement method to tunnels in rock masses exhibiting Hoek–Brown strain-softening behaviour". International Journal of Rock Mechanics and Mining Sciences **47**, 150-160.

Alejano, L.R., Rodriguez-Dono, A., Alonso, E., Fdez.-Manín, G. (2009) "Ground reaction curves for tunnels excavated in different quality rock masses showing several types of post-failure behaviour". Tunnelling and Underground Space Technology **24**, 689-705.

Aydin, A., Ozbek, A.,Acar, A. (2014) "Geomechanical characterization, 3-D optical monitoring and numerical modeling in Kirkgecit-1 tunnel, Turkey". Engineering Geology **181**, 38-47.

Aziz, N., Hossein, J., Hadi, M.S.N. (2005) "The Influence of Resin Thickness on Bolt Bending". The 19th International Mining Congress and Fair of Turkey, IMCET2005, İzmir, Turkey, June 09-12, 65-71.

Aziz, N., Jalalifar, H., Remennikov, A., Sinclair, S., Green, A. (2008) "Optimisation of the Bolt Profle Confguration for Load Transfer Enhancement". In: AZIZ, N. (ed.) Coal Operators' Conference. University of Wollongong & the Australasian Institute of Mining and Metallurgy, pp. 125-131.

Bao, H. (2010) "Nodal-based discontinuous deformation analysis", Ph.D. Thesis, Nanyang Technological University, Singapore.

Barton, N., Lien, R., Lunde, J. (1974) "Engineering classification of rock masses for the design of tunnel support". Rock mechanics **6**, 189-236.

Barton N. and Choubey V. (1978) Recent experiences with the Q-system of tunnel support design: Oslo : Norwegian Geotechnical Institute.

Bawden, W.F. (2011) "Ground control using cable and rock bolting", In: Darling, P. (Ed.), SME Mining Engineering Handbook (3rd Edition). Society for Mining, Metallurgy, and Exploration (SME).

Benmokrane, B., Chennouf, A., Mitri, H.S. (1995) "Laboratory evaluation of cement-based grouts and grouted rock anchors". International Journal of Rock Mechanics and Mining Sciences & Geomechanics Abstracts **32**, 633-642.

Bertuzzi, R., Douglas, K., Mostyn, G. (2016) "Comparison of quantified and chart GSI for four rock masses". Engineering Geology **202**, 24-35.

Bieniawski, Z. T. (1978) "Determining rock mass deformability: experience from case histories". International Journal of Rock Mechanics and Mining Sciences & Geomechanics Abstracts **15**, 237-247.

Bieniawski, Z. T. (1984) Rock Mechanics Design in Mining and Caverning, A. A. Balkema, Rotterdam, 97-133.

Bieniawski, Z. T. (1989) Engineering Rock Mass Classifications, John Wiley and Sons, New York

Blanco Martín, L., Tijani, M., Hadj-Hassen, F. (2011) "A new analytical solution to the mechanical behaviour of fully grouted rockbolts subjected to pull-out tests". Construction and Building Materials **25**, 749-755.

Blanco Martín, L., Tijani, M., Hadj-Hassen, F., Noiret, A. (2013) "Assessment of the bolt-grout interface behaviour of fully grouted rockbolts from laboratory experiments under axial loads". International Journal of Rock Mechanics and Mining Sciences **63**, 50-61.

Bobet, A. and Einstein, H.H., 2011. "Tunnel reinforcement with rockbolts". Tunnelling and Underground Space Technology **26**, 100-123.

Brady, B.H.G. and Brown, E.T. (2006) "Rock support and reinforcement". Rock Mechanics for underground mining (3rd edition). Springer Netherlands, Dordrecht, pp. 312-346.

Brown, E.T., ASCE, M., Bray, J.W., Branko Ladanyi, ASCE, F., Hoek, E. (1983) "Ground Response Curves for Rock Tunnels". Journal of Geotechnical Engineering **109**, 15-39.

Cai, M. (2008) "Influence of stress path on tunnel excavation response – Numerical tool selection and modeling strategy". Tunnelling and Underground Space Technology **23**, 618-628.

Cao, C., Nemcik, J., Aziz, N., Ren, T. (2013) "Analytical study of steel bolt profile and its influence on bolt load transfer". International Journal of Rock Mechanics and Mining Sciences **60**, 188-195.

Cao, C., Ren, T., Cook, C., Cao, Y. (2014) "Analytical approach in optimising selection of rebar bolts in preventing rock bolting failure". International Journal of Rock Mechanics and Mining Sciences **72**, 16-25.

Carranza-Torres, C. and Fairhurst, C. (2000) "Application of the Convergence-Confinement method of tunnel design to rock masses that satisfy the Hoek-Brown failure criterion". Tunnelling and Underground Space Technology **15**, 187-213.

Chen, Y.and Li, C.C. (2015) "Performance of fully encapsulated rebar bolts and D-Bolts under combined pull-and-shear loading". Tunnelling and Underground Space Technology **45**, 99-106.

Choquet, P. and Hadjigeorgiou, J. (1993) The design of support for underground excavations. Oxford; New York : Pergamon Press, 1993.

Crawford, A.M. and Bray, J.W. (1983) "Influence of the in-situ stress field and joint stiffness on rock wedge stability in underground openings". Canadian Geotechnical Journal **20**, 276-287.

Deb, D. and Das, K.C. (2011) "Modelling of fully grouted rock bolt based on enriched finite element method". International Journal of Rock Mechanics and Mining Sciences **48**, 283-293.

Deb, D. and Das, K.C. (2014) "A new doubly enriched finite element for modelling grouted bolt crossed by rock joint". International Journal of Rock Mechanics and Mining Sciences **70**, 47-58.

Deb, D., Gujjala, Y.K., 2018. "Extended finite element procedures for analysis of bolt crossing multiple intersecting rock joints". International Journal of Rock Mechanics and Mining Sciences **107**, 249-260.

Dias, D. (2011) "Convergence-confinement approach for designing tunnel face reinforcement by horizontal bolting". Tunnelling and Underground Space Technology **26**, 517-523.

Dwivedi, R.D., Singh, M., Viladkar, M.N., Goel, R.K. (2014) "Estimation of support pressure during tunnelling through squeezing grounds". Engineering Geology, **168**, 9-22.

Farmer, I.W. (1975) "Stress distribution along a resin grouted rock anchor". International Journal of Rock Mechanics and Mining Sciences & Geomechanics Abstracts **12**, 347-351.

Feng, X., Zhang, N., Yang, S., He, F. (2018) "Mechanical response of fully bonded bolts under cyclic load". International Journal of Rock Mechanics and Mining Sciences **109**, 138-154.

Feng, X.T., Guo, H.S., Yang, C.X., Li, S.J. (2018) "In situ observation and evaluation of zonal disintegration affected by existing fractures in deep hard rock tunnelling". Engineering Geology **242**, 1-11.

Forbes, B., Vlachopoulos, N., Hyett, A.J., Diederichs, M.S. (2017) "A new optical sensing technique for monitoring shear of rock bolts". Tunnelling and Underground Space Technology **66**, 34-46.

Gerdeen, J.C., Snyder, V.W., Viegelahn, G.L.U.O. (1977) "Design criteria for roof bolting plans using fully resin-grouted nontensioned bolts to reinforce bedded mine roof". Synthesis and design criteria **46**(5), 129

Ghadimi, M., Shahriar, K., Jalalifar, H. (2014) "Analysis profile of the fully grouted rock bolt in jointed rock using analytical and numerical methods". International Journal of Mining Science and Technology **24**, 609-615.

Goodman, R. E. and Shi, G.H. (1985) Block Theory and Its Application to Rock Engineering. Prentice-Hall, INC.

Goodman, R.E. (1995) "Block theory and its application". Géotechnique **45**, 383-423.

Grasselli, G. (2005) "3D Behaviour of bolted rock joints: experimental and numerical study". International Journal of Rock Mechanics and Mining Sciences **42**, 13-24.

Gurung, N. (2001) "1-D analytical solution for extensible and inextensible soil/rock reinforcement in pull-out tests". Geotextiles and Geomembranes **19**, 195-212.

Hatzor, H. Yossef, Ma, G., Shi, G.H. (2018) "Discontinuous deformation analysis in rock mechanics practice". ISRM Book Series, CRC Press, London, UK.

He, L., An, X.M., Zhao, Z.Y. (2015) "Fully grouted rock bolts: an analytical investigation". Rock Mechanics and Rock Engineering **48**, 1181-1196.

He, L., An, X.M., Zhao, X.B., Zhao, Z.Y., Zhao, J. (2018) "Development of a unified rock bolt model in discontinuous deformation analysis". Rock Mechanics and Rock Engineering **51**, 827-847.

He, M., Gong, W., Wang, J., Peng, Q., Tao, Z., Du, S., Peng, Y. (2014) "Development of a novel energy-absorbing bolt with extraordinarily large elongation and constant resistance". International Journal of Rock Mechanics and Mining Sciences **67**, 29-42.

Hijazo, T. and González de Vallejo, L.I. (2012) “In-situ stress amplification due to geological factors in tunnels: The case of Pajares Tunnels, Spain. Engineering Geology, **137-138**:13-20

Hobst, L. and Zajíc, J., (1983) "Anchoring in rock and soil", in: LeoŠ, H., Josef, Z. (Eds.), Developments in Geotechnical Engineering. Elsevier, pp. 60-88.

Hoek, E., (2007) Practical rock engineering. E-book, https://www.rocscience.com.

Hoek, E., Kaiser P.K., Bawden, W.F. (2000) “Rockbolts and dowels”, Support of Underground Excavations in Hard Rock. CRC Press, pp. 152-164.

Hyett, A. J., Bawden, W. F., Reichert, R. D. (1992) “The effect of rock mass confinement on the bond strength of fully grouted cable bolts”. International Journal of Rock Mechanics and Mining Sciences & Geomechanics Abstracts, **29**, 503-524.

Hyett, A.J., Bawden, W.F., Macsporran, G.R., Moosavi, M. (1995) "A constitutive law for bond failure of fully-grouted cable bolts using a modified hoek cell". International Journal of Rock Mechanics and Mining Sciences & Geomechanics Abstracts **32**, 11-36.

Itasca Consulting Group, Inc., (2011) UDEC Ver3.0, Special features. Mineapolis: Itasca Consulting Group, Inc.

Itasca Consulting Group, Inc., (2012) FLAC Ver5.0, Structural Elements. Mineapolis: Itasca Consulting Group, Inc.

Ito, F., Nakahara, F., Kawano, R., Kang, S.-S., Obara, Y. (2001) “Visualization of failure in a pull-out test of cable bolts using X-ray CT”. Construction and Building Materials **15**, 263-270.

Jalalifar, H., Aziz, N., Hadi, M., (2006) "The effect of surface profile, rock strength and pretension load on bending behaviour of fully grouted bolts". Geotechnical & Geological Engineering **24**, 1203-1227.

Janin, J.P., Dias, D., Emeriault, F., Kastner, R., Le Bissonnais, H., Guilloux, A. (2015) “Numerical back-analysis of the southern Toulon tunnel measurements: A comparison of 3D and 2D approaches”. Engineering Geology **195**, 42-52.

Jiao, Y.Y., Zhang, H.Q., Tang, H.M., Zhang, X.L., Adoko, A.C., Tian, H.N. (2014) “Simulating the process of reservoir-impoundment-induced landslide using the extended DDA method”. Engineering Geology, **182**, 37-48.

Jiao, Y.Y., Zhang, X.L., Zhao, J. (2012) “Two-Dimensional DDA Contact Constitutive Model for Simulating Rock Fragmentation”. Journal of Engineering Mechanics **138**(2):199-209.

Jing, L. (2003) "A review of techniques, advances and outstanding issues in numerical modelling for rock mechanics and rock engineering". International Journal of Rock Mechanics and Mining Sciences **40**, 283-353.

Kaiser, P.K., Yazici, S., Nosé, J. (1992) "Effect of stress change on the bond strength of fully grouted cables". International Journal of Rock Mechanics and Mining Sciences & Geomechanics Abstracts **29**, 293-306.

Karakus, M., (2007) "Appraising the methods accounting for 3D tunnelling effects in 2D plane strain FE analysis". Tunnelling and Underground Space Technology **22**, 47-56.

Kim, Y.L., Amadei, B., Pan, E. (1999) "Modeling the effect of water, excavation sequence and rock reinforcement with discontinuous deformation analysis". International Journal of Rock Mechanics and Mining Sciences **36**, 949-970

Kitchah, F. and Benmebarek, S. (2016) "Finite difference analysis of an advance core pre-reinforcement system for Toulon's south tube". Journal of Rock Mechanics and Geotechnical Engineering **8**, 703-713.

Kılıc, A., Yasar, E., Atis, C.D., (2003) "Effect of bar shape on the pull-out capacity of fully-grouted rockbolts". Tunnelling and Underground Space Technology **18**, 1-6.

Kılıc, A., Yasar, E., Celik, A.G., (2002) "Effect of grout properties on the pull-out load capacity of fully grouted rock bolt". Tunnelling and Underground Space Technology **17**, 355-362.

Ko, H., Matthys, S., Palmieri, A., Sato, Y., (2014) "Development of a simplified bond stress–slip model for bonded FRP–concrete interfaces". Construction and Building Materials **68**, 142-157.

Kwon, S., Lee, C.S., Cho, S.J., Jeon, S.W., Cho, W.J. (2009) "An investigation of the excavation damaged zone at the KAERI underground research tunnel". Tunnelling and Underground Space Technology **24**, 1-13.

Lang, T.A. and Bischoff, J.A. (1982) "Stabilization Of Rock Excavations Using Rock Reinforcement". in: Proceedings of the Symposium on Rock Materials, American Rock Mechanics Association, pp. 935–944.

Lang, T.A., Bischoff, J.A., (1983) "Research study of coal mine rock reinforcement": US Bureau of Mines report OFR 72-82, Jan 1981, 227P. International Journal of Rock Mechanics and Mining Sciences & Geomechanics Abstracts **20**, A27-A28.

Lee, S. W., Kang, S.-B., Tan, K. H., Yang, E.-H. (2016) “Experimental and analytical investigation on bond-slip behaviour of deformed bars embedded in engineered cementitious composites”. Construction and Building Materials **127**, 494-503.

Li, C. and Stillborg, B. (1999) "Analytical models for rock bolts". International Journal of Rock Mechanics and Mining Sciences **36**, 1013-1029.

Li, C.C. (2006) "Rock support design based on the concept of pressure arch". International Journal of Rock Mechanics and Mining Sciences **43**, 1083-1090.

Li, C.C. (2010) “A new energy-absorbing bolt for rock support in high stress rock masses”. International Journal of Rock Mechanics and Mining Sciences. **47**(3), 396-404.

Li CC, Stjern G, Myrvang A. (2014) “A review on the performance of conventional and energy-absorbing rockbolts”. Journal of Rock Mechanics and Geotechnical Engineering **6**(4), 315-327.

Li, C.C. (2017a) “Chapter Five - Rockbolting Design”, Rockbolting. Butterworth-Heinemann, pp. 125-176.

Li, C.C. (2017b) “Principles of rockbolting design”. Journal of Rock Mechanics and Geotechnical Engineering **9**, 396-414.

Li, C.C., Kristjansson, G., Høien, A.H. (2016) “Critical embedment length and bond strength of fully encapsulated rebar rockbolts”. Tunnelling and Underground Space Technology **59**, 16-23.

Li, C.C., Stjern, G., Myrvang, A., (2014) "A review on the performance of conventional and energy-absorbing rockbolts". Journal of Rock Mechanics and Geotechnical Engineering **6**, 315-327.

Li, C.C, (2010) “A new energy-absorbing bolt for rock support in high stress rock masses”. International Journal of Rock Mechanics and Mining Sciences **47**, 396-404.

Li, L., Hagan, P.C., Saydam, S., Hebblewhite, B., (2016) "Shear resistance contribution of support systems in double shear test". Tunnelling and Underground Space Technology **56**, 168-175.

Li, X., Nemcik, J., Mirzaghorbanali, A., Aziz, N., Rasekh, H., (2015) "Analytical model of shear behaviour of a fully grouted cable bolt subjected to shearing". International Journal of Rock Mechanics and Mining Sciences **80**, 31-39.

Lin, CT, Amadei, B, Jung, J, Dwyer, J. (1996) "Extension of discontinuous deformation analysis for jointed rock masses". International Journal of Rock Mechanics and Mining Sciences and Geomechanical Abstract **33**, 671–694.

Liu, J., Yang, H., Wen, H., Zhou, X. (2017) "Analytical model for the load transmission law of rock bolt subjected to open and sliding joint displacements". International Journal of Rock Mechanics and Mining Sciences **100**, 1-9.

Low, B.K. and Einstein, H.H. (2013) "Reliability analysis of roof wedges and rockbolt forces in tunnels". Tunnelling and Underground Space Technology **38**, 1-10.

Lü, Q., Chan, C.L., Low, B.K., (2012) "Probabilistic evaluation of ground-support interaction for deep rock excavation using artificial neural network and uniform design". Tunnelling and Underground Space Technology **32**, 1-18.

Lü, Q., Sun, H.-Y., Low, B.K. (2011) "Reliability analysis of ground–support interaction in circular tunnels using the response surface method". International Journal of Rock Mechanics and Mining Sciences **48**, 1329-1343.

Ma, S., Nemcik, J., Aziz, N., (2013) "An analytical model of fully grouted rock bolts subjected to tensile load". Construction and Building Materials **49**, 519-526.

Ma, S., Nemcik, J., Aziz, N., Zhang, Z., (2014) "Analytical model for rock bolts reaching free end slip". Construction and Building Materials **57**, 30-37.

Ma, S., Zhao, Z., Nie, W., Gui, Y. (2016) "A numerical model of fully grouted bolts considering the tri-linear shear bond–slip model". Tunnelling and Underground Space Technology **54**, 73-80.

Ma, S., Zhao, Z., Nie, W., Zhu, X. (2017) "An analytical model for fully grouted rockbolts with consideration of the pre- and post-yielding behaviour". Rock Mechanics and Rock Engineering **50**: 3019-3028.

MacLaughlin, M.M. and Doolin, D.M. (2006) "Review of validation of the discontinuous deformation analysis (DDA) method". International Journal for Numerical and Analytical Methods in Geomechanics **30**, 271-305.

McHugh, E., Signer, S., (1999) "Roof Bolt Response to Shear Stress: Laboratory Analysis", in: S. Peng and C. Mark (Ed.), 18th International Conference on Ground Control in Mining, Morgantown,WV, USA, pp. 232-238.

Mertoğlu, Ç., Anil, Ö., Durucan, C., (2016) "Bond slip behavior of anchored CFRP strips on concrete surfaces". Construction and Building Materials **123**, 553-564.

Moosavi, M., Grayeli, R. (2006) “A model for cable bolt-rock mass interaction: integration with discontinuous deformation analysis (DDA) algorithm”. International Journal of Rock Mechanics and Mining Sciences **43(4)**, 661–670

Moosavi, M., Jafari, A., Khosravi, A., (2005) "Bond of cement grouted reinforcing bars under constant radial pressure". Cement and Concrete Composites **27**, 103-109.

Mousavi, S.S., Dehestani, M., Mousavi, K.K., (2017). "Bond strength and development length of steel bar in unconfined self-consolidating concrete". Engineering Structures **131**, 587-598.

Napa-García, G.F., Santos, R.A., Beck, A.T., Celestino, T.B. (2018) “Improvement of analytical factor of safety estimation of falling failure mode in roof wedge stability”. International Journal of Rock Mechanics and Mining Sciences **103**, 116-122.

NGI (2015) Using the Q-system: Rock mass classification and support design. Postboks, Norway.

NHI (2009). Technical manual for design and construction of road tunnels – civil elements. U.S. Department of Transportation, Federal Highway Administration.

Nie, W., Zhao, Z.Y., Ma, S.Q., Guo W. (2018) “Effects of joints on the reinforced rock units of fully-grouted rockbolts”. Tunnelling and Underground Space Technology **71**, 15-26.

Nie, W., Zhao, Z.Y., Ning, Y.J., Guo, W. (2014a) “Numerical studies on rockbolts mechanism using 2D discontinuous deformation analysis”. Tunnelling and Underground Space Technology **41**, 223-233.

Nie, W., Zhao, Z.Y., Ning, Y.J. and SUN, J.P. (2014b) “Development of Rock Bolt Elements in Two-Dimensional Discontinuous Deformation Analysis”. Rock Mechanics and Rock Engineering **47**, 2157-2170.

Nie, W., Zhao, Z.Y., Ma S.Q., (2016) "Numerical evaluation of rockbolt reinforcement unit in joiuted rock mass by DDA method". In Reşat Ulusay, Ömer Aydan,Hasan Gerçek, Ali Mehmet Hindistan and Ergün Tuncay(Eds), Rock Mechanics and Rock Enineering: From the past to the future, Taylor & Francis Group, pp. 487-492.

Nie, W., Zhao, Z.Y., Ma, S.Q., Guo, W. (2018a) “Effects of joints on the reinforced rock units of fully-grouted rockbolts”. Tunnelling and Underground Space Technology **71**, 15-26.

Nie, W., Zhao, Z.Y., Goh, A.T.C., Song, M.K., Guo, W., Zhu, X. (2018b). “Performance based support design for horseshoe-shaped rock caverns using 2D numerical analysis”. Engineering Geology **245**, 266-279.

Ning, Y., Yang, J., An, X., Ma, G. (2011) "Modelling rock fracturing and blast-induced rock mass failure via advanced discretisation within the discontinuous deformation analysis framework". Computers and Geotechnics **38**, 40-49.

Nomikos, P.P., Sofianos, A.I., Tsoutrelis, C.E. (2002) "Structural response of vertically multi-jointed roof rock beams". International Journal of Rock Mechanics and Mining Sciences **39**, 79-94.

Nomikos, P.P., Yiouta-Mitra, P.V., Sofianos, A.I. (2006) "Stability of Asymmetric Roof Wedge Under Non-Symmetric Loading". Rock Mechanics and Rock Engineering **39**, 121-129.

Owen, D.R.J. and Hinton, E., (1980) Finite Elements in Plasticity: Theory and Practice. Pineridge Press, Swansea, UK

Özsan, A. and Başarır, H. (2003). "Support capacity estimation of a diversion tunnel in weak rock". Engineering Geology **3**, 319-331.

Palmstrom, A. (2000) "On classification systems". Proceedings GeoEng2000, Melbourne, Australia.

Pellet, F., Egger, P., (1996) "Analytical model for the mechanical behaviour of bolted rock joints subjected to shearing". Rock Mechanics and Rock Engineering **29**, 73-97.

Pellet, F., Roosefid, M., Deleruyelle, F. (2009) "On the 3D numerical modelling of the time-dependent development of the damage zone around underground galleries during and after excavation". Tunnelling and Underground Space Technology **24**, 665-674.

Potyondy DO, Cundall PA. (2004) "A bonded-particle model for rock". International Journal of Rock Mechanics and Mining Sciences **41**(8), 1329-64.

Ren, F.F., Yang, Z.J., Chen, J.F., Chen, W.W., (2010) "An analytical analysis of the full-range behaviour of grouted rockbolts based on a tri-linear bond-slip model". Construction and Building Materials **24**, 361-370.

Rocscience Inc. (2011) Phase2 Version 8.0 - Finite Element Analysis for Excavations and Slopes. www.rocscience.com, Toronto, Ontario, Canada.

Rong, G., Zhu, H.C., Zhou, C.B., (2004) "Testing study on working mechanism of fully grouted bolts of thread steel and smooth steel". Chinese Journal of Rock Mechanics and Engineering **23**, 469-475. (in Chinese)

Salcher, M. and Bertuzzi, R. (2018) “Results of pull tests of rock bolts and cable bolts in Sydney sandstone and shale”. Tunnelling and Underground Space Technology **74**, 60-70.

Sari, D. and Pasamehmetoglu, A.G. (2004) “Proposed support design, Kaletepe tunnel, Turkey”. Engineering Geology **72**, 201-216.

Serafim, J. L. and Pereira, J. P. (1983) “Considerations of the geomechanics classification of Bieniawski”. Proc. of the International Symposium on Engineering Geology and Underground Construction, Lisbon, A.A. Balkema, Rotterdam, the Netherlands. Vol. 1, 1133-1142.

Shi, G.H. (1988) “Discontinuous deformation analysis: A new numerical model for the statics and dynamics of block systems”. Ph.D. thesis, University of California, Berkeley.

Singer, S.P., (1990) “Field verification of load transfer mechanics of fully grouted roof bolts”. US Bureau of Mines, pp. 9301.

Sinha, R.S. (1989) Underground Structures: Design and Instrumentation. Elsevier, U.S.A.

Siren, T., Kantia and P., Rinne, M. (2015) “Considerations and observations of stress-induced and construction-induced excavation damage zone in crystalline rock”. International Journal of Rock Mechanics and Mining Sciences **73**, 165-174.

Stillborg, B., (1986). Professional users handbook for rock bolting. Clausthal-Zellerfeld, W. Germany : Trans Tech Publications.

Sun, J., Ning, Y., Zhao, Z. (2011) “Comparative study of Sarma's method and the discontinuous deformation analysis for rock slope stability analysis”. Geomechanics and Geoengineering **6**(4), 293-302.

Swoboda, G. (1979) “Finite element analysis of the New Austrian Cavernling Method (NATM)”. In: Proceedings of the 3rd International Conference on Numerical Methods in Geomechanics, Vol. 2, Aachen, 581–586.

Tan, C.H. (2016) “Passive bolts reinforcement around a circular opening in strain-softening elastoplastic rock mass”. International Journal of Rock Mechanics and Mining Sciences **88**, 221-234.

Tiryaki, B. (2008) “Predicting intact rock strength for mechanical excavation using multivariate statistics, artificial neural networks, and regression trees”. Engineering Geology **99**, 51-60.

Tsesarsky, M. and Hatzor, Y. H., 2006. "Tunnel roof deflection as a function of joint spacing and friction in blocky rock masses – a parametric study using Discontinuous Deformation Analysis (DDA)". Tunnelling and Underground Space Technology **21**, 29-45.

Vlachopoulos, N., Diederichs, M.S. (2009) "Improved Longitudinal Displacement Profiles for Convergence Confinement Analysis of Deep Tunnels". Rock Mechanics and Rock Engineering **42**, 131-146.

Vlachopoulos, N. and Diederichs, M.S. (2014) "Appropriate Uses and Practical Limitations of 2D Numerical Analysis of Tunnels and Tunnel Support Response". Geotechnical and Geological Engineering **32**, 469-488.

Windsor CR, Thompson AG. "Rock Reinforcement - Technology, Testing, Design and Evaluation". New York : Pergamon Press, 1993.

Windsor, C.R. (1997) "Rock reinforcement systems". International Journal of Rock Mechanics and Mining Sciences **34**, 919-951.

Wittke, W. (2014) "Stability of Rock Wedges and Excavation Surfaces", in: Wittke, W. (Ed.), Rock Mechanics Based on an Anisotropic Jointed Rock Model (AJRM).

Wu, J.H and Chen, C.H. (2011) "Application of DDA to simulate characteristics of the Tsaoling landslide". Computers and Geotechnics **38**, 741-750.

Wu, X., Jiang, Y., Gong, B., Deng, T., Guan, Z. (2018). "Behaviour of rock joint reinforced by energy-absorbing rock bolt under cyclic shear loading condition". International Journal of Rock Mechanics and Mining Sciences **110**, 88-96.

Yazici, S. and Kaiser, P.K. (1992) "Bond strength of grouted cable bolts". International Journal of Rock Mechanics and Mining Sciences & Geomechanics Abstracts **29**, 279-292.

Yeih, W., Huang, R., Chang, J.J., Yang, C.C. (1997) "A pullout test for determining interface properties between rebar and concrete". Advanced Cement Based Materials **5**, 57-65.

Yokota, Y., Zhao Z., Nie, W., Date K., Iwano K., Okada Y. (2018) "Interface behaviour along the boundary between the rock bolt and bond material", in: Eurock 2018 – The ISRM European Rock Mechanics Symposium, pp. 607–615.

Zhandarov, S. and Mäder, E. (2004). "Determining of interfacial parameters in fiber-polymer systems from pull-out test data using a bilinear bond law". Composite Interfaces **11**, 361-391.

Zhandarov, S., Mäder, E., (2016). "Determining the interfacial toughness from force–displacement curves in the pull-out and microbond tests using the alternative method". International Journal of Adhesion and Adhesives **65**, 11-18.

Zhang, X.P. and Wong, L.N.Y. (2014) "Displacement field analysis for cracking processes in bonded-particle model". Bulletin of Engineering Geology and the Environment **73**, 13-21.

Zhang, X.P. and Zhang, Q. (2017). "Distinction of Crack Nature in Brittle Rock-Like Materials: A Numerical Study Based on Moment Tensors". Rock Mechanics and Rock Engineering **50**(10), 2837-2845.

Zhang, W.G. and Goh, A.T.C. (2015) "Regression models for estimating ultimate and serviceability limit states of underground rock caverns". Engineering Geology **188**, 68-76.

Zhao, Z., Gu, J., Bao, H. (2007) "Understanding fracture patterns of rock mass due to blast load – a DDA approach. Ju, Y., Fang, X. and Bian H. (Eds.) Proceedings of the Eighth International Conference on the Analysis of Discontinuous Deformation., Beijing, China, 147-150.

Zhao, Z. Y., Zhang, Y., Liao H. J. (2008) "Design of ensemble neural network using Akaike information criterion". Engineering Application of Artificial Intelligence **21**(8), 1182-1188.

Zhou, Y., Teo, T.Y., Cai, J.G. (2017) "Rock engineering practice for development of underground caverns in Singapore". GeoSS 10th Anniversary Conference, Sinagpore.

Zhu, C., Chang, X., Men, Y., Luo, X. (2015) "Modeling of grout crack of rockbolt grouted system". International Journal of Mining Science and Technology **25**, 73-77.

APPENDIX A

MATLAB PROGRAM FOR MAPPING THE RELATIONSHIP BETWEEN THE SEM DESIGNS AND THE SUPPORT PERFORMANCES

```
%%TITLE: ANN model for mapping the SEM parameters and performance
%Inputs: P1-ground class, P2-width of heading, P3-height of heading, P4-round length
%Target: O1-roof displacement (or O2-normal stress, O3-damage depth)
%Structure: 4-n-1, n is a variable in the program
%Treat the inputs and output with pre-set max. and min. values
%          P1    P2      P3      P4              O1      O2      O3
% Max:  40    40      54      50      ||      0.3     10      50
% Min:  0.1   3       5       0       ||      0       0       0
% Outcomes: (a) the structure of the ANN model will be determined based on the R^2
%                   (b) the weights and bias will be used in the further adoption of the model
%Note: The normalizations are preprocessed when generate data sets.
%          Thus, this code is not including normalization

%%
clear all;
clc;
%%
X1=load('1.txt');
%---------------------------------- Examples ----------------------------------
% -1.00000     -0.85294        -0.99804        -0.99285        -0.91973
%-1.00000      -0.85294        -0.99804        -0.96978        -0.87113
%-1.00000      -0.85294        -0.99804        -0.91578        -0.82187
```

```
%-1.00000    -0.85294    -0.99804    -0.83644    -0.78487
%-1.00000    -0.85294    -0.99804    -0.71450    -0.68913
%-1.00000    -0.85294    -0.99804    -0.26610    -0.62327
%-1.00000    -0.98529    -0.99804    -0.99285    -0.94667
% …
%%
[M,N]=size(X1);
Y1=X1(:,1:4)';          %inputs
O1=X1(:,5)';            %target

[fid,message]=fopen('weight.txt','w');
if fid==-1
   disp(message);
end
%%
trainRatio=0.7;
testRatio=0.3;
hiddenminno1=6;
hiddenminno2=6;
%%
maxepoch=500;
fb=10;                  %
if(trainRatio+testRatio>1.0)
   disp('total ratio>1');
end

% hiddenminno (3 ~ 8) is a variable to determine the numbers of hidden nodes
% in each case, fb = 10 times of training and testing are carried out
for hiddenminno=3:1:8
     for run=1:1:fb
          [trainInd,valInd,testInd] = dividerand(M,trainRatio,valRatio,testRatio);
          traininput1=Y1(:,trainInd);
          traintarget1=O1(:,trainInd);
          traininput=traininput1;
```

```
traintarget=traintarget1;
% testing data
testinput1=Y1(:,testInd);
testtarget1=O1(:,testInd);
%assign same normalization as training
testinput = testinput1;
testtarget = testtarget1;
%%
% 'attrno' is the number of attributes,
%'trainexpno' is the number of training examples
[attrno,trainexpno] = size(traininput);
%%
% train the neural networks
net = newff(minmax(traininput),[hiddenminno 1],{'tansig' 'tansig'});
        net.trainParam.epochs = maxepoch;
        net.trainParam.goal = 0.0;
        net.trainParam.max_fail=100;
        net.trainParam.min_grad=1e-15;
        net.trainParam.mu_max=1e20;
        net.trainParam.mu_dec=0.7;
        net.trainParam.mu_inc=1.03;
        net.trainParam.lr=0.01;
        net.trainParam.show=10;
[net,tr] = train(net,traininput,traintarget);
%%
fprintf(fid,'run = %d \n',run);
fprintf(fid,'span\tbenching-h\tQ-value\tdistance\tbias1\troof-disp\tbias2\n');
%The weights to layer i from input j are net.IW{i,j}.
 w1=net.iw{1,1}
 b1=net.b{1}
 w2=net.lw{2,1}
 b2=net.b{2}
%%
for i=1:1:hiddenminno
```

```
        for j=1:1:4
            fprintf(fid,'%f\t',w1(i,j));
        end
        fprintf(fid,'%f\n',b1(i));
    end
    for i=1:1:hiddenminno
        fprintf(fid,'%f\t',w2(i));
    end
    fprintf(fid,'%f\n',b2);
    %%
    % test the model
    [m,trexpno] = size(traininput);
    output2 = zeros(trexpno);
    output2 = sim(net,traininput);
    [n,testexpno] = size(testinput);     % 'testexpno' is the number of test examples
    output1 = zeros(testexpno);
    output1 = sim(net,testinput);
    [l,allexpno]=size(Y1);
    output = zeros(allexpno);
    output = sim(net,Y1);
    %%
    % training data showing
    [m1,b1,r1]=postreg(output_tr(1,:),traintarget1(1,:));
    mse_te1 = mse(output_tr(1,:) - traintarget1(1,:)); % the mean squared error of
the ensemble
    fprintf(fid,'Training single hidden=%g  ',hiddenminno);
    fprintf(fid,'r1=%-12.5g   mse_te_O=%-12.5g ', r1, mse_te1);
    fprintf(fid,'\n');%%
    saveas(gcf,num2str(run*3-1),'jpg');
    %testing data showing
    [m2,b2,r2]=postreg(output_te(1,:),testtarget1(1,:));
    mse_tr2 = mse(output_te(1,:) - testtarget1(1,:));
    fprintf(fid,'Testing single hidden=%g  ',hiddenminno);
    fprintf(fid,'r2=%-12.5g   mse_te_O=%-12.5g ', r2, mse_tr2);
```

```
        fprintf(fid,'\n');%%
        saveas(gcf,num2str(run*3-2),'jpg');
        %all data showing
        figure;
        [m3,b3,r3]=postreg(output,O1);
        mse_t3 = mse(output-O1);
        fprintf(fid,'All double hidden=%g',hiddenminno);
        fprintf(fid,'r3=%-12.5g   mse_t_O=%-12.5g ', r3, mse_t3);
        fprintf(fid,'\n\n');
        saveas(gcf,num2str(run*3),'jpg');
    end
end
fclose(fid);
%%
%-------------Examples of the 'weight.txt' file--------
```

```
run = 1
span    benching-h  Q-value distance    bias1    p1  p2  p3  p4  p5  p6  bias2
-0.874875   -0.023479   0.743237    -3.414145   -4.604178
-0.335203   0.030200    0.179569    0.520864    0.268795
-0.876515   1.842096    -17.693453  -0.418437   20.876628
-0.804022   -0.151996   0.749273    -3.154846   -4.400650
-0.843004   -0.086953   0.748501    -3.277270   -4.494313
482.140385  -1.789533   247.006190  484.477759  -959.760906 -242.135865
Training double hidden=5 r1=0.97747        mse_te_O=0.0015271
Testing double hidden=5r2=0.9512         mse_te_O=0.0033692
All double hidden=5r3=0.96894        mse t O=0.0020855
```

```
%....
```